Unveiling the Role of Interstellar Filaments in Massive Star Formation

A thesis submitted

in partial fulfilment of the requirements

for the degree of

Doctor of Philosophy

by

Naval Kishor Bhadari

(Roll No. 18330016)

Under the Supervision of

Dr. Lokesh Kumar Dewangan

Associate Professor

Astronomy & Astrophysics Division

Physical Research Laboratory, Ahmedabad, India

Department of Physics

Indian Institute of Technology Gandhinagar

2023

To my beloved Nana-Nani

DECLARATION

I, **Naval Kishor Bhadari (Roll No: 18330016)**, hereby declare that, this thesis titled **"Unveiling the Role of Interstellar Filaments in Massive Star Formation"** submitted to Indian Institute of Technology Gandhinagar towards partial requirement of **Doctor of Philosophy** in **Physics** is an original work carried out by me under the supervision of **Dr. Lokesh Kumar Dewangan** at Physical Research Laboratory, Ahmedabad, India. I have sincerely tried to uphold the academic ethics and honesty. Whenever an external information or statement or result is used, every effort is made to indicate this clearly, with due reference to the literature.

Date:

Naval Kishor Bhadari

CERTIFICATE

This is to certify that the work presented in this thesis titled **"Unveiling the Role of Interstellar Filaments in Massive Star Formation"** submitted by **Naval Kishor Bhadari** (**Roll No: 18330016**) to Indian Institute of Technology, Gandhinagar has been carried out by him under my supervision and it has not been submitted elsewhere for the award of any degree.

Date:

Dr. Lokesh Kumar Dewangan

(Thesis Supervisor)

Associate Professor

Astronomy & Astrophysics Division

Physical research Laboratory

Navarangpura, Ahmedabad, India

Contents

ACKNOWLEDGEMENT

First and foremost, I would like to express my deepest gratitude to my thesis supervisor, Dr. Lokesh Kumar Dewangan. His unwavering support, guidance, and mentorship have been invaluable throughout my learning, studies, and PhD work. Not only has he helped shape my academic journey, but he has also played a significant role in shaping me as a person. His constant motivation to aim high in my career and his willingness to share his own experiences have played a pivotal role in shaping my personal and academic growth. I am truly indebted to his guidance, as this thesis would not have reached its current stage without him.

I am immensely grateful to my DSC members, Dr. Arvind Singh Rajpurohit, Dr. Sanjay Kumar Mishra, and Dr. Vishal Joshi, for their constant support during my PhD journey. They have not only served as mentors but also as friendly and encouraging individuals. I must highlight Arvind, whose friendly demeanor and passion for sports have made our interactions a delightful combination of guidance and laughter. He has consistently encouraged me to strike a balance between work and leisure. I am grateful to my collaborators, especially Prof. Devendra Ojha. His support and guidance have been invaluable throughout this journey, and I've learned important lessons in time management from him. I deeply appreciate Prof. Lev Pirogov's prompt and supportive email responses and marathon discussion over research problems, and Dr. Saurabh Sharma's assistance during my visit to ARIES. Special thanks to collaborators Dr. Tapas Baug, Peter, Dr. Alexander Men'shchikov, Andray, Devaraj, Prof. Igor Zinchenko, Dr. Eswaraiah, and others for their invaluable contributions. I would also like to extend my thanks to my thesis reviewers whose insightful comments enhanced the quality of this thesis.

I sincerely thank the director, dean, academic committee, and division faculties of my parent institution, PRL, for providing me the opportunity to pursue research in my field of interest and for their unwavering support throughout my PhD journey. I also express my gratitude to all the faculties and staff members of PRL, specifically the Astronomy and Astrophysics division, for their continuous support and fruitful interactions. Special mention goes to Priti ma'am, Vaibhav *bhai, and Dr. Nurul Alam for their prompt support whenever needed. I express my gratitude to the individuals in the accounts, purchase, library, administration, canteen, CMD, dispensary, transport, and housekeeping departments for their invaluable assistance throughout my PhD tenure.*

I would like to acknowledge the online facilities NASA ADS, SIMBAD, IRSA data archive, and Python libraries, as without them, this work would not have been possible. My heartfelt gratitude goes to all those who have contributed to the development of these exceptional tools and have played a crucial role in telescope operations. Special mention goes to Arup, my brother and junior, for his invaluable contribution in proof reading of the thesis. Additionaly, his sense of humor always lighten the office environment. I must also mention Dr. Sushant Dutta (Sushi da), a constant supporter whose helpful nature, witty talks, and guidance have made him like an elder brother to me. I cannot express my gratitude enough to Dr. Abhijit Kayal, who always extends his help and has taught me the value of patience. I would like to acknowledge the presence of other past office mates, including Vipin, Rakesh da, Parveen bhai, Aditya (all Drs.), whose company has made the office a joyful place.

I consider myself incredibly fortunate to have a garden full of wonderful friends among my batchmates. It's difficult to prioritize them, as each one is unique and loving in their own way. Vikas, with whom I spent most of my time exploring Ahmedabad on cycles and improving my badminton skills. Yash, with whom I shared delightful meals and engaging table tennis matches, and Daya, my companion in few, but endless talks leading to enlightening conclusions. Learning swimming was the most exciting time we all shared together. Deepak Rai, Sandeep, Sunil, Pranav, Yogesh have created cherished memories during our senseless discussions on various personal and current topics. The list of friends is long and includes Sanjeet, Devaprasad, Deepak, Arijit, Supriyo, Siddharth, Naba, Partha, Anupam, and more. Among my female friends, I hold precious memories of our time together. Namita and Akanksha, have been amazing companions for discussions on life issues and ongoing research. Anju and Monika always bring a lightness to our conversations, and Meghna and Binal have been incredibly sweet *and joyful to be around. I would like to acknowledge the presence of my all juniors and seniors, whose companionship has created a harmonious environment. Special mention to Ankit, Sandeep, Subir da, Aravind, Abhay, Biswajit, Partha, Sana, Neeraj, Alka, Shanwlee, Birendra, Vineet, Sandipan, Goldy, Omkar, Varsha, Malika, Ashish, Trinesh, Saumya, Tanya, Sanjay, Arijit, Archita di, Nisha di and more... Maintaining constant contact with my school and MSc friends throughout my PhD journey has greatly contributed to its smoothness, and I am grateful to all of them for being such wonderful friends.*

When it comes to acknowledging the backbone of my journey, I must mention my school and college teachers. Special thanks to Dr. K. D. Purohit whose MSc astronomy course led me to pursue PhD in this field. All of my school teachers were skilled goldsmiths, shaping me into someone capable of achieving great things. Special mention to Jamal guruji, Badoni, Semwal, Maithani guruji, and Kothiyal acharyaji for always inspiring and their friendly behavior.

Last but not the least, I am immensely grateful to my loving and supportive family, who have been there for me every step of the way. My mother and nanaji have been my pillars of support, and I am thankful for their unwavering encouragement. I also want to express my gratitude to my nani, mamaji, mousi, and papa for their love and care. My sisters, Kavi and Savi, have been a constant source of care and support. A special mention goes to my little sister, Khushi, whose genuine interest in my research and loving nature have brought joy to my life. I wish her all the success in her own endeavors. Lastly, I cannot find enough words to thank my close friend Rim for her constant engagement and conversations that have played a significant role in bringing me this far.

Once again, I express my deepest gratitude to everyone mentioned above and all those whose names I may have inadvertently missed. Your contributions, support, and presence in my life have made this thesis journey meaningful and memorable. Thank you all!

Naval

ABSTRACT

Massive stars ($M_\star$ $\geq$8 $M_\odot$) play a crucial role in structural and chemical evolution of galaxies, yet their formation processes are still not fully understood. The problem remains unsettled because of theoretical as well as observational challenges. The high radiation pressure exerted by young massive stars limits their maximum mass. On the other hand, these stars generally found to be deeply embedded in the clustered environments located at far distances ($d \gtrsim$1 kpc). A rapid evolution of young massive stars compared to their low-mass counterparts limits their observed population. Therefore, a systematic process explaining the formation of a massive star is necessary.

Recent observations, most prominently after the launch of *Herschel Space Observatory*, unravel that the interstellar medium (ISM) is full of web-like elongated gaseous/dusty features (i.e., filaments) that span from the size of protostellar envelope ($\sim$0.1 pc) to the extent of a giant molecular cloud ($\sim$100 pc). These filaments are universal in the ISM and often found to be linked with the star-forming sites, embedded clumps, H II regions, and the clusters of young stellar objects (YSOs). How these filaments play a role in the formation of stars and star clusters is still a topic of debate. Furthermore, studying the the link between filaments and the massive star-forming sites can improve our understanding of the physical processes of mass accumulation involved in massive star formation (MSF).

This thesis explores the potency of interstellar filaments in the mass accumulation processes of MSF. It combines multi-scale and multi-wavelength dust continuum and line data to study the gas kinematics and physical environments of filaments and the ongoing star formation activities within them. The range of specific objectives includes observational assessment of a rare recent theoretical models of the End-dominated collapse (EDC) process in filaments, studying MSF in a hub-filament system (HFS), investigating the coexistence of multiple physical processes of star formation within a single filamentary cloud system, exploring the innermost region of a hub in an HFS, and examining the interactions of massive stars with their surrounding environment. The thesis presents the

results derived from the analysis of multi-scale and multi-wavelength data of six star-forming sites: RAFGL 5085 (d =3.3 kpc), Monoceros R1 (d =760 pc), GMF G45.3+0.1 (d =8 kpc), IC 5146 dark Streamer (d =600 pc), W42 region (d =3.8 kpc), and S305 Hii region (d =3.7 kpc) in chronological order. The Key findings from this thesis include the identification of a prominent HFS in RAFGL 5085, consisting of a central massive clump ($\sim$225 $M_\odot$) surrounded by multiple parsec-scale filaments with longitudinal velocity gradients. RAFGL 5085 is found to be a promising candidate HFS hosting the early stages of MSF prior to the influence of UV radiation from the compact Hii region. The analysis of ^{12}CO/^{13}CO line data in the Monoceros R1 complex reveals a supercritical filamentary cloud named Mon R1 filament ($\sim$1465 $M_\odot$, length $\sim$14 pc) at $V_{\rm LSR} \sim -2$ km s^{-1}. The higher surface density of YSOs and relatively large velocity gradients ($\sim$0.6 km s^{-1} pc^{-1}) at both the ends of filament support the onset of EDC process. A giant molecular filament, GMF G45.3+0.1 ($\sim$1.1$\times$10^6 $M_\odot$, length $\sim$75 pc), is discovered exhibiting signatures of both EDC and HFSs, with a $V_{\rm LSR}$ of $\sim$58 km s^{-1}. The HFSs are primarily found at the ends of GMF G45.3+0.1. In addition to the HFSs and EDC signatures, the intertwined sub-filaments in IC 5146 dark Streamer are observed in the derived high-resolution column-density map ($\sim$13$''$.5). The curved magnetic fields in nearby EDC filaments is found to be a new and novel indicator of the EDC process. The inner environment of a known HFS in the W42 region, hosting a massive protostar, highlights the role of turbulence and supports the hierarchical and chaotic collapse scenario. The collisions between two ridges in the S305 Hii region (with $V_{\rm LSR}$ of $\sim$42 and $\sim$45 km s^{-1}) may have formed the known massive stars. The [Cii] 158 μm line data further unlocked the expanding neutral shells ($V_{\rm exp} \sim 1.3$ km s^{-1}) that triggered the dense clump formation at the boundary of S305 Hii region supporting the "collect and collapse" scenario of triggered star formation.

Overall, this thesis contributes to our current understanding of the complex processes involved in the MSF within interstellar filaments. The insights gained from this research provide a foundation for future investigations and shed light on the new intricate mechanisms driving MSF in the ISM.

List of Publications

Part of this Thesis

1. **Bhadari, N. K.**, Dewangan, L. K., Pirogov, L. E., Ojha, D. K., 2020, ApJ, 899, 167, "Star-forming sites IC 446 and IC 447: an outcome of end-dominated collapse of Monoceros R1 filament".

2. **Bhadari, N. K.**, Dewangan, L. K., Zemlyanukha, P. M., Ojha, D. K., Zinchenko, I. I., Sharma, Saurabh, 2021, ApJ, 922, 207, "Probing gas kinematics and PDR structure around O-type stars in Sh 2-305 HII region".

3. **Bhadari, N. K.**, Dewangan, L. K., Ojha, D. K., Pirogov, L. E., Maity, A. K., 2022, ApJ, 930, 169, "Simultaneous evidence of edge collapse and hub-filament configurations: A rare case study of a Giant Molecular Filament G45.3+0.1".

4. Dewangan, L. K., **Bhadari, N. K.**, Men'shchikov, A., Chung, E. J., Devaraj, R., Lee, C. W., Maity, A. K., Baug, T., 2023, ApJ, 946, 22, "IC 5146 Dark Streamer: The First Reliable Candidate of Edge Collapse, Hub-filament Systems, and Intertwined Sub-filaments".

5. Dewangan, L. K., **Bhadari, N. K.**, Maity, A. K., Pandey, Rakesh, Sharma, Saurabh, Baug, T., Eswaraiah, C., 2023, JApA, 44, 23, "Star-forming site RAFGL 5085: Is a perfect candidate of hub-filament system?".

6. **Bhadari, N. K.**, Dewangan, L. K., Pirogov, L. E., Pazukhin, A. G., Zinchenko, I. I., Maity, A. K., Sharma, Saurabh, 2023, MNRAS, 526, 4402, "Fragmentation and dynamics of dense gas structures in the proximity of massive young stellar object W42-MME".

Contributory

7. Dewangan, L. K., Ojha, D. K., Sharma, Saurabh, del Palacio, S., **Bhadari, N. K.**, Das, A., 2020, ApJ, 903, 13, "New insights in the HII region G18.88-0.49: hub-filament system and accreting filaments".

8. Zinchenko, I. I., Dewangan, L. K., Baug, T., Ojha, D. K., Bhadari, N. K., 2021, MNRAS: Letters, 506, 45, "ALMA discovery of a dual dense probably rotating outflow from a massive young stellar object G18.88MME".

9. Dewangan, L. K., Dhanya, J. S., **Bhadari, N. K.**, Ojha, D. K., Baug, T., 2021, MNRAS, 506, 6081, "Lynds Bright Nebulae: Sites of possible twisted filaments and ongoing star formation".

10. Maity, A. K., Dewangan, L. K., Sano, H., Tachihara, K., Fukui, Y., **Bhadari, N. K.**; 2022, ApJ, 934, 2, "Unraveling the observational signatures of cloud-cloud collision and hub-filament systems in W31".

11. Dewangan, L. K., Pirogov, L. E., **Bhadari, N. K.**, Maity, A. K., 2022, MNRAS, 516, 2988, "Ionized filaments and ongoing physical processes in star-forming sites around l = 345.5 degree".

12. Maity, A. K., Dewangan, L. K., **Bhadari, N. K.**, Ojha, D. K., Chen, Z., Pandey, Rakesh, 2023, MNRAS, 523, 5388, "AFGL 5180 and AFGL 6366S: sites of hub-filament systems at the opposite edges of a filamentary cloud".

13. Dewangan, L. K., Maity, A. K., Mayya, Y. D., **Bhadari, N. K.**, Bhattacharyya, Suman, Sharma, Saurabh, Banerjee, Gourav, 2023, ApJ, 958, 51D, "New Insights in the Bubble Wall of NGC 3324: Intertwined Substructures and a Bipolar Morphology Uncovered by JWST".

14. Dewangan, L. K., **Bhadari, N. K.**, Maity, A. K., Eswaraiah, C., Sharma, Saurabh, Jadhav, O. R., 2024, MNRAS, 527, 5895, "Galactic 'Snake' IRDC G11.110.12: a site of multiple hub-filament systems and colliding filamentary clouds".

Under Preparation

15. **Bhadari, N. K.**, Dewangan, L. K., et al. "Multiwave-length investigation of star formation activities toward S306 and S309 H II region"(*under preparation*).

List of Abbreviations

ALMA Atacama Large Millimeter/submillimeter Array

AU Astronomical Unit

ATLASGAL APEX Telescope Large Area Survey of the Galaxy

cm Centimeter

CMF Core Mass Function

CCC Cloud-Cloud Collision

CCD Color-Color Diagram

CMD Color-Magnitude Diagram

CADC Canadian Astronomy Data Centre

CHIMPS $^{13}CO/C^{18}O$ (J = 3→2) Heterodyne Inner Milky Way Plane Survey

DSS2 Digitized Sky Survey II

EUV Extreme Ultraviolet

EDC End-Dominated Collapse

FIR Far-Infrared

FUV Far-Ultraviolet

FWHM Full Width at Half Maximum

FUGIN FOREST Unbiased Galactic plane Imaging survey with the Nobeyama 45-m telescope

GMC Giant Molecular Cloud

GPS Galactic Plane Survey

GMF Giant Molecular Filament

GMRT Giant Metrewave Radio Telescope

GHC Global Hierarchical Collapse

GLIMPSE *Spitzer* Galactic Legacy Infrared Mid-Plane Survey Extraordinaire

GRSMC Galactic Ring Survey Molecular Cloud

GNIC Global Nonisotropic Collapse

HFS Hub Filament System

HMSC High-Mass Starless Core

HGBS *Herschel* Gould Belt Survey

Hi-GAL *Herschel* Infrared Galactic Plane Survey

HC Hypercompact

IC Index Catalogue

IR Infrared

IMF Initial Mass Function

IRDC Infrared Dark Cloud

ISM Interstellar Medium

IRAS Infrared Astronomical Satellite

JCMT James Clerk Maxwell Telescope

kpc kilo-parsec

LSR Local Standard of Rest

MCSs Millimeter Continuum Sources

MHD Magneto Hydrodynamics

MIR Mid-Infrared

MYSO Massive Young Stellar Object

MME	Methanol Maser Emission
mm	Millimeter
MSF	Massive Star Formation
MIPSGAL	MIPS Inner Galactic Plane Survey
MWISP	Milky Way Imaging Scroll Painting
NIR	Near-Infrared
NN	Nearest Neighbor
NVSS	NRAO VLA Sky Survey
PACS	Photoconductor Array Camera and Spectrometer
PAH	Polycyclic Aromatic Hydrocarbon
PCC	Pearson Correlation Coefficient
PV	Position-Velocity
PPV	Position-Position-Velocity
PP	Position-Position
PPP	Position-Position-Position
pc	parsec
PDR	Photo Dissociation Region
PSF	Point Spread Function
RAFGL	Revised Air Force Geophysical Laboratory
RMS	Root Mean Square
SED	Spectral Energy Distribution
SFR	Star-forming Regions
SPIRE	Spectral and Photometric Imaging Receiver
submm	Sub-Millimeter
SOFIA	Stratospheric Observatory for Infrared Astronomy
TRAO	Taeduk Radio Astronomy Observatory

2MASS	Two Micron All Sky Survey
UC	Ultracompact
uGMRT	Upgraded Giant Metrewave Radio Telescope
UV	Ultraviolet
UKIDSS	UKIRT Infrared Deep Sky Survey
VLT	Very Large Telescope
VSF	Velocity Structure Function
WISE	Wide Field Infrared Survey Explorer
YSO	Young Stellar Object

List of Figures

List of Tables

Chapter 1

Introduction

Stars are universally known celestial objects that serve as the fundamental constituents of galaxies. They form in the densest and coolest regions of the interstellar medium (ISM) throughout the Galaxy and primarily consists of gas, dust, and cosmic rays. Hydrogen, a most abundant element (approximately 70% by mass; Smith, 2004) in the visible Universe exists in three different forms such as molecular hydrogen (H_2), atomic hydrogen (H I), and ionized hydrogen (H II). The majority of the remaining mass is contributed by helium and all other heavier elements (or collectively referred to metals in astrophysics). Molecular clouds, comprising a small volume fraction (∼2–4%; Smith, 2004) among the various phases of the ISM, play a crucial role as potential sites for star formation (Kennicutt & Evans, 2012). Apart from H_2, molecular clouds include CO, OH, H_2O, HCN, NH_3, and other complex organic (carbon based) molecules.

In general, by mass, stars are categorized as low-mass stars ($M_\star \leq 2\ M_\odot$), intermediate-mass stars ($2 < M_\star < 8\ M_\odot$), and the major focus of this thesis, high-mass (or massive) stars ($M_\star \geq 8\ M_\odot$). This distinction is primarily based on the Chandrasekhar limit (remnant core mass $\sim$1.4 $M_\odot$) so that the progenitor massive star undergoes core collapse supernova during its death and forms either a neutron star ($M_\star \sim 8 - 25\ M_\odot$) or a black hole ($M_\star > 25\ M_\odot$). Stars of all masses are primarily formed in clustered environments (Lada et al., 2003), sharing similar ages and chemical compositions. In later stages, these star clusters may remain bound system (e.g., globular clusters) or disperse (e.g., open clusters) to contribute the field population stars. Therefore, studying the physical environment of star-forming sites may disclose their formation processes and the history of galactic evolution.

1.1 General picture of star formation in molecular clouds

Molecular clouds as mentioned in previous section are composed of dust and gas and differ from one another based on the variation in their physical properties (e.g., number density, temperature, size, and extinction). Giant molecular clouds (GMCs) are the largest molecular cloud structures of mass 10^5–$10^6 M_\odot$, density $\sim 100 - 300$ cm^{-3}, and size ∼50–100 pc. Within GMCs, the smaller scale sub-structures are either referred to as clouds (>10 pc), clumps (∼1–3 pc), and cores (<0.1 pc; e.g., Smith, 2004)[1]. Some clouds appear darker at infrared (IR) wavelengths are known as infrared dark clouds (IRDCs) and serve as a potential sites of massive star formation (MSF; e.g., Rathborne et al., 2006). Chapter 6 presents the investigation of MSF in such a site.

A prevailing question is how substructures form within a molecular cloud in the first place and why stars form within smaller-sized cores compared to much larger-sized clump structures. The answer to this lies in the role of supersonic turbulence and its interplay with gravity (e.g., Krumholz, 2014; Krumholz & Burkhart, 2016). Some earlier works describe turbulence as the "one in which velocity at any point fluctuates irregularly" (McKee & Ostriker, 2007) or "non linear fluid motion, resulting in the excitation of an extreme range of correlated spatial and temporal scales" (Elmegreen & Scalo, 2004). The energy from the large scale generally translates to the smaller scales and sustain the observed turbulence level seen in observations and simulations of molecular clouds (e.g., Ballesteros-Paredes, 2004; Krumholz & McKee, 2005; Ballesteros-Paredes et al., 2006). These power suppliers can be in the form of galactic shear, gravitational instability in spiral arms, collision between clouds, outflows from young stars,

[1] These values represent typical figures commonly used in research community.

stellar winds/radiation, and supernova explosions (Smith, 2004). Therefore, the turbulence in molecular clouds introduces velocity fluctuations that play a crucial role in shaping the density structure of the cloud. These fluctuations lead to density variations, which are essential for initiating star formation. The substructures reach a critical point where the gravitational force overcomes the counteracting effects of turbulence, thermal pressure, and magnetic field, the collapse process is started, ultimately giving rise to the formation of stars.

In general, stars can form through two main mechanisms: spontaneous and triggered. In spontaneous star formation, stars form without any specific trigger or external agent initiating the process. This mode of formation is considered an ideal assumption, although there may be underlying mechanisms yet to be observed, which primarily depend on the shape of the molecular cloud (e.g., Section 1.3). However, in a real scenario, all the star formation processes seem to be driven by the presence of external feedback agents or triggering mechanisms to initiate star formation process within molecular clouds. Examples of such triggering agents include the radiative and mechanical feedback from existing massive stars, such as the expansion of ionized regions (H II regions) or supernova explosions. Galactic shear and supersonic collisions between clouds are also triggering agents (see Elmegreen, 1998, for an overview of triggered star formation).

The conditions for the cloud to collapse and form the stars were first given by Sir James Jeans (1877–1946) in 1902. A simplifying assumption is considered in the analysis neglecting the effects due to turbulence, galactic magnetic field, and cloud rotation. For a spherical cloud in hydrostatic equilibrium the governing equation is:

$$\frac{dP(r)}{dr} = -\frac{G\rho(r)m(r)}{r^2} \tag{1.1}$$

where, r is the radius of spherical cloud enclosing mass $m(r)$, $\rho(r)$ is the gas density at radius r, $P(r)$ is the outward pressure exerted by gas due to its kinetic energy, and G is the gravitational constant. The cloud will become gravitationally unstable when its gas kinetic energy fails to balance the gravitational potential energy. In this case the cloud begins to contract once it overcomes the critical mass limit and continues collapsing unless opposing force impedes the collapse.

This critical mass is known as Jean's mass and can be derived from Equation 1.1 and expressed as (e.g., Shu et al., 1987):

$$M_J = \left(\frac{5k_bT}{\mu m_H G}\right)^{3/2}\left(\frac{3}{4\pi\rho_0}\right)^{1/2} \tag{1.2}$$

where, T is the gas temperature, k_b is the Boltzman's constant, ρ_0 is the initial gas density, μ is the mean molecular weight, m_H is the mass of hydrogen atom, and G is defined earlier. Such a spherical gas cloud of uniform density ρ will collapse under its self gravity and without any pressure support on a time scale of

$$t_{\rm ff} = \sqrt{\frac{3\pi}{32\rho G}}, \tag{1.3}$$

which resulted in $\sim 4 \times 10^5$ yr, for the initial density of $\sim 10^4$ cm^{-3}.

For a significant period, the prevailing assumption was that molecular clouds had a near-spherical shape. However, recent observational results support the existence of arbitrary structures within molecular clouds, where the simple Jeans formalism may not be applicable (e.g., Section 1.2). Additionally, the inclusion of other factors such as turbulence and magnetic fields may further complicate the problem. Nevertheless, it is still believed that local variations in the density distribution can lead to the formation of small gravitationally unstable condensations (∼0.1 pc), where subsequent stages of star formation take place.

1.1.1 Low-mass star formation

In the previous sections, we learned about the substructures within molecular clouds, namely clumps and cores, which are formed as a result of the combined effects of self-gravity and turbulence in the ISM. The cores, which are the ultimate structures, undergo gravitational collapse to form single or multiple stars. These cores can be categorized as starless, prestellar, and protostellar cores (Smith, 2004).

A starless core refers to a dense core that does not contain any embedded stars. However, these cores may have a less centrally condensed structure and could be either gravitationally collapsing or on the verge of dispersing. The starless cores that are gravitationally bound and prone to collapse are known as prestellar cores. These cores often exhibit infall motion and have centrally peaked structures. Protostellar cores, on the other hand, are cores that host developing self-luminous sources (e.g., Enoch et al., 2008). When a prestellar core undergoes collapse, it initially maintains a relatively constant temperature (isothermal collapse) around 15 K, with densities ranging from 10^4 to 10^{11} cm^{-3}. The radiative cooling through reprocessed dust emission at millimeter (mm) wavelengths is efficient during this phase. However, as the collapse progresses, the density increases, resulting in higher radiation opacity, which heats the central regions. At this stage, the collapse transits from isothermal to adiabatic, and a phase known as the "first hydrostatic core" forms when thermal pressure is able to counteract gravity. This occurs at densities around 10^{13} to 10^{14} cm^{-3} and temperatures of 100-200 K. During the adiabatic collapse at temperatures of around 2000 K, molecular hydrogen dissociates, requiring energy due to its endothermic nature. This leads to a brief gravitational collapse. Once all the H_2 is dissociated, the collapse is halted again, resulting in the formation of a more compact core (density around 10^{23} cm^{-3} and temperature around 10^4 K), referred to as a protostellar core. Subsequently, material accretion continues from the protostellar envelope onto the central protostar (Smith, 2004).

The evolution from the protostellar core to young stars can be traced through observations across the wavelength range from near-infrared (NIR) to sub-millimeter (sub-mm) wavelengths. These baby stars show excess emission at IR bands due to the presence of dusty circumstellar environment, hence, also known as IR-excess sources. Generally, four broad classes of protostars, also known as young stellar objects (YSOs), are discussed based on their geometry and spectral energy distribution (SED). These are classified as Class 0, I, II (also known as classical T-Tauri stars), and III (weak-line T-Tauri stars) YSOs, as shown in Figure 1.1 (e.g., Andre et al., 1999). The youngest protostars are designated as Class 0 YSOs, which subsequently evolve into the phases of Class I, II, and III YSOs before becoming main-sequence stars. Main-sequence stars are the final stage often referred to simply as 'stars,' as their energy is generated through nuclear hydrogen burning in the central core. These stars are located along the main sequence in the Hertzsprung-Russell (H-R) diagram. The slope of the SED, denoted as α_λ is defined as:

$$\alpha_\lambda = \frac{d(\log \lambda S_\lambda)}{d(\log \lambda)}, \tag{1.4}$$

where S_λ represents the flux at a given wavelength λ. Below is a brief description of the different phases of YSOs (see also Figure 1.1):

Class 0: This indicates the phase in which the central protostar is embedded in its thick dusty envelope and is barely visible at optical and NIR wavelengths. However, its SED peaks in the sub-mm portion of the spectrum. The mass of infalling material exceeds that of the central region and the signature of outflow and rotating disk become observable (Smith, 2004).

Class I: The SED of this source has a positive slope in the wavelength range of 2–25 μm (i.e., $\alpha_\lambda > 0$) and has evolved its envelope and widen the outflows. From this stage the infalling envelope contains less mass compared to the central protostar.

Class II: These sources refer to the pre-main sequence stars which develop significant circumstellar disks and loss most of their envelope. The spectral index found in the range $-1.5 < \alpha_\lambda < 0$. These sources are also known as T Tauri ($M < 1.5\ M_\odot$) and Herbig Ae/Be ($1.5 < M < 10\ M_\odot$) stars (Smith, 2004).

Class III: These pre-main sequence stars cease to accrete material and therefore do not exhibit outflow activity. They may undergo disk dissipation during the formation of planetary bodies. The slope of their SED becomes steeper and more negative (i.e., $\alpha_\lambda < -1.5$).

It is to be noted that the main source of energy for pre-main-sequence stars is gravitational contraction (e.g., Lada, 1999; Andre et al., 1999). The timescale for this period in which nuclear reactions are not started is known as Kelvin-Helmholtz phase (Huang & Yu, 1995; Smith, 2004), and is given by:

$$t_{\rm KH} = \frac{GM^2}{RL}, \tag{1.5}$$

where M, R, and L are the mass, radius, and luminosity of protostellar object, respectively. This timescale is around 5×10^7 yr for a 1 $M_\odot$ star, and 6×10^4 yr for a 15 $M_\odot$ star.

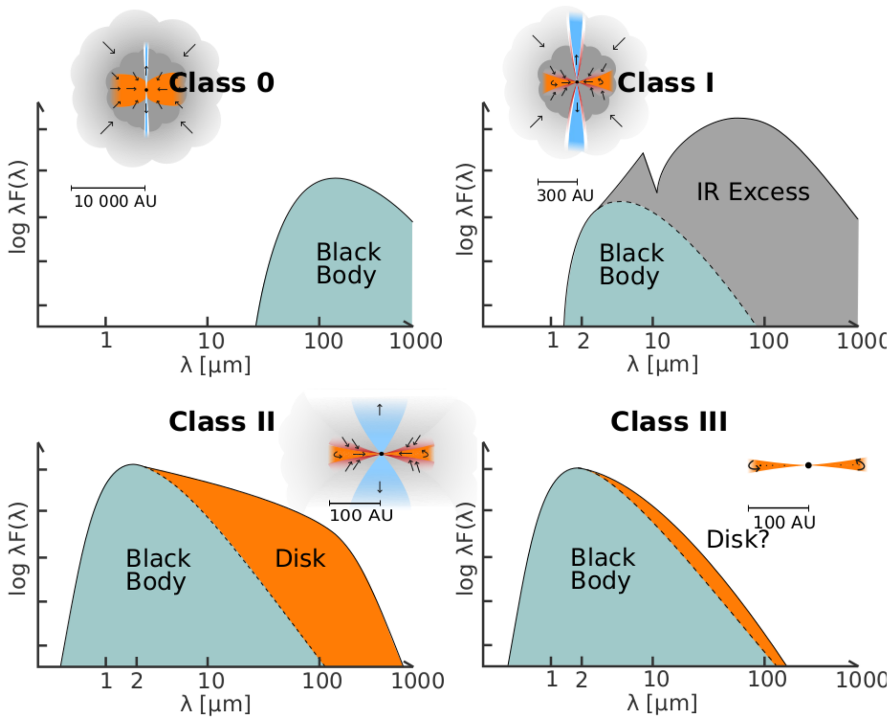

Figure 1.1: Schematic diagram of geometrical structures and corresponding SEDs of low-mass protostellar evolutionary phases. Credit: M. V. Persson (https://doi.org/10.6084/m9.figshare.1121574.v2 and https://doi.org/10.6084/m9.figshare.654555.v7).

1.1.2 High-mass star formation

In comparison to low-mass stars, which make up an overwhelming fraction of the stars in the Galaxy and host planetary systems, massive stars are relatively rare but of great interest. This is concluded by the shape of initial mass function (IMF; see Salpeter, 1955; Kroupa, 2001; Chabrier, 2007, for more discussion), which is given as:

$$\frac{dN}{dM} \propto M^{-2.35}, \tag{1.6}$$

where dN is the number of stars per mass bin of dM. This equation implies that for the stellar population of young stars including massive ones, most of the mass is concentrated in low-mass end. However, most luminosity comes from massive stars (assuming $L \propto M^3$; Salaris & Cassisi, 2006). These rare massive OB stars are known to play a major role in the energy budget of galaxies through their ionizing ultraviolet (UV) radiation, stellar winds, and supernova events. The mechanical and radiative energy output from these stars lead to either the disruption of star-forming clouds (i.e., negative feedback) or the triggering of a new generation of stars, including young massive star(s) (i.e., positive feedback; e.g., Deharveng et al., 2005, 2010). The collective impact of these feedback processes serves as a source of turbulence within the ISM, which is considered a significant mechanism that regulates the process of star formation (e.g., Section 1.1). Therefore, they play a major role not only maintaining the matter flow and promoting further star formation in the ISM, but also injecting the heavier elements throughout the ISM, serving as essential components for the creation of organic matter in the Universe.

Unlike low-mass stars, which have well-established evolutionary phases (such as Class 0/I/II/III phases; see Section 1.1.1), the evolutionary sequence for massive stars is not well-established (Zinnecker & Yorke, 2007; Rodríguez, 2006; Motte et al., 2018). For massive stars $t_{\rm KH} \ll t_{\rm ff}$ (see Equations 1.3 and 1.5) compared to their low-mass counterparts, indicating that the star begins nuclear fusion while still in accretion phase (Palla & Stahler, 1993; Keto & Wood, 2006). Therefore, the primary challenges arise from the strong radiation pressure exerted by young massive stars (or massive protostars), which inhibits the infall of material from their parent cloud (or clump) once the massive stars begin to form. This interaction between radiation and accretion flows sets it apart from the formation of low-mass stars and demands a comprehensive understanding.

In line with the classical model of low-mass star formation, the radiation pressure ($P = \frac{L}{4\pi r^2 c}$, where r and c are the distance at which the pressure is estimated and the speed of light, respectively) from young massive stars ($L > 10^3\ L_\odot$) is capable of halting their accretion process for stars above 7 $M_\odot$ (Shu et al., 1987). However, more massive stars, infact found in abundance (e.g., Vink, 2015; Hirschi, 2017; Bestenlehner et al., 2020, and references therein). As a result, several theories have been proposed to explain the mechanisms behind the formation of massive stars (e.g., Zinnecker & Yorke, 2007; Rodríguez, 2006; Motte et al., 2018). A decade ago, three main classes of theories describing the formation of massive stars were put forward, which are core accretion (or monolithic collapse; McKee & Tan, 2003), competitive accretion (Bonnell et al., 2004; Bonnell & Bate, 2006), and stellar coalescence (or stellar mergers; Bonnell et al., 1998).

Monolithic collapse is the scaled-up version of the low-mass star formation with an increasing accretion rate of 10^{-4}–10^{-3} $M_{\odot}$ yr^{-1} (McKee & Tan, 2003), where accretion primarily happens through accreting disk (e.g., Yorke & Sonnhalter, 2002). This theory provoke the existence of single and isolated massive prestellar cores, which is enigmatic. In the case of competitive accretion, the material for forming massive star does not initially bound to a star, rather, it funneled onto it via a collective gravitational attraction of a star cluster. In this way, the low mass protostars compete for material from the entire parent molecular clump (Bonnell et al., 2004). The protostars at the cluster centre have advantage to gather more material than off-centre participants, thus, they grow faster to become massive stars (Bonnell & Bate, 2006). However, it has shortcomings as it depends on spherical accretion, which is more prone to be disrupted by stellar feedback (e.g., Rodríguez, 2006). On the other hand, stellar coalescence advocates for the collision of low-mass protostellar objects to form massive star, but it requires a stellar density of 10^8 pc^{-3}, much higher than the observed densities. Therefore, these models have serious shortcomings, but they collectively support the requirement of a sufficient mass reservoir for the formation of massive stars.

The study of MSF faces challenges not only in theoretical aspects but also in observational limitations. Massive star-forming regions are typically located at far distances from the Sun ($d \geq 1$ kpc), necessitating high-angular resolution observations. Moreover, these regions are deeply embedded, requiring observations at centimeter (cm), mm, sub-mm, and mid/far-infrared (MIR/FIR) wavelengths to penetrate through the obscuring material. Additionally, the rapid evolution of massive star-forming cores presents difficulties in target selection. This is also reflected in the lifetime of massive stars, which is much shorter compared to that of their low-mass counterparts, posing challenges in studying their earliest evolutionary phases. The combined effects of stellar feedback and high column densities of star-forming materials complicate the interpretation of observational data.

1.1.2.1 Early phases of a massive star

HII regions, formed through the ionization of hydrogen by intense UV radiation emitted by massive OB stars, serve as valuable observational proxies for these stars. These HII regions are found to be associated with the Galactic massive star-forming regions. In recent years, IR and submm data have revealed plenty of bubbles and filamentary structures in star-forming regions (e.g., Churchwell et al., 2006; André et al., 2010), which are often found to host several HII regions, star-forming clumps, and clusters of YSOs. The 6.7 GHz Class II methanol maser emission (MME) and its IR counterpart possibly indicates the presence of a massive young stellar object (MYSO). The absence of radio continuum emission further tells us that the massive YSO is embedded in its dusty envelope and has not produced the HII region yet. A general classification of various components at the early stages of massive stars are given in the literature (e.g., Churchwell, 1999; Beuther et al., 2006; Zinnecker & Yorke, 2007) Below, we highlight the major early evolutionary phases of massive stars:

High-mass starless core: The MSF occurs in a high-mass starless core (HMSC) within a molecular clump, where density reaches local maximum $> 10^6$ cm^{-3} and temperature is local minimum $T < 20$ K. The typical mass of these clumps (size∼0.2–0.5 pc) range from 100 to 1000 $M_\odot$ (Beuther, 2002; Sridharan et al., 2005). The IRDCs are believed to provide such a potential sites meeting aforementioned conditions (Rathborne et al., 2006). However, HMSCs are rare, possibly because of their short lifetime (e.g., Ragan et al., 2012).

High-mass protostellar object: This phase is categorized based on the presence of infall signatures, the absence of radio (cm-wavelength) emission, and the limited or weak detection of complex molecule emissions. The lack of radio emission expected from the ionized gas indicates that these forming star still have low to intermediate masses and have not yet started nuclear hydrogen burning.

Hot molecular core: This phase is distinguished by the intense emission from the complex organic molecules, including CH_3OH, $HCOOCH_3$, C_2H_5CN, and more. The molecular outflow signature is also prominent in this phase. The presence of these molecules, as observed in previous studies (e.g., Kurtz et al., 2000; Cesaroni, 2005; Beuther, 2006; Rolffs & Schilke, 2011), indicates that a substantial portion of these star-forming cores have experienced heating, resulting in the evaporation of ice on dust grains and subsequent high-temperature gas-phase chemistry (Herbst & van Dishoeck, 2009).

Hypercompact and Ultracompact HII regions: Once the nuclear hydrogen burning start in the central regions of forming massive stars, the intense UV radiation ionize its surrounding environment and forms the hypercompact (HC) or ultracompact (UC) HII regions (Kurtz & Franco, 2001; Kurtz, 2005; Gonzalez-Aviles et al., 2005). The major distinction between these two phases is their sizes and electron densities, that is given for HC HII (UC HII) as ≤ 0.03 (≤ 0.1) pc, and $n_e \geq 10^6$ ($\geq 10^4$) cm^{-3}, respectively (e.g., Kurtz, 2005; Yang et al., 2021). HC HII regions are thought to originated from the photoevaporation of the disk, while UC HII regions lack a disk and are formed by the photoionization of molecular cocoon.

Compact or Classical HII regions: As the young massive star evolves, the ionization process leads to the hydrodynamic expansion of the region, causing the disruption of the parent molecular cloud. During this stage, embedded massive stars, along with their associated low-mass stellar population, can be observed at optical and NIR wavelengths. This thesis primarily investigates the compact/classical HII regions as a proxy of massive stars.

All of these above-mentioned phases may not entirely indicate a sequential evolutionary phase of MSF. It is challenging to differentiate between evolutionary stages based solely on differences in luminosity, especially considering the rapid evolution of these objects. Therefore, some of the phases described above may coexist during the MSF such as the hot molecular core phase may exist simultaneously with the HC HII and UC HII regions.

1.1.3 Modern scenarios of MSF

In recent years, it has been observed that the star formation process is not solely regulated by core-scale dynamics. Instead, the ongoing physical processes at cloud scales have also been found to play a significant role in shaping star formation (e.g., Motte et al., 2018; Fukui et al., 2021a; Hacar et al., 2022).

The theories of MSF can be broadly categorized based on their primary emphasis on mass accumulation processes and the presence of a significant mass reservoir. The *core-fed* scenario suggests that the stars acquire mass from their parent core (or envelope) in a similar fashion to low-mass stars (McKee & Tan, 2003; Rodríguez, 2006). This scenario demands that the pre-stellar core must be sufficient massive (>30 $M_{\odot}$), leading the star formation efficiency of ∼40% from cores to stars (Könyves et al., 2015, 2020). Based on the analysis of FIR/sub-mm Galactic plane data/surveys, previous studies suggest that massive pre-stellar cores are extremely rare (e.g., Traficante et al., 2018a; Motte et al., 2018, and references therein). Moreover, with the advent of Atacama Large Millimeter/submillimeter Array (ALMA) in recent years, the fragmentation of clumps at sub-parsec scales has been observed, and it is commonly noted that the existence of massive pre-stellar cores seems to be negligible (Svoboda et al., 2019; Sanhueza et al., 2019). This indicates that the phase of massive pre-stellar cores is likely to be very short-lived, making their detection rare (Ginsburg et al., 2012). The supersonic collision between two gas clouds may lead to the formation of such massive prestellar cores, however, a comprehensive picture is not yet well established (see review article by Fukui et al., 2021a, and Section 1.3.4 for a brief overview).

Alternatively, it is possible that the massive prestellar cores may not exist at all and the MSF is thus a much more dynamical process. In this case, favoring the competitive accretion model (Bonnell & Bate, 2006), the smallest seeds compete for material and form massive protostars. However, such processes should be regulated from the scales of the cloud to cores, in order to have sufficient mass reservoir for MSF. Therefore, in this *clump-fed* scenario, a global hierarchical collapse process (GHC; Vázquez-Semadeni et al., 2019) occurs within a cloud that form the dynamically connected structures from the scales of cloud to clumps and cores (e.g., Smith et al., 2009; Ballesteros-Paredes et al., 2011; Peretto et al., 2013; Vázquez-Semadeni et al., 2019).

In the GHC model, Vázquez-Semadeni et al. (2019), local centers of collapse form throughout the cloud while the cloud as a whole contracts. The collapse occurs at various scales and may not start simultaneously. According to this scenario, a small number of stars may form early in different regions of the cloud, while the majority of the stellar population forms later as the gas density increases due to global contraction. This understanding is supported by the observations of massive sub-parsec fragments (e.g., scale ∼1000–10000 AU Csengeri et al., 2017) in high-resolution dust continuum and line observations (Beuther et al., 2018; Sanhueza et al., 2019; Svoboda et al., 2019). Furthermore, this scenario finds observational support from clumps that exhibit high accretion rates of $\dot{M} = 10^{-4} - 10^{-3}$ $M_\odot$ yr^{-1} (Wyrowski et al., 2016; Yuan et al., 2017a; Traficante et al., 2018a). However, a direct connection between the formation of sub-parsec scale fragments and the accretion at parent clumps has not yet been definitively established. There are instances in the literature where regions exhibit accretion at core scales (Yuan et al., 2017a; Cortes et al., 2019), sometimes accompanied by simultaneous accretion at the clump scale and evidence of global collapse of parent structures (Peretto et al., 2013). However, it remains uncertain whether this large-scale accretion is directly responsible for the observed small-scale accretion.

After the launch of the *Herschel space observatory*, a new understanding of star formation has emerged. It became evident that nearly all molecular clouds exhibit either linear substructures or are themselves formed in a linear manner (e.g., André et al., 2010, 2014; Arzoumanian et al., 2011). These elongated structures, characterized by an aspect ratio ($A = \frac{\text{length}}{\text{width}}$) of 3–5 or more, are now commonly referred to as filaments (or filamentary structures André et al., 2010). They are ubiquitous in the ISM and are often found to be associated with star-forming sites, H II regions, embedded clumps, and clusters of YSOs. The star formation studies in filaments suggest that filamentary clouds break into fragments of dense clumps and cores, which can further collapse to form YSOs as well as massive stars (e.g., Kainulainen et al., 2016; Dewangan et al., 2017a,b).

Based on the observed morphologies of filamentary structures, there have been at least two different scenarios concerning the role of filaments in star formation. One is the “Hub-Filament Systems” (HFSs; Myers, 2009), which are thought to be reliable sites for MSF (e.g., Motte et al., 2018). HFSs represent the complex of filamentary molecular clouds/filaments merging at the central hub. In another scenario, which is a less explored process named as “End-Dominated Collapse” (EDC), is found to occur in isolated filaments. The EDC scenario suggests that the collapse occurs faster at the ends of the filament compared to central regions (e.g., Bastien, 1983; Pon et al., 2012; Clarke & Whitworth, 2015; Hoemann et al., 2022). The presence of HFSs is widely known in the literature, but the observational evidence for the EDC scenario is relatively scarce. This serves as the primary motivation for the thesis, which aims to explore the role of interstellar filaments in the formation of massive stars and their associated stellar clusters. The thesis offers novel observational insights into the physical processes underlying star formation within filaments, encompassing scales ranging from clouds to clumps. A detailed description of these processes is presented in Sections 1.3.3 and 1.3.2.

In the following sections, a comprehensive review on interstellar filaments and their role in star formation process is presented.

1.2 Filaments in the interstellar medium

E. E. Barnard’s pioneering work in 1907 established the direct connection between elongated features in the ISM, dense cores, and stars, referred to as dark lanes, holes, and nebulae in his paper, respectively (Barnard, 1907). However, the subsequent advent of molecular line observations further reinforced the connection between interstellar geometry and star formation processes (Wilson et al., 1970). Despite over a century of research and numerous breakthroughs, understanding the physics of star formation across multiple scales and the significance of ubiquitous filamentary structures in the ISM remains a challenge (see an extensive review by Hacar et al., 2022).

Filamentary clouds are observed as the dark lanes in the optical and NIR/MIR wavelengths. In other words, these structures appear darker (or absorption feature) in shorter wavelengths due to the dust extinction of background starlight (e.g., Jackson et al., 2010; Dewangan, 2022). However, at longer wavelengths i.e., FIR to submm/mm, these structures appear in emission (e.g., Hacar et al., 2016; Dewangan et al., 2019b). This happens because of the thermal dust emission at low temperature. The longer wavelength light is less extincted (scattered and absorbed) by the intervening dust particles compared to the shorter wavelength light (Draine, 2003).

In recent years, the extensive presence of filamentary structures in the ISM and molecular clouds has been revealed, building upon earlier studies (Schneider & Elmegreen, 1979; Abergel et al., 1994). After the launch of the *Herschel Space Observatory* (Pilbratt et al., 2010) in 2009, the picture of the Galactic ISM has changed significantly, leading to new questions in the field of star formation rather than resolving existing ones. This substantial progress has been made possible by the high resolution and dynamic range observations of the *Herschel* observatory, particularly in the sub-mm wavelength ranges (André et al., 2010; Molinari et al., 2010a). *Herschel* has unveiled the intricate networks of elongated features in dust emission throughout the ISM, which are widely distributed and often associated with young stars and star-forming regions. The presence of YSOs is often closely tied to the long spines of the filaments (e.g., Beuther et al., 2015; Kainulainen et al., 2016; Mattern et al., 2018; Dewangan, 2022). Furthermore, the *Planck* satellite has also provided all-sky maps of sub-mm emission, capturing total and polarized intensity. These maps have shed light on the hierarchical filamentary structure of the Galactic ISM on large scales (Ade et al., 2015; Adam et al., 2016a). The combined data from *Herschel* and *Planck* missions have revealed that interstellar matter is organized in a web-like network of filaments, arising naturally as a result of the physical processes at work in the ISM.

The dust continuum and molecular line data have revealed that the filaments are present across a wide range of scales and environments. For example, these structures have been identified from the scale of sub-parsec features within clouds ($\sim$0.1 pc; e.g., protostellar envelope; Hacar et al., 2013) to the extent of GMCs (i.e., $\sim$100 pc Goodman et al., 2014; Abreu-Vicente et al., 2016a; Mattern et al., 2018; Zucker et al., 2018) and kpc-sized objects associated with spiral arms (Li et al., 2021). Furthermore, filaments have been observed in the densest high-mass star-forming regions (Treviño-Morales et al., 2019a) as well as in the atomic interstellar medium (Syed et al., 2022). The *Herschel* Gould Belt Survey (HGBS) was a dedicated survey to understand the formation mechanisms of prestellar cores from the diffuse ISM (André et al., 2010).

The HGBS and *Herschel* Infrared Galactic Plane Survey (Hi-GAL; Molinari et al., 2010a), for the first time, mapped the dust emission throughout the Galactic plane within the range $-70° < l < 68°$ and approximately 145 deg^2 field, providing us with many valuable insights into the star formation processes in filaments. The Gould belt is a giant, flat structure with dimensions of approximately 700×1000 pc^2 and is inclined by around 20° to the Galactic plane. The HGBS is based on FIR/sub-mm observations of nearby molecular clouds ($d \lesssim 0.5$ kpc) using both the Spectral and Photometric Imaging Receiver (SPIRE; 70 and 160 μm; Griffin et al., 2010) and Photoconductor Array Camera and Spectrometer (PACS; 250, 350, 500 μm; Poglitsch et al., 2010) bolometer cameras.

In the literature, gravitational instability of a filament is defined by its critical line mass parameter. One can calculate the critical line mass of a filament ($M_{\rm line,cri}$) by considering it as an infinite and non-magnetized isothermal cylinder, which is in equilibrium between gravitational and thermal pressures. $M_{\rm line,cri}$ is a function of the kinetic temperature (T) of the gas only, and can be expressed as follows (Ostriker, 1964):

$$M_{\rm line,cri} = \frac{2c_s^2}{G} \simeq \frac{16M_\odot}{\rm pc}\left(\frac{T}{10K}\right), \tag{1.7}$$

where $c_{\rm s} = \sqrt{\frac{kT}{\mu m_H}}$ is the isothermal speed of sound at temperature T, and G is the universal gravitational constant. To incorporate the effect of non-thermal motions on the stability of a filament, the term c_s can be substituted with the total velocity dispersion ($\sigma_{\rm total} = \sqrt{c_{\rm s}^2 + \sigma_{\rm NT}^2}$), where $\sigma_{\rm NT}$ is the non-thermal velocity dispersion, resulting in the determination of the virial line mass ($M_{\rm line,vir}$) as follows:

$$M_{\rm line,vir} = \frac{2\sigma_{\rm total}^2}{G} \simeq \frac{465 M_\odot}{\rm pc} \left(\frac{\sigma_{\rm total}}{1 \ {\rm km\ s^{-1}}} \right). \tag{1.8}$$

According to Ostriker (1964), a cylindrical filament can only resist collapse thermally if its line mass stays below a critical value $M_{\rm line,cri}$. However, if the line mass exceeds this critical value, even small perturbations within the filament can grow due to self-gravity. This ultimately results in radial collapse and fragmentation, as described in the models of fragmenting cylinders (Nagasawa, 1987; Inutsuka & Miyama, 1992; Fischera & Martin, 2012). Also, the contribution of non-thermal gas motions effectively enhance the line mass and thus further support the filament against gravitational collapse.

The observed line mass ($M_{\rm line,obs}$) of filaments can be calculated as $M_{\rm line,obs} = \frac{M}{L}$, where M and L are the mass and length of filament, respectively. Observationally, the thermal supercritical filaments having $M_{\rm line,obs} > M_{\rm line,cri}$ show the signature of star formation activities and prestellar cores along their long spines, whereas the subcritical filaments for which $M_{\rm line,obs} < M_{\rm line,cri}$ do not generally show these signatures (André et al., 2010). Hence, $M_{\rm line,cri}$ represents the threshold line mass above which a filament undergoes gravitational instability, leading to radial contraction and fragmentation along its major axis (Inutsuka & Miyama, 1997). The results from *Herschel* observations support the universality of filamentary structures in the ISM. André et al. (2010) presented the results for two exemplar regions, Aquila rift and Polaris Flare, demonstrating that most of the bound prestellar cores are concentrated in the *supercritical* filaments ($M_{\rm line,obs} > M_{\rm line,cri}$), and show the close relationship between the core mass function (CMF) and the IMF. They also emphasized that the stages of star formation involve the formation of filaments by interstellar magneto hydrodynamic (MHD) turbulence, followed by the formation of gravitationally bound and unstable cores, leading to the formation of stars. Figure 1.2, which is adapted from André et al. (2010), presents the column-density ($N(\rm H_2)$) maps of the Aquila rift and Polaris Flare regions. These maps also provide the information of gravitational stability parameter (i.e., $\frac{M_{\rm line,obs}}{M_{\rm line,cri}}$) that infers the *supercritical* or *subcritical* states of a filament. The Aquila rift region contains much denser gas and, consequently, has gravitational unstable cores and Class 0 YSOs, compared to the Polaris Flare region, which does not host any Class 0 YSOs and exhibits unbound starless cores.

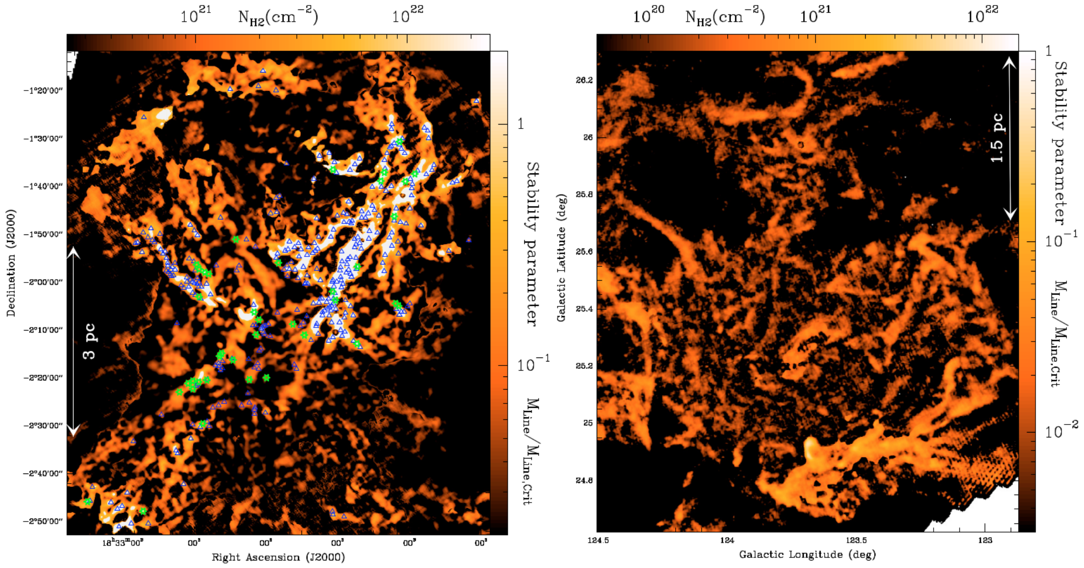

Figure 1.2: The column density maps of Aquila rift (*left*) and Polaris Flare (*right*) regions. The bound prestellar cores and Class 0 YSOs (see Bontemps et al., 2010; Könyves et al., 2010) are indicated by blue triangles and green stars, respectively. The figure is adopted from André et al. (2010).

Therefore, filaments play a crucial role in various astrophysical processes, particularly in star formation. They are frequently associated with star-forming sites where dense molecular gas initially accumulates, eventually leading to the formation of stars and star clusters.

1.2.1 Formation of interstellar filaments

The widespread presence of filaments associated with both star-forming regions (e.g., Könyves et al., 2010; Bontemps et al., 2010) and non star-forming regions (or a quiescent cloud such as Polaris; Men'shchikov et al., 2010; Ward-Thompson et al., 2010) suggests that the formation of filamentary structures is an inherent outcome of the physical processes occurring in the magnetized turbulent cold ISM (André et al., 2010; Arzoumanian et al., 2013). This also suggests that the filament formation precedes the star formation in any GMCs. The origin of the filamentary structures in GMCs is still a topic of debate. However, they are likely to form in gas that has experienced strong compression due to converging supersonic and anisotropic gas accretion (e.g., Chen et al., 2020a, and references therein). Numerical simulations incorporating colliding flows and turbulence have shown the formation of filaments within post-shock regions, accompanied by the emergence of self-gravitating cores (e.g., Vazquez-Semadeni et al., 2007; Gong & Ostriker, 2011; Chen & Ostriker, 2014).

The presence of filamentary structures in the gravitationally unbound cloud complex, such as Polaris (Figure 1.2), suggests that turbulence, rather than gravity, plays a major role in their formation at large scales. It has been found that turbulence compression of interstellar gas can give rise to the formation of filaments (Padoan et al., 2001). Along these filaments, the relative velocity difference between two layers of gas remnants is minimized, resulting in low (or transonic) velocity dispersion (e.g., Klessen et al., 2005; Arzoumanian et al., 2013). Arzoumanian et al. (2013) discovered that thermally supercritical filaments are self-gravitating structures that exist in approximate virial equilibrium ($M_{\rm line,vir} \sim M_{\rm line,obs}$), while subcritical filaments are unbounded structures that exhibit overvirial states (i.e., $\frac{M_{\rm line,vir}}{M_{\rm line,obs}} \geq 2$). Furthermore, these authors found that filaments with column densities $N(H_2) < 8 \times 10^{21}$ cm^{-2} (or equivalent to $M_{\rm line,obs} < M_{\rm line,cric}$ at $T = 10$ K; see Figure 6 in Arzoumanian et al., 2013) exhibit a constant velocity dispersion, while those with high column densities (i.e., $N(H_2) > 8 \times 10^{21}$ cm^{-2} or $M_{\rm line,obs} > M_{\rm line,cric}$) display a linear trend with $\sigma_v \propto N(H_2)^{0.5}$. This suggests that the central column density of thermally supercritical filaments is expected to increase over time due to radial collapse and the accretion of background material. Since the observed velocity dispersion directly measures $M_{\rm line,vir}$ (see Equation 1.8), which subsequently increases with $N(H_2)$, it is possible that the observed velocity dispersion reflects not only the evolutionary state of filaments but also the level of turbulence in the parent cloud. There is further direct evidence supporting the process of accretion and growth in $M_{\rm line,obs}$ for supercritical filaments, which is observed in several cases as low-density striations or subfilaments perpendicular to the main filaments. These striations appear to feed the main filaments from the side. Examples of such observations include the B211/B213 filament in Taurus, where the signature of infalling material is observed from CO observations (Goldsmith et al., 2008; Palmeirim et al., 2013), and the alignment of magnetic field lines to that of striations is found (e.g., Shimajiri et al., 2019b). Similar evidence is found in the Musca filament (Cox et al., 2016) and the DR21 ridge in Cygnus X (Schneider et al., 2010). Hence, once the structure forms, further material accretion enhances the formation of filaments.

1.3 Role of filaments in star-formation

The *Herschel* observations, along with other multi-wavelength studies, revealed that the interstellar filaments favor universal properties (Arzoumanian et al., 2011, e.g., characteristic width of ∼0.1 pc) and almost serve as the intermediate steps for the star formation processes from clouds to core scales (André et al., 2010). This also includes the hot debate on the role of filaments in MSF, which is still far from complete understanding (André et al., 2014; Beuther et al., 2015). According to André et al. (2010), there are two key steps for the formation of stars in filaments. The first step is the formation of the filament itself, and the second step involves the processes that lead to the formation of young stars within filaments. In general, the filaments fragment due to the effect of their self-gravity and ambient turbulence into smaller dense structures that further collapse to form protostars. Observations infer that the magnetic field helps to grow filamentary structures that nurture the young stars within them (Cox et al., 2016; Shimajiri et al., 2019a).

Below, we discuss the major filament configurations and their role in the formation of dense clumps and subsequently stars and star clusters.

1.3.1 Fragmentation and collapse of filaments

The generic models of equilibrium filaments suggest that a filament is likely to fragment into a chain of cores that are quasi-periodically spaced (Inutsuka & Miyama, 1992, 1997; Fischera & Martin, 2012) and it depends upon a fastest growning wavelength density perturbation. The separation between these cores is approximately four times the filament's width. Furthermore, the non-equilibrium model proposed by Clarke et al. (2016), which considers the effects of accretion, also support the formation of quasi-periodically spaced cores when realistic initial density perturbations are taken into account. However, the theoretical studies examining the substructures of filaments face challenges as the cores are not the only form of substructure and the quasi-periodically spaced cores are relatively rare (André et al., 2014). Filaments also appear to fragment into smaller filaments known as "fibers" when observed in position-position-velocity (PPV) space, or "sub-filaments" when observed in position-position (PP) or position-position-position (PPP) space (e.g., Hacar et al., 2013; Tafalla & Hacar, 2015; Dhabal et al., 2018; Suri et al., 2019). In this way, Tafalla & Hacar (2015) proposed a formation scenario known as "fray and fragment" to explain the creation of large filamentary structures through the encounter of two gas fronts. Within these filaments, coherent velocity structures known as 'fibers' form, as observed in turbulent self-gravitating simulations (e.g., Moeckel & Burkert, 2015; Clarke et al., 2017). However, it is not clear whether these sub-filaments (or fibers) form within the parent filament or originate separately and then gather together to form a larger-scale filament (Smith et al., 2016; Clarke et al., 2017). In both scenarios, it is found that these sub-filaments undergo fragmentation to form cores.

Recently, Clarke et al. (2018) found that the sub-filaments bear a resemblance to fibers, formed through the in situ fragmentation of a filament driven by turbulence caused by filament accretion. Although the fibers observed in PPV space may not always directly correspond to the sub-filaments observed in PPP or PP space, both structures arise due to the internal turbulence within a filament. Therefore, a filament containing fibers also contains sub-filaments and the distinction between these structures is supported by cloud-scale simulations presented by Zamora-Avilés et al. (2017).

1.3.2 End dominated collapse in filaments

Previous studies have extensively explored the collapse modes of spherical and infinite non-spherical structures (Ostriker, 1964; Larson, 1969, 1985; Penston, 1969; Shu, 1977; Inutsuka & Miyama, 1992, 1997; Fiege & Pudritz, 2000; Myers, 2009). However, the collapse properties of finite non-spherical structures have only recently gained attention and are not well understood due to their inherent global and local instabilities, as well as the critical influence of initial conditions (e.g., Bastien, 1983; Bastien et al., 1991; Burkert & Hartmann, 2004; Hsu et al., 2010; Pon et al., 2011; Toalá et al., 2012; Pon et al., 2012; Clarke & Whitworth, 2015). Analytical studies have demonstrated that non-spherical cloud structures take longer to collapse compared to spherical clouds of the same initial density (Burkert & Hartmann, 2004; Pon et al., 2012), which is further supported by the simulations (Bastien, 1983; Vazquez-Semadeni et al., 2007; Clarke & Whitworth, 2015).

For the case of long but finite-sized filaments, there are two possible longitudinal (along the major axis of filaments) collapse modes: "homologous collapse" (Pon et al., 2012), and EDC (or edge-collapse; Bastien, 1983; Burkert & Hartmann, 2004; Pon et al., 2011, 2012; Clarke & Whitworth, 2015). This happens because of the longitudinal gas acceleration is found to be a function of distance from the centre of the cylindrical cloud. In the case of self-gravitating cylinder with uniform density ρ, length $2L$, and radius R, the longitudinal acceleration of the gas at axial distance $d(< L)$ along the filament is given as (Burkert & Hartmann, 2004):

$$a(d) = 2\pi G\rho(2L + \sqrt{R^2 + (L-d)^2} - \sqrt{R^2 + (L+d)^2}). \tag{1.9}$$

In homologous collapse, all regions should have similar collapse timescales and the density remains approximately uniform in space. Therefore, in order to undergo a homologous collapse, the acceleration across the object must be a linear function of the axial distance from the center of collapse. However, we note that the Equation 1.9 is not a linear function of d, and hence the filament collapse is homologous at specific condition if $L \gg R$ or at some point away from the exact end of filament (i.e., $L - d \gg R$), which results in the $a(d)$ as:

$$a(d) \approx \pi\rho G R^2 \left(\frac{2d}{L^2 - d^2}\right). \tag{1.10}$$

Although, this equation is also not a linear function of d, for the central regions of filament (i.e., if $d^2 \ll L^2$), the acceleration becomes a linear function of d and can be given as:

$$a(d) \approx \pi\rho G R^2 \left(\frac{2d}{L^2}\right). \tag{1.11}$$

Hence, the interior of cylindrical clouds seems to collapse homologously.

The nonlinear terms in Equation 1.9 become significant at the filament edges (i.e., if $d \sim L$) such that the edges gain high acceleration and impart higher momentum to the inner gas particles. Therefore, in the collapse journey, filament grows clumps at both the edges, which continuously gain mass. This collapse process is known as EDC process. Here we note that in the current scenario, the radial motion of gas particle are neglected and hence only axial (or along the longer axis) motions are considered. Pon et al. (2012) in their analytical calculations found that the filaments with aspect ratio, $A > 5$ tend to show the EDC signatures. The resulting accelerations can be turned into instantaneous collapse timescales (t_{collapse}; time taken for filament to collapse at its centre). For homologous collapse, $t_{\text{collapse}} \propto A$, while for EDC, it is $t_{\text{collapse}} \propto \sqrt{A}$ (Pon et al., 2012).

In continuation of this work, Clarke & Whitworth (2015), performed smoothed particle hydrodynamic (SPH) simulations of cold, uniform density, self-gravitating filaments. They indeed found similar results of EDC, but the collapse timescales in filaments are now satisfied with a single equation (for $A > 2$) as:

$$t_{\text{collapse}} = \frac{(0.49 + 0.26A)}{\sqrt{G\rho}}. \tag{1.12}$$

They also observed that for all $A > 2$, the collapse mode is EDC. It is also interesting to notice that the dependencies of ρ on t_{collapse} of filament is $\propto \rho^{-1/2}$, similar to that of the free-fall timescale of a spherical cloud (see Equation 1.3).

Here, we point out that very few clear samples of filaments demonstrating the EDC process have been observed and published in the literature. These include

NGC 6334 (Zernickel et al., 2013), Sh 2-242 (or S242; Dewangan et al., 2019b; Yuan et al., 2020), IC 5146 (Wang et al., 2019b), Monoceros R1 (or Mon R1; Bhadari et al., 2020), G341.244-00.265 (Yu et al., 2019), and G45.3+0.1 (Bhadari et al., 2022).

1.3.3 Hub-filament Systems (HFSs)

The observations made in the past decade, including the Gould belt survey, have revealed a significant concentration of star formation activities within density-enhanced filamentary structures of molecular clouds. One particular configuration that has gained considerable attention is the HFS. The HFSs exhibit a distinctive arrangement wherein multiple filamentary structures merge at a common gravitational center known as the "hub". In general, in HFSs, filaments are traced with high aspect ratio ($A > 3$) and lower column densities ($\lesssim 10^{21}$ cm^{-2}) compared to hub region that is identified with low aspect ratio ($A < 3$) and high column density ($\gtrsim 10^{22}$ cm^{-2}; e.g., Myers, 2009; Schneider et al., 2012). Observational evidence suggests that filaments within the HFSs serve as channels for material flow, transporting material from the larger cloud scale down to the clump/core scales. Most recent study by Zhou et al. (2023) suggests the funnel-like feature in the PPV space of a HFS which translates to a V shaped feature in the PV diagram. This is supported by the observations of a coherent velocity gradient seen from the filament ends toward the hub regions, aligning with local gravity centers (e.g., Treviño-Morales et al., 2019b; Motte et al., 2018). The filaments in HFSs themselves often exhibit a tree-like configuration, with several branches linked to a major stem, resembling subfilaments within a larger filament. Chapter 5 presents such HFSs in a Giant Molecular Filament (GMF) at the physical scales of ~5–10 pc. The smaller subfilaments converge into the main filament, and these structures continue to merge towards the hub, resulting in higher column density in the hub region. These structures, resembling conveyor belts in factories, act as carriers or material flow pathways. They serve as bridges, connecting different density structures within the molecular clouds and support star formation.

In recent years, HFSs have become popular in MSF research and are cited as the potential nurseries of protocluster and MSF. More specifically, they are found to play a crucial role in mass accumulation processes. An evolutionary model based on gravity-driven inflow has been proposed to elucidate the MSF (Tigé et al., 2017; Motte et al., 2018). This scheme does not favour the existence of high-mass prestellar cores. Instead, it proposes that low-mass prestellar cores first develop within the starless phase of massive dense cores/clumps (MDCs) on a scale of ∼0.1 pc, within a time scale of around 10,000 years. The protostellar phase of MDCs begins with the formation of low-mass protostellar cores. The local (∼0.02 pc) collapse of these cores is accompanied by the global (∼0.1–1 pc) collapse of MDCs and hub region. As a result of these gravity-driven inflows, the low-mass protostellar core accumulates mass and evolves into a high-mass protostar over a period of ∼30,000 years.

In the later stages of this evolutionary scheme, the formation of H II regions is favored around massive protostars with masses exceeding 8 $M_{\odot}$. The H II region emerges when the intense UV radiation emitted by the massive protostar ionizes the surrounding protostellar envelope. Simultaneously, the main accretion phase comes to an end. According to this schematic model, one can expect the simultaneous growth of stars, cores, and ridges as they draw mass from their parent cloud. It is to be noted here that this scenario is in line with the *clump-fed* scenario (see Section 1.1.3) of MSF where the massive protostar does not form initially, however low-mass protostar gains mass and become massive protostar.

Most recent study by Kumar et al. (2020) showed that nearly 3700 (∼11%) *Herschel* Hi-GAL survey clumps (Elia et al., 2017) are associated with HFSs. The mean length of filaments in HFSs was found to be $\sim 10-20$ pc, with the mass of $\sim 5 \times 10^4$ $M_{\odot}$ and $M_{\rm line,obs}$ of $\sim 2 \times 10^3$ $M_{\odot}$ pc^{-1}. These authors also found that all the clumps having bolometric luminosity of $L_{\rm bol} > 10^4$ $L_{\odot}$ located within 2 kpc and $L_{\rm bol} > 10^5$ $L_{\odot}$ located within 5 kpc are part of the hubs in HFSs.

In addition to their significance in MSF, the formation of HFSs remains a subject of ongoing debate. Recent numerical and observational investigations propose the cloud-cloud collision (CCC) scenario as one of the potential mechanisms for the formation of HFSs. Another possibility involves the fragmentation of clumps along magnetic field lines that are initially oriented perpendicular to the main filament (Wang et al., 2019b). This scenario is feasible because density perturbations along the magnetic field grow more rapidly compared to those perpendicular to the field (Nagai et al., 1998; Van Loo et al., 2014).

1.3.4 Intertwined filaments and filament collision

In addition to the previously mentioned physical configurations of filaments in star formation, there are other possibilities that have received less exploration or are considered rare in the literature. Recent numerical simulations and observations have confirmed the existence of intertwined filaments (or interacting subfilaments), although their role in star formation remains a subject of debate. As discussed earlier in Section 1.3.1, the "fray and fragment" scenario, which describes the formation and fragmentation of filaments, also supports the presence of closely spaced (or interacting) filaments (Smith et al., 2014; Shimajiri et al., 2019a). This may also suggest the possibility of intertwined (or twisted) filaments resembling a filamentary braid or a double helix like structure. Previous study by Dewangan et al. (2021) has observed double helix-like structures in Lynds Bright Nebulae, evident in both dust continuum and molecular line emission maps. Such structures should be ideally distinguishable in PPP space, and one would expect oscillatory velocity profiles or two distinct intensity features in PPV or position-velocity (PV) diagrams (e.g., Hartmann & Burkert, 2007; Hacar et al., 2017; Dewangan et al., 2021). In systems where filaments exhibit twisting, it is conceivable that multiple overlapping regions with high column density may be present, potentially favoring star formation. According to Dewangan et al. (2021), these intersection areas may host dense star-forming clumps or exhibit signatures of ongoing star formation activities, such as the presence of YSOs. Chapter 6 emphasizes the importance of intertwined subfilaments in IC 5146 dark Streamer and presents a new picture of star formation in this site.

Additionally, the collision of filaments can be seen as a special case of the CCC process, as extensively reviewed by Fukui et al. (2021a). In this scenario, two filaments collide head-on or along the directions of their long axes (e.g., Dewangan, 2019). Such a collision can result in the formation of dense and massive clumps at the collision interface, where turbulent mass accretion onto the core is enhanced due to the increase in sound speed (Takahira et al., 2014, 2018). The observational signatures of this process include an intense double-peaked velocity profile with a less intense bridge feature in PV diagrams, as well as complementary features observed in molecular line intensity maps at different velocities (see Maity et al., 2022, 2023, and references therein). In the case of a collision between filaments along their shorter axes, it becomes challenging to observe the complementary distribution as the collision occurs along our line of sight. However, the line spectra would exhibit two velocity peaks with a bridge feature. In Chapter 6, we observed colliding or interacting subfilaments in the IC 5146 region, which also contributed to the formation of the known HFSs in this area.

Therefore, despite the popularity of the CCC process, filament collisions are less frequently observed, and there is a current lack of theoretical insights into the observations of filament twisting and its impact on star formation processes. Consequently, further observational investigations are crucial to unravel the significance of filament twisting and collisions and understand their implications for star formation.

1.4 Motivation and outline of the thesis

This thesis aims to uncover the formation processes of massive stars within interstellar filamentary clouds through observational investigations. By utilizing a combination of multi-scale and multi-wavelength dust continuum and line data, the study explores the new physical processes of star formation occurring within filaments and examines their potential role in MSF. The primary scientific objective of this thesis is to conduct observational assessments of recent theoretical models of star formation in filaments and investigate their suitability for the MSF. To accomplish this objective, the thesis pursues the following specific goals:

1. To investigate the observational assessments of the recent theoretical models of EDC process in filaments (e.g., Bastien, 1983; Pon et al., 2012; Clarke & Whitworth, 2015; Hoemann et al., 2022), and look for its suitability in mass accumulation process and the formation of massive stars. Also, exploring the new possibilities of observable proxies for this scenario using dust polarisation emission.

2. Investigating MSF in a prominent HFS from the physical scale of the cloud (>10 pc) to core (<0.1 pc) using multi-wavelength and multi-scale data set and compare its evolutionary sequence with the recent schematic model proposed by Motte et al. (2018). This also includes the examination of the physical environments including the role of turbulence and gravity within a hub (or dense clump) of HFS, which harbors a diverse population of massive stars.

3. The exploration of simultaneous occurrence of multiple physical processes of MSF within a single filamentary cloud system. Additionally, it involves investigating and searching for other possible filamentary configurations that play a role in the process of star formation.

4. To examine the formation process of massive stars within a filamentary cloud and investigate their interaction with the surrounding environments, including the observational assessments of a recent model proposed by Whitworth & Priestley (2021) concerning the escape and the trapping of the ionizing radiation emitted by an O-type star that forms within a filament.

1.5 Target identification

To achieve the objectives of this thesis, the first and foremost crucial task is to identify the filaments that host massive stars. We conducted a systematic search for elongated dust emission features (>2-3 pc) in sub-mm wavelength images obtained from the *Herschel* observatory, and also examined the corresponding radio continuum emission counterparts, and catalogs of massive stars. The presence of radio continuum emission along the elongated structures may indicate the existence of HII regions formed by massive stars. To study the gas kinematics within the filaments, molecular line data were required which we have obtained from various molecular line surveys. Therefore, our primary focus was on selecting massive star-forming sites associated with filamentary clouds or complexes comprising several filaments. In this way, we analysed the mult-wavelength data for target sites, Monoceros R1 (d =760 pc; Chapter 4, Bhadari et al., 2020), GMF G45.3+0.3 (d =8 kpc; Chapter 5, Bhadari et al., 2022), Sh 2-305 (S305, d =3.7 kpc; Chapter 8, Bhadari et al., 2021), RAFGL 5085 (d =3.3 kpc; Chapter 3, Dewangan et al., 2022a), IC 5146 (d =600 pc; Chapter 6, Dewangan et al., 2023), and W42 (d =3.8 kpc; Chapter 7, Bhadari et al., 2023).

1.6 Thesis organization

This thesis is organized into nine chapters. Chapters 3 to 8 provide case studies of individual star-forming sites and the results are published in peer-reviewed journals. The overall conclusion from the thesis is discussed in Chapter 9. Below, a brief description of each of the nine chapters in this thesis is provided.

Chapter 1: Introduction

This chapter provides a comprehensive overview of star formation in the ISM. We commence by briefly discussing the known star formation processes and highlight the challenges associated with studying massive stars. We further discuss the pivotal role of interstellar filaments in star formation, specifically in the context of massive stars, and highlight the various mechanisms by which they actively participate in the process. Next, we present the significance of multi-wavelength and multi-scale observations in understanding the intricate processes of MSF. As we approach the conclusion of this chapter, we elucidate the motivation driving the thesis work, thereby setting the stage for the research to be presented.

Chapter 2: Multi-wavelength data and methods

This chapter presents the multi-wavelength (optical–radio wavelengths) and multi-scale data obtained from various ground and space-based observatories and existing surveys that are utilised in this thesis work. This chapter also provides the basic principles and physics behind the continuum and line emissions from interstellar environments. In addition, we provide a discussion on the methods and principles employed for data analysis, highlighting their role in deriving observable physical quantities.

Chapter 3: Star-forming site RAFGL 5085: Is a perfect candidate hub-filament system?

This chapter focuses on RAFGL 5085, a massive star forming site located 3.3 kpc away. By adopting a multi-wavelength approach, we aim to understand the underlying physical processes driving star formation in RAFGL 5085, which has not been previously explored. Our findings reveal the presence of a potential HFS in RAFGL 5085, suggesting that it represents an early phase of MSF rather than hosting an evolved HII region. These findings are discussed in comparison with the schematic model proposed by Motte et al. (2018). The results presented in this chapter have been published as Dewangan et al. (2022a).

Chapter 4: Star-forming sites IC 446 and IC 447: an outcome of end-dominated collapse of Monoceros R1 filament

This chapter is dedicated to the observational exploration of the EDC process. It provides detailed multi-wavelength analysis of a nearby massive star-forming complex Monoceros R1, situated at a distance of 760 pc. Through the analysis of *Herschel* dust continuum data and FUGIN ^{12}CO/^{13}CO (1–0) line data, the presence of a filamentary cloud known as the Mon R1 filament is discovered and detailed discussion of the onset of a rare EDC process in Mon R1 is presented. The results highlighted in this chapter have been published as Bhadari et al.

(2020).

Chapter 5: Simultaneous evidence of edge collapse and hub-filament configurations: A rare case study of a Giant Molecular Filament G45.3+0.1

The primary focus of this chapter is to investigate the simultaneous onset of the EDC process and the presence of HFSs within a filamentary cloud. It aims to provide new insights into the physical processes occurring in the massive complexes G045.49+00.04 (G45E) and G045.14+00.14 (G45W), which are part of a large cloud complex in the Aquila constellation located at a distance of 8 kpc. Our findings reveal the existence of a GMF, denoted as GMF G45.3+0.1, which hosts G45E and G45W at its opposite ends harbouring HFSs as well. Additionally, our results suggest that these sites are formed through the EDC scenario, with mass accumulation occurring through sub-filaments towards the hub regions. This chapter builds upon the findings published as Bhadari et al. (2022).

Chapter 6: IC 5146 dark Streamer: is a first reliable candidate of edge collapse, hub-filament systems, and intertwined sub-filaments?

This chapter highlights the occurrence of multiple physical processes in a filamentary cloud. Through a comprehensive multi-wavelength analysis of IC 5146 Dark Streamer, a nearby potential site for MSF located at a distance of 600 pc, our results unveil the first reliable candidate exhibiting edge collapse, HFSs, and interconnected sub-filaments. Furthermore, the distribution of the plane-of-sky magnetic field in nearby candidate EDC filaments is investigated using Planck polarization data, and the implications of these findings are thoroughly discussed. This chapter incorporates the results published as Dewangan et al. (2023).

Chapter 7: Unveiling the innermost environments of a hub-filament system hosting massive stars

This chapter focuses on a case study of the physical environments surrounding a MYSO W42-MME, which is formed within a known HFS along with an evolved massive O-type star in the W42 region. The chapter presents a comprehensive analysis of the ALMA $H^{13}CO^{+}$ data of the W42 region hosting the MYSO, aiming to investigate the role of gravity and turbulence on sub-parsec scales. The findings discussed in this chapter have been published as Bhadari et al. (2023).

Chapter 8: Formation and interaction of O-type stars in filaments: insights from the S305 HII Region

This chapter aims to provide insights into the formation of O-type stars and their interaction to surrounding environments in the S305 region. With the extensive discussion on the MSF processes in the filamentary cloud of S305, the chapter further presents the results obtained from the analysis of the SOFIA [CII] 158 μm line data, providing valuable insights into the feedback processes of massive stars in the S305 region. The part of results obtained in this chapter have been published as Bhadari et al. (2021).

Chapter 9: Summary and future plan

This chapter serves as a comprehensive summary of the significant findings obtained from the thesis and offers a broad overview of the advancements made in relation to our existing knowledge. It provides valuable insights into how this research study will contribute to establishing a solid groundwork for future investigations in the field. Additionally, the chapter discusses the limitations of the overall work and provides immediate future prospects.

Chapter 2

Multi-wavelength data and methods

To investigate the various physical processes involved in MSF across different spatial scales, it is necessary to utilize comprehensive data sets spanning multiple wavelengths. Figure 2.1 presents a schematic diagram illustrating the significance of incorporating multi-wavelength data (optical to radio wavelength) to study MSF. In the subsequent sections, we provide a general overview of the methodologies employed to obtain the results and the data sets utilized in this thesis.

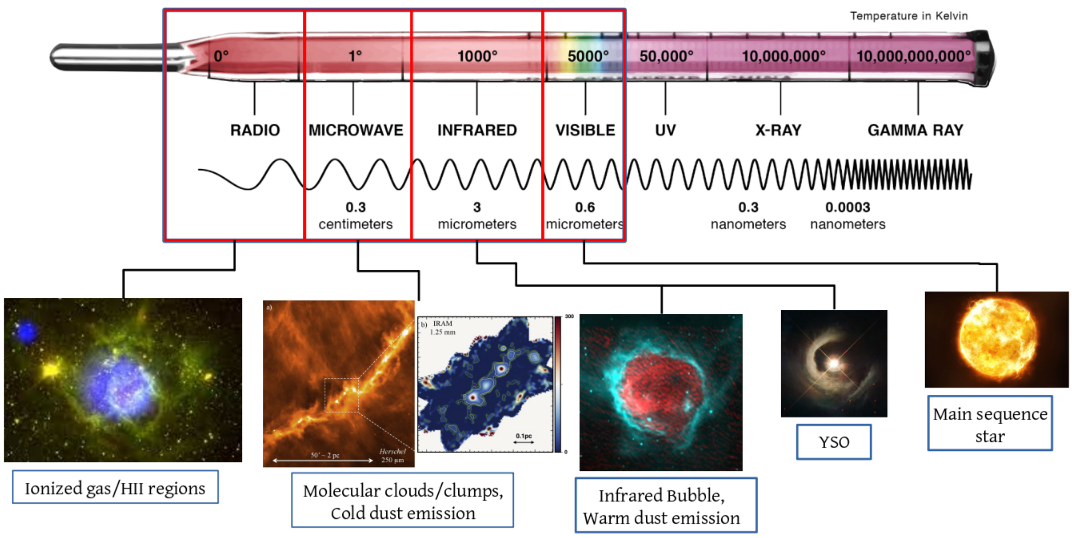

Figure 2.1: Schematic diagram illustrating the significance of multi-wavelength data in the study of MSF. Various components are traced at different wavelengths.

2.1 Necessity of multi-wavelength and multi-scale data

Hydrogen, being the most abundant (∼75%) element in the Universe found in different phases in the ISM, i.e., HII (ionized hydrogen), HI (atomic or neutral hydrogen), and H_2 (molecular hydrogen), plays a crucial role in star formation. In environments with high densities ($> 10^3$ cm^{-3}) and cold temperatures ($T \sim 10$ K), such as those important for star formation, hydrogen tends to be in the molecular form rather than atomic. However, directly observing H_2 is extremely challenging due to its homonuclear nature, which prohibits $\Delta J = 1$ rotational transitions (e.g., no $J = 1-0$ emission; $\Delta E^{\mathrm{H_2}}_{J=1-0} = 175$ K). The lowest energy transition available is the $J = 2-0$ quadrupole transition, which is weak and requires even higher temperatures for excitation (i.e., $\Delta E^{\mathrm{H_2}}_{J=2-0} = 510$ K). This high temperature requirement is due to the low-mass of the H_2 molecule, which, in contrast, necessitates less energy for the excitation of relatively heavier molecules (e.g., CO, O_2, N_2). It is worth noting that the energy level spacing depends on the reduced mass (μ_r) of a molecule (or quantum rotor) as $\Delta E \propto \mu_r^{-0.5}$. Therefore, the observations of H_2 can only be indirectly achieved through other proxies.

The thermal dust emission serves as an indirect proxy for studying the interstellar gas (or molecular clouds) since the gas is always mixed with dust grains that thermally radiate. On the other hand, gas primarily emits through its line emissions. As mentioned earlier, direct observation of H_2 is challenging, so one of the most common proxies used is the rotational lines of CO. This is because CO is the second most abundant molecule after H_2 in the ISM and has rotational transitions that can be excited at low temperatures (e.g., $\Delta E^{\mathrm{CO}}_{J=1-0} = 5.5$ K). The structures observed in the dust continuum emission can be morphologically traced using line emissions (e.g., ^{13}CO and ^{12}CO), which provides deeper insights into the physical properties of the molecular clouds (for comparison, refer to Figures 4.1 and 4.5 in Chapter 4).

The physical environment of massive star-forming regions at different spatial scales, ranging from clouds (>10 pc) to cores (<0.1 pc), is traced using a combination of dust continuum and molecular line emission. When considering continuum data, optical and NIR data are useful for tracing point-like sources, which are direct manifestations of main-sequence and YSOs (or pre-main sequence) stars, respectively. MIR/FIR continuum emission traces the locations of warm dust emission, where the physical environment is heated by UV photons from massive stars, and may reveal the Photo Dissociation Regions (PDRs). The mm/sub-mm range traces the cold dust emission environment and is very important for the overall study. This wavelength range traces the morophology and kinematics of molecular clouds through dust continuum and molecular line emission, and is useful to detect prestellar cores. Ionized emission from HII regions is depicted in radio continuum maps, although signatures of the ionized regions can also be observed in the optical-MIR range (e.g., H_α emission and Polycyclic Aromatic Hydrocarbons (PAH) emission). In addition to the multi-wavelength data, the high-resolution data (tracing the physical scale of $\lesssim$0.05 pc) is necessary to trace the substructures at different scales within molecular clouds. Hence, multiscale observations are also equally important. The following section provides the overview of data sets used in this thesis.

2.2 Multi-wavelength data sets

To investigate the formation processes of massive stars, we utilize multiwavelength and multi-scale data spanning from optical to radio wavelengths, obtained from national and international telescope facilities, including both spacebased and ground-based observations. The MIR and sub-mm data trace the warm and cold dust emission respectively, while the ionized emission tracing HII regions is depicted in the radio continuum maps. The kinematics of molecular cloud associated with the star-forming sites are primarily studied by the use of molecular line data (e.g., ^{12}CO/^{13}CO/C^{18}O(J = 1–0)).

Table 2.1 presents a comprehensive overview of the multi-wavelength data utilized in this thesis.

Table 2.1: List of multi-wavelength data sets used in this thesis.

	Survey name/data source	Telescope(s)/Dish size	Coverage/Target/Proposal Id.	Wavelength/band(s)/Transitions	Resolution ($\Theta_{spatial}/\Theta_{velocity}$)	Reference
Radio	Giant Metrewave Radio Telescope (GMRT)	GMRT; 30 ant × 45 m	#33_065; (PI: Rakesh Pandey)	23, 50 cm	∼10″	Gupta et al. (2017); Dewangan et al. (2020b)
	NRAO VLA Sky Survey (NVSS)	Very Large Array (VLA; C,D config.), 25 ant × 25 m	all sky, north of −40 deg δ_{2000}	21 cm	∼45″	Condon et al. (1998)
	Multi-Array Galactic Plane Imaging Survey (MAGPIS)	VLA (B,C,D config.), 25 ant × 25 m	$5° < l < 48°.5$, $\lvert b\rvert < 0°.8$	20 cm	∼6″	Helfand et al. (2006)
Millimeter/Sub-millimeter	FUGIN [a]	Nobeyama 45-m telescope (45 m)	($10° \le l \le 50°$, $\lvert b\rvert \le 1°$, and $198° \le l \le 236°$, $\lvert b\rvert \le 1°$)	$^{12}CO/^{13}CO(1–0)$ ($\lambda \sim$2.6–2.7 mm)	∼20″, ∼21″ /(1.3 km s^{-1})	Umemoto et al. (2017)
	Milky Way Imaging Scroll Painting (MWISP)[b]	Purple Mountain Observatory (PMO; 13.7 m)	$-10° \le l \le +250°$, $b \le 5°.2$	$^{12}CO(1–0)$ ($\lambda \sim$2.6 mm)	∼50″ /(0.16 km s^{-1})	Su et al. (2019)
	Taeduk Radio Astronomy Observatory (TRAO)	TRAO (14 m)	IC 5146 site	$^{13}CO/C^{18}O$ (1–0) ($\lambda \sim$2.7 mm)	∼49″ /(0.1 km s^{-1})	Chung et al. (2021)
	Bolocam Galactic Plane Survey (BGPS)	Caltech Submillimeter Observatory (CSO; 10.4 m)	$-10° < l < 90°$, $\lvert b\rvert < 0°.5$	1.1 mm	∼33″	Aguirre et al. (2011); Ginsburg et al. (2013)
	James Clerk Maxwell Telescope (JCMT)	JCMT (15 m)	M08BU18, M06BGT02	$^{13}CO/C^{18}O$ (3–2) ($\lambda \sim$0.9 mm)	∼14″ /(∼0.5 km s^{-1})	Buckle et al. (2009)
	$^{13}CO/C^{18}O$ (J = 3→2) Heterodyne Inner Milky Way Plane Survey (CHIMPS)	JCMT (15 m)	$28° < l < 46°$, $\lvert b\rvert < 0°.5$	$^{13}CO/C^{18}O$ (3–2) ($\lambda \sim$0.9 mm)	∼15″ /(0.5 km s^{-1})	Rigby et al. (2016)
	Atacama Large Millimeter/submillimeter Array (ALMA)	ALMA (54 ant. × 12 m, 12 ant. × 7 m)	#2018.1.01318.S; (PI: Lokesh Kumar Dewangan) and #2019.1.00195.L; (PI: Molinari, Sergio)	($HCO^+/H^{13}CO^+$(4–3) ($\lambda \sim$840–864 μm), CH_3CCH ($21_K–20_K$) ($\lambda \sim$366–836 μm), and 865 μm, 1.35 mm continuum)	∼0″.31 × 0″.25 /(∼1 km s^{-1})	Dewangan et al. (2022c)
	APEX Telescope Large Area Survey of the Galaxy (ATLASGAL)	Atacama Pathfinder Experiment (APEX) Telescope (12 m)	$60° < l < 280°$, $\lvert b\rvert < 1°.5$	870 μm	∼19″.2	Schuller et al. (2009)
Sub-mm/FIR	*Planck* Survey	Planck spacecraft (1.5 m)	all sky	550, 850 μm	4′.8	Ade et al. (2014)
	Herschel Infrared Galactic Plane Survey (Hi-GAL)	Herschel Space Observatory (3.5 m)	$-70° < l < 68°$, $\lvert b\rvert \le 1°$	70, 160, 250, 350, 500 μm	5″.8, 12″, 18″, 25″, 37″	Molinari et al. (2010a, 2016)
	Stratospheric Observatory for Infrared Astronomy (SOFIA)/upGREAT	SOFIA (2.5 m)	#06_0226; (PI: Loren Dean Anderson)	[CII] ($^2P_{3/2}$–$^2P_{1/2}$; $\lambda \sim$158 μm)	14′.1 /(0.385 km s^{-1})	Anderson et al. (2019); Schneider et al. (2020)
MIR	Spitzer MIPS Inner Galactic Plane Survey (MIPSGAL)	Spitzer Space Telescope (0.85 m)	$4° < l < 50°$, $\lvert b\rvert \le 1°$	24 μm	∼6″	Carey et al. (2009)
	Wide Field Infrared Survey Explorer (WISE)	WISE telescope (0.4 m)	all sky	12, 22 μm	6″.5, 12″	Wright et al. (2010)
NIR	*Spitzer* Galactic Legacy Infrared Mid-Plane Survey Extraordinaire 360 (GLIMPSE360)	Spitzer Space Telescope (0.85 m)	$9°.95 < l < 49°.05$, $\lvert b\rvert < 1°$	3.6, 4.5, 5.8, 8.0 μm	∼2″	Benjamin et al. (2003); Whitney et al. (2011)
	VLT NAOS-CONICA (NACO) adaptive-optics system	Very Large Telescope (VLT); 4 × 8 m)	W42	2.18 μm	∼0″.2	Lenzen et al. (2003); Dewangan et al. (2015)
	UKIRT near-infrared Galactic Plane Survey (GPS)	United Kingdom Infrared Telescope (UKIRT; 3.8 m)	$15° < l < 107°$, $\lvert b\rvert < 5°$, $142° < l < 230°$, $\lvert b\rvert < 5°$, and $-2° < l < 15°$, $\lvert b\rvert < 2°$	1.25–2.2 μm	∼0″.8	Lawrence et al. (2007)
	Two Micron All Sky Survey (2MASS)	Fred Lawrence Whipple Observatory (1.3 m) on Mount Hopkins, Arizona and Cerro Tololo Inter-American Observatory (1.3 m) in Chile	all sky	1.25–2.2 μm	∼2″.5	Skrutskie et al. (2006)
Optical	Digitized Sky Survey II (DSS2-blue)	Oschin Schmidt Telescope (1.22 m) on Palomar Mountain and UK Schmidt Telescope (1.24 m)	45% of the sky	0.47 μm	∼2″	McLean et al. (2000)

[a]FOREST Unbiased Galactic plane Imaging survey with the Nobeyama 45-m telescope (FUGIN) survey

[b]Observations for MWISP are still ongoing.

However, the detailed description of the specific data used is provided within each respective chapter. In the following section, we provide a brief discussion on the general procedure for data analysis.

2.3 Methods & Techniques

This section presents an overview of the methods employed to extract observable parameters from the multi-wavelength data. These methods were crucial in obtaining the scientific results necessary to achieve the objectives of this thesis.

2.3.1 Moment Maps

In radio astronomy, a moment map is a way to visualize the distribution and properties of the emission of a particular spectral line. It is obtained by calculating the moments of the spectral line intensity over a specific spectral/velocity range. Concerning the moment maps of particular region of interest, one needs to collapse the molecular line data cube along the spectral axis by taking a moment of the data. The moment maps for the given 3D PPV data cube having spectral line intensity I(x, y, v) are defined as follows (e.g., Teague, 2019):

- **Moment-0 map:** The zeroth moment map ($M_0(x, y)$) is simply the integrated intensity along the spectral (or velocity) axis and can be expressed as:

$$M_0(x, y) = \int_{v_1}^{v_2} I(x, y, v) dv. \tag{2.1}$$

  This map provides the spatial morphology of molecular cloud and can be related to the N(H_2) column density distribution (see Section 2.3.3.3 for details). On the other hand, a peak intensity map ($F_{\text{peak}}(x, y)$) infers the spatial distribution of maximum intensity and can be expressed as:

$$F_{\text{peak}}(x, y) = \max(I(x, y, v)). \tag{2.2}$$

- **Moment-1 map:** The first moment map ($M_1(x,y)$) is the intensity-weighted velocity of the line and is expressed as:

$$M_1(x,y) = \frac{\int_{v_1}^{v_2} vI(x,y,v)dv}{M_0(x,y)}. \tag{2.3}$$

This provides the kinematics of molecular cloud and is useful to distinguish different velocity components present in the direction of our target site. A peak velocity map ($V_{\text{peak}}(x,y)$), which indicates the velocity at peak emission is expressed as:

$$V_{\text{peak}}(x,y) = V(x,y) \text{ at } \max(I(x,y,v)). \tag{2.4}$$

- **Higher order moment maps:** The higher order moments (i.e., $M_K(x,y)$ for $K \geq 2$) are expressed as follows:

$$M_K(x,y) = \frac{\int_{v_1}^{v_2}(v - M_1(x,y))^K I(x,y,v)dv}{M_0(x,y)}. \tag{2.5}$$

Following Equation 2.5, the second moment map ($M_2(x,y)$) generally infers the intensity-weighted velocity variance of the line, and has a unit of $km^2\ s^{-2}$. However, in usual practice, the intensity weighted velocity dispersion (or line-width) is useful measure of the thermal and turbulent properties of gas. Therefore the quantity $\sqrt{M_2(x,y)} = \sqrt{\frac{\int_{v_1}^{v_2}(v-M_1(x,y))^2 I(x,y,v)dv}{M_0(x,y)}}$ is the actual measure of velocity dispersion ($\sigma(x,y)$) and is referred to second moment line-width (or moment-2 line-width) map throughout the following chapters. It is also to be noted that the Full Width at Half Maximum (FWHM) line-width is equally popular in literature and is related to $\sigma(x,y)$ as $\text{FWHM}(x,y) = \sigma(x,y)\sqrt{8ln2}$. We have consistently highlighted this distinction throughout the relevant chapters, wherever it was necessary. Here, in the mentioned equations, x, y, and v are the three dimensions of PPV cube (or molecular line data cube), and $I(x,y,v)$ refers to the line intensity. In this thesis, all these moment maps including V_{peak} and F_{peak} are produced using either the Python package `SpectralCube`[1] or the *IDL* based routines.

[1]https://spectral-cube.readthedocs.io/en/latest/moments.html

2.3.2 Kinematic parameters of gas

- **Thermal/Non-thermal velocity dispersion:** An expression of the non-thermal velocity dispersion ($\sigma_{\rm NT}$) is defined below:

$$\sigma_{\rm NT} = \sqrt{\sigma_{\rm obs}^2 - \sigma_{\rm T}^2} = \sqrt{\frac{\Delta V^2}{8\ln 2} - \frac{kT_{kin}}{\mu m_H}}, \tag{2.6}$$

where $\sigma_{\rm obs}$ is the observed velocity dispersion and is related to ΔV, which is the measured FWHM line width ($\Delta V = \sigma_{\rm obs} \times \sqrt{8ln2}$), and

$$\sigma_{\rm T} = \sqrt{\frac{kT_{kin}}{\mu m_H}} \tag{2.7}$$

is the thermal broadening (or thermal velocity dispersion) for specific molecule having mean molecular weight of μ (i.e., μ for ^{13}CO, ^{13}CO, and H^{13}CO$^+$ are 29, 30, and 30, respectively) at gas kinetic temperature (T$_{kin}$), and m_H is the mass of hydrogen atom.

2.3.3 Column density (N(H$_2$)) and temperature (T_d) estimates

The knowledge of N(H$_2$) and T_d directly manifest as observable physical parameters of the system, such as mass, density, and turbulent properties of gas. Below we discuss the methods to estimate the N(H$_2$) and T_d maps.

2.3.3.1 Using cold dust continuum emission

The analysis of thermal cold dust emission in the FIR wavelength range allows us to derive important physical parameters such as dust temperature and column density of a region (Battersby et al., 2011; Launhardt et al., 2013). In this thesis, we utilize SED modeling of the thermal dust emission, focusing on the Rayleigh-Jeans regime covered by the *Herschel* FIR bands (160-500 μm). In this scenario, the standard procedure assumes that the emission is optically thin, following the power-law opacity of $\kappa_\nu \propto \nu^\beta$, where β is a constant value. It is also assumed that the dust temperature remains constant along the line of sight and that there is no contamination from radiation in front of or behind the observed structures. The following steps were followed in this order to obtain the N(H_2) and T_d maps.

Firstly, the surface brightness unit for all images needs to be calibrated to Jy pixel^{-1}. This conversion is necessary as the SPIRE images (250, 350, and 500 μm) are calibrated in MJy sr^{-1} and the PACS images (70 and 160 μm) are calibrated in Jy pixel^{-1}. The conversion was performed using the pixel scales specific to each SPIRE band. Next, the images at wavelengths of 160-350 μm are convolved to match the resolution of the 500 μm image, which had the lowest resolution among all the images ($\sim$37″). This is generally achieved by applying the convolution kernels provided by Aniano et al. (2011). The convolved images are also regridded to a common pixel scale of 14″, which match the pixel scale of the 500 μm image. Using these final images, the background flux level (I_{bg}) is determined. This is done by selecting a smooth and relatively dark region of the sky, without any abrupt clumpy structures. The distribution of pixel values in this region is now iteratively fitted with a Gaussian, with pixel values outside $\pm 2\sigma$ being rejected in each iteration until the fit converged. The same region of the sky is used for all wavelength bands.

A modified blackbody (or gray-body) fitting approach is then employed to analyze the data on a pixel-by-pixel basis. The *Herschel* 70 μm image is generally not used in the spectral fitting due to the contamination caused by warm emission originating from UV-heated dust (e.g., PAHs or transiently heated small dust grains), thus leading to overestimation in dust temperature (i.e., underestimation in column density). The formulation used for the fitting is given by the gray-body equation as follows (e.g., Battersby et al., 2011; Sadavoy et al., 2012; Mallick et al., 2015):

$$I_\nu(\nu) - I_{\mathrm{bg}}(\nu) = B_\nu(\nu, T_{\mathrm{d}})\Omega(1 - e^{-\tau(\nu)}), \tag{2.8}$$

where, I_ν is the observed flux density and I_{bg} is the background flux density. The Planck function (B_ν) accounts for the emission from a blackbody at the given frequency (ν) and dust temperature (T_d). The term Ω represents the solid angle subtended by each pixel (14″× 14″ in this case), and $\tau(\nu)$ denotes the optical depth, which is determined by the equation

$$\tau(\nu) = \mu m_{\rm H} \kappa_\nu N({\rm H}_2), \tag{2.9}$$

where, $\mu = 2.8$ is the mean molecular weight per H_2 molecule, $m_{\rm H}$, κ_ν, and $N({\rm H}_2)$, represent the mass of hydrogen, dust opacity, and column density of molecular hydrogen, respectively. In this analysis, a functional form of $\kappa_\nu = 0.1 \left(\frac{\nu}{1({\rm THz})}\right)^\beta$ cm^2 g^{-1} was adopted for the dust opacity, with β set to 2 (e.g., Könyves et al., 2015). The fitting procedure involved using the four data points corresponding to each wavelength (160–500 μm), and allowing T_d and $N({\rm H}_2)$ to vary as free parameters. For pixels where the fit did not converge or the error exceeded 10%, the values were replaced with the median of the eight neighboring pixels. This method is adopted to derive the $N({\rm H}_2)$ and T_d in Chapter 3.

2.3.3.2 Using *hires* and `PPMAP` methods

Considering the *Herschel* images at 160–500 μm wavelengths, it is possible to estimate three sets of N(H_2) and T_d maps as described in the previous section. However, it should be noted that the high-resolution maps, obtained through the fitting of two images (e.g., $\sim$18″; estimated using *Herschel* 160 μm and 250 μm images), are less accurate. On the other hand, the lowest-resolution maps, which incorporate all four *Herschel* images, are more accurate.

The previously proposed *hires* method (Palmeirim et al., 2013) aimed to combine the higher accuracy of lower-resolution N(H_2) and T_d maps with the high-resolution but less accurate maps using the unsharp masking technique. Unsharp masking involves measuring the difference between two maps at different spatial resolutions. However, this method was limited to generating maps at the resolution of the *Herschel* 160 μm image ($\sim$18″). Recently, Men'Shchikov (2021) introduced a different approach that allows for the creation of N(H_2) and T_d maps at the resolution of the highest-resolution *Herschel* image ($\sim$6″). From now on, in the following chapters, this method will be referred to as *hires*, as named by Men'Shchikov (2021).

In this case, the extended version of aforementioned algorithm allows for the derivation of N(H_2) and T_d using observed images (70–500 μm) with any arbitrarily high angular resolution (6″–37″). The three independent derived T_d maps (18″, 24″, and 37″) and five observed *Herschel* images with their native resolutions O_λ of 6″–37″ can be used to estimate 15 N(H_2) maps using gray-body equation for the optically thin case and neglecting $I_{bg}(\nu)$ in Equation 2.8. Combining Equations 2.8 and 2.9, we can obtain for N(H_2) as follows:

$$N(\mathrm{H}_2)_{O_\lambda(2|3|4)} = \frac{I_\nu}{B_\nu(T_{d(2|3|4)})\kappa_\nu \mu m_H}, \tag{2.10}$$

where, (2|3|4) indicates the respective number of images used in the gray-body fitting procedure. Later using these N(H_2) maps at different resolutions, a high resolution N(H_2) map is computed by adding the higher-resolution information on the 37″ resolution map using unsharp masking technique (see more details in Men'Shchikov, 2021). The *getsf* utilities (e.g., *modfits* and *resample*; Men'Shchikov, 2021) were used in the analysis. The utility *modfits* was used to convert the *Herschel* flux densities at 70 and 160 μm from units of Jy pixel^{-1} to MJy sr^{-1}, while the utility *resample* was utilized to regrid all the *Herschel* images at 70–500 μm to the pixel scale of the image at 70 μm (i.e., 3″). Thereafter, images with different possible resolutions (i.e., 8.″4, 13.″5, 18.″2, 24.″9, and 36.″3) were generated, and the final spectral fitting was performed (excluding the image at 70 μm) to generate high-resolution column density and temperature maps. In this thesis, the *hires* method is utilized in Chapter 6.

Apart from the *hires*, we have utilized the `PPMAP` based high-resolution N(H_2) and T_d maps at ∼12″. The `PPMAP` refers to the *point-process mapping*, which is based on a Bayesian approach known as the point process formalism, where the structure of interest, such as a filament or pre-stellar core, is represented as a collection of points in a defined state space. These maps were generated using the *Herschel* images at 70, 160, 250, 350, and 500 μm for the *EU-funded ViaLactea project* (Molinari et al., 2010b; Marsh et al., 2017). The `PPMAP` algorithm is designed to create image cubes that depict the differential N(H_2) as a function of angular position and T_d for dusty structures associated with star formation. It takes a set of observational images at different wavelengths and their corresponding point spread functions (PSFs) as input data. The algorithm operates on the observational images at their native resolution without requiring any smoothing or resampling (see more details in Marsh et al., 2015). These maps were obtained from a publicly accessed website[2] and are used in Chapters 4 and 8.

2.3.3.3 Using ^{12}CO/^{13}CO molecular line data

Considering local thermodynamical equilibrium (LTE), one can estimate the ^{13}CO(1–0) column density ($N(^{13}\mathrm{CO})$) using the following equation (e.g., Garden et al., 1991; Bourke et al., 1997; Mangum & Shirley, 2015)

$$N(^{13}\mathrm{CO}) = 2.42 \times 10^{14} \frac{T_{\mathrm{ex}} + 0.88}{1 - \exp(-5.29/T_{\mathrm{ex}})} \int \tau_{13} dv, \tag{2.11}$$

where τ_{13} is the optial depth of ^{13}CO(1–0), T_{ex} is the mean excitation temperature, and v is the local standard of rest (LSR) velocity measured in km s^{-1}. Since the ^{12}CO(1–0) emission is optically thick, one can calculate the T_{ex} using ^{12}CO(1–0) as follows (Garden et al., 1991; Xu et al., 2018)

$$T_{\mathrm{ex}} = \frac{5.53}{\ln\left[1 + \frac{5.53}{T_{\mathrm{mb}}(^{12}\mathrm{CO}) + 0.82}\right]}, \tag{2.12}$$

where T_{mb} is the main-beam brightness temperature. Here, one can assume that the excitation temperatures of ^{12}CO(1–0) and ^{13}CO(1–0) are the same for the entire cloud. We can then derive optical depth (τ) using the equation (Garden et al., 1991; Xu et al., 2018)

$$\tau(^{13}\mathrm{CO}) = -\ln\left[1 - \frac{T_{\mathrm{mb}}(^{13}\mathrm{CO})}{\frac{5.29}{\exp(5.29/T_{\mathrm{ex}}) - 1} - 0.89}\right] \tag{2.13}$$

Once N(^{13}CO) is known, we can use the the column density conversion factor $N(\mathrm{H_2})/N(^{13}\mathrm{CO}) \simeq 7 \times 10^5$ from Frerking et al. (1982) to estimate the N(H$_2$) distribution.

[2]http://www.astro.cardiff.ac.uk/research/ViaLactea/

2.3.4 Mass Estimates

Once we estimate the spatial distribution of N(H_2), we can calculate the mass of emitting dust structure as:

$$M_{\rm c} = \mu \; m_{\rm H} \; a_{\rm pixel} \; \Sigma N({\rm H_2}) \tag{2.14}$$

where, μ is the mean molecular weight (assumed to be 2.8), $a_{\rm pixel}$ is the area subtended by one pixel, $m_{\rm H}$ is the mass of hydrogen atom, and $\Sigma N({\rm H_2})$) is the integrated column density over the area of the dusty structure.

Apart from this, one can estimate the mass of clouds/clumps by knowing the fluxes of dust emission at frequency ν as follows (e.g., Hildebrand, 1983; Dewangan et al., 2016a):

$$M_c = \frac{D^2 \, S_\nu \, R_t}{B_\nu(T_d) \, \kappa_\nu}, \tag{2.15}$$

where S_ν is the total flux at frequency ν, D is the distance of source (kpc), R_t is the gas-to-dust mass ratio (assumed to be 100 Weingartner & Draine, 2001), B_ν is the Planck function for a dust temperature T_d, and κ_ν is the dust absorption coefficient.

2.4 Detection of Filaments

In order to analyze filamentary structures and extract meaningful information, it is necessary to accurately identify the ridges and extent of the filaments. However, this can be challenging due to observational data noise. While structure identification by eye can sometimes be effective, the use of automated filament detection algorithms provides a bias-free choice. In general, for the past few years, the widely used algorithms to detect filament skeletons in an astronomical image are `DisPerSE` (Sousbie, 2011), and `filfinder` (Koch & Rosolowsky, 2015). The operation of `DisPerSE` involves the connection of critical points, such as maxima and minima, through integral lines following the gradients present in a given map. These critical points are characterized by a zero gradient within the map. A crucial parameter required for the algorithm is the "persistence level," which quantifies the absolute difference between the values of the critical points. In another scenario, `filfinder` adopts adaptive thresholding on flattened and smoothed data to detect filaments. It creates a mask of filamentary structures and removes background noise by applying a globally thresholded mask. The filamentary structures are then represented by their skeletal form using a Medial Axis Transform.

In this thesis, we used a recently developed filament finding tool `getsf` by Men'Shchikov (2021) which is an updated version of `getfilaments` (Men'Shchikov, 2013) algorithm. This takes a different approach by decomposing the original image into different spatial scales and identifying filament skeletons along with the sources that are nearly circular in geometry. The popularity of `getsf` among other available filament detection tool is that it does not require user intervention. The only user-definable parameter to extract the structures (i.e., sources and filament skeletons) using `getsf` is the maximum width/size (FWHM, in arcsec) of the structure of interest. This parameter can be roughly estimated using `ds9` by placing a circular region encompassing the width of the larger structure. Chapters 3, 5, and 6 present the application of `getsf` to identify subfilaments in the parent molecular cloud.

The major steps involved in the `getsf` are: 1) image preparation for structure extraction, 2) separating the structural elements of sources and filaments from their backgrounds, (3) reducing noise and background fluctuations in the source and filament images, (4) combining the flattened source and filament components, (5) identifying sources and filaments in the combined component images, and (6) measuring the properties of the identified sources and filaments.

2.5 Identification of clumps/sources

In this section, we discuss a few methods utilized in the thesis to identify density structures within molecular clouds.

2.5.1 Dendrogram Method

The extraction of hierarchical structures in astronomical data can be achieved using a Python-based tool called "astrodendro." A dendrogram analysis is performed on the map of star-forming molecular clouds, where the dendrogram represents a tree-like structure with branches and leaves. Branches can further split into sub-structures, while leaves do not have any sub-structures. Figure 2.2 illustrates a schematic dendrogram representation of a 2D map of hierarchical structures.

The "astrodendro" tool is capable of identifying dendrogram structures in both 2D (PP) and 3D (PPV) astronomical datasets. It provides physical properties such as size, position angle, velocity, etc., of these structures. Before running the "astrodendro" tool, three key input parameters need to be set: "min˙value," "min˙delta," and "min˙npix." The "min˙value" represents the minimum emission value required for dendrogram consideration, typically taken as 3-5 times the standard deviation (i.e., 3–5σ) of the data. The "min˙delta" determines the significance of a leaf to be considered an independent entity. The "min˙npix" specifies the minimum number of pixels required for a leaf to be regarded as an independent entity. Chapter 7 utilizes the dendrogram method to extract the substructures withing a hub region.

2.6 Identification of YSOs

The presence of infrared excess sources or YSOs in a star-forming region is a strong indicator of ongoing star formation activity. The excess infrared emission originates from the thick circumstellar material, such as envelopes and disks, which reprocesses the starlight. To identify the YSOs in our study, we utilized photometric data at NIR-MIR wavelengths ranging from 1 to 24 μm. These data were obtained from various infrared surveys, including UKIDSS-GPS, 2MASS, GLIMPSE, and MIPSGAL. The identification of YSOs in the target region was based on color-color diagram (CCD) and color-magnitude diagrams (CMD),

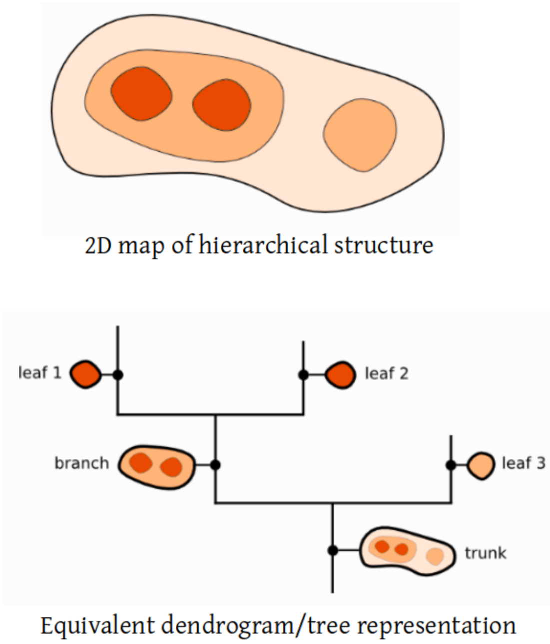

Figure 2.2: A 2D map of hierarchical structure (e.g., molecular cloud) and its equivalent dendrogram representation is shown (credit: https://dendrograms.readthedocs.io/en/stable/).

which provide valuable information for distinguishing these young objects from other sources. The color represents the ratio of intensities in two spectral bands, while the magnitude represents the flux in a standard band. CMD and CCD can provide information on relative ages (or YSO class) of star clusters.

Although, the description on the CCD and CMDs are given in Chapters 4 and 5, here we briefly discuss the importance of NIR/MIR CCD and CMD in identification of YSOs. In this thesis, we examined the CCD [4.5]–[5.8] vs. [3.6]–[4.5] and the dereddened CCD (i.e., $[[3.6]-[4.5]]_0$ vs $[K-[3.6]]_0$) of point-like objects. We also explored the [3.6]–[24] vs. [3.6] and $H-K$ vs. K CMDs to infer the candidate YSOs. We primarily followed the color criteria of Gutermuth et al. (2009); Getman et al. (2007); Hartmann et al. (2005). The respective Chapters 4 and 5 present the conditions followed.

2.6.1 YSO surface density estimate

To investigate the spatial distribution of YSOs in the target star-forming region, we conducted a nearest neighbor (NN) surface density analysis of the selected YSOs (e.g., Casertano & Hut, 1985; Gutermuth et al., 2009; Bressert et al., 2010;

Dewangan et al., 2016b).

To construct a YSO surface density map, we adjusted the radial distance in a manner that includes the sixth nearest YSO from each grid position (i.e., include 5 YSOs within a circular region). For our analysis, we chose a grid size of 15″, which is a conservative approach to deal with a large number of YSOs in a field (Dewangan et al., 2016b). The local stellar surface density Σ at each grid position $[i, j]$ is then calculated using the following equation:

$$\Sigma(i,j) = \frac{N}{\pi R_N^2(i,j)} \tag{2.16}$$

In this equation, N denotes the number of stars within circular region of projected radius $\mathrm{R}_N(i, j)$. Thus, $\mathrm{R}_N(i, j)$ represents the projected radial distance to the $N + 1^{\mathrm{th}}$ nearest star.

Chapter 3

Star-forming site RAFGL 5085: Is a perfect candidate hub-filament system?[†]

3.1 Introduction

The impact of massive OB stars ($\gtrsim 8\ M_\odot$) through their radiative and mechanical feedback on the surrounding environment of galaxies is well-documented in the literature (e.g., Zinnecker & Yorke, 2007; Rodríguez, 2006; Motte et al., 2018). However, despite significant advancements in recent years, our understanding of the formation of such massive stars remains incomplete (e.g., Rosen et al., 2020). With recent observations, our understanding of star formation processes has expanded from molecular cloud to core scales (e.g., Bonnell et al., 2001, 2004; Bonnell & Bate, 2006; Vzquez-Semadeni et al., 2009; Vázquez-Semadeni et al., 2017, 2019; Padoan et al., 2020, see Section 1.1.3). In order to observationally study the formation of massive stars, one needs to explore the embedded morphology and the gas motion around a newly formed massive star that may hold clues to its origin. Despite the ubiquity of filaments in the ISM and their association with

[†]Dewangan, L. K., **Bhadari, N. K.**, Maity, A. K., Pandey, Rakesh, Sharma, Saurabh, Baug, T., Eswaraiah, C., 2023, JApA, 44, 23D, "Star-forming site RAFGL 5085: Is a perfect candidate of hub-filament system?"

star-forming regions, their role in star formation including massive stars remains an ongoing topic of intense debate (see Hacar et al., 2022, and references therein, see also Section 1.3).

The focus of this study is the star-forming region RAFGL 5085/IRAS 02461+6147/G136.3833+02.2666, located at a distance of 3.3 kpc (Lumsden et al., 2013). RAFGL 5085 is known to host a MYSO with $L_{\rm bol}$ of 6580 $L_\odot$ (Lumsden et al., 2013). It is associated with weak centimeter continuum emission (i.e., total flux = 1.7 mJy; Condon et al., 1998) and a NIR cluster (e.g., Carpenter et al., 2000; Bica et al., 2003). The NIR cluster was identified using the K′ stellar surface density map (see Figure 3 related to IRAS 02461+6147 in Carpenter et al., 2000), which is embedded in a molecular ^{12}CO(1–0)/^{13}CO(1–0) condensation/clump (at $V_{\rm LSR}$ $\sim$$-$44 km s^{-1}; Carpenter et al., 2000) traced by the FCRAO Outer Galaxy ^{12}CO(1–0) Survey (Heyer et al., 1998). Dense cores and compact millimeter continuum sources (MCSs) have also been reported in the direction of the ^{12}CO/^{13}CO clump using C^{18}O(1–0) line data and continuum maps at 98 GHz and 110 GHz (Saito et al., 2006, 2007). Water maser emission and ammonia emission have been detected toward the NIR cluster (Ouyang et al., 2019). Previous studies have investigated a bipolar molecular outflow toward RAFGL 5085 (e.g., Wu et al., 2004; Li et al., 2019), indicating ongoing star formation activities, including the presence of a MYSO. However, the detailed structure and morphology of the emission at different wavelengths, from NIR to sub-mm, in RAFGL 5085 have not been extensively explored. Additionally, no study has examined the gas motion in the previously reported molecular clump hosting RAFGL 5085. This work aims to fill these gaps by investigating the physical processes underlying star formation in RAFGL 5085 using a multi-wavelength approach. In particular, we utilize the *Herschel* sub-mm images at 250, 350, and 500 μm (e.g., Elia et al., 2010; Griffin et al., 2010) to derive the dust column density and temperature maps of RAFGL 5085, which have not been studied before. Furthermore, we analyze the ^{12}CO (1–0) and ^{13}CO (3–2) line data to gain insights into the gas dynamics in the region.

The work is organized in the following. §3.2 deals with the observational data sets used in this work. We present the outcomes extracted from the analysis of multi-wavelength data sets in §3.3. We discuss our findings in §3.4. In §3.5, we present the summary of the work.

3.2 Data and analysis

Observational data sets were obtained for a region spanning approximately 0.22 $\times$ 0.22 deg^2 (central coordinates: l = 136°.38 ; b = 2°.26) around RAFGL 5085 (see Table 5.1). Photometric magnitudes of point-like sources in the H and K$_s$ bands were extracted from the 2MASS Point Source Catalog. However, it should be noted that the Hi-GAL observations at 70 and 160 μm and the *Spitzer*-GLIMPSE360 map at 3.6 μm do not cover the specific target site of RAFGL 5085 and thus are not available for analysis. Additionally, this study incorporates photogeometric distances ("rpgeo") of point-like sources obtained from the Gaia early data release 3 (EDR3; Brown et al., 2021; Fabricius et al., 2021).

The bolocam source catalog at 1.1 mm (v2.1; Ginsburg et al., 2013) was also utilized for RAFGL 5085. We retrieved the processed James Clerk Maxwell Telescope (JCMT) ^{13}CO (3–2) spectral data cube (rest frequency = 330.587960 GHz) and the C^{18}O (3–2) line data cube (rest frequency = 329.3305453 GHz) for the specific object "G136.3833+02.2666/RAFGL5085" (proposal id: M08BU18) from the JCMT Science Archive/Canadian Astronomy Data Centre (CADC). These data cubes are calibrated in terms of antenna temperature. The observations were carried out using the Heterodyne Array Receiver Programme/Auto-Correlation Spectral Imaging System (HARP/ACSIS; Buckle et al., 2009) spectral imaging system, with an integration time of 59.358 s for ^{13}CO and 59.290 s for C^{18}O. The pixel scale and the resolution of the JCMT line cube are $\sim$7$''$.3 and $\sim$14$''$, respectively.

Survey/data source	Wavelength/Frequency/line(s)	Resolution ($''$)	Reference
NRAO VLA Sky Survey (NVSS)	1.4 GHz	$\sim$45	Condon et al. (1998)
Milky Way Imaging Scroll Painting (MWISP)	^{12}CO(1–0)	$\sim$50	Su et al. (2019)
James Clerk Maxwell Telescope (JCMT)	^{13}CO(3–2), C^{18}O (3–2)	$\sim$14	Buckle et al. (2009)
Bolocam Galactic Plane Survey (BGPS)	1.1 mm	$\sim$33	Aguirre et al. (2011)
Herschel Infrared Galactic Plane Survey (Hi-GAL)	250, 350, 500 μm	$\sim$ 18, 25, 37	Molinari et al. (2010a)
Wide Field Infrared Survey Explorer (WISE)	12, 22 μm	$\sim$6.5, $\sim$12	Wright et al. (2010)
Spitzer Galactic Legacy Infrared Mid-Plane Survey Extraordinaire 360 (GLIMPSE360)	4.5 μm	$\sim$2	Whitney et al. (2011)
Two Micron All Sky Survey (2MASS)	1.65, 2.2 μm	$\sim$2.5	Skrutskie et al. (2006)

3.3 Result

Below we discuss the results derived from the analysis of multi-wavelength data sets.

3.3.1 Physical environments around RAFGL 5085

The region of interest exhibits bright extended emission or diffuse nebulosity in the *Spitzer* 4.5 μm image which is shown by Figure 3.1a. Within this central region, where RAFGL 5085 is located (inset in Figure 3.1a), several point-like sources and an elongated feature are identified. IR-excess sources (or candidate YSOs; see Section 1.1.1) and outflow activities are often indicative of ongoing star formation. IR-excess sources are typically identified by their distinctive emission patterns across different IR bands. However, since the *Spitzer* 3.6 μm image is not available for RAFGL 5085, the usual color criteria based on the 3.6 and 4.5 μm bands cannot be applied in this case (e.g., Gutermuth et al., 2009). Instead, we rely on the 2MASS NIR data to identify potential sources with IR-excess within our target region. Figure 3.1a shows the positions of 2MASS point-like sources with H$-$K$_s$ $>$ 0.65 (represented by open circles) overlaid on the *Spitzer* 4.5 μm image. This specific color criterion is determined based on the analysis of sources in a nearby control field. Consequently, 2MASS sources with H$-$K$_s$ $>$ 0.65 are considered as potential candidates for IR-excess sources.

Figure 3.1b displays the WISE 12 μm image, revealing at least five filamentary features (length $>$ 1 pc) directed toward the central region hosting RAFGL 5085. In the WISE image, a bright source is also seen toward the central region, which does not appear as a point-like source. The dust continuum emission at 1.1 mm

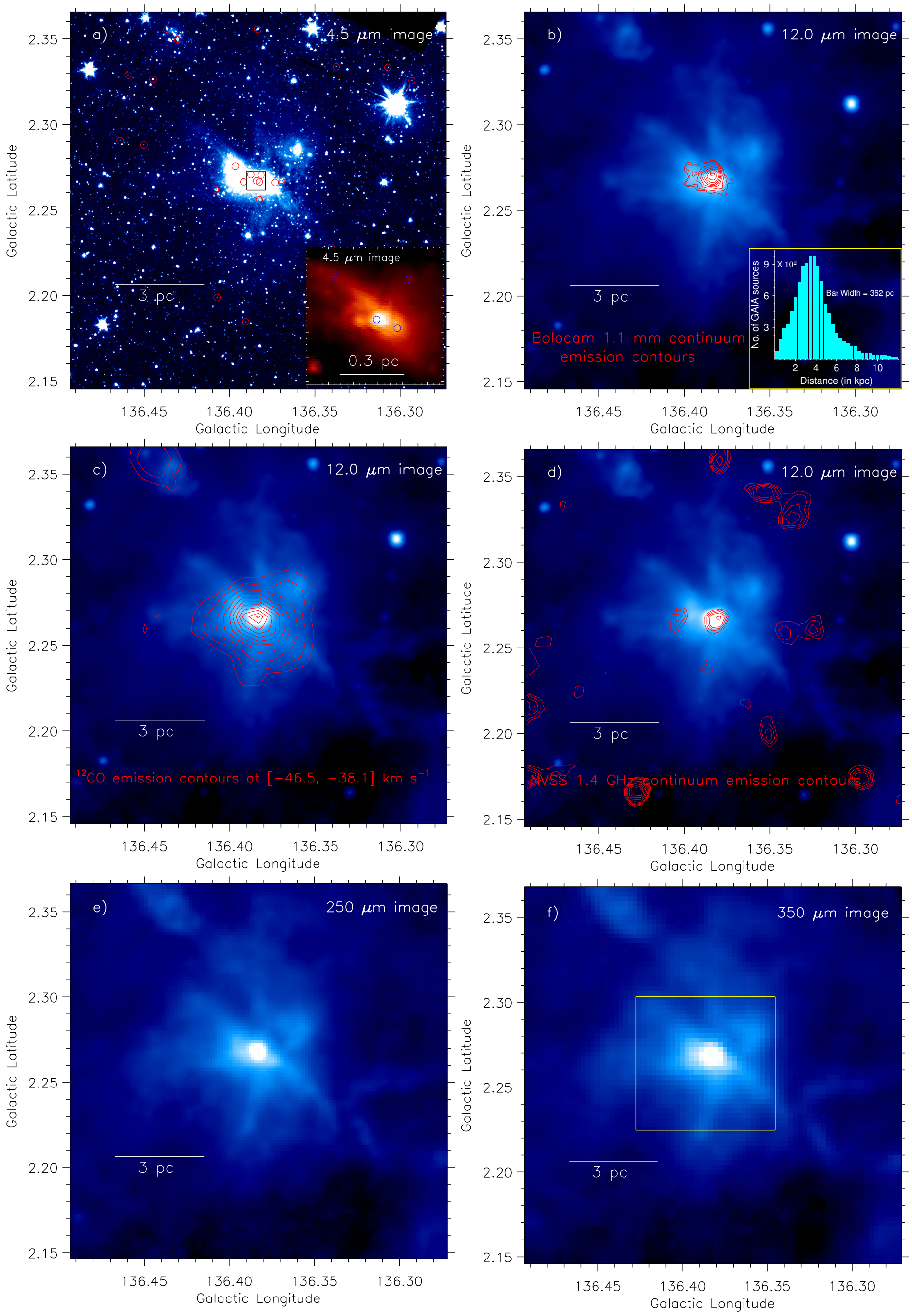

Figure 3.1: Multi-wavelength view of RAFGL 5085. The images are shown at different wavelengths, which are highlighted in the panels. a) Overlay of IR-excess source candidates with H$-$K$_s$ > 0.65 (see red circles) on the *Spitzer* 4.5 μm image. Using the *Spitzer* 4.5 μm image, a zoomed-in view of the central region is shown using the inset on the bottom right (see a solid box in Figure 3.1a). IR-excess source candidates are also indicated by circles. b) Overlay of the bolocam 1.1 mm continuum emission contours on the WISE 12 μm image, and the levels of the contours are 0.697 Jy beam^{-1} $\times$ (0.25, 0.3, 0.4, 0.5, 0.6, 0.7, 0.8, 0.9, 0.98). The inset on the bottom right shows the distance distribution of Gaia point-like sources toward our selected target area. c) Overlay of the MWISP ^{12}CO (1–0) emission contours at [$-$46.5, $-$38.1] km s^{-1} on the WISE 12 μm image, and the levels of the contours are 63.1 K km s^{-1} $\times$ (0.07, 0.12, 0.2, 0.3, 0.4, 0.5, 0.6, 0.7, 0.8, 0.9, 0.98). d) Overlay of the NVSS 1.4 GHz radio continuum emission contours on the WISE 12 μm image, and the levels of the contours are 2.467 mJy beam^{-1} $\times$ (0.35, 0.4, 0.45, 0.5, 0.6, 0.7, 0.8, 0.9, 0.98). e) The panel shows the *Herschel* 250 μm image. f) The panel displays the *Herschel* 350 μm image. A solid box highlights the area shown in Figures 3.2a and 3.2b. In all panels, a scale bar (at a distance of 3.3 kpc) is presented.

is distributed toward the WISE bright source (Figure 3.1b). We find a clump in the bolocam 1.1 mm map (see Figure 3.1b), and its total flux at 1.1 mm has been reported to be 1.824 Jy (Ginsburg et al., 2013). We have also computed the total mass of the clump using the formula given by Equation 2.15. The analysis uses $S_\nu = 1.824$ Jy at $\lambda = 1.1$ mm (Ginsburg et al., 2013), $\kappa_\nu = 1.14\,\mathrm{cm}^2\,\mathrm{g}^{-1}$ (Enoch et al., 2008; Bally et al., 2010), $D = 3.3$ kpc, and $T_d = 22$ K (see Figure 3.4b). Using these values, we have computed the mass of the bolocam clump (M_c) to be ∼225 $M_\odot$. This M_c value is estimated to be ∼255 $M_\odot$ at $D = 3.5$ kpc. We assume an uncertainty on the estimate of the clump mass to be typically ∼20% and at most ∼50%, which could be contributed from the error on the adopted dust temperature, opacity, measured flux, and the distance of the source.

We have also examined the distance distribution of Gaia point-like sources in the direction of our selected target area. We find a peak of distance distribution around 3.5±0.36 kpc (see an inset in Figure 3.1b), which is in agreement with our adopted distance to the target source.

In Figure 3.1c, a molecular condensation is traced towards the bolocam clump using the MWISP ^{12}CO(1–0) line data. This condensation is depicted in a V_{LSR} range of [−46.5, −38.1] km s^{-1}. Additionally, the NVSS 1.4 GHz continuum emission is observed towards the WISE bright source, as shown in Figure 3.1d. The filamentary features become more prominent in the *Herschel* images at 250 and 350 μm, as seen in Figures 3.1e and 3.1f. Overall, the multi-wavelength images suggest the presence of a HFS (refer to Section 1.3.3 for more details). It is interesting to note that ionized emission and potential IR-excess source candidates are observed towards the central hub of the HFS (i.e., RAFGL 5085 HFS).

Here we note that the MWISP ^{12}CO(1–0) line data do not resolve the HFS as observed in the WISE and *Herschel* images due to a coarse beam size. To overcome this limitation, we analyzed the high-resolution JCMT ^{13}CO(3–2) and C^{18}O(3–2) line data (resolution ∼14″). However, it is important to mention that the JCMT line observations do not cover the entire area shown in Figure 3.1a but are limited to a specific region indicated by a solid box in Fig-

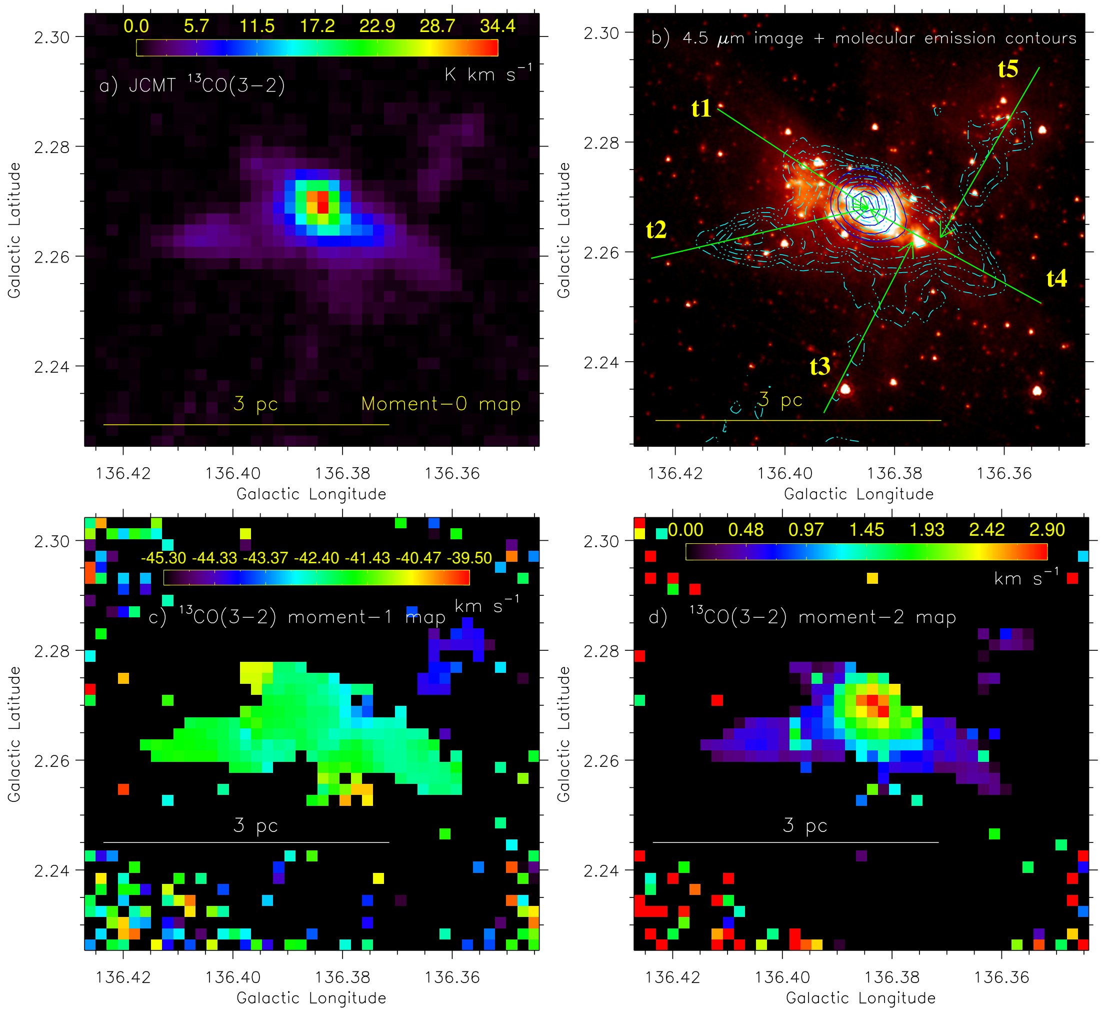

Figure 3.2: a) The panel shows the JCMT ^{13}CO(3–2) integrated intensity (moment-0) map (at [−45.35, −39.48] km s^{-1}) of an area hosting the target site (see a box in Figure 3.1f). b) Overlay of the ^{13}CO(3–2) emission contours on the *Spitzer* 4.5 μm image. The ^{13}CO(3–2) contours (in cyan) are 34.13 K km s^{-1} × (0.03, 0.05, 0.07, 0.09, 0.12, 0.2, 0.3, 0.4, 0.5, 0.6, 0.7, 0.8, 0.9, 0.98). Solid blue contours of the JCMT C^{18}O(3–2) integrated intensity map (at [−45.35, −39.48] km s^{-1}) are also presented with the levels of 1, 1.5, 2.1, 2.6, and 2.9 K km s^{-1}. Five arrows "t1–t5" are marked in the panel, where the PV diagrams are generated (see Figures 3.5a–3.5e). c) The panel shows the line-of-sight velocity map (moment-1 map) of the JCMT ^{13}CO(3–2) emission. d) JCMT ^{13}CO(3–2) intensity-weighted FWHM line width map (moment-2 map). A scale bar corresponding to 3 pc (at a distance of 3.3 kpc) is shown in each panel.

ure 3.1f. We have further studied the moment maps of JCMT ^{13}CO/C^{18}O(3–2) emission (see Section 2.3.1 for details on how the moment maps are estimated). In Figure 3.2a, we display the JCMT ^{13}CO(3–2) integrated intensity (moment-0) map (at $V_{\rm LSR}$ ∼[−45.35, −39.48] km s^{-1}), which reveals a central molecular condensation surrounded by parsec-scale molecular filaments. Figure 3.2b shows the *Spitzer* 4.5 μm image overlaid with the JCMT ^{13}CO emission contours. The central molecular condensation, surrounded by molecular filaments, is associated with a bright diffuse nebulosity observed in the *Spitzer* 4.5 μm image. The molecular filaments are highlighted by five arrows labeled as “t1–t5”. Additionally, the contours of JCMT $C^{18}O$(3–2) emission are overlaid on the *Spitzer* 4.5 μm image and are primarily distributed around the central hub of the HFS. No $C^{18}O$ emission is detected along the molecular filaments, which contrasts with the distribution observed in the ^{13}CO map. Collectively, the JCMT ^{13}CO(3–2) moment-0 map also supports the existence of the HFS.

In Figures 3.2c and 3.2d, the moment-1 and moment-2 (FWHM line width) maps are presented, respectively. Some velocity variations may be inferred toward the HFS. Higher line widths are evident toward the central hub compared to the filaments (see Section 3.3.4).

3.3.2 Identification of filament skeletons and their configuration

In order to reveal the structures of filaments or filamentary skeletons, we employed the *getsf* (Men’Shchikov, 2021, see Section 2.4 for an overview) algorithm on the *Herschel* 250 μm image. This particular image has better spatial resolution compared to other *Herschel* images at 350 and 500 μm. The filament skeletons, depicted in Figure 3.3a, represent structures identified on a scale of 51″. For the *getsf* analysis, we defined a maximum filament width size of 60″. Figure 3.3b displays the same filament skeletons as in Figure 3.3a, along with the contours of ^{13}CO(3–2) emission (see Figure 3.2b). These figures clearly demonstrate the presence of HFS and its association with the molecular gas.

3.3.3 *Herschel* column density and temperature maps

Figures 3.4a and 3.4b display the column density and temperature maps obtained from the *Herschel* observations, respectively. These maps were created using the Hi-GAL continuum images at 250, 350, and 500 μm, following the methods described in (e.g., Mallick et al., 2015, see also Section 2.3.3). It should be noted that the analysis does not include the *Herschel* 160 μm image due to its

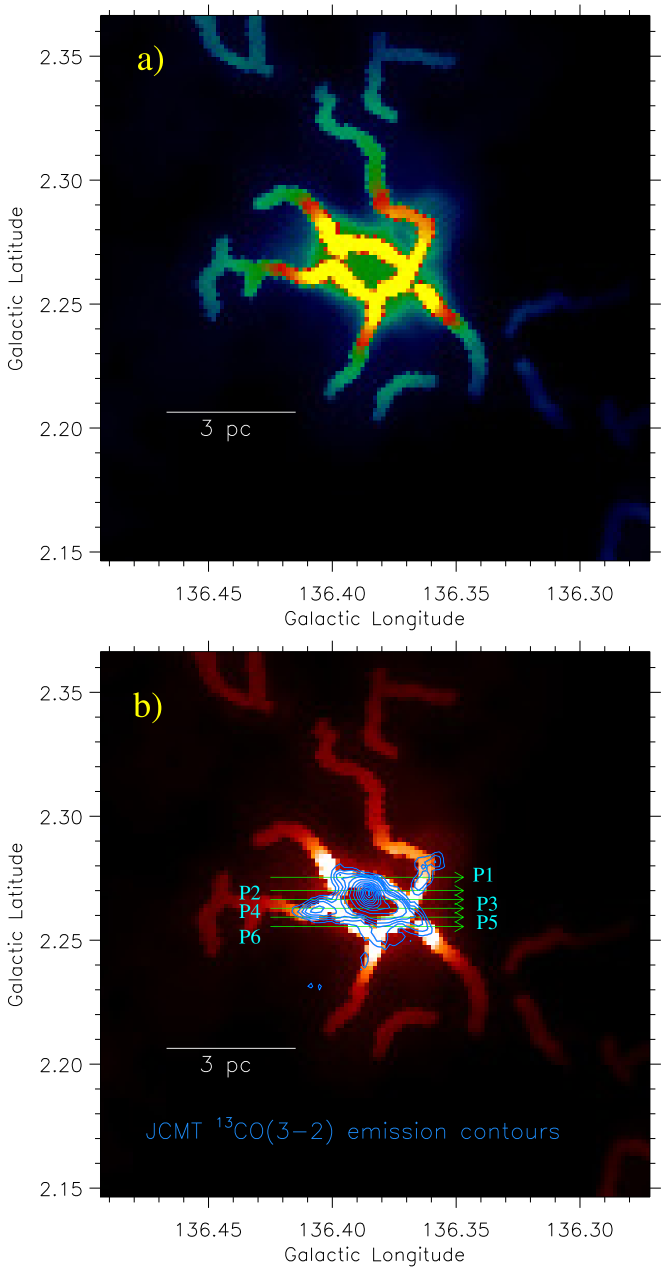

Figure 3.3: a) The panel shows the emission skeletons (on the scale of 51′′) identified from the *Herschel* 250μm image (resolution $\sim$18′′) using the algorithm *getsf*. b) Same as Figure 3.3a, but it is overlaid with the ^{13}CO(3–2) contours (see Figure 3.2b). Six arrows "p1–p6" are indicated in the panel, where the PV diagrams are generated (see Figures 3.6a–3.6f). A scale bar corresponding to 3 pc (at a distance of 3.3 kpc) is shown in each panel.

unavailability.

The column density and temperature maps were generated by fitting a modified blackbody model to the sub-mm emission at 250–500 μm for each pixel. The background flux level was estimated for each wavelength, resulting in values of 0.18, 0.13, and 0.06 Jy/pixel for the 250, 350, and 500 μm images, respectively.

These estimates were obtained from a selected featureless dark region with a size of approximately $9' \times 9'$ centered at coordinates ($l = 135^{\circ}.412$, $b = 2^{\circ}.092$). In the analysis, we considered a mean molecular weight per hydrogen molecule (μ_{H2}) of 2.8 (Kauffmann et al., 2008), an absorption coefficient (κ_ν) of 0.1 $(\nu/1000\mathrm{GHz})^\beta$ cm^2 g^{-1}, where the dust spectral index (β) was assumed to be 2 (see Hildebrand, 1983). Additionally, a gas-to-dust ratio of 100 was taken into account.

The *Herschel* column density map does not exhibit a prominent HFS, but the central hub is associated with warm dust emission, with temperatures ranging from approximately 19 to 22.5 K. It is worth mentioning that there may be uncertainties of around 10-20% in the estimation of column densities and dust temperatures (e.g., Launhardt et al., 2013).

Figure 3.4c presents filaments identified by *getsf* on the *Herschel* 250 μm image (see Figure 3.3a), which are utilized to mask the column density map as shown in Figure 3.4a. Figure 3.4c exhibits filaments with high aspect ratios and lower column densities ($\sim$0.1–2.4 $\times 10^{21}$ cm^{-2}), while the central hub is found with a low aspect ratio and high column density ($\sim$3.5–7.0 $\times 10^{21}$ cm^{-2}). Figure 3.4d is the same as Figure 3.4c, but it also displays the ^{13}CO(3–2) emission contours (see Figure 3.2b). We find the spatial connection of molecular gas with the structures seen in the column density map (see Figure 3.4d).

3.3.4 JCMT PV diagrams and σ_{NT} map

As previously mentioned, the JCMT molecular line data only cover the central area of the HFS as observed in the Herschel maps. To investigate the gas motion within the HFS, we generated PV diagrams along specific paths that traverse the molecular filaments and the central hub. These paths are indicated by arrows t1–t5 in Figure 3.2b, which correspond to the outermost edge of each filament towards the central hub. Additionally, horizontal arrows p1–p6 in Figure 3.3b represent paths passing through both the central hub and some molecular filaments. Therefore, the t1–t5 and p1–p6 paths may intersect common regions within the HFS.

The PV diagrams along arrows t1–t5 are presented in Figures 3.5a–3.5e. These

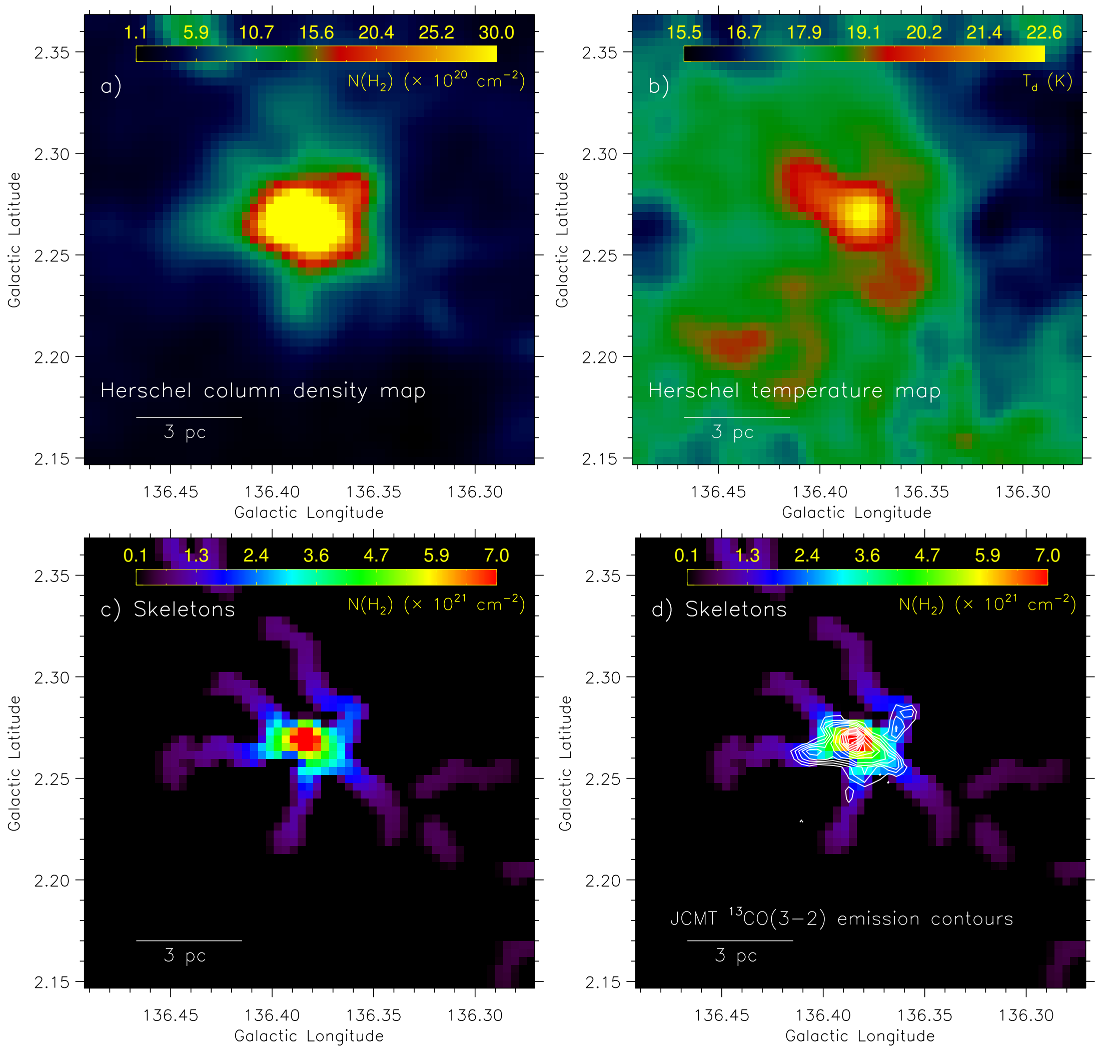

Figure 3.4: a) The panel displays the *Herschel* column density map (resolution ∼37″) of an area presented in Figure 3.1a. b) The panel shows the *Herschel* temperature map (resolution ∼37″). c) The panel displays filaments identified on the *Herschel* 250 μm by the algorithm *getsf*, which are utilized to mask the column density map as shown in Figure 3.4a. d) Same as Figure 3.4c, but it is overlaid with the ^{13}CO(3–2) contours (see Figure 3.2b). A scale bar corresponding to 3 pc (at a distance of 3.3 kpc) is shown in each panel.

diagrams hint at the presence of a noticeable velocity gradient along the molecular filaments (see Figures 3.5b, 3.5d, and 3.5e). In the direction of the filament "t2", a velocity gradient is determined to be about 1.6 km s^{-1} pc^{-1}. In Figures 3.6a–3.6f, we also display the PV diagrams along arrows p1–p6. Arrows p2–p4 intersect the central hub of the HFS, as indicated by the arrow "t2" in Figure 3.2b. The PV maps along these paths reveal the presence of outflow activity associated with the central hub, where IR-excess source candidates are also observed (Figures 3.6b–3.6d). Arrows p4 and p5 pass through the molecular filaments of the HFS, and noticeable velocity gradients along these filaments toward the HFS are evident in

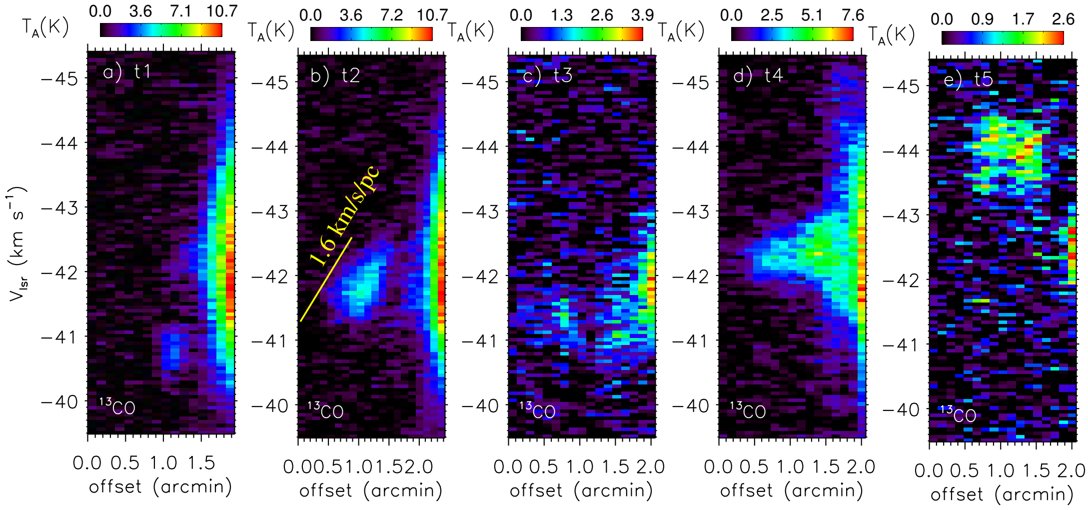

Figure 3.5: Position-velocity diagrams of the ^{13}CO(3–2) emission along arrows a) "t1"; b) "t2"; c) "t3"; d) "t4"; e) "t5" (see arrows in Figure 3.2b). In panel "b", a reference bar at 1.6 km s^{-1} pc^{-1} is marked to show a velocity gradient.

the PV maps (Figures 3.6d, 3.6e, and Figure 3.5b). These observations hint at the presence of a velocity gradient towards the HFS. To further investigate this aspect, high-resolution molecular line observations covering a wider area around RAFGL 5085 will be necessary. We have also utilized the JCMT ^{13}CO(3–2) line data to infer the non-thermal velocity dispersion ($\sigma_{\rm NT}$), sound speed, Mach number ($\mathcal{M}$), ratio of thermal to non-thermal pressure toward the molecular features traced in the JCMT moment-0 map. We followed the Equation 2.6 to derive the $\sigma_{\rm NT}$ map. For ^{13}CO, thermal velocity dispersion is expressed as $\sigma_{\rm T} = (kT_{kin}/29m_H)^{1/2}$ indicating thermal broadening for ^{13}CO at gas kinetic temperature ($T_{\rm kin}$).

The value of $\mathcal{M}$ can be determined by taking the ratio of $\sigma_{\rm NT}$ to sound speed (a_s). An expression of the sound speed is $a_s = (kT_{kin}/\mu m_H)^{1/2}$, where μ is the mean molecular weight (μ=2.37; approximately 70% H and 28% He by mass). Such estimates also allow us to compute the ratio of thermal to non-thermal (or turbulent) pressure (Lada et al., 2003), and its expression is $R_p = a_s^2/\sigma_{NT}^2$. Note that we do not have the knowledge of $T_{\rm kin}$. Hence, dust temperature is used in the calculation, and is taken from the *Herschel* temperature map (see Figure 3.4b).

Figure 3.7a presents the moment-2 map of ^{13}CO(3–2) emission overlaid with contours representing dust temperature ranging from 18.5 to 22.5 K. Fig-

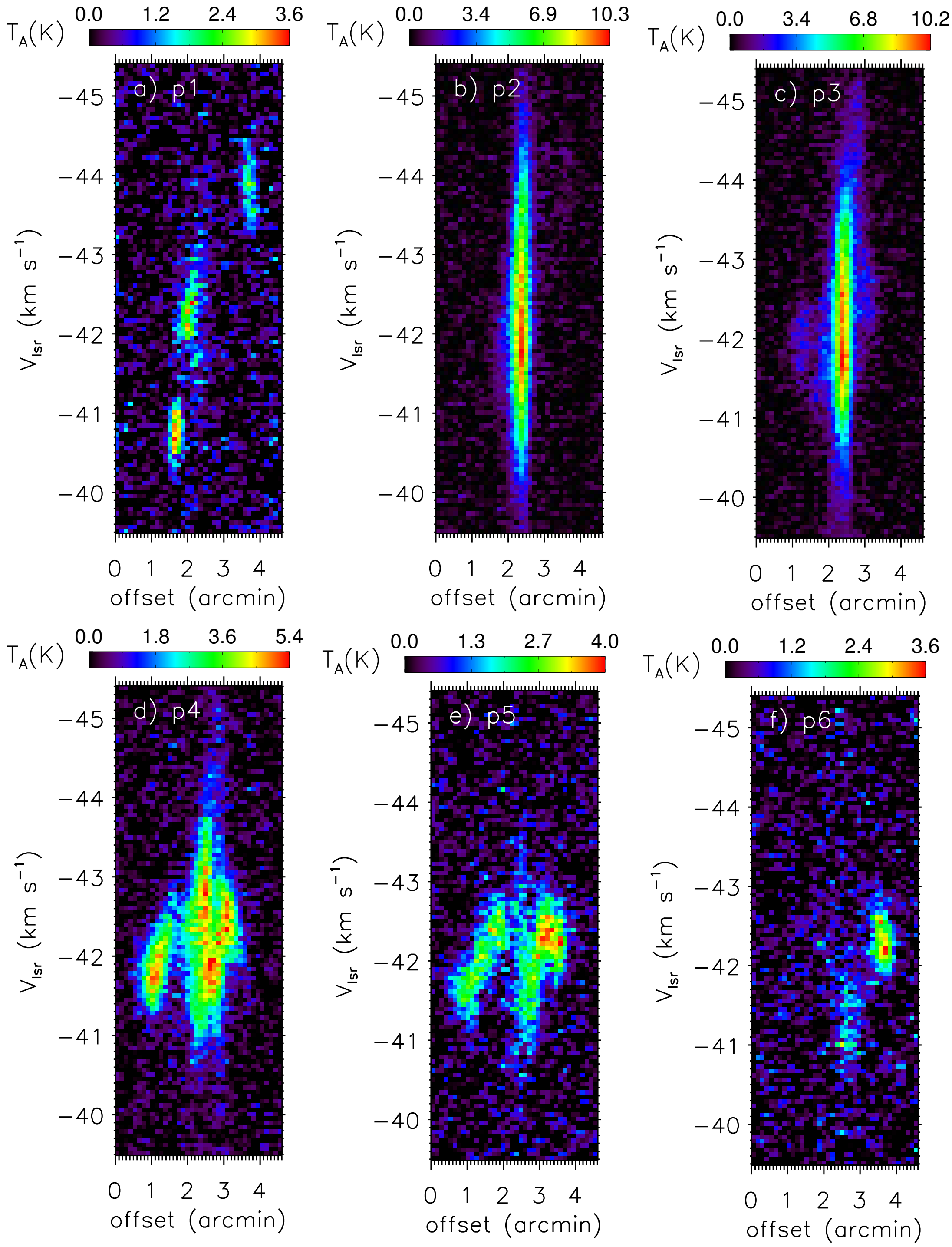

Figure 3.6: Position-velocity diagrams of the ^{13}CO(3–2) emission along arrows a) "p1"; b) "p2"; c) "p3"; d) "p4"; e) "p5"; f) "p6") (see arrows in Figure 3.3b).

ures 3.7b, 3.7c, and 3.7d show the $\sigma_{\rm NT}$ map, $\mathcal{M}$ map, and R$_p$ map of JCMT ^{13}CO(3–2) emission, respectively. The central hub exhibits larger values of ΔV, $\sigma_{\rm NT}$, and $\mathcal{M}$ compared to other molecular features. Additionally, the R$_p$ value is smaller than 1 towards the central hub, indicating a higher non-thermal pressure

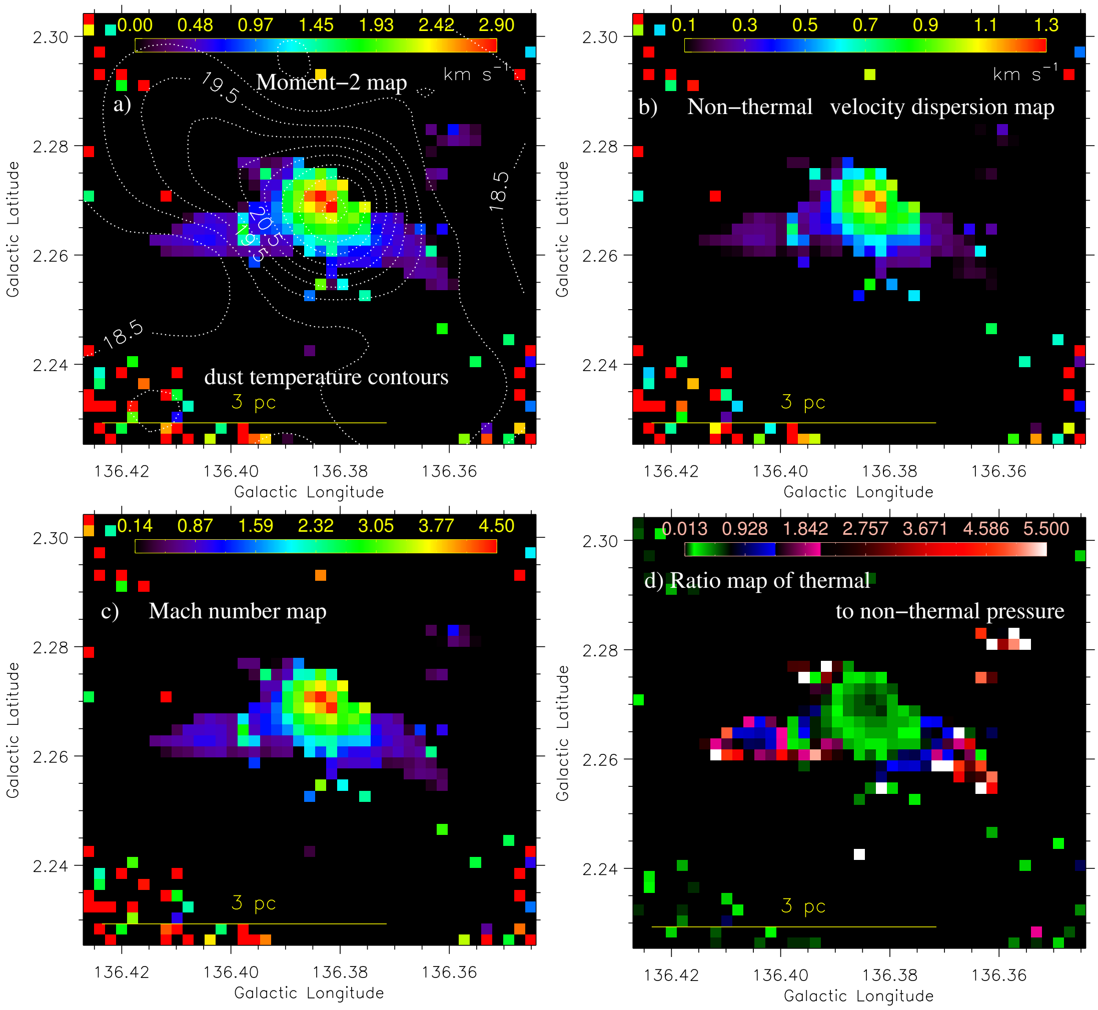

Figure 3.7: a) JCMT ^{13}CO(3–2) moment-2 map (see also Figure 3.2d). The contours of dust temperature at [18.5, 19.0, 19.5, 20.0, 20.5, 21.0, 21.5, 22.0, 22.5] K are also overlaid on the moment-2 map (see also Figure 3.4b). b) JCMT ^{13}CO(3–2) σ_{NT} map. c) JCMT ^{13}CO(3–2) $\mathcal{M}$ map. d) JCMT ^{13}CO(3–2) ratio map of thermal to non-thermal (or turbulent) pressure.

relative to the thermal pressure in the hub.

3.4 Discussion

To examine a wider scale environment of our selected target area containing the site RAFGL 5085, in Figure 3.8, we present a color-composite map created using the 250 μm (in red), 22 μm (in green), and 12 μm (in blue) images. The map is overlaid with the NVSS 1.4 radio continuum emission. Notably, the HII regions associated with the sites S192 and S196 are visible, and their sky-projected separations from our target site RAFGL 5085 are indicated. The extended MIR

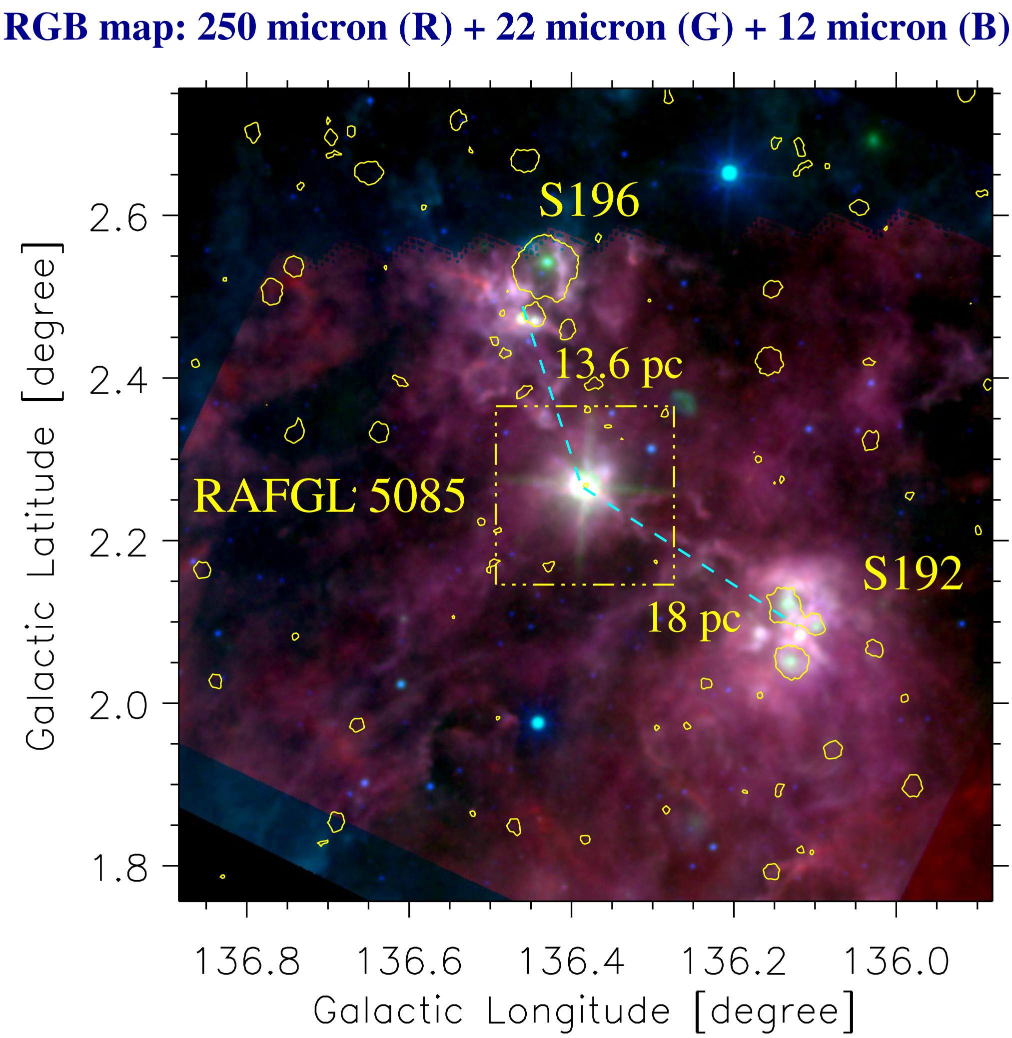

Figure 3.8: Large-scale view of an area containing the site RAFGL 5085. The panel displays a 3-color composite map made using the *Herschel* 250 μm (in red), WISE 22 μm (in green), and WISE 12 μm (in blue) images. The NVSS 1.4 GHz radio continuum emission contour at 1.35 mJy beam^{-1} is also overlaid on the color composite map. The target area of this work is indicated by a dotted-dashed box.

emission is observed towards the sites S192 and S196, while the compact MIR emission is detected towards RAFGL 5085. From Figure 3.8, we observe that RAFGL 5085 is positioned between the two evolved HII regions, S192 and S196.

Previously, the NIR cluster – associated with the outflow signature, MSF and water maser – has been reported toward the molecular and dust clump hosting the location of RAFGL 5085 (Carpenter et al., 2000; Wu et al., 2004; Saito et al., 2006, 2007; Lumsden et al., 2013; Li et al., 2019; Ouyang et al., 2019), where dense molecular cores have been identified (e.g., Saito et al., 2006). Due to the detection of weak radio continuum emission (i.e., total flux = 1.7 mJy; Condon et al., 1998), we do not favour the presence of any evolved HII region in RAFGL 5085. Hence, the site RAFGL 5085 seems to be associated with an early stage of MSF (see also Lumsden et al., 2013). In this work, using the *Herschel* sub-mm images and the WISE image at 12 μm, our findings reveal a new picture in RAFGL 5085, which is the existence of a HFS. In this connection, the algorithm *getsf* identified at least five filaments (having $N(H_2)$ ~0.1–2.4 $\times 10^{21}$ cm^{-2}), which appear to direct to the central hub (having $N(H_2)$ ~3.5–7.0 $\times 10^{21}$ cm^{-2}). This finding is also supported by the JCMT ^{13}CO(3–2) line data. All the signatures of star formation (including radio continuum emission) are found toward the central hub of the HFS (see Section 3.3.1), where higher values of $\mathcal{M}$ and non-thermal pressure are depicted (see Section 3.3.4).

In hub-filament configurations, it is thought that filaments are instrumental in channelling interstellar gas and dust to the central hub, where massive stars are assembled by the inflow material (André et al., 2010; Schneider et al., 2012; Motte et al., 2018; Treviño-Morales et al., 2019a; Rosen et al., 2020). In this context, velocity gradients (e.g., 0.5–2.5 km s^{-1} pc^{-1}) along molecular filaments have been observed in HFSs, and are suggested as a signature of gas accretion along the filaments (Kirk et al., 2013; Nakamura et al., 2014; Olmi et al., 2016; Hacar et al., 2017; Baug et al., 2018; Treviño-Morales et al., 2019a; Chen et al., 2020b; Dewangan et al., 2020a). Such material/gas flow is thought to feed star-forming cores and proto-clusters in the hub (e.g., Treviño-Morales et al., 2019a).

The previously observed velocity gradients in the filaments were found to exceed the sound speed of ~0.2 km s^{-1} at T = 10 K, indicating the presence of turbulent gas flow (e.g., Baug et al., 2018). Our findings also suggest the existence of a velocity gradient towards the HFS, as depicted in Figures 3.5 and 3.6, indicating a potential gas flow along the filaments towards the central hub. However, due to limited molecular line data coverage of the entire HFS, further investigation of the velocity gradients is warranted (e.g., Hacar & Tafalla, 2011; Hacar et al., 2013). Therefore, it is necessary to acquire new high-resolution and high-sensitivity molecular line data for a broader region surrounding the RAFGL 5085 HFS to validate our proposed hypothesis.

The presence of a hub-filament configuration aligns with the clump-fed scenario discussed in Section 1.1.3. According to this scenario, the birth of massive stars is attributed to inflow material originating from large scales of 1–10 pc. These inflow materials can be driven by gravity or generated by supersonic turbulence (e.g., Motte et al., 2018; Padoan et al., 2020; Liu et al., 2022a). However, conducting a detailed study on this aspect extends beyond the scope of the current work, considering the available data sets mentioned in Table 5.1.

The HFSs are very common structures in the massive star-forming sites, but a perfect hub-filament configuration is not often seen in most cases. This is because of the stellar feedback from HII regions (or proto clusters) which gradually destroys the HFS as the proto cluster evolves (see Baug et al., 2015, 2018; Dewangan et al., 2017b, 2020a; Dewangan, 2022; Treviño-Morales et al., 2019a; Dewangan, 2021, 2022). The evolutionary scheme of MSF in HFS suggests this as a last stage (e.g., Tigé et al., 2017; Motte et al., 2018, See Section 1.3.3 for more details). It seems that the observed RAFGL 5085 HFS is not yet influenced by UV radiation from the HII region. Hence, our target source RAFGL 5085 appears to be one of the perfect HFS candidates where the young sources (including massive protostar) are found to be formed in the hub region.

3.5 Conclusion and Summary

In this study, we have investigated the physical environment of RAFGL 5085, a massive star-forming site, using a multi-wavelength approach. Our visual inspection of the continuum images at different wavelengths, including 12, 250, 350, and 500 μm, has revealed a hub-filament configuration of RAFGL 5085. This configuration consists of a central region with a clump mass of $\sim$225 $M_\odot$, surrounded by five parsec-scale filaments. We have also utilized the *getsf* tool in the *Herschel* sub-mm images, and the extracted filament skeletons support the presence of the HFS in RAFGL 5085.

In the *Herschel* column density map, filaments are identified with higher aspect ratios (length/width) and lower $N(H_2)$ values ($\sim$0.1–2.4 $\times 10^{21}$ cm^{-2}), while the central hub is found with a lower aspect ratio and higher $N(\mathrm{H_2})$ values ($\sim$3.5–7.0 $\times 10^{21}$ cm^{-2}). The central hub of the RAFGL 5085 HFS is associated with warmer dust emission, with temperatures ranging from $\sim$19 to 22.5 K. The signs of ongoing star formation, including radio continuum emission, are concentrated towards the central hub. Our analysis of the JCMT ^{13}CO(3–2) line data further confirms the presence of the RAFGL 5085 HFS. It should be noted that the JCMT molecular line data cover mainly the central area of the HFS and do not extend to the entire region as observed in the *Herschel* maps. The central hub exhibits supersonic and non-thermal motions, characterized by higher Mach numbers and a lower thermal to non-thermal pressure ratio. The ^{13}CO(3–2) PV diagrams show velocity gradients along the filaments towards the HFS, indicating gas flow within the RAFGL 5085 HFS and supporting the applicability of the clump-fed scenario. Our findings suggest that RAFGL 5085 is in the early phase of MSF and is unlikely to be affected by an evolved HII region. Therefore, our selected target site appears to be a perfect HFS candidate, which is not yet affected by UV photons from the HII region.

Chapter 4

Star-forming sites IC 446 and IC 447: an outcome of end-dominated collapse of Monoceros R1 filament†

4.1 Introduction

In previous Chapter (Chapter 3), we discussed the role of multiple filamentary structures forming HFSs in MSF processes. However, as discussed in Section 1.3.2, the isolated and single filamentary cloud may support the mass accumulation in MSF. In this regard, analytical investigations and numerical simulations have demonstrated that infinitely long cylindrical clouds exhibit gravitational instability, leading to fragmentation at equal spacing (e.g., Inutsuka & Miyama, 1992, 1997; Nakamura et al., 1995). For finite-sized filaments, collapse occurs faster at the ends than in the central region (i.e., end-dominated collapse or EDC scenario; Bastien, 1983; Burkert & Hartmann, 2004; Pon et al., 2011, 2012; Clarke & Whitworth, 2015; Hoemann et al., 2022). Despite some

†**Bhadari, N. K.**, Dewangan, L. K., Pirogov, L. E., Ojha, D. K., 2020, ApJ, 899, 167, "Star-forming sites IC 446 and IC 447: an outcome of end-dominated collapse of Monoceros R1 filament"

observational and numerical evidence, research focusing specifically on EDC scenario remains limited (e.g., Zernickel et al., 2013; Beuther et al., 2015; Hacar et al., 2016; Kainulainen et al., 2016; Dewangan et al., 2017b, 2019a; Yu et al., 2019). In order to evaluate the validity of numerical simulations related to star-forming filaments, we have chosen a star-forming region within the Monoceros R1 (hereafter Mon R1) complex. Our approach involves the use of multi-scale and multi-wavelength observations to examine this nearby site.

Mon R1 is a grouping of reflection nebulae (i.e., R-association), situated near the Galactic plane and associated with the well-studied OB association Mon OB1 (van den Bergh, 1966). It is located approximately 2° away from the center of Mon OB1 (i.e., Cone Nebula NGC 2264; see an inverted C-like structure of Mon R1 association at coordinates ~RA: $6^{\rm h}\ 31^{\rm m}\ 0^{\rm s}$, Dec: $+10^\circ\ 00'\ 00''$ in Figure 1 of Montillaud et al., 2019). The distance to Mon R1 has been reported with varying values in the literature, such as 715 pc (van den Bergh, 1966), 800 pc (Stahler & Palla, 2005), 900 pc (Oliver et al., 1996), and 1000 pc (Kutner et al., 1979). In this study, we adopt a heliocentric distance of ~760 pc for Mon R1 (e.g., Montillaud et al., 2019).

The Mon R1 association includes reflection nebulae NGC 2245, NGC 2247, IC 446, IC 447, as well as several early-type (B3-B7) stars, including VdB 76, VdB 77, VdB 78 (Kutner et al., 1979). Figure 4.1a shows a *Planck* sub-millimeter image at 550 μm of the R-association, indicating the positions of NGC 2245, NGC 2247, IC 446, and IC 447. The image is presented in Galactic coordinates. Figure 4.1b displays a false-color optical image from the Digitized Sky Survey II (DSS2) at 0.47 μm, covering a size of approximately $1^\circ.04 \times 0^\circ.89$ (equivalent to a physical extent of ~13.8 pc × 11.8 pc at a distance of ~760 pc). The optical image highlights the locations of the reflection nebulae and previously known bright OB-type stars, as listed in Table 4.1. Notably, two sites, IC 446 and IC 447, are connected by a curved section of dark nebulosity, indicated by arrows in Figure 4.1b. This dark nebulosity appears bright in the *Planck* image at 550 μm, forming an elongated filamentary structure. In other words, IC 446 (or IC 2167) and IC 447 (or IC 2169) are located at opposite ends of this filamentary structure. Additionally, a MYSO named VY Mon is reported to be present near IC 446 (e.g., Casey & Harper, 1990).

Table 4.1: List of bright stars known toward Mon R1 complex (see Figure 4.1b). The positions and spectral type of stars are given in the table.

ID	Name	l (degree)	b (degree)	Spectral-type	Association	References
1	TYC 737-255-1	201.32	+00.30	B2.5V D	IC 446	–
2	VY Mon	201.34	+00.29	A5 Vep	IC 446	Mora et al. (2001)
3	V727 Mon	201.79	+00.07	B8V D	IC 447	–
4	VdB 76	201.63	+00.05	B7IIIp	IC 447	Racine (1968)
5	VdB 77	201.88	−00.03	B5III D	IC 447	Racine (1968)
6	VdB 78	201.93	+00.02	B3 E	IC 447	Cannon & Pickering (1993)
7	BD+09 1264	201.82	−00.09	OB E	IC 447	Nassau et al. (1965)
8	V699 Mon	201.77	+00.51	B7IIne C	NGC 2245	Herbst et al. (1982)
9	VdB 82	201.67	+00.67	B6ep D	NGC 2247	Herbst et al. (1982)

Using the molecular CO line observations (resolution $\sim1'.1$–$2'.6$), Kutner et al. (1979) studied the molecular gas toward R-association and Mon OB1. The Mon R1 molecular cloud, traced in a radial velocity ($V_{\rm LSR}$) range of [−1, 5] km s^{-1}, was found to be kinematically distinct from the Mon OB1 molecular complex at [5, 10] km s^{-1}. A partial ring structure of the Mon R1 molecular cloud was observed in the molecular map at [−1, 5] km s^{-1}, which hosts the above mentioned reflection nebulae in its periphery. The *Planck* continuum image at 550 μm also shows a semi-ring structure in Figure 4.1a. However, Kutner et al. (1979) found at least two velocity components toward Mon R1 at [−1, 1] and [3, 5] km s^{-1} (see Figure 2 in Kutner et al., 1979). The cloud at [3, 5] km s^{-1} was associated with NGC 2245 and NGC 2247, while a semi-circular arc of cloud hosting the sites IC 446 and IC 447 was reported in a velocity range of [−1, 1] km s^{-1} (see Figure 2 in Kutner et al., 1979). The elongated morphology of the cloud component at [−1, 1] km s^{-1} is also observed in other wavelengths; thus we prefer to categorize it as a filament and named it Mon R1 filament. Kutner et al. (1979) proposed that a previous energetic event, such as expanding H II regions, stellar winds, or supernova (SN) blast waves, was responsible for the existence of the partial ring structure in the Mon R1 molecular cloud at [−1, 5] km s^{-1}.

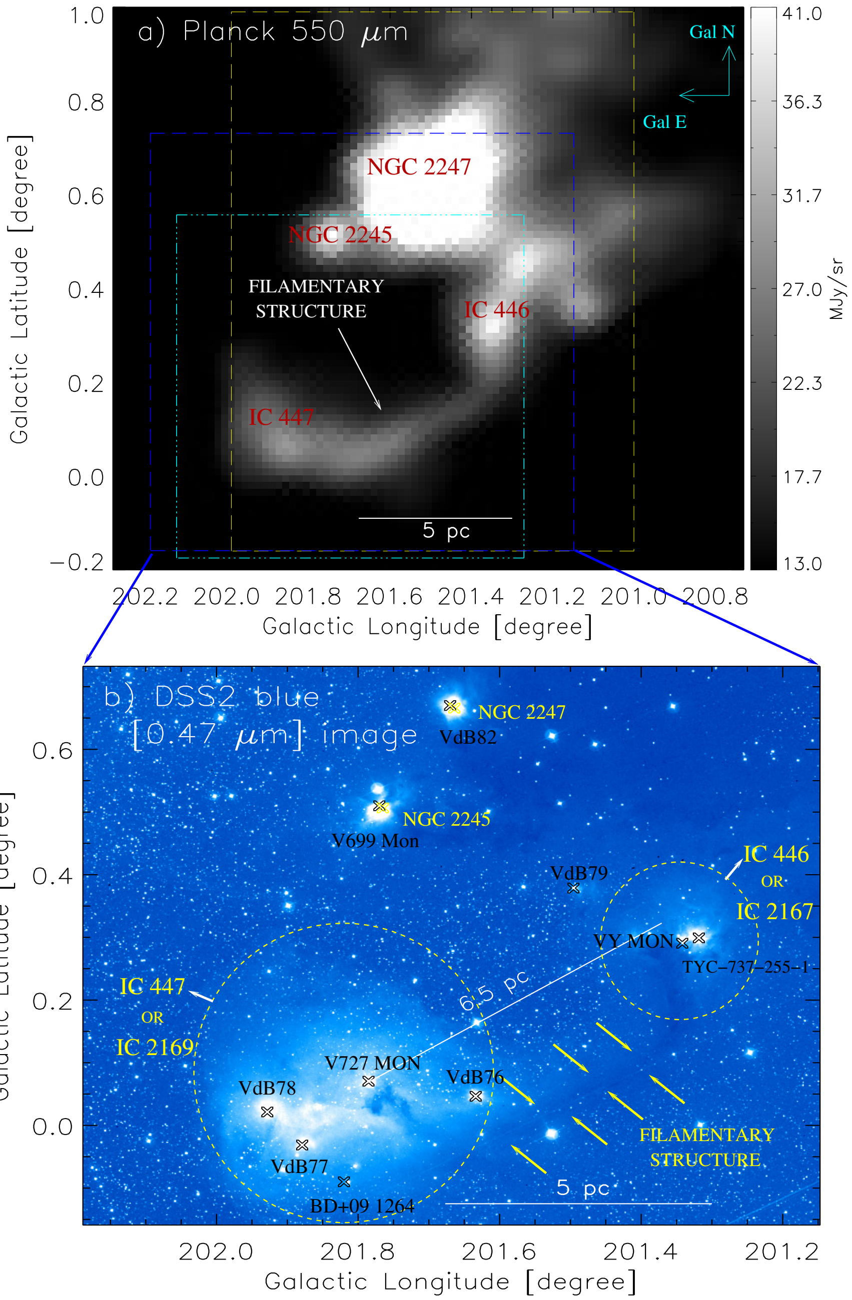

Figure 4.1: The R-association in Mon R1 complex. a) *Planck* dust continuum image at 550 μm. A filamentary structure seen in the image is marked by an arrow. A dashed box (in blue) shows the area presented in Figure 4.1b. A dotted-dashed box (in cyan) and a rectangular box (in yellow) represent the areas shown in Figures 4.2 and 4.5, respectively. b) A zoomed-in optical image at DSS2 0.47 μm of Mon R1 (see a dashed blue box in Figure 4.1a). The extent of known reflection nebulae IC 446 and IC 447 are shown by dashed circles. A dark-filament connecting these nebulae is highlighted by yellow arrows. The positions of previously known B-type stars and reflection nebulae (i.e., NGC 2245 and NGC 2247) are indicated and labeled by black and yellow color cross symbols, respectively (see Table 4.1). A scale bar representing 5 pc (at d $\sim$760 pc) is shown in each panel.

They also pointed out that the physical process, which governs the formation of observed OB-stars toward the region, might be different. In this connection, we observationally try to resolve the ambiguity of physical process governing the star formation activity toward the filamentary cloud at [−1, 1] km s^{-1}. To understand the physical mechanism(s) of star formation in Mon R1 cloud, we have examined the distribution of molecular gas, ionized emission, dust (i.e., warm and cold) emission, and YSOs.

Based on the previous studies, we find that Mon R1 is a relatively nearby star-forming complex hosting the elongated filamentary structure as well as massive B-type stars, making Mon R1 as an important target site for probing star formation processes. The *Herschel* temperature and column density maps (resolution $\sim$12″) are utilized to study the distribution of dust temperature and column density, while high resolution FOREST Unbiased Galactic plane Imaging survey with the Nobeyama 45-m telescope (FUGIN; Umemoto et al., 2017) molecular line data (resolution $\sim$20″) are employed to examine the gas flow toward the Mon R1 molecular cloud. Furthermore, the observational findings derived in this work have been used to assess the existing theoretical models related to star-forming filaments.

Following the introduction in this section, we present the adopted data sets in §4.2. The observational outcomes are presented in §4.3. In §4.4, we discuss our observational results against the existing theoretical models. Finally, §4.5 gives the main conclusions of this work.

4.2 Data and analysis

Figure 4.1a depicts the target area of the study, with central coordinates at l = 201°.5 and b = 0°.5. The selected target area covers an angular extent of $\sim$1°.5 × 1°.4, corresponding to a physical scale of about 20.3 pc × 18.1 pc (at a distance of $\sim$760 pc).

To conduct the analysis, we utilized various publicly available multi-wavelength and multi-scale datasets, as listed in Table 4.2. In the direction of our target area, we retrieved ^{12}CO(J = 1–0) and ^{13}CO(J = 1–0) line data from the FUGIN survey, calibrated in main beam temperature ($T_{\rm mb}$) (see Umemoto et al., 2017). The typical root mean square (RMS) noise levels for ^{12}CO and ^{13}CO lines are ∼1.5 K and 0.7 K, respectively (Umemoto et al., 2017). The FUGIN survey provides data with a velocity resolution of 1.3 km s^{-1}. To enhance sensitivities, we applied a smoothing process to each FUGIN molecular line data cube using a Gaussian function with a half-power beamwidth of 3 pixels. The temperature and column density ($N(\mathrm{H_2})$) maps from the *Herschel* telescope were obtained from the publicly accessed website of the *EU-funded ViaLactea project* (Molinari et al., 2010b). These maps, with a resolution of ∼12″, were generated using the Bayesian algorithm `PPMAP` method (e.g., Marsh et al., 2015, 2017, see Section 2.3.3.2 also). The *Herschel* images at 70, 160, 250, 350, and 500 μm were used as input for the `PPMAP` algorithm to derive the temperature and column density maps.

Table 4.2: List of multi-wavelength surveys used in this work.

Survey	band(s)	Resolution	Reference
NRAO VLA Sky Survey (NVSS)	21 cm	∼45″	Condon et al. (1998)
FUGIN survey	^{12}CO(J = 1–0),^{13}CO(J = 1–0)	∼20″, ∼21″	Umemoto et al. (2017)
Planck Survey	550 μm	4′.8	Ade et al. (2014)
Herschel Infrared Galactic Plane Survey (Hi-GAL)	70, 160, 250, 350, 500 μm	5″.8, 12″, 18″, 25″, 37″	Molinari et al. (2010a)
Wide Field Infrared Survey Explorer (WISE)	22 μm	∼12″	Wright et al. (2010)
Warm-*Spitzer* GLIMPSE360 Survey	3.6, 4.5 μm	∼2″	Benjamin et al. (2003)
UKIRT near-infrared Galactic Plane Survey (GPS)	1.25–2.2 μm	∼0″.8	Lawrence et al. (2007)
Two Micron All Sky Survey (2MASS)	1.25–2.2 μm	∼2″.5	Skrutskie et al. (2006)
Digitized Sky Survey II (DSS2)	0.47 μm	∼2″	McLean et al. (2000)

4.3 Results

4.3.1 *Herschel* column density and temperature maps

Figures 4.1a and 4.1b provide evidence for the presence of an elongated filamentary structure. To further investigate this filament, we present the *Herschel* temperature and column density ($N(\mathrm{H_2})$) maps of the target region in Figures 4.2a and 4.2b, respectively. These maps correspond to the area outlined by a dashed cyan box in Figure 4.1a. The *Herschel* temperature map reveals the extended emission of warm dust, with temperatures ranging from ∼15 to 21 K, towards the sites IC 446, IC 447, and NGC 2245. This suggests the presence of heated material or warm dust emission in these regions.

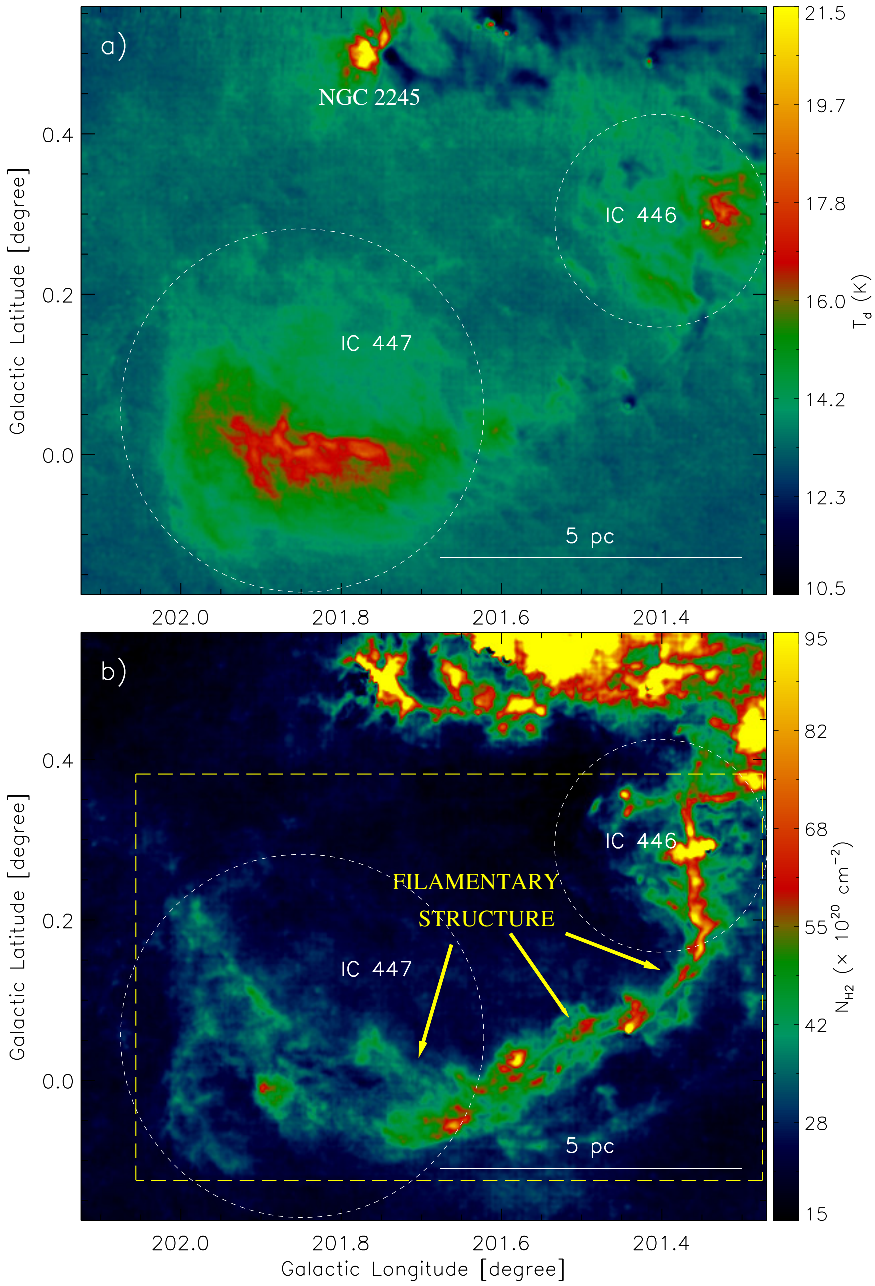

Figure 4.2: a) *Herschel* temperature map of the region containing the filament (see a dotted-dashed cyan box in Figure 4.1a). b) *Herschel* column density map. The identification of *Herschel* dust clumps is carried out in the area shown by a dashed yellow box (see Figure 4.3). In each panel, broken circles indicate the extent of IC 446 and IC 447. A scale bar corresponding to 5 pc is shown in both panels.

The *Herschel* column density map clearly reveals the presence of the elongated filament as the most prominent feature. This filament, with a curved geometry, is traced using a contour level of $N(\mathrm{H_2}) = 3.2 \times 10^{21}$ cm^{-2}. The map also shows the existence of several regions with high column densities (i.e., 6–9 $\times$ 10^{21} cm^{-2})

toward the filament. To identify the boundary of the elongated filament, we employed the IDL *clumpfind* algorithm (Williams et al., 1994). This algorithm decomposes the 2D or 3D data into separate clumps of emission by finding positions of peak intensity that correspond to the clumps. It requires contouring of the data using a multiple of the RMS noise level, and the input parameters include the lowest contour level that defines the rejection criteria for data, as well as the interval between contours (Williams et al., 1994). Figure 4.3a shows the *clumpfind* decomposition of column density map tracing the filamentary cloud (in blue).

Based on the morphology of the elongated filament, it can be divided into three distinct parts: eastern, central, and western. The eastern part, located towards the site IC 447, appears more diffuse and exhibits a single peak in column density. In contrast, the central part (with a length of ∼5 pc) and the western part (with a length of ∼2-4 pc) of the filament are denser and contain multiple peaks in column density. Figure 4.3b displays the boundaries of sub-filaments, which were identified using a contour level of $N(\mathrm{H_2}) = 4.1 \times 10^{21}$ cm^{-2} as input for the *clumpfind* algorithm. These sub-filaments are primarily observed in the central and western parts of the elongated filament, as indicated in Figure 4.3a. Although these sub-filaments appear linear, they are not aligned with each other.

To calculate the total mass of the elongated filament (length ∼14 pc) and sub-filaments, we have used the Equation 2.14 and computed the total mass of the elongated filament (M_{filament}) to be ∼1465 $M_\odot$. The total mass of the central and western parts of the filament is determined to be ∼319 and ∼365 $M_\odot$, respectively. The importance of these results is discussed in Section 4.4.2.

The observed line mass $M_{\mathrm{line,obs}}$ of a filament is calculated as the ratio of the filament mass (M_{filament}) to its length. In this study, with M_{filament} estimated to be ∼1465 $M_\odot$ and a filament length of ∼14 pc, $M_{\mathrm{line,obs}}$ is determined to be around 105 $M_\odot$ pc^{-1}. The length of the filament is measured along its major axis using the DS9 software[‡]. The line mass of a filament is influenced by the inclination angle (denoted as *"i"*) and depends on the "cos *i*" factor (e.g., Kainulainen et al.,

[‡]http://hea-www.harvard.edu/RD/ds9/

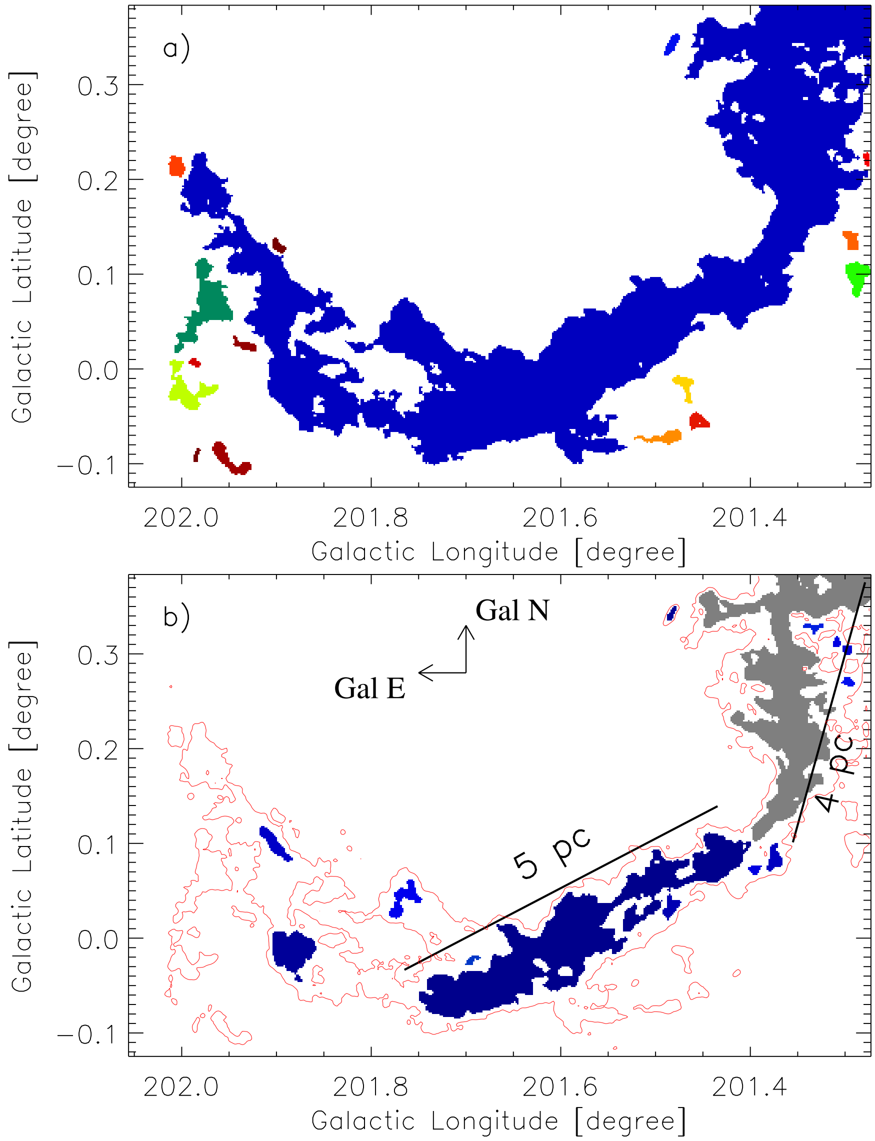

Figure 4.3: a) An elongated filament is depicted in the column density map with the $N(\mathrm{H_2})$ contour level of 3.2 $\times$ 10^{21} cm^{-2}. b) Two sub-filaments (central in blue, and western in gray) are identified in the direction of the elongated filament using the $N(\mathrm{H_2})$ contour level of 4.1 $\times$ 10^{21} cm^{-2}. The projected length of each sub-filament is indicated by a scale bar. The $N(\mathrm{H_2})$ contour (in red) is also overplotted to show the elongated filament as shown in Figure 4.3a.

2016). The angle *"i"* is the angle between the filament's major axis and the sky plane. In this work, since the inclination angle is unknown, we assume that the filament lies in the same plane as the sky plane, i.e., $i = 0$. Consequently, the value of cos i becomes 1, and the observed line mass per unit length can be considered as an upper limit. It is important to note that the total mass of the filament ($\sim$1465 $M_\odot$) may be underestimated due to the unavailability of a small portion of the filament (Field of View (FoV) approximately $8'$–$14'$) in the *Herschel* column density map at higher latitudes. A comparison between Figures 4.3a and 4.5c highlights this missing portion. It is clear from Eq. 2.14, the uncertainty in the mass of filament varies linearly with the $N(\mathrm{H_2})$ uncertainties.

4.3.2 Infrared and Radio view of R-association

Figure 4.4a displays the WISE 22 μm MIR image of the R-association, which captures the emission from warm dust in our selected target area. The WISE image is overlaid with contours of NVSS 1.4 GHz continuum emission (with a beam size of $\sim$45$''$ and a 1σ sensitivity of $\sim$0.45 mJy beam^{-1}; Condon et al., 1998). Within our selected target area, no extended HII region is detected. However, it is worth noting that several massive stars have been reported in the vicinity of the IC 447 and IC 446 sites (refer to Figure 4.1b and Table 4.1), where extended warm dust emission is observed.

Figure 4.4b showcases the *Spitzer* ratio map of 4.5 μm/3.6 μm continuum emission, derived from the *Spitzer* 3.6 and 4.5 μm continuum images. The ratio map reveals regions of both bright and dark features, representing areas where the flux at 4.5 μm dominates over the flux at 3.6 μm and vice versa. Notably, the 3.6 μm band includes emission from PAHs at 3.3 μm, while the 4.5 μm band encompasses the molecular hydrogen line (ν = 0–0 S(9); 4.693 μm) and the Br-α emission (at 4.05 μm). The bright emission in the ratio map corresponds to the IC 446 region, where no NVSS continuum emission (or ionized emission) is detected. This suggests that the area with bright emission near IC 446 may be associated with outflow activity (see also Section 4.3.4). Conversely, the dark or grey regions observed towards IC 447 indicate the dominance of the 3.3 μm PAH feature, indicating the presence of PDRs (see Tielens, 2008). This supports the idea of the influence of massive stars in the vicinity of IC 447.

4.3.3 Gas kinematics from spectral line data

In this section, we present the results derived using the analysis of the FUGIN ^{12}CO(J =1$-$0) and ^{13}CO(J =1$-$0) line data.

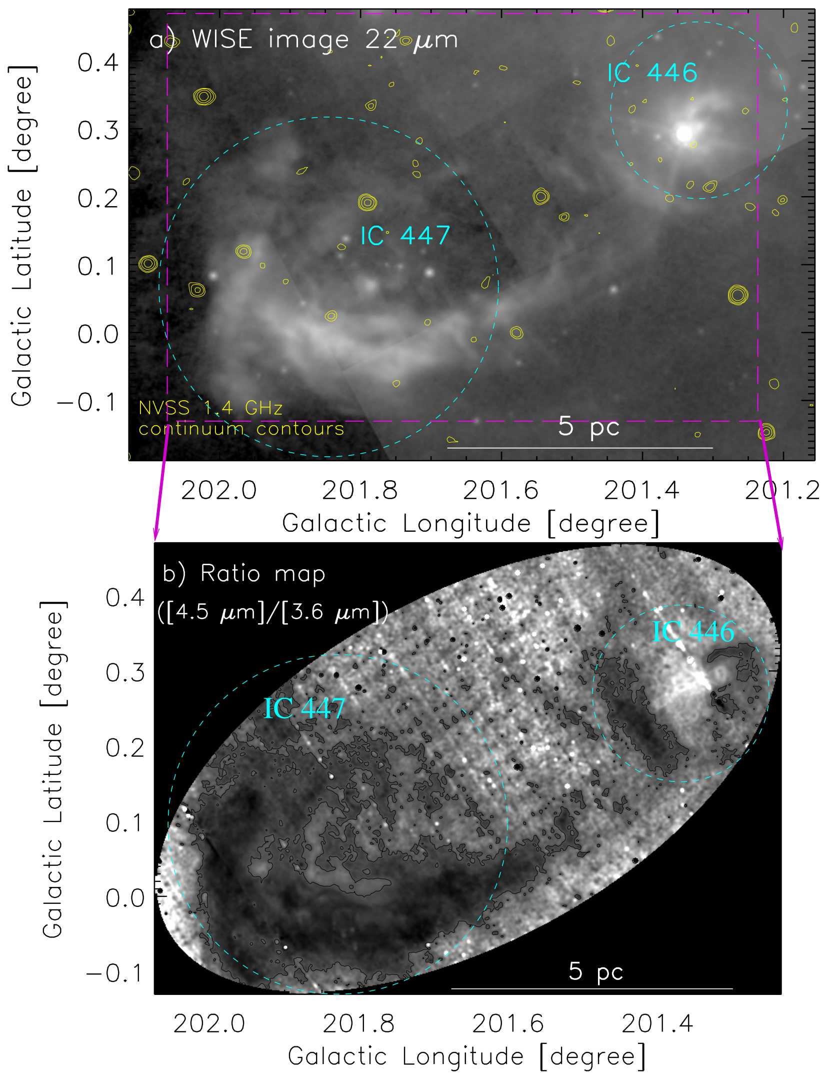

Figure 4.4: a) Overlay of the NVSS radio 1.4 GHz continuum emission contours on the MIR image at *WISE* 22 μm toward the filament. The NVSS contours are shown with the levels (3, 5, 10, 20) $\times$ 1σ, where 1σ = 0.45 mJy beam^{-1}. A dashed box (in magenta) encompasses the area shown in Figure 4.4b. b) *Spitzer* ratio map of 4.5 μm/3.6 μm emission. Broken circles show the extent of IC 446 and IC 447 in each panel. The ratio map is smoothened using a Gaussian function with radius of three pixels. A scale bar corresponding to 5 pc is displayed in both panels.

4.3.3.1 Integrated molecular maps

In this section, using the FUGIN ^{12}CO(J = 1–0) and ^{13}CO(J= 1–0) line data, we present kinematic properties of the molecular cloud(s) associated with our selected target area (see a broken yellow box in Figure 4.1a). Figures 4.5a–4.5f display the CO maps of intensity (moment-0) in the direction of Mon R1. In Figures 4.5a and 4.5b, the ^{12}CO and ^{13}CO emissions are integrated over a velocity range of [−7.8, 10.4] km s^{-1}, respectively.

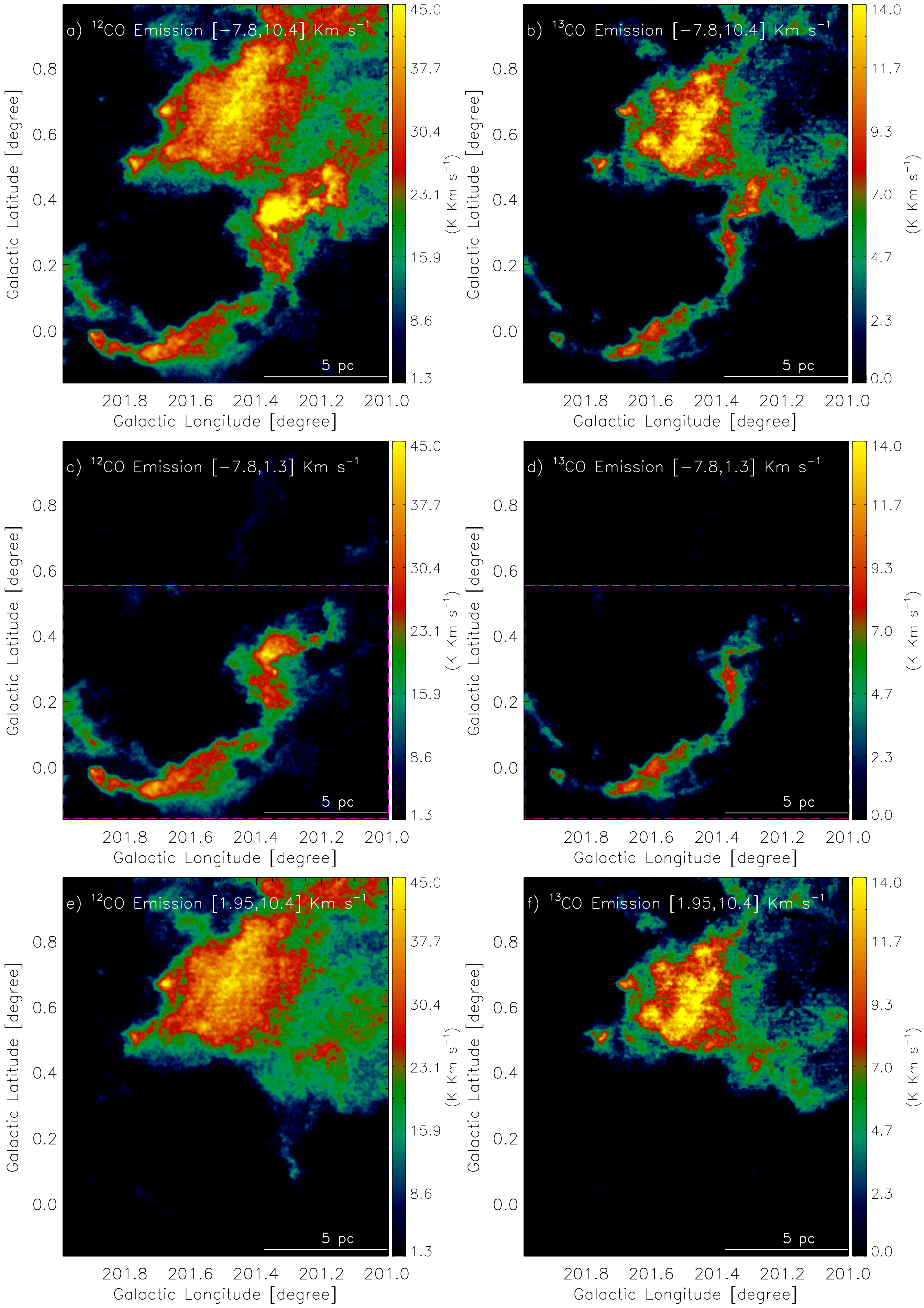

Figure 4.5: Left column: "a)", "c)", "e)" FUGIN ^{12}CO(1–0) map of intensity (moment-0) in the direction of Mon R1. Right column: "b)", "d)", "f)" FUGIN ^{13}CO(1–0) map of intensity (moment-0) in the direction of Mon R1. In panels "a" and "b", the molecular emission is integrated over a velocity range of [−7.8, 10.4] km s^{-1}. In panels "c" and "d", the molecular emission is integrated over a velocity range of [−7.8, 1.3] km s^{-1}. In panels "e" and "f", the molecular emission is integrated over a velocity range of [1.95, 10.4] km s^{-1}. A scale bar corresponding to 5 pc is shown in each panel. In panels "c" and "d", the molecular emission is observed mainly toward the filament, which is highlighted by a broken box (in magenta).

The molecular maps at velocities ranging from [−7.8, 10.4] km s^{-1} provide insights into the gas distribution towards NGC 2245, NGC 2247, and the filament containing IC 446 and IC 447. Figures 4.5c and 4.5d display the integrated

^{12}CO and ^{13}CO maps, respectively, over the velocity range of [−7.8, 1.3] km s^{-1}. These maps reveal that the molecular emission is primarily concentrated within the filament containing IC 446 and IC 447. On the other hand, Figures 4.5e and 4.5f show the integrated ^{12}CO and ^{13}CO emissions, respectively, over the velocity range of [1.95, 10.4] km s^{-1}, highlighting the molecular emission towards NGC 2245 and NGC 2247. The previous study by Kutner et al. (1979) on the Mon R1 clouds proposed the presence of two distinct clouds within the velocity ranges of [−1, 1] and [3, 5] km s^{-1}. Our analysis, leveraging the availability of high-resolution molecular line data, supports the existence of these two distinct molecular clouds in the direction of Mon R1, in agreement with the findings of Kutner et al. (1979).

To investigate the gas flow within the filament, we have focused on a specific area within the target region, as indicated by the broken box in Figure 4.5. This area has an angular extent of $\sim 0^\circ.99 \times 0^\circ.71$, corresponding to a physical scale of about 13.14 pc × 9.42 pc at a distance of ∼760 pc. Figures 4.6a and 4.6b display the channel maps of ^{12}CO and ^{13}CO emission, respectively, covering a velocity range of [−7.8, 1.95] km s^{-1}. The *Herschel* 160 μm continuum emission contour is overlaid on these maps to outline the extent of the filament. The molecular emission is particularly prominent in the velocity range of [−2.6, −0.65] km s^{-1}, which allows us to trace the boundary of the filament. However, the gas flow towards the filament is observed in a broader velocity range of [−5, +1] km s^{-1} as evident in the channel maps of ^{12}CO and ^{13}CO.

4.3.3.2 PV diagrams

To further investigate the presence of two distinct clouds in Mon R1, we have analyzed the PV diagrams of the molecular gas. Figures 4.7a and 4.7c display the latitude-velocity (b–v) diagrams of ^{12}CO and ^{13}CO emission, respectively, covering the field of view shown in Figure 4.5. The molecular emission is integrated over the longitude range from 201° to 202° to extract these b–v diagrams.

Similarly, Figures 4.7b and 4.7d show the longitude-velocity (l–v) diagrams of ^{12}CO and ^{13}CO, respectively. In these diagrams, the molecular emission is

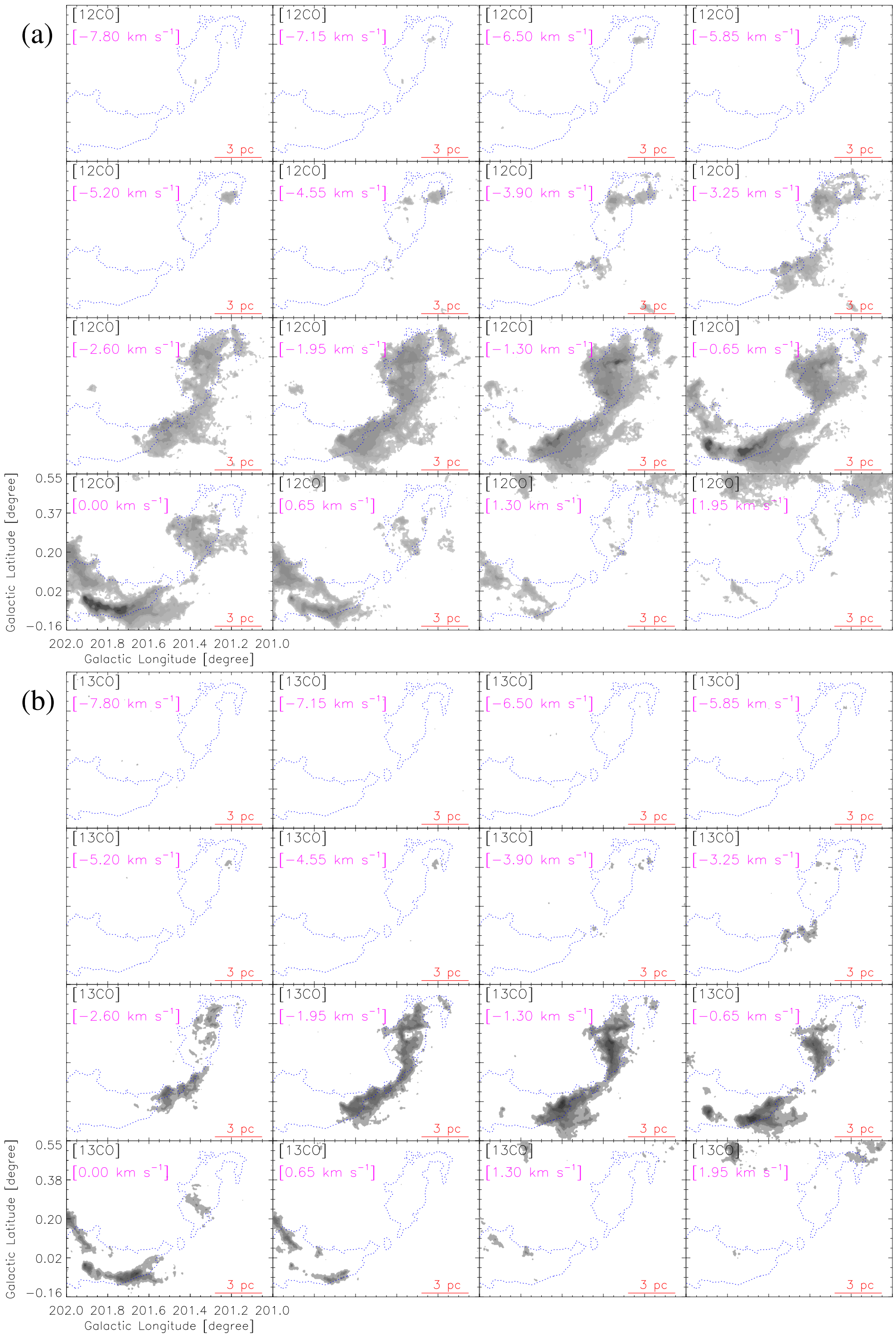

Figure 4.6: a) Velocity channel maps of ^{12}CO(1–0) toward the region marked by a dashed magenta box in Figures 4.5c and 4.5d. The contour levels are 1.5, 3, 5, 7, 10, 13, 15, 16, 20, and 23 K km s^{-1}. b) Velocity channel maps of ^{13}CO(1–0). The contour values are 0.1, 0.5, 1, 1.5, 2, 3, 4, 5, 6, and 7 K km s^{-1}. The *Herschel* 160 μm continuum emission contour (in blue with a level of 0.02 Jy pixel^{-1} is overplotted in each panel. In each panel, the velocity information (in km s^{-1}) and a scale bar representing 3 pc are shown.

integrated over the latitude range from $-0^{\circ}.16$ to $0^{\circ}.45$. All the PV diagrams clearly exhibit two distinct velocity components towards Mon R1, which do not appear to be connected in velocity space. This indicates the presence of two separate clouds. Furthermore, we find that the molecular gas associated with the filament is predominantly traced in a velocity range of $[-5, +1]$ km s^{-1}, as indicated by the dashed rectangular box in Figure 4.7. These analyses provide valuable insights into the exact boundary of the filamentary cloud and support the existence of a single and isolated filament in Mon R1, as observed in Figure 4.6.

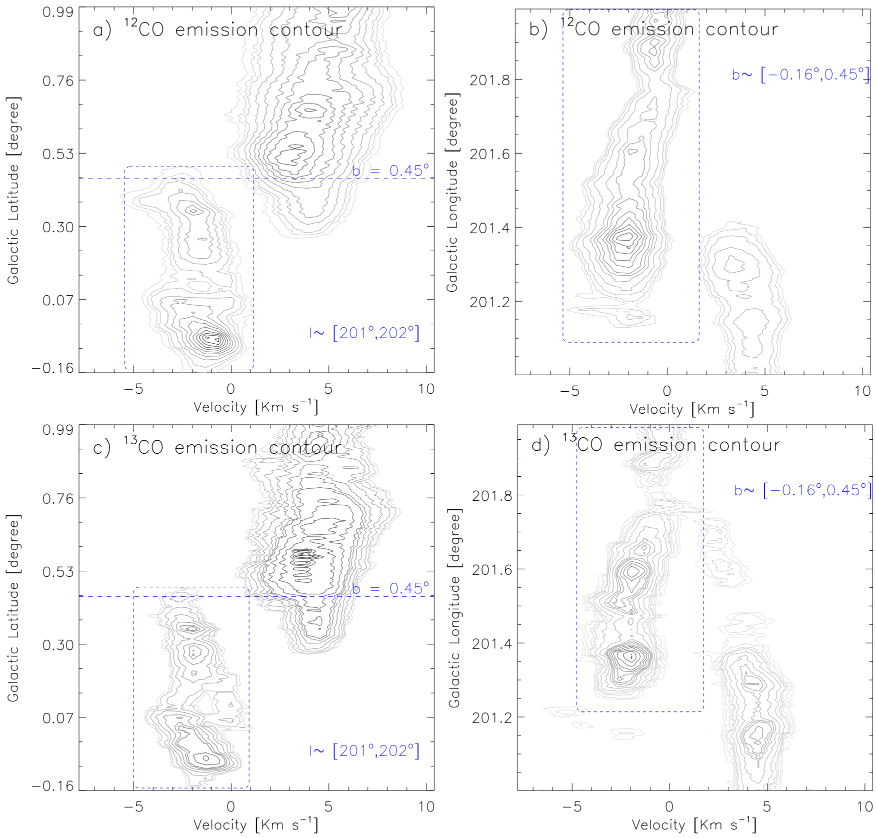

Figure 4.7: a) Latitude-velocity diagram of ^{12}CO. b) Longitude-velocity diagram of ^{12}CO. c) Latitude-velocity diagram of ^{13}CO. d) Longitude-velocity diagram of ^{12}CO. In the latitude-velocity diagrams (see panels "a" and "c"), the molecular emission is integrated over the longitude range from 201° to 202° (see a broken box in Figures 4.5c and 4.5d). In the longitude-velocity diagrams (see panels "b" and "d"), the molecular emission is integrated over the latitude range from $-0^{\circ}.16$ to $0^{\circ}.45$. In each panel, a dashed rectangular box (in blue) depicts the CO emission toward the filament (see text for more details).

4.3.3.3 Velocity field of the gas

In Figure 4.8a, the integrated intensity (or moment-0) map of ^{13}CO emission is shown, with 31 distinct positions along the filament marked by filled blue circles (each with a radius of $\sim 10''$). These positions were selected based on locally maximum ^{13}CO integrated intensities compared to their surroundings. To investigate the velocity variation of the gas along the filament, averaged spectra were extracted toward each marked circle in Figure 4.8a. These observed spectra were then fitted with Gaussian profiles to derive spectral parameters such as the radial velocity ($V_{\rm LSR}$) and linewidth (ΔV).

The velocity profile, which represents the variation of velocity along the major axis of the filament, is displayed in Figure 4.8b. It indicates a maximum velocity variation of approximately 3 km s^{-1} within the filament. The profile also exhibits an oscillatory pattern with a periodicity of approximately 3-4 pc, which becomes more pronounced when the linear gradient is removed from the profile. Two prominent velocity peaks separated by approximately 8–9 pc are observed in Figures 4.8b and 4.8c, corresponding to the central and western parts of the filament. The negative and positive velocity gradients between these peaks may be attributed to different inclinations of different parts of the filament.

The velocity profile after removing the linear gradient is presented in Figure 4.8c. It shows a clear linear velocity gradient along the central part of the filament ($\sim$0.4 km s^{-1} pc^{-1}) and velocity gradients ($\sim$0.6 km s^{-1} pc^{-1}) at the ends, which are likely associated with star-forming regions. The linewidth (ΔV) profile is depicted in Figure 4.8d, revealing an average linewidth of approximately 1.5 km s^{-1}. The significance of these results regarding filamentary fragmentation is discussed in Section 4.4.

4.3.4 Distribution of young stellar objects

In order to trace the star formation activity within the R-association, we examined the population of YSOs using color-color and color-magnitude diagrams (see also Section 2.6). Figure 4.9a displays the dereddened color-color diagram ($[[3.6] - [4.5]]_0$ vs $[K - [3.6]]_0$) of point-like objects extracted from the Warm-*Spitzer* Glimpse360[§] survey (Whitney et al., 2011). In this diagram, triangles represent Class I YSOs, while circles represent Class II YSOs. Following the cri-

[§]http://www.astro.wisc.edu/sirtf/glimpse360/

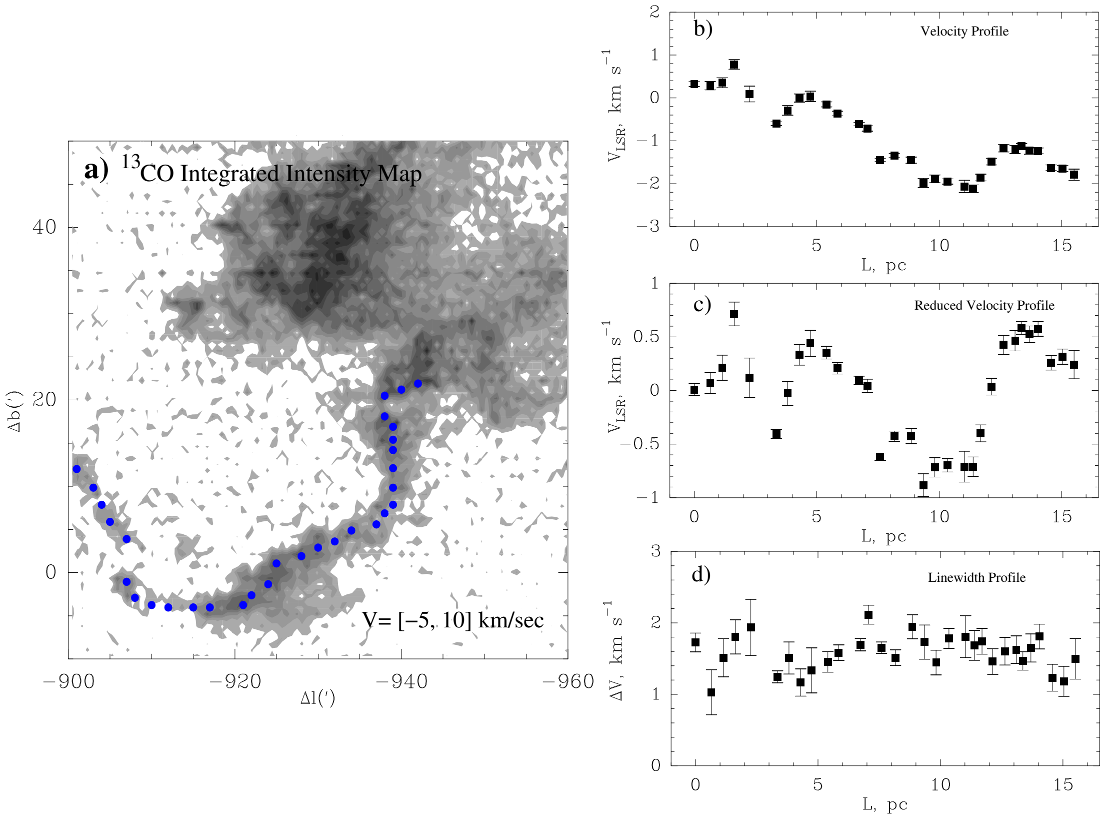

Figure 4.8: a) FUGIN ^{13}CO(1–0) map of intensity (moment-0) in the direction of Mon R1. The molecular emission is integrated over a velocity range of [−5, 10] km s^{-1}. Blue dots are marked toward the filamentary structure, where spectra are extracted. b) Velocity profile along the filament obtained from distinct positions (see blue dots in panel "a"). c) Velocity profile after removing the linear gradient from profile shown in panel "b". d) Linewidth profile (average linewidth ∼1.5 km s^{-1}). In panels "b", "c", and "d", the x-axis represents the physical length.

teria outlined in Gutermuth et al. (2009), a total of 201 YSOs were identified in our selected target area, consisting of 8 Class I and 193 Class II YSOs.

In addition to the YSOs identified in the dereddened color-color diagram, we further examined the NIR color-magnitude ($H - K$ vs K) diagram to identify additional sources with color-excess emission. The photometric data for this analysis were obtained from the 2MASS and UKIDSS-GPS surveys. To ensure the reliability of the photometric magnitudes, we selected sources with photometric uncertainties of $\sigma < 0.1$ mag in the H and K bands. This selection criterion ensures more accurate and reliable measurements (see Dewangan et al., 2016b, for more details). Applying the color condition of $H - K > 1$ mag, we identified a total of 182 YSO candidates in our selected area (represented by blue squares in Figure 4.9b). This color condition was determined based on the color-magnitude analysis of a nearby control field. These additional YSO candidates with color-excess emission provide further evidence of ongoing star formation activity in the R-association.

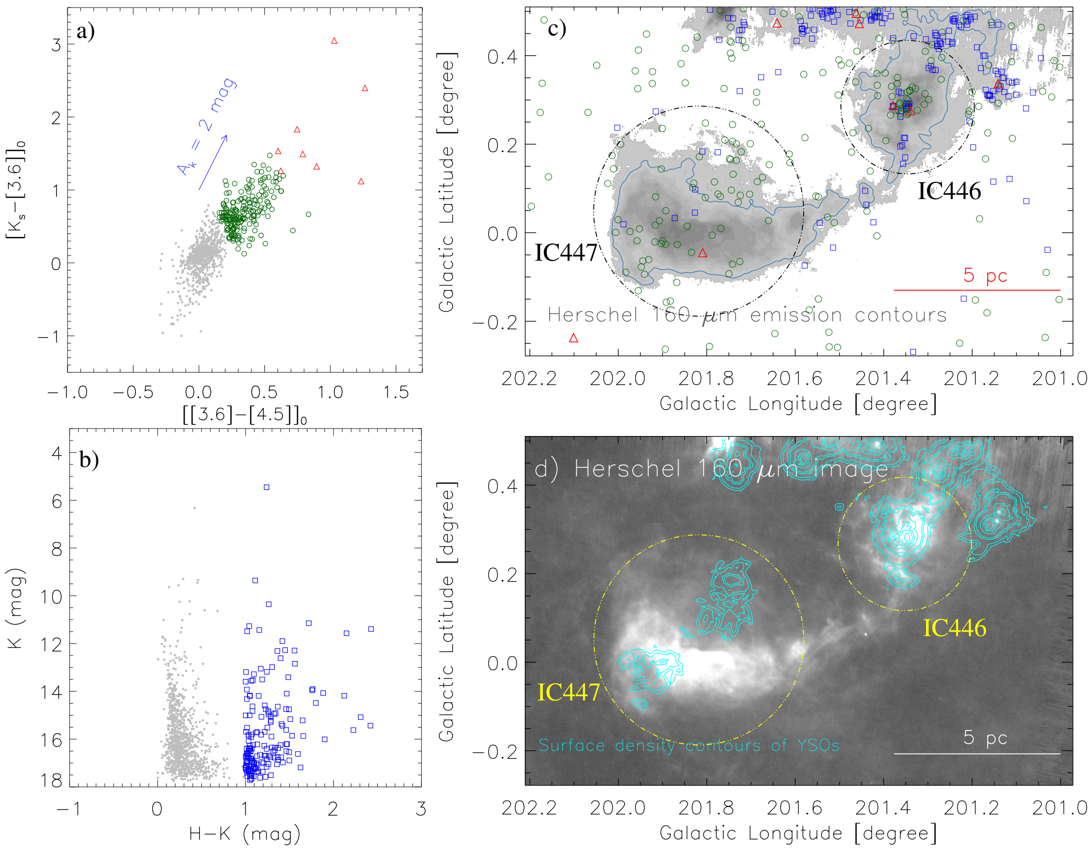

Figure 4.9: a) Dereddened color-color ($[[3.6]-[4.5]]_0$ vs $[K-[3.6]]_0$) diagram of point-like objects toward Mon R1. Red triangles represent Class I YSOs, while green circles indicate Class II YSOs (see text for more details). Following the extinction law given in Flaherty et al. (2007), an extinction vector (A_K= 2 mag) is drawn in the figure. b) Color-magnitude ($H-K$ vs K) diagram of point-like sources. The color excess sources are highlighted by blue squares. c) Overlay of the selected YSOs (from panels "a" and "b") on the *Herschel* 160 μm gray-scale filled contour map. The contour values are 0.8%, 1.5%, 2%, 2.5%, 3%, 4%, 5%, 7%, 9%, 15%, 30%, 50%, 70%, 90%, 95% of the peak value (i.e., 1.68 Jy pixel^{-1}). A contour (in sky-blue color) with a level of 0.02 Jy pixel^{-1} is also displayed in the figure. d) Overlay of the surface density contours (in cyan) of YSOs on the *Herschel* continuum map at 160 μm. The surface density contours are presented with the levels of 4, 5, 8, 10, 20, 35, 55, and 125 YSOs pc^{-2}. In panels "c" and "d", a scale bar corresponding to 5 pc is shown, and big dotted circles represent the extent of IC 446 and IC 447. In panels "a" and "b", sources with photospheric emission are shown by dots (in grey). Due to a large number of these sources, a small fraction is randomly displayed in panels "a" and "b".

After considering the YSO candidates identified in both dereddened color-color and NIR color-magnitude diagrams (Figures 4.9a and 4.9b), a total of 370 YSO candidates have been selected. To examine the spatial distribution of these YSO candidates, Figure 4.9c presents their positions overlaid on the *Herschel* 160

μm continuum image of Mon R1. The contour of the *Herschel* 160 μm continuum emission is also shown to indicate the location of the filament. In order to quantify the concentration of YSOs in our selected area, we performed a nearest neighbor (NN) surface density analysis (see Section 2.6.1 for an overview). This analysis is commonly used to study the clustering of YSOs (e.g., Casertano & Hut, 1985; Gutermuth et al., 2009; Bressert et al., 2010; Dewangan et al., 2016b). Following similar procedures as described in Dewangan et al. (2016b), we generated a surface density map of YSOs using a 15$''$ grid and considering 6 nearest neighbors at a distance of 760 pc. In Figure 4.9d, the surface density contours (shown in cyan) of YSOs are overlaid on the *Herschel* 160 μm image. These contours represent different levels of surface density, ranging from 4 to 125 YSOs per square parsec. The contours trace the regions of active star formation in our selected site. The YSOs are primarily clustered towards the ends of the filament, specifically IC 446 and IC 447. In the direction of IC 446, we observe higher surface density values of YSOs, ranging from 4 to 125 YSOs pc^{-2}. On the other hand, the surface density values towards IC 447 range from 4 to 12 YSOs pc^{-2}. This analysis suggests that the star formation activity is more intense towards IC 446 compared to IC 447 within the filament. It is worth noting that IC 447 is associated with several evolved massive B-type stars.

The recent narrow-band Hα and [S II] imaging observations conducted by Movsessian et al. (2020) in the Mon R1 region, including sites NGC 2245, NGC 2247, and IC 446, have revealed the presence of at least four Herbig-Haro (HH) objects along the filament. Specifically, three HH objects (HH 1202A, HH 1202B, and HH 1202C) are observed towards the site IC 446, while the fourth HH object (HH 1203) is located near the junction of the central and western parts of the filament. The detection of these HH objects provides further evidence for the high level of star formation activity within the filament. These objects are associated with the outflow phenomena driven by young stellar objects and indicate ongoing star formation processes in the region.

4.4 Discussion

The presence of a filament itself represents first step toward the formation of embedded cores and stars. However, second and major step is gravitational fragmentation which leads to the fabrication of self-gravitating cores (André et al., 2010, 2014). In this context, our observational results can be compared with the existing theoretical models of filamentary fragmentation and collapse.

4.4.1 Mon R1 filament: a supercritical filament

The critical line mass parameter defines the gravitational instability of a filament (e.g., Ostriker, 1964, see Section 1.2 for details). Following Equation 1.7 and considering T_k = 10 K and the mean molecular weight of μ = 2.33, the value of isothermal sound speed (c_s) comes out to be ∼0.19 km s^{-1}. Thus, $M_{\rm line,cri}$ is estimated to be ∼24–32 $M_\odot$ pc^{-1} for a temperature range of 15–20 K. In this work, the value of $M_{\rm line,obs}$ is determined to be ∼105 $M_\odot$ pc^{-1} (see Section 4.3.1), which greatly exceeds the value of $M_{\rm line,cri}$.

According to the findings of Inutsuka & Miyama (1992), isothermal filaments with $M_{\rm line,obs}$ greater than $M_{\rm line,cri}$ are prone to axisymmetric perturbations and exhibit radial collapse towards their axis. These filaments are classified as thermally *supercritical* and are known to facilitate the formation of prestellar cores and embedded YSOs (e.g., André et al., 2010; Dewangan et al., 2017b). Conversely, isothermal filaments that satisfy the condition $M_{\rm line,obs} < M_{\rm line,cri}$ are referred to as "*subcritical*" filaments, which generally exhibit a lack of significant star formation activity (e.g., André et al., 2010; Dewangan et al., 2017b). Applying this framework to the Mon R1 filament, we find that it falls into the thermally *supercritical* category. The presence of Herschel clumps/sub-filaments and groups of YSOs along the thermally *supercritical* filament in Mon R1 suggests its susceptibility to fragmentation and subsequent collapse into cores due to gravitational instability (André et al., 2010).

There is a possibility that the non-thermal microturbulent gas motions can provide extra support to the filament against gravitational collapse as these motions are associated with the gas turbulence (e.g., Hacar & Tafalla, 2011). This additional support increases the $M_{\rm line,cri}$ of the filament. The new line mass is termed as virial line mass ($M_{\rm line,vir}$) and can be estimated by replacing c_s with the effective sound speed i.e., $c_{\rm s,eff} = \sqrt{c_{\rm s}^2 + \sigma_{\rm NT}^2}$ in Equation 1.7 (e.g., Kainulainen et al., 2016; Dewangan et al., 2019a).

In this work, the linewidth of ^{13}CO spectra is observed to be ∼1.5 km s^{-1} (see Figure 4.8d), which leads the value of $M_{\rm line,vir}$ ∼211–219 $M_\odot$ pc^{-1} for a temperature range of ∼15–20 K. The values of $M_{\rm line,vir}$ and $M_{\rm line,obs}$ are close to each other within a factor of ∼2. Mach number, defined as the ratio of $\sigma_{\rm NT}/c_s$, is determined in a range of 2.4–2.7 for the filament, which suggests the supersonic nature of the filament.

4.4.2 Age Estimates

The fragmentation of the Mon R1 filament is evident from the presence of several high column density regions or fragments observed in the *Herschel* column density map, as noted by Kainulainen et al. (2016). The curved morphology of the filament leads to its division into three distinct parts, as discussed in Section 4.3.1. This division is also apparent in the molecular maps of CO, as shown in Figures 4.5c and 4.5d. The eastern part of the filament, which includes the site IC 447, exhibits a separate filamentary branch in the CO maps. On the other hand, the central and western parts of the filament appear as linear structures. By considering the lengths of the central and western sub-filaments, estimated to be approximately 5 pc and 4 pc, respectively (see Section 4.3.1), the observed line mass ($M_{\rm line,obs}$) is calculated to be around 64 $M_\odot$ pc^{-1} and 91 $M_\odot$ pc^{-1}.

One can estimate the critical timescale ($\tau_{\rm cri}$) at which a filament grows via accretion and reaches its critical line mass $M_{\rm line,cri}$. The critical timescale represents the lower age limit of the filament and is influenced by the fragmentation length scale (i.e., fragment/core separation, $\lambda_{\rm core}$), which can be expressed as follows

(Williams et al., 2018):

$$\tau_{\rm age} \geq \tau_{\rm cri} \simeq \frac{\lambda_{\rm core}}{2c_{\rm s}} \tag{4.1}$$

We have estimated $\lambda_{\rm core}$ along the central and western parts of Mon R1 filament, which is ∼0.5 pc and ∼0.2 pc, respectively (see Figures 4.2b and 4.8c). For $c_{\rm s}$ ∼0.23 km s^{-1} (at T_k = 15 K), these core separation values lead $\tau_{\rm cri}$ to be ∼1.1 Myr and ∼0.4 Myr for the central and western parts, respectively. The corresponding average accretion rate during the assembly of filament can also be calculated using $\dot{M} = \frac{M_{\rm line,cri}}{\tau_{\rm cri}}$ (e.g., Clarke et al., 2016; Williams et al., 2018). Thus, considering $M_{\rm line,cri}$ ∼24 $M_\odot$ pc^{-1} (at T_k = 15 K) for both the central and western parts of the filament, the average accretion rate experienced during the growth of these parts of filament is ∼22 and ∼60 $M_\odot$ pc^{-1} Myr^{-1}, respectively.

If we assume that the accretion rate remained constant over the filament's lifetime, then the age of the filament can be estimated using $\tau_{\rm age} = \frac{M_{\rm line,obs}}{\dot{M}}$ (e.g., Williams et al., 2018). This exercise yields the values of $\tau_{\rm age}$ to be ∼3 and ∼1.5 Myr for the central and western parts of the filament, respectively. Therefore, the elapsed time since the central and western parts of the filament become critical, is ∼1.9 and ∼1.1 Myr, respectively. However, considering the turbulence into account $c_{\rm s}$ can be replaced by $c_{\rm s,eff}$ in Eq. 4.1. Adopting T_k = 15 K and ΔV∼ 1.5 km s^{-1} (i.e., FWHM(^{13}CO)), the corresponding critical age for the central and western parts becomes ∼0.4 and ∼0.2 Myr, respectively. The projection effects are not taken into account in the estimations of $\lambda_{\rm core}$. Therefore, all these calculations give lower limits on the derived values of ages.

We utilize the ^{13}CO line data to investigate the velocity profile of the filament in Mon R1. The velocity profiles shown in Figures 4.8b and 4.8c exhibit an ordered oscillatory pattern along the major axis of the filament, with a characteristic period of approximately 3–4 pc. This behavior is reminiscent of the velocity profiles observed in previous studies, such as the investigation of the L1517 dark cloud by Hacar & Tafalla (2011). In their study, they found a similar trend in the velocity profile and demonstrated that the velocity centroids peak at the locations of fragments, indicating gas motion associated with the fragments. Similar velocity patterns have been observed in other studies as well, including those by Hacar et al. (2016), Kainulainen et al. (2016), Lu et al. (2018), and Dewangan et al. (2019a). These observational signatures of fragmentation in filaments are also consistent with the observations in the Mon R1 filament. However, a detailed modeling of the filament is required to study the nature of the fragments, which necessitates information about properties such as the orientation, geometry, and strength of the magnetic field, which are currently unknown. Additionally, the availability of dense gas tracers in the filaments (e.g., HNC (1–0); Jackson et al. (2010), HCO^+ (3–2); Zernickel et al. (2013), N_2H^+ (1–0); Beuther et al. (2015), NH_3 (1–1, 2–2); Lu et al. (2018), CS (2–1); Dewangan et al. (2019a)) can further constrain the velocity field which is the observational limitation of our current work.

4.4.3 Star Formation Scenario

In their study, Pon et al. (2012) discuss two different collapse modes of a filament. They propose that the interior of the filament collapses homologously, meaning that the density remains uniform and all regions have a similar collapse timescale. On the other hand, the ends of the filament are preferentially given more momentum, causing them to collapse faster. Analytical studies of elongated but finite-sized filaments suggest that the collapse timescale depends on the relative position along the filament, with faster collapse observed at the edges compared to the central regions (Bastien, 1983; Pon et al., 2011; Clarke & Whitworth, 2015). The collapse timescale at the edges of a filament with an initial aspect ratio (A) of 5 is found to be 2-3 times shorter compared to the central regions, while filaments with higher aspect ratios collapse even faster at the ends (Pon et al., 2011). The faster collapse at the edges of the filament is supported by the high preferential acceleration of the gas, leading to density enhancements in those regions (see Section 2.2 in Pon et al., 2012). Interestingly, in the Mon R1 filament, the western part exhibits a higher accretion rate of approximately 60 $M_\odot$ pc^{-1} Myr^{-1} compared to the central part, which has an accretion rate of around 22 $M_\odot$ pc^{-1} Myr^{-1} (see Section 4.4.2). This suggests that the faster collapse at the ends of the filament, known as the end-dominated collapse (or EDC), may be dominant in the western part of the filament. The occurrence of homologous collapse is typically observed for $A < 5$ filaments, while the EDC is dominant for filaments with $A \geq 5$ (Pon et al., 2011, 2012). By using the ^{13}CO moment-0 map (Figure 4.5d), the aspect ratio of the Mon R1 filament is estimated to be approximately 11.5, considering a length of $\sim$14 pc and a diameter of $\sim$1.2 pc. This value is larger than 5, suggesting that the filament is more likely to undergo faster collapse at its ends rather than homologous collapse.

Our observational findings support the ongoing fragmentation and formation of gravitationally bound cores within the Mon R1 filament. We observe embedded high column density regions/fragments and detect oscillations in the velocity profile, indicating the presence of fragmentation and the formation of potential star-forming cores. Moreover, we observe clusters of YSOs, as well as the presence of sites IC 446 and IC 447 hosting massive B-type stars at the ends of the filament. This suggests that star formation activity is more intense at the filament ends compared to the central part, indicating that local collapse may have occurred faster at the ends of the filament.

These observational results are consistent with the EDC model of star formation in the Mon R1 filament. Here we note that the filaments showing EDC process are rare and a few are reported in the literature (see Section 1.3.2). Among these examples, the filament in S242 shows the evolved phase of filamentary fragmentation, with one end hosting the S242 H II region, which may have formed through the process of EDC. The rest of the mentioned filaments are in their very early phases of fragmentation, as they exhibit dense clumps along their major axis. It is worth noting that some of these filaments also display higher velocity gradients at one or both ends, indicating the influence of the EDC process. For example, the southern end of the Musca cloud exhibits a velocity gradient of 0.5 km s^{-1} pc^{-1} (Hacar et al., 2016; Kainulainen et al., 2016), both ends of S242 show a velocity gradient of 1 km s^{-1} pc^{-1} (Dewangan et al., 2017b, 2019a), and one end of G341.244$-$00.265 shows a velocity gradient of 0.6–0.8 km s^{-1} pc^{-1} (Yu et al., 2019). However, there are also cases where the velocity gradient within the filament is observed from the ends toward the center, such as in the NGC 6334 filament (Zernickel et al., 2013), or where a transverse velocity gradient is observed at one end instead of a velocity gradient along the major axis, as seen in the IRDC 18223 filament.

In comparison to the listed filaments, Mon R1 filament can be treated as the best example of a more evolved stage of the filamentary fragmentation, which reveals end dominated collapse thus forming the known massive star-forming sites at the ends. Our observational analysis shows the clear linear velocity gradient along the central part of the filament (~0.4 km s^{-1} pc^{-1}), and relatively higher velocity gradients (~0.6 km s^{-1} pc^{-1}) at the ends, which are probably associated with star-forming regions.

4.5 Summary and Conclusions

This work aims to understand the physical processes governing the star formation activities in Mon R1 filament. In this context, a multi-wavelength observational approach has been employed in Mon R1 complex. The optical and infrared images show the existence of a filament (length ~14 pc, mass ~1465 $M_\odot$) in Mon R1, which is the most prominent feature in the *Herschel* column density map. We named it Mon R1 filament. The ^{12}CO and ^{13}CO line data have allowed us to identify two molecular clouds within our selected target area, identified at velocities of [−5, 1] km s^{-1} and [2, 10] km s^{-1}. The molecular gas associated with the Mon R1 filament is studied in a velocity range of [−5, 1] km s^{-1}, which is found to be isolated from another diffuse cloud at [2, 10] km s^{-1}. The filament is found to contain two previously known sites IC 446 and IC 447 at its opposite ends. Several massive B-type stars are identified toward the site IC 447, while a massive YSO (i.e., VY Mon) is observed toward the site IC 446. The presence of extended temperature features, PDRs, and outflow activity toward both ends of the filament indicates ongoing star formation activity. The clustering of YSOs is observed prominently at the filament edges, with a higher surface density of YSOs observed toward IC 446 compared to IC 447. The surface density ranges from 4 to 125 YSOs pc^{-2} toward IC 446, while it is found to be 4 to 12 YSOs pc^{-2} in the direction of IC 447. This disparity suggests more intense star formation activity toward IC 446. The estimated mass and length of filament are ~1465 $M_\odot$ and ~14 pc, respectively. This corresponds to $M_{\rm line,obs}$ of ~105 $M_\odot$ pc^{-1}. The $M_{\rm line,obs}$ is found to be ~3 to 4 times higher than $M_{\rm line,cri}$. This suggests that the Mon R1 filament is thermally *supercritical*, indicating that it is prone to gravitational fragmentation and the formation of self-gravitating cores.

The western part of the filament takes about 0.4 Myr to grow its line mass by its critical value with an average accretion rate of ~60 $M_\odot$ pc^{-1} Myr^{-1}. In the case of the central part of the filament, this critical timescale and the accretion rate are estimated to be ~1.1 Myr and ~22 $M_\odot$ pc^{-1} Myr^{-1}, respectively. The velocity and linewidth profiles of the filament show an oscillatory pattern with a periodicity of 3–4 pc along the direction of its major axis. The velocity gradient along the central part of the filament is found to be ~0.4 km s^{-1} pc^{-1}, however the relatively higher velocity gradients (~0.6 km s^{-1} pc^{-1}) are observed at both ends of the filament. The aspect ratio (A) of the filament is found to be greater than 5, suggesting the end dominated collapse mode is dominated over the homologous collapse mode.

Taken together, all the observational outcomes, the fragments distributed toward both ends of the filament are found to undergo a faster collapse compared to its central part, showing the presence of massive star-forming regions at its opposite ends. Overall, the elongated filament in Mon R1 is a promising candidate favouring the EDC model of star formation as discussed by Pon et al. (2011, 2012).

Chapter 5

Simultaneous evidence of edge collapse and hub-filament configurations: A rare case study of a Giant Molecular Filament G45.3+0.1[†]

5.1 Introduction

Chapters 3 and 4 have provided evidence for the potential of MSF through the complex HFSs and EDC scenario in isolated filaments. While HFSs associated with MSF activities are commonly observed in our Galaxy (e.g., André et al., 2010; Schneider et al., 2012; Motte et al., 2018; Anderson et al., 2021), the observational signatures of the EDC scenario in star-forming filaments hosting massive stars (including HII regions powered by massive stars) are rare (Dewangan et al., 2017b, 2019b; Bhadari et al., 2020, and references therein). Molecular line observations unveil that the filaments in HFSs act as a channel of material flows to feed

[†]**Bhadari, N. K.**, Dewangan, L. K., Ojha, D. K., Pirogov, L. E., Maity, A. K., 2022, ApJ, 930, 169, "Simultaneous evidence of edge collapse and hub-filament configurations: A rare case study of a Giant Molecular Filament G45.3+0.1"

the dense clumps/cores (e.g., Kirk et al., 2013; Peretto et al., 2013; Dewangan et al., 2017c; Hacar et al., 2018; Treviño-Morales et al., 2019b; Chen et al., 2020b; Dewangan et al., 2020a; Dewangan, 2021, 2022), where massive stars and young stellar clusters are observed (Liu et al., 2012; Treviño-Morales et al., 2019b, and references therein). In this regard, the HFSs can be considered as an intermediate step in MSF within a molecular cloud. It is important to note that the configurations of filaments involved in HFSs and the EDC scenario are scale-independent. HFSs are typically observed at sizes ranging from 2 to 20 pc (Kumar et al., 2020), while the filaments that exhibit EDC signatures, although fewer in number, are observed at physical scales ranging from ∼1–75 pc (Dewangan et al., 2023, and references therein).

It is crucial to note that the EDC model is based on simplistic and idealized assumptions (Clarke & Whitworth, 2015; Hoemann et al., 2022). However, it is considered one of the major collapse modes in filaments. Recently, attempts have been made to analytically address the question of whether two neighboring filaments will first interact to each other or independently collapse via the EDC process, providing insights into real cases of interstellar medium dynamics (see Hoemann et al., 2021). However, there is still a gap in our theoretical understanding regarding the connection between observed HFSs and the EDC process in filaments. By studying the link between HFSs and the EDC scenario in filaments, we aim to gain insights into the mass accumulation processes from cloud to core scales that drive the formation of massive stars. The investigation of mass accumulation in different scales helps us understand how material flows and accumulates within a filament, leading to the formation of dense cores and ultimately the birth of massive stars. This knowledge is essential for developing comprehensive models of MSF and advancing our understanding of the physical processes involved.

While the theoretical insights are currently lacking, the observational results from this work contribute to the understanding of the interplay between HFSs and the EDC process in filaments. In this context, the present work deals with two major star-forming complexes (i.e., G045.49+00.04 and G045.14+00.14) located in the Aquila constellation (l=45^o, b=0^o). These sites were primarily identified and catalogued as extended clouds with the prefix name of Galactic Ring Survey Molecular Cloud (GRSMC; see more details in Rathborne et al., 2009).

The two complexes, G045.49+00.04 (hereafter, G45E) and G045.14+00.14 (hereafter, G45W), are well-known for hosting massive star-forming regions, numerous ultracompact (UC) HII regions, maser emission, and outflow activities from young stars, including massive star(s) (e.g., Wood & Churchwell, 1989; Blum & McGregor, 2008; Paron et al., 2009; Rivera-Ingraham et al., 2010). The eastern complex, G45E, contains the sources IRAS 19120+1103 (or G45.45+0.06) and IRAS 19117+1107 (or G45.48+0.13), while the western complex, G45W, is home to two active massive star-forming regions, IRAS 19110+1045 and IRAS 19111+1048. Extensive exploration of both complexes has been conducted using IR, sub-mm, and radio data sets (e.g., Vig et al., 2006; Rivera-Ingraham et al., 2010). Notably, the eastern complex exhibits significant extended sub-mm emission, as shown in Figure 2 of Rivera-Ingraham et al. (2010). In the direction of the western complex, the distribution of dust and ionized gas around IRAS 19110+1045 is less extensive compared to that of IRAS 19111+1048 (Vig et al., 2006), and it is observed to be much younger than the latter source (Hunter et al., 1997; Vig et al., 2006). Figure 5.1 presents a MIR view of an area containing G45E and G45W, represented as a 3-color composite map created using the *Spitzer* 24 μm (red), *WISE* 12 μm (green), and *Spitzer* 8 μm (blue) images.

Figure 5.1 also includes the positions of dust continuum clumps at 870 μm identified by Urquhart et al. (2018) from the APEX Telescope Large Area Survey of the Galaxy (ATLASGAL). These clumps, marked by red and blue diamonds, are traced in a velocity range of [55.5, 62.2] km s^{-1}. Each ATLASGAL clump has radial velocity and distance information available (see Urquhart et al., 2018, for more details). The red diamonds correspond to clumps located at a kinematic distance of 8.4 kpc, while the blue diamonds represent clumps at a kinematic distance of 8 kpc. However, based on the spatial distribution of the ATLASGAL clumps and the morphology of the parent molecular cloud toward G45E and G45W, we adopt a distance of 8 kpc for both sites in this study (see Section 5.3.1).

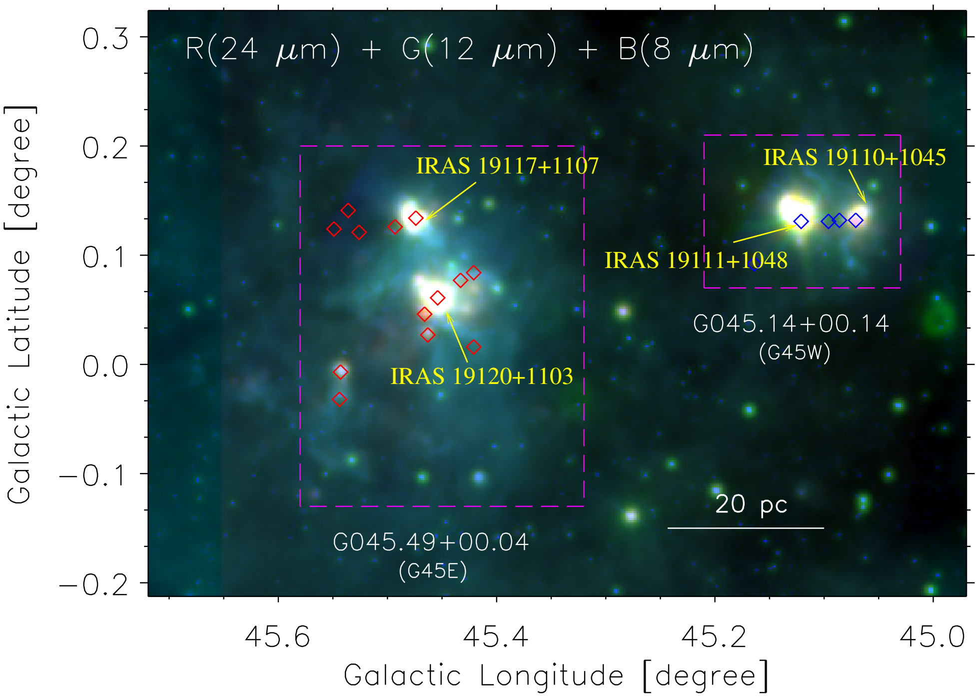

Figure 5.1: Three-color composite image (Red: *Spitzer* 24 μm, Green: *WISE* 12 μm, Blue: *Spitzer* 8 μm) of a field containing star-forming complexes G045.49+00.04 (G45E) and G045.14+00.14 (G45W). Two dashed rectangular boxes (in magenta) enclose the areas of G45E and G45W (from GRSMC; Rathborne et al., 2009), and are presented in Figures 5.2b and 5.2c. The red and blue diamonds represent the positions of ATLASGAL dust clumps at distances of 8.4 kpc and 8.0 kpc, respectively, from Urquhart et al. (2018). The positions of the IRAS sources are shown by arrows. A scale bar of 20 pc (at d = 8 kpc) is also displayed.

Previous studies considered distances to these sites in the range of approximately 6-8 kpc (see Rivera-Ingraham et al., 2010, and references therein). A detailed investigation of the molecular gas encompassing both complexes is yet to be conducted, which is crucial for understanding the ongoing physical processes and exploring the HFSs and EDC scenarios. The sub-mm continuum maps are also employed to carefully analyze the observed spatial structures.

We organize this work into five major sections. §5.2 describes data sets used in this work. In §5.3, we present the results obtained using the continuum and line data. In §5.4, we discuss the implications of our derived results for explaining the star formation processes. A summary of this work is given in §5.5.

Table 5.1: List of multi-wavelength and multi-scale data/surveys used in this work.

Survey	Wavelength/line(s)	Angular Resolution (″)	Reference
Multi-Array Galactic Plane Imaging Survey (MAGPIS)	20 cm	~6	Helfand et al. (2006)
FUGIN	^{12}CO, ^{13}CO, C^{18}O (J=1–0)	~20	Umemoto et al. (2017)
CHIMPS	^{13}CO, C^{18}O (J=3–2)	~15	Rigby et al. (2016)
APEX Telescope Large Area Survey of the Galaxy (ATLASGAL)	870 μm	~19.2	Schuller et al. (2009)
Herschel Infrared Galactic Plane Survey (Hi-GAL)	70, 160, 250, 350, 500 μm	~6, 12, 18, 25, 37	Molinari et al. (2010a)
Spitzer MIPS Inner Galactic Plane Survey (MIPSGAL)	24 μm	~6	Carey et al. (2009)
Wide Field Infrared Survey Explorer (WISE)	12 μm	~6.5	Wright et al. (2010)
Spitzer Galactic Legacy Infrared Mid-Plane Survey Extraordinaire (GLIMPSE)	3.6, 4.5, 5.8, 8.0 μm	~2	Benjamin et al. (2003)
UKIRT near-infrared Galactic Plane Survey (GPS)	1.25–2.2 μm	~0.8	Lawrence et al. (2007)
Two Micron All Sky Survey (2MASS)	1.25–2.2 μm	~2.5	Skrutskie et al. (2006)

5.2 Data Sets

In this work, we analyzed the publically available multiscale and multiwavelength data sets toward our target region, primarily in the area of $0^\circ.67\times0^\circ.50$ or 93.5×70.4 pc^2 (centred at $l = 45^\circ.30$; $b = 0^\circ.05$). The overview of data sets used in this work is presented in Table 5.1. We utilized the ^{12}CO(J=1−0), ^{13}CO(J=1−0), and C^{18}O(J=1−0) line data obtained from the FUGIN survey. The FUGIN data are calibrated in main beam temperature ($T_{\rm mb}$), and the typical rms is ~1.5 K for ^{12}CO and ~0.7 K for ^{13}CO and C^{18}O lines. The survey data provide a velocity resolution of 1.3 km s^{-1} (see more details in Umemoto et al., 2017). We also used ^{13}CO(J=3−2), and C^{18}O(J=3−2) line data downloaded from the ^{13}CO/C^{18}O (J = 3→2) Heterodyne Inner Milky Way Plane Survey (CHIMPS). The high-resolution ($\theta_{\rm spatial}$=15″, $\theta_{\rm velocity}$=0.5 km s^{-1}) CHIMPS survey covers the Galactic plane within $|b| \leq 0^\circ.5$ and $28^\circ \lesssim l \lesssim 46^\circ$. The survey data have a median rms of ~0.6 K, and are calibrated in antenna temperature ($T_{\rm A}^*$) scale. We converted the intensity scales from $T_{\rm A}^*$ to $T_{\rm mb}$ by using the relation $T_{\rm mb} = \frac{T_{\rm A}^*}{\eta_{\rm mb}}$, where the mean detector efficiency is $\eta_{\rm mb}$= 0.72 (Rigby et al., 2016). In order to improve the sensitivity, the molecular line data from the FUGIN and CHIMPS were smoothed with a Gaussian function having 3 pixels half-power beamwidth. This exercise yields the final spatial resolutions of the FUGIN and CHIMPS molecular line data to be 21″.73 and 16″.82, respectively.

5.3 Results

5.3.1 Kinematics of molecular gas

In this section, we study the spatial-kinematic structures of the molecular gas in the direction of our target sites.

5.3.1.1 Morphology of the molecular cloud

In Figure 5.2a, we present a three-color composite map at sub-mm wavelengths (Red: ATLASGAL 870 μm, Green: *Herschel* 350 μm, Blue: *Herschel* 160 μm) of the target area depicted in Figure 5.1. The map reveals the presence of elongated structures, or filaments, in both the star-forming complexes, G45E and G45W. To further investigate these complexes, Figures 5.2b and 5.2c display the ATLASGAL 870 μm continuum images overlaid with the MAGPIS 20 cm radio contours for the sites G45E and G45W, respectively. The MAGPIS radio contours highlight the zones of ionized emission or the HII regions in the target sites.

To investigate the kinematics of the parent molecular cloud, we analyzed the averaged molecular spectra obtained from a rectangular strip that passes through both major star-forming complexes (as indicated by the dotted dashed rectangle in Figure 5.2a). Figure 5.3a presents the averaged spectra of different molecular species, including FUGIN ^{12}CO/^{13}CO/C^{18}O (1–0) and CHIMPS ^{13}CO/C^{18}O (3–2). The line profiles of the different molecular species suggest that the molecular cloud can be effectively studied in a velocity range of [50, 70] km s^{-1}. The ^{12}CO(1–0) profile appears broader compared to the other line profiles, which can be attributed to its high optical depth and lower critical density. It is well-known that ^{12}CO(1–0) primarily traces the outer diffuse cloud. Therefore, we utilized the relatively optically thin ^{13}CO(1–0) line data to delineate the boundary of the molecular cloud.

For fitting the ^{13}CO(1–0) spectra, we employed the `curve_fit` function from the `SciPy` library (Virtanen et al., 2020) using double Gaussian profiles. The

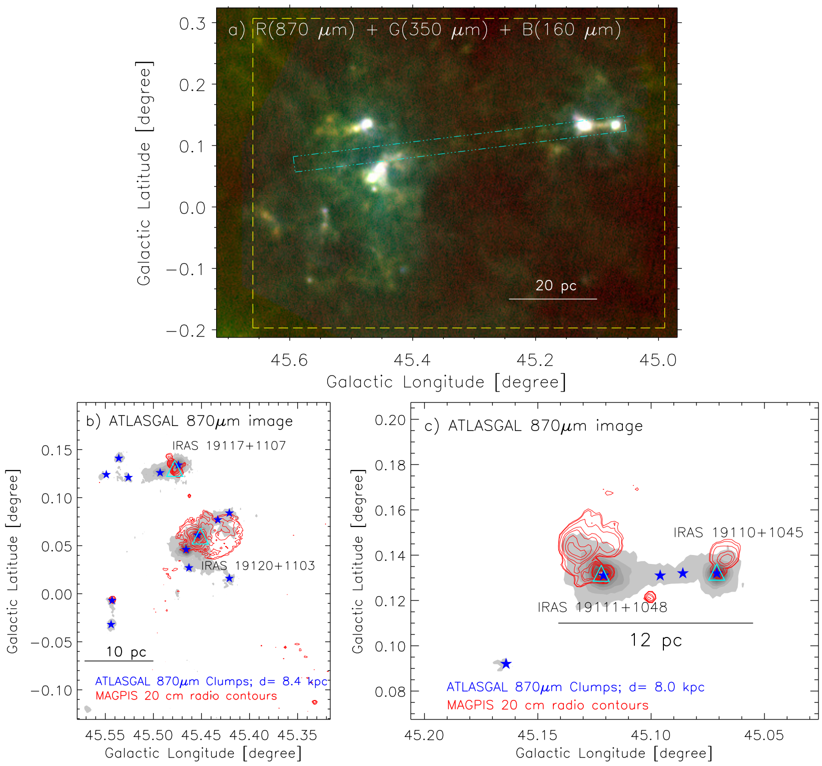

Figure 5.2: (a) Three-color composite image (Red: ATLASGAL 870 μm, Green: *Herschel* 350 μm, Blue: *Herschel* 160 μm) of a field shown in Figure 5.1. A dotted dashed rectangular strip (in spring green) indicates an area where the averaged gas spectra are extracted (see Figure 5.3). A dashed box in yellow highlights an area studied in this work. Panels (b) and (c) display the ATLASGAL dust continuum contour maps (in grey scale) of G045.49+00.04 and G045.14+00.14 regions at 870 μm, respectively (see dashed boxes in Figure 5.1). In panels (b) and (c), the ATLASGAL contour levels range from 5% to 95% in steps of 9%, of the map peak value (i.e., 5.49(7.56) Jy beam^{-1} for panel "b"("c")). The maps are overlaid with the MAGPIS 20 cm continuum emission contours with the levels of 0.96, 1.36, 2.73, 8.19, 13.64, 27.29, 40.93, 54.57, 109.15, 163.72, 218.30, 259.23, 267.41 mJy beam^{-1}. The star symbols in panels (b) and (c) represent the positions of ATLASGAL dust clumps (see also Figure 5.1), and the cyan triangles indicate the positions of IRAS sources.

fitted Gaussian profiles, along with the original ^{13}CO(1–0) profile, are presented in Figure 5.3b. The main Gaussian component, traced in a velocity range of [53, 63] km s^{-1}, yields a mean (μ) of 58.30±0.03 km s^{-1} and a standard deviation (σ) of 2.34±0.03 km s^{-1}. The other Gaussian component is associated with μ= 65.01±0.20 km s^{-1} and σ= 2.43±0.19 km s^{-1}, and contributes to the redder tail of the observed ^{13}CO(1–0) profile.

Figure 5.4 illustrates the spatial distribution of the molecular cloud at [53, 63] km s^{-1}, corresponding to the major Gaussian component of the ^{13}CO(1–0) spectra. Figure 5.4a presents the moment-0 map of ^{13}CO(1–0) emission, with overlaid contours of C^{18}O (1–0) emission. The ^{13}CO(1–0) moment-0 map reveals

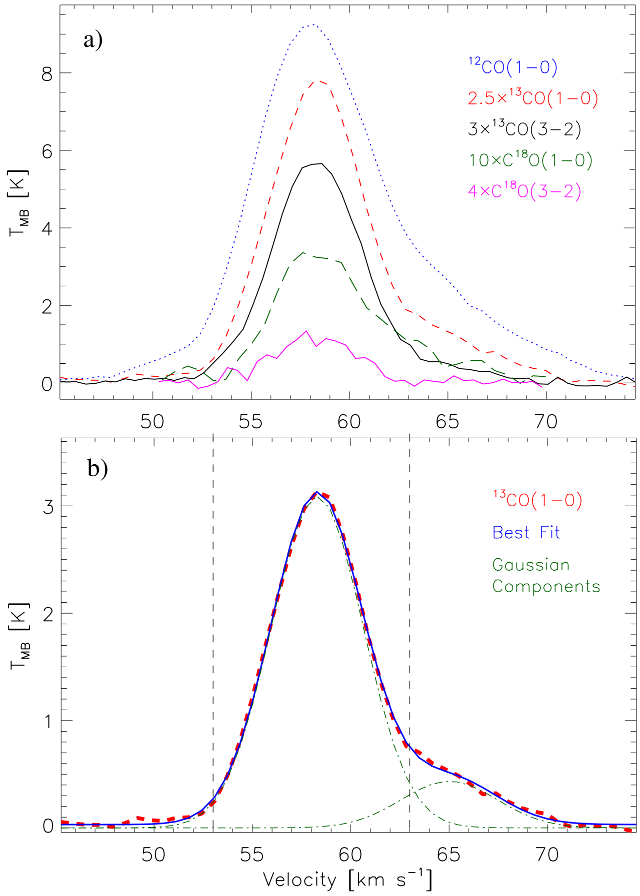

Figure 5.3: (a) Averaged spectral profiles of different molecular species along the dotted-dashed strip shown in Figure 5.2a. (b) ^{13}CO(1–0) line profile (dashed (red) curve) fitted with the two Gaussian components (dotted-dashed (green) curves). The best fit profile is shown in a thick blue curve. The two vertical dashed lines are marked at the velocity of 53 and 63 km s^{-1}.

an elongated molecular cloud hosting the two previously identified star-forming complexes, G45E and G45W, located at the ends of the cloud. Additionally, the C^{18}O (1–0) emission highlights dense substructures along the direction of the major massive star-forming sites, namely IRAS 19120+1103, IRAS 19117+1107, IRAS 19110+1045, and IRAS 19111+1048.

The moment-1 map of the ^{13}CO(1–0) emission is shown in Figure 5.4b. A continuous velocity structure around 58 km s^{-1} further supports the idea of an elongated molecular cloud. We can also notice a relatively redshifted emission around 63 km s^{-1}, which belongs to the minor Gaussian component (Figure 5.3). However, the moment maps related to the minor Gaussian component are not studied in this work. The moment-2 map is shown in Figure 5.4c. The linewidth value is about ∼2–5 km s^{-1} throughout the cloud structure. There are clear

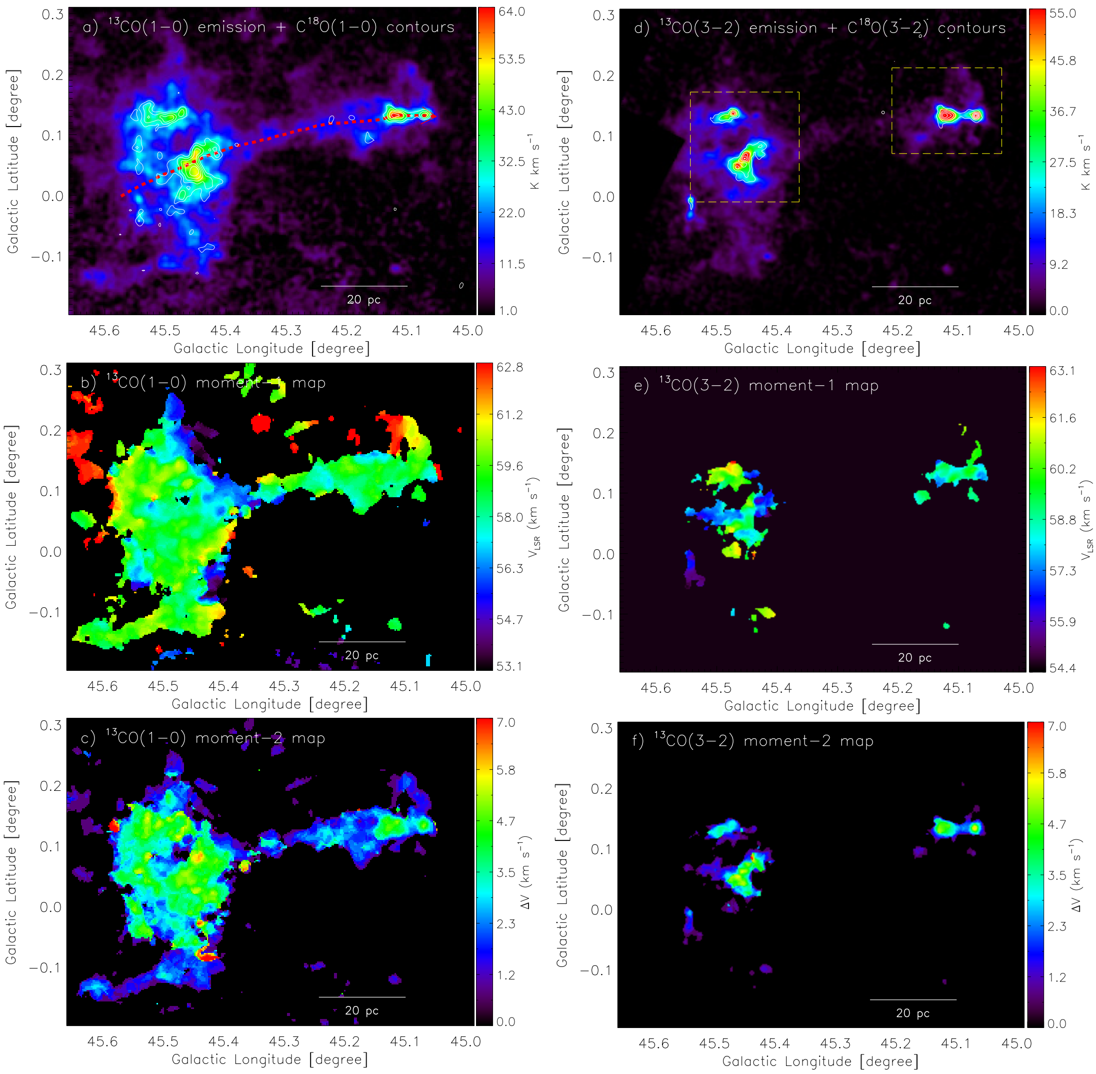

Figure 5.4: Left column of panels shows the FUGIN ^{13}CO(1–0) moment maps; (a) moment-0 map, (b) moment-1 map, and (c) moment-2 map in the direction of our selected target area (see a dashed box in Figure 5.2a). Right column of panels shows the similar maps for CHIMPS ^{13}CO(3–2) emission. The moment-0 maps are obtained in the velocity range of [53, 63] km s^{-1}. In panel (a), C^{18}O(1–0) emission contours are overlaid on the ^{13}CO(1–0) moment-0 map. The contour levels range from 3 to 8.7 K km s^{-1} in steps of 1.3 K km s^{-1}. In panel (d), the C^{18}O(3–2) emission contours are overlaid with the levels ranging from 3.2 to 20 K km s^{-1} in steps of 3.36 K km s^{-1}. Two dashed boxes in panel (d) show the area presented in Figure 5.12. In panel (a), a dashed (red) curve is indicative of filament's length, where the PV diagram is also studied (see Figure 5.6c). In all the panels, the respective color bars are shown to the right of each panel.

velocity dispersion enhancements at the edges of the cloud, which are of the order of ∼4.5 km s^{-1}. We have also displayed the moment maps of ^{13}CO(3–2) emission in Figures 5.4d, 5.4e, and 5.4f. The ^{13}CO(3–2) emission traces the dense gas compared to the ^{13}CO(1–0) emission, thus allowing us to study the structures and kinematics of dense molecular clumps. From Figures 5.4a and 5.4d, the dense gas/clumps are primarily identified towards the ends of elongated cloud, and the entire cloud structure is traced in the ^{13}CO(1–0) emission only. Overall, Figure 5.4 collectively displays the spatial-kinematic distribution of molecular cloud associated with the target sites G45E and G45W.

To examine the velocity distribution of the gas toward the elongated cloud observed in a velocity range of [53, 63] km s^{-1}, we have shown the velocity channel maps in Figure 5.5. Additionally, the C^{18}O(3–2) integrated emission contour (in red) is shown in Figure 5.5 at a level of 3.2 K km s^{-1} to visualize the gas motion in the direction of the cloud. The elongated morphology of the cloud becomes apparent starting from a velocity of 55.67 km s^{-1} and takes a complete shape between 57.62 km s^{-1} and 59.58 km s^{-1}. Notably, the dense substructures are predominantly observed at the edges of the elongated cloud.

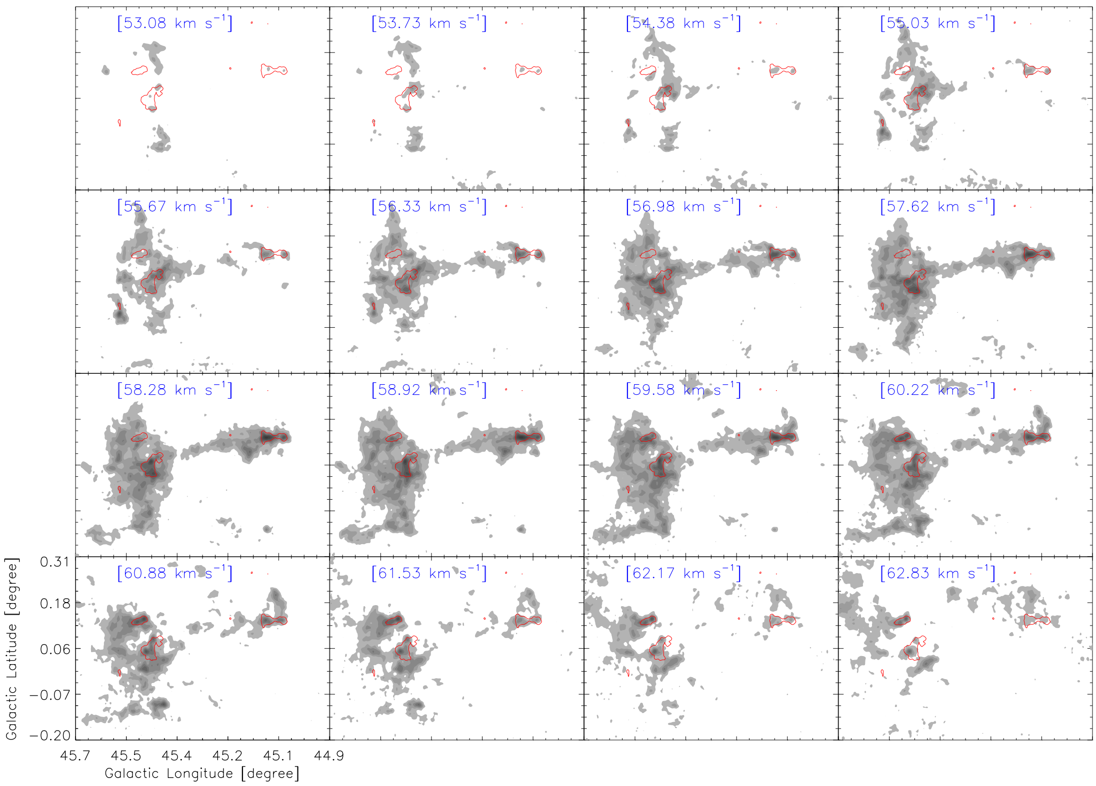

Figure 5.5: Velocity channel maps of ^{13}CO(1–0) emission (in grayscale). The contour levels range from 1.2 to 14 K in steps of 1.28 K. The overlaid red contours represent the integrated emission of C^{18}O(3–2) at a level of 3.2 K km s^{-1} (see also Figure 5.4b). The velocities are labeled in each panel.

5.3.1.2 Position-velocity diagrams

We have also examined the PV diagrams to analyze the kinematics of the molecular gas. PV diagrams provide valuable insights into the gas motion along specific spatial axes. Figures 5.6a and 5.6b display the longitude-velocity (l–v) and latitude-velocity (b–v) diagrams, respectively. The positions of the ATLASGAL dust clumps are overlaid on these diagrams, illustrating their spatial and velocity associations with the cloud. Figure 5.6c presents a PV diagram along a selected path with a physical length of ∼75 pc. This path is indicated by a dashed (red) curve in Figure 5.4a. Along this path, several small circular regions with radii of ∼15″ are selected. The average ^{13}CO(1–0) profile is obtained for each circular region, and the peak velocity is determined by fitting a Gaussian function to each average profile.

In Figure 5.6c, to study the pattern of velocity, we have also overlaid the peak velocity of each observed ^{13}CO(1–0) profile. In the PV diagram, the velocity distribution along the path shows an oscillatory pattern, and has a maximum velocity variation of ∼4 km s^{-1}. In addition to the oscillatory pattern, the velocity profile shows the linear gradient at both ends of the filament. In the direction of G45E, the velocity gradient is observed to have a value of −0.064 km s^{-1} pc^{-1}, while it is +0.032 km s^{-1} pc^{-1} toward G45W.

Figure 5.7a highlights two straight lines, indicating the presence of different velocity gradients in the PV plot (also seen in Figure 5.6c). Notably, the largest velocity gradient of approximately 0.5 km s^{-1} pc^{-1} is associated with the western border of G45E, suggesting accelerated gas motions in that region. Figure 5.7b displays the residual velocity profile, which is obtained by subtracting the velocity gradients from the data. This profile is generated using a "data−model" approach, where the model represents the best fit straight lines corresponding to the two different velocity gradient regimes. It has been suggested that the large-scale velocity oscillations in the PV diagram along the filaments may be related to the kinematics of core formation and to the physical oscillations present in the filaments (e.g., Liu et al., 2019, see Figure 7 therein).

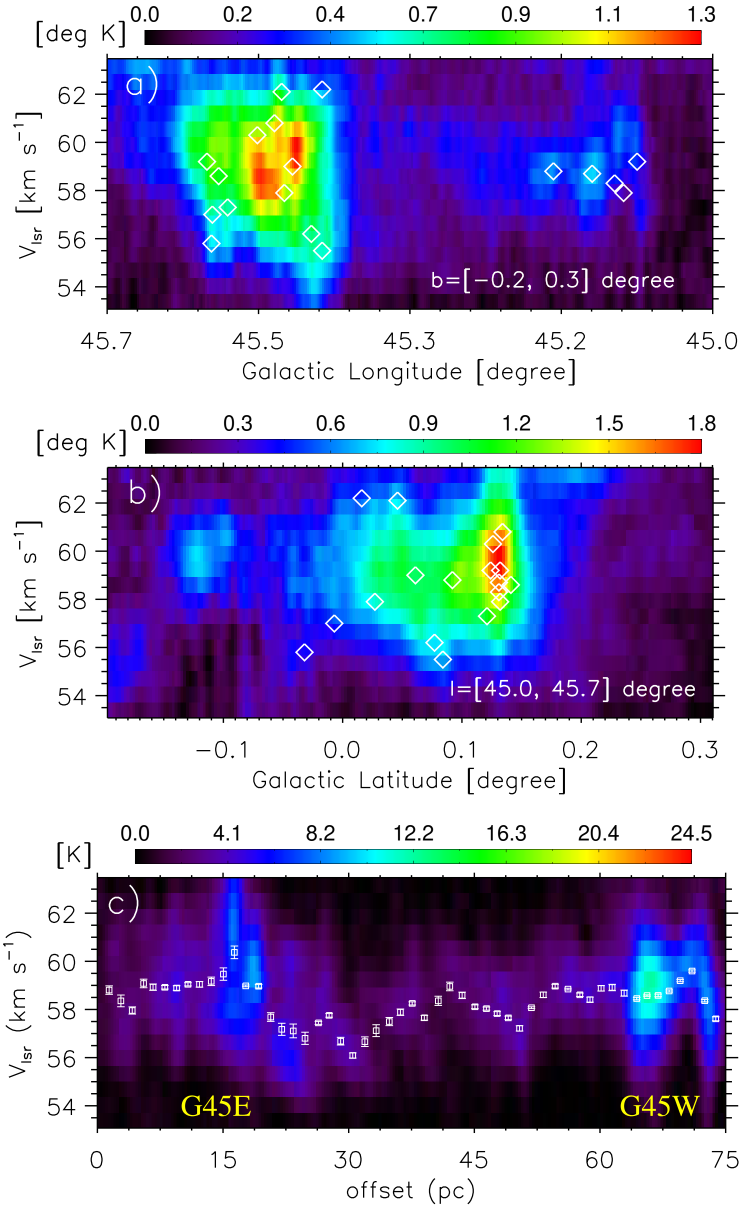

Figure 5.6: Position-velocity (PV) diagrams of ^{13}CO(1–0) emission: (a) Longitude-velocity diagram, (b) Latitude-velocity diagram, toward an area displayed in Figure 5.5. The diamond symbols represent the positions of ATLASGAL clumps from Urquhart et al. (2018) (see also Figure 5.1). (c) The PV diagram along a dashed curve marked in Figure 5.4a, where zero point in the x-axis corresponds to the eastern end of the curve. The data points with error bars are the velocity averaged points at their respective position (see text for more details).

In order to compare the velocity oscillations with the column density enhancements in the observed molecular cloud, we have generated a column density profile along a path indicated by a dashed (red) curve in Figure 5.4a. The resulting column density profile is shown in Figure 5.7c, where the x-axis zero point corresponds to the eastern end of the path. To obtain the column density map, we utilized *Herschel* multiwavelength images at 160–500 μm and applied a procedure described in Section 2.3.3. Both the ^{13}CO(1–0) molecular line data and the *Herschel* column density map were convolved to a common spatial resolution of 38$''$ using the `imsmooth` task in `CASA`. In Figure 5.7, vertical dashed lines are marked across all the plots, indicating the positions of local column density peaks. Upon comparing the velocity and column density plots (Figures 5.7a and 5.7c), it is observed that the velocity peaks are shifted relative to the column density peaks in the direction of G45E. However, this shift is not apparent in other parts of the filaments. The implications of these findings are further discussed in Section 5.4.1.

5.3.2 Physical properties of the cloud associated with G45E and G45W

To derive the mass of the filamentary cloud at [53, 63] km s^{-1}, we have employed the ^{13}CO(1–0) line emission. We have used the Equations given in Section 2.3.3.3 to estimate the ^{13}CO(1–0) column density ($N(^{13}\mathrm{CO})$). Figure 5.8a presents the excitation temperature (T_{ex}) map of ^{12}CO(1–0) emission. The estimated mean excitation temperature is about 8.7 K.

The optical depth map of ^{13}CO(1–0) is shown in Figure 5.8b. We found that the optical depth ranges from $\sim$0.1 to 1, suggesting the optically thin nature of the ^{13}CO emission toward the entire filamentary cloud. By applying Equations 2.11, 2.12, and 2.13, we have obtained an average value of $N(^{13}\mathrm{CO})$ around 2.04×10^{16} cm^{-2}. This corresponds to a mean H$_2$ column density ($N(\mathrm{H_2})$) of approximately 1.43×10^{22} cm^{-2}, considering a column density conversion factor of $N(\mathrm{H_2})/N(^{13}\mathrm{CO}) \simeq 7\times10^5$ as determined by Frerking et al. (1982). To derive the $N(\mathrm{H_2})$ map shown in Figure 5.8c, we incorporated the minimum $N(^{13}\mathrm{CO})$ emission value of 8×10^{15} cm^{-2} and considered the emission within the filamentary cloud. Here, we also note that the $N(\mathrm{H_2})$ maps derived from the *Herschel* continuum images and the molecular line data are consistent with each other. The mass of the filamentary cloud is calculated using Equation 2.14, considering a

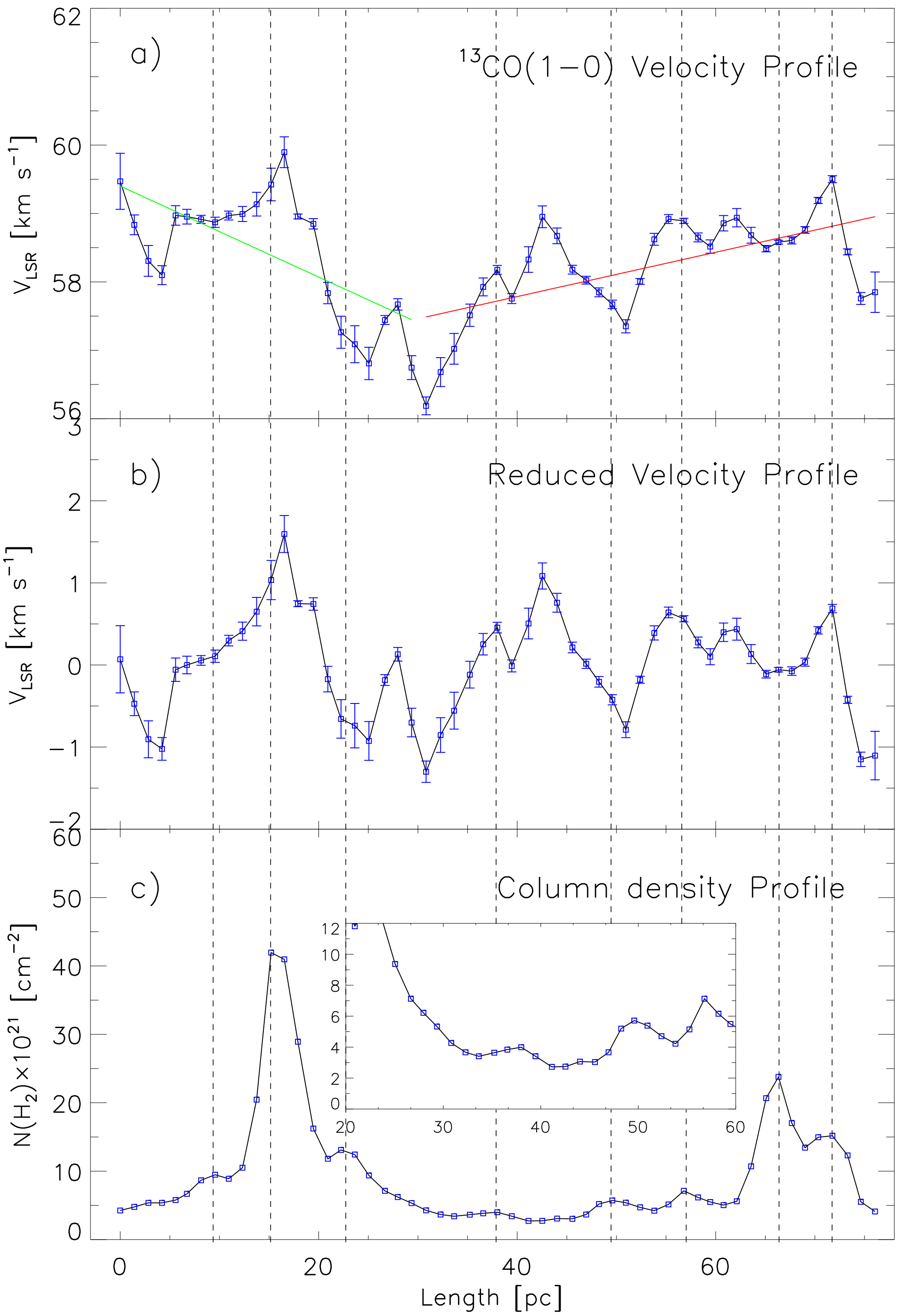

Figure 5.7: (a) Position-velocity profile of ^{13}CO(1–0) emission, similar to that shown in Figure 5.6c. The green and red lines indicate the velocity gradient of −0.064 km s^{-1} pc^{-1} and +0.032 km s^{-1} pc^{-1}, respectively. (b) Residual velocity profile after removing the velocity gradients shown in panel (a). (c) Column density profile. The inset shows a similar column density profile in the length range of 20 to 60 pc.

mean molecular weight of 2.8 and a distance of 8 kpc. The total estimated mass of the cloud is $\sim 1.1 \times 10^6$ M$_\odot$.

It is important to acknowledge that there are uncertainties associated with

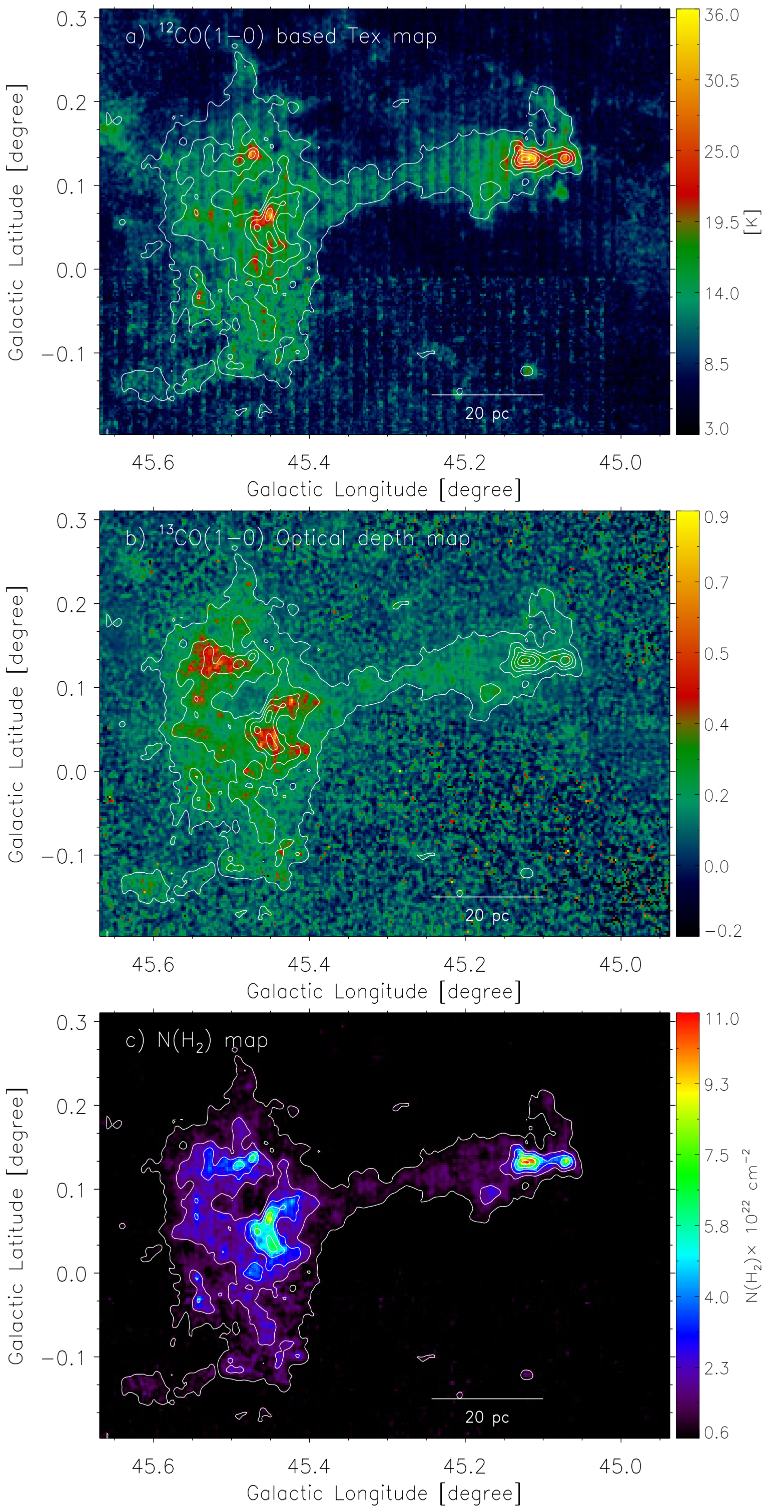

Figure 5.8: (a) The excitation temperature map derived from ^{12}CO(1–0) emission in the velocity range of [53, 63] km s^{-1}. (b) ^{13}CO(1–0) optical depth map. (c) H_2 column density map. In all the panels, the contours represent ^{13}CO(1–0) integrated emission ranging from 8 to 60 K km s^{-1} in steps of 10.4 K km s^{-1}.

the column density and mass calculations. These uncertainties primarily arise from factors such as the choice of the $N(\mathrm{H_2})/N(^{13}\mathrm{CO})$ conversion factor, distance estimation, and observational random errors, which can contribute to a 30-50% uncertainty range. The length of the filamentary cloud is estimated to be ~75 pc, measured along its major axis (as indicated by the dashed (red) curve in Figure 5.4a). Based on this measurement, the observed line mass of the cloud is calculated to be $\sim 1.5\times10^4$ $M_\odot$/pc. It is important to consider the "cos i" factor in the calculation of the line mass, where "i" represents the angle between the sky plane and the major axis of the filament. In our calculations, we assume i=0, indicating that the filament is in the sky plane. Therefore, the derived line mass represents an upper limit. In addition to the uncertainty in "i", the line mass is mainly influenced by the uncertainty in distance estimation, which is approximately 20-30% (as discussed in Section 8.1).

To assess the gravitational instability of the filamentary cloud, one can compare the observed line mass with the virial line mass. The virial line mass contains the effect of gas turbulence helping the filament to resist the collapse due to gravity. Following the Equation 2 of Dewangan et al. (2019b), the virial line mass of the entire cloud is found to be $\sim 4.5\times10^3$ $M_\odot$/pc. In the virial line mass calculation, we considered the expression of non-thermal velocity dispersion ($\sigma_{\rm NT}$) as defined in the Equation 3 of Bhadari et al. (2020), where the observed linewidth (ΔV) of ^{13}CO(1–0) spectra is used as 6.8 km s^{-1}, and the gas kinetic temperature (T_K) of 18 K. The ΔV and T_K values are obtained from the Gaussian fitting of averaged ^{13}CO(1–0) spectra and the dust temperature map for the entire cloud region, respectively. We have also calculated the line mass parameters of the central region (size $\sim 0^\circ.29 \times 0^\circ.056$; position angle = 13°; $l = 45^\circ.29$, $b = 0^\circ.109$) of the cloud. Concerning to the central region, the observed line mass and the virial line mass are estimated to be $\frac{3.24\ \times\ 10^4\ M_\odot}{40\ \rm pc}$ $\simeq$800 $M_\odot$/pc and $\sim 3.5\times10^3$ $M_\odot$/pc, respectively. Here, the calcuation uses T_K = 18 K and ΔV = 6 km s^{-1}. We note that the uncertainties in these analyses may be relatively high ($\geq$50%) due to distance uncertainty, an unknown inclination of the filament, and the derived ΔV and T_K values. The non-thermal velocity dispersion derived from ΔV could be overestimated due to the optical depth effect and multicomponent structure of the ^{13}CO(1–0) line. The implications of these results are discussed in Section 5.4.1.

5.3.3 Identification and Distribution of YSOs

We obtained the photometric magnitudes of point-like objects at 3.6, 4.5, and 5.8 μm wavelengths from the *Spitzer* GLIMPSE-I Spring' 07 highly reliable catalog. In this selection, we considered only objects with a photometric error of less than 0.2 mag in the selected *Spitzer* bands.

Figure 5.9a shows the color-color plot ([4.5]–[5.8] vs. [3.6]–[4.5]) of point-like objects toward our line of sight. We followed the IR color conditions of [4.5]–[5.8] $\geq$ 0.7 mag and [3.6]–[4.5] $\geq$ 0.7 mag from previous works of Hartmann et al. (2005) and Getman et al. (2007), and this selection provided us a sample of Class I YSOs in the extended physical system. A total of 55 Class I YSOs are identified using this scheme, which are shown by open red circles in Figure 5.9a.

In our analysis, we have also made use of photometric data from *Spitzer* at 3.6 and 24 μm to classify the YSOs into different categories. Following the methodology introduced by Guieu et al. (2010), we have employed a color-magnitude plot of [3.6] versus [3.6]–[24] to distinguish between various classes of YSOs and identify potential contaminant sources such as galaxies and diskless stars. Based on this classification scheme, we have identified a total of 87 YSOs, which include 29 Class I sources, 25 Flat spectrum sources, and 33 Class II sources. These YSOs are represented by red circles for Class I, green diamonds for Flat spectrum, and blue triangles for Class II in the color-magnitude plot shown in Figure 5.9b.

Additional color excess sources are also obtained from the color-magnitude diagram of K vs. $H-K$ (see Figure 5.9c). A large number of 1486 color excess sources (marked by green dots) are identified following the color cutoff condition of $H-K > 1.65$. This condition is decided based upon the upper limit of $H-K$ detection of main sequence stars in the nearby control field. Altogether, after taking account of the common sources identified from different schemes, a total of 1628 YSO candidate sources are identified toward our selected target area. The positions of all the YSOs are presented in Figure 5.10a.

We have also performed the surface density analysis of all the selected YSO

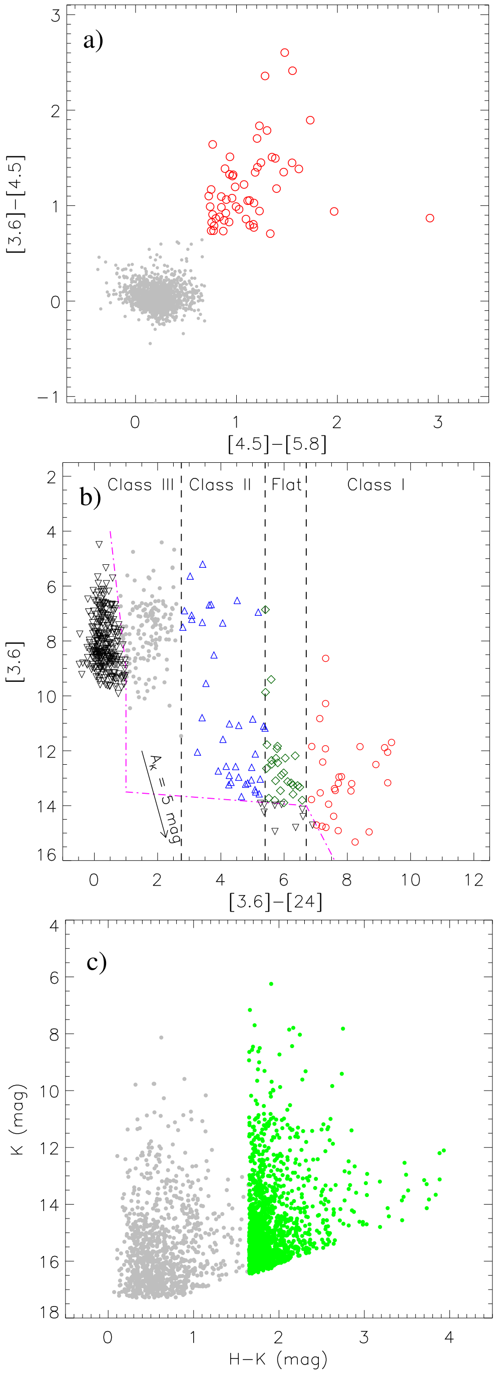

Figure 5.9: (a) Color-color plot ([3.6]–[4.5] vs. [4.5]–[5.8]) of point-like sources in the direction of G045.49+00.04 and G045.14+00.14. (b) Color–magnitude plot ([3.6] vs. [3.6]–[24]) of the sources. The plot enables to identify YSOs belonging to different evolutionary stages (see dashed lines). The boundary of YSOs against contaminated candidates (galaxies and disk-less stars) is shown by dotted-dashed lines (in magenta). (c) Color–magnitude (K vs. H–K) diagram of point-like sources. The YSO candidate sources are shown by green dots. In panels "(a)" and "(b)", the Class I sources are marked by red circles. In all the panels, sources with photospheric emission are shown by dots (in gray), which are randomly drawn from a large sample of our survey catalog.

candidates using the nearest neighbour (NN) method (e.g., Gutermuth et al., 2009, see Section 2.6.1 for an overview). To generate the surface density map, we

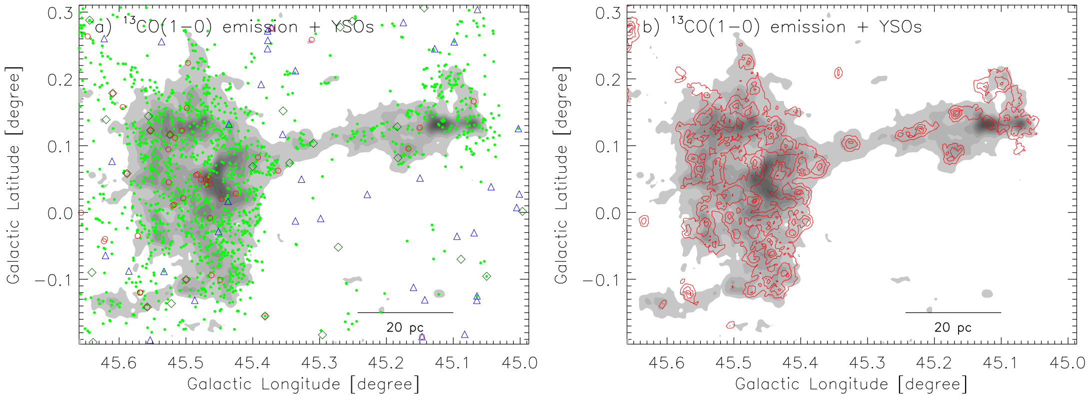

Figure 5.10: (a) The spatial distribution of YSOs (from Figure 5.9) overlaid on the ^{13}CO(1–0) moment-0 map (see Figure 5.4a). The symbols are same as discussed in Figure 5.9. (b) Overlay of the YSO surface density contours (in red) on the ^{13}CO(1–0) emission map. The contour values are 0.6, 1.1, 2, 3 YSOs pc^{-2}.

considered a grid size of 15″ and the 6 NN YSOs at the distance of 8 kpc (see formalism in Casertano & Hut, 1985). Figure 5.10b presents the overlay of surface density contours (in red) on the ^{13}CO(1–0) moment-0 map. The surface density distribution is primarily concentrated at the positions of G45E and G45W.

5.3.4 Structure of the dense gas and hub-filament systems

We have utilized the ^{13}CO(3–2) line data to investigate the morphology and kinematics of dense gas in the G45W region. The velocity channel maps of ^{13}CO(3–2) emission are displayed in Figure 5.11. Overlaid on the maps are the contours representing the velocity-averaged emission at each 1 km interval, which are derived from the ^{13}CO(1–0) moment-0 map. Through this analysis, we are able to identify elongated and filamentary structures in the dense gas, particularly in the velocity range from 55.59 km s^{-1} to 61.59 km s^{-1}. These elongated gas structures extend towards the positions of the two IRAS sources, IRAS 19110+1045 and IRAS 19111+1048. The last two panels of the channel maps present the moment-0 and moment-1 maps of the ^{13}CO(3–2) emission, respectively, which are obtained for the velocity range specified in the channel maps ([52.59, 64.59] km s^{-1}). The moment maps provide further evidence of the elongated structures and reveal the presence of a velocity gradient along them, indicating coherent motion in the gas.

Based on the visual inspection of Figure 5.2a, we have identified possible fil-

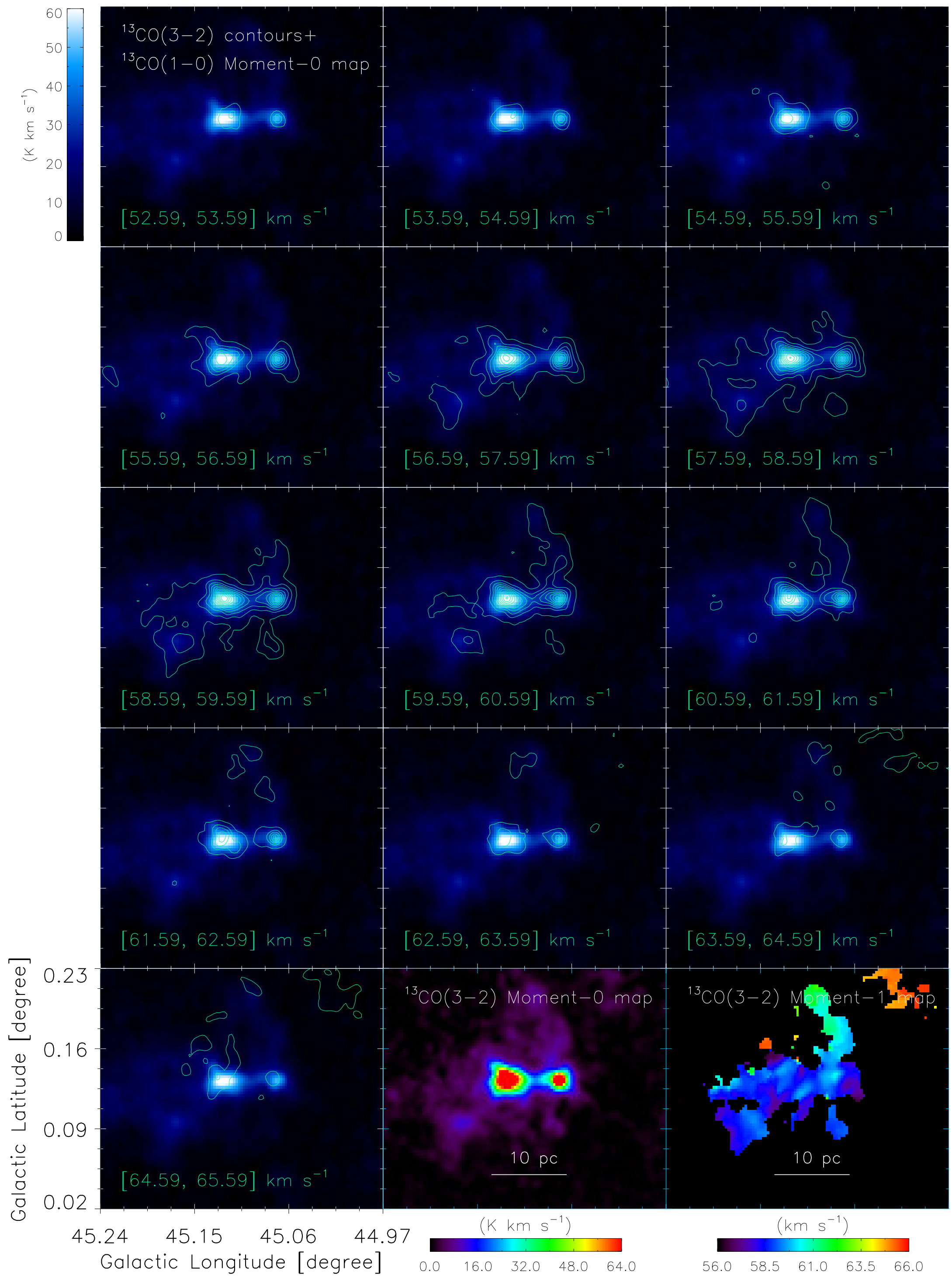

Figure 5.11: Velocity channel maps of ^{13}CO(3–2) emission (green contours) in the direction of G045.14+00.14 (i.e., G45W) region. The contour levels range from 1.2 to 26 K km s^{-1} in steps of 2.48 K km s^{-1}. The background image is ^{13}CO(1–0) moment-0 map obtained in the velocity range of [53, 63] km s^{-1}, and the color bar is shown at the top left corner. The last two panels display the moment-0 and moment-1 maps of ^{13}CO(3–2) emission with their respective color bars. The velocities are labeled in each panel.

amentary structures (subfilaments) in our target site. To further analyze and extract these structures, we have employed *getsf*, which is designed for the extraction of sources and filaments in astronomical images (Men'Shchikov, 2021, see also Section 2.4).

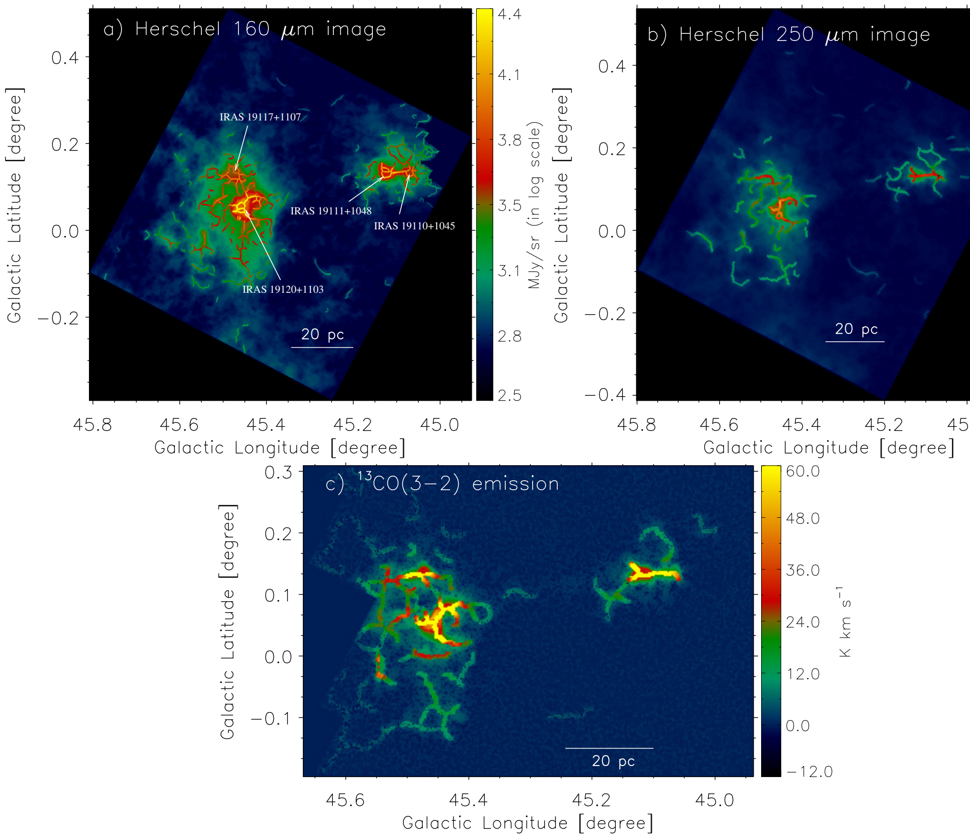

Figure 5.12: Overlay of the *getsf* identified filament skeletons on the *Herschel* continuum images at (a) 160 μm and (b) 250 μm, and on the (c) CHIMPS ^{13}CO(3–2) moment-0 map (see text for more details). The positions of the IRAS sources are marked by arrows in panel (a).

Figure 5.12 presents the *getsf* identified filament skeletons in our target site. We have used the *Herschel* continuum images at 160 μm and 250 μm to identify the subfilaments. Figure 5.12a shows the *Herschel* 160 μm filament skeletons identified on the image scales of 12″-543″. Figure 5.12b displays the *Herschel* 250 μm filament skeletons identified on the scales of 18″-576″. In order to trace the genuine subfilaments in a star-forming site, one should also look for filaments in molecular line emission apart from the continuum maps. The *getsf* procedure is also applied to the CHIMPS ^{13}CO(3–2) moment-0 map (V$_{\rm LSR}$ ~53–66 km s^{-1}, $\theta_{\rm spatial}$=15″). In Figure 5.12c, the *getsf* identified filaments on the scales of 15″-679″ are highlighted on the CHIMPS ^{13}CO(3–2) moment-0 map. In the whole exercise, the input parameter of maximum width (FWHM, in arcsec) of filaments to be extracted was used as 260″, 420″, and 400″ for the *Herschel* 160 μm, the *Herschel* 250 μm, and the CHIMPS ^{13}CO(3–2) emission maps, respectively.

From the comparison of the maps displayed in Figure 5.12, we observe that the filamentary structures in the direction of dense regions (i.e., high intensity regions), are consistent with the structures seen in the continuum and molecular emission maps. This consistency confirms the presence of potential subfilaments in our target sites. An intriguing observation is that the structures of the subfilaments in sites G45E and G45W exhibit similarities to the characteristics of HFSs, as discussed in Section 1.3.3. The hub-filament configurations are clearly evident in both complexes (i.e., toward G45E and G45W), which are primarily associated with the previously known massive star-forming sites (i.e., IRAS sources; see Figure 5.12a). These findings provide valuable insights into the presence and nature of HFSs in our target sites, and their implications are further discussed in Section 5.4.2.

5.4 Discussion

5.4.1 End dominated collapse in a giant molecular filament GMF G45.3+0.1

In Section 5.3.1, we have investigated that the sites G45E and G45W are part of a filamentary cloud (see also Section 8.1), and are located at the ends of it. Based on the physical length of 75 pc and the derived mass of $\sim$1.1$\times$10^6 M$_\odot$ (see Section 5.3.2), the cloud can be considered as a giant molecular cloud (GMC; Solomon et al., 1987). Hence, considering the position in the Galactic system, we named this filamentary cloud as a giant molecular filament, GMF G45.3+0.1. However, previously the eastern part of GMF G45.3+0.1 (i.e., G45E) was itself considered to be a large filament and cataloged as “F39” by Wang et al. (2016, see Figure 6 therein). Zhang et al. (2019) further included the western part of GMF G45.3+0.1 (i.e., G45W) and cataloged the entire filament as “GMF 37”. The clear definition of a GMF is not available in the literature. However, according to Zhang et al. (2019), one must see a clear elongation in the cloud over some column-density regime, and the cloud should show coherence in the PPV space. The GMFs have lengths of the order of ∼100 pc and masses of $\sim 10^3$-10^6 $M_\odot$ (e.g., Li et al., 2013b; Ragan et al., 2014; Su et al., 2015; Abreu-Vicente et al., 2016b; Zhang et al., 2019). Adopting a typical cloud width range of ∼8–10 pc, which can vary along the major axis of the cloud because of its evolution in terms of structure, shaped by the feedback from embedded stars (e.g., McKee & Ostriker, 2007), the GMF G45.3+0.1, always have a high aspect ratio (A∼7–10). Such high aspect ratio (A>5) filaments are considered to collapse at the edges due to the gravitational instability induced by the high gas acceleration (Bastien, 1983; Pon et al., 2012; Clarke & Whitworth, 2015; Hoemann et al., 2022).

Till now, very few observational examples of filaments showing end-dominated collapse are available in the literature, which include NGC 6334 (Zernickel et al., 2013), IRDC 18223 (Beuther et al., 2015), Musca cloud (Kainulainen et al., 2016), S242 (Dewangan et al., 2017b, 2019b), G341.244−00.265 (Yu et al., 2019), and Monoceros R1 (Bhadari et al., 2020). The key features of such physical process include at least one of the following possibilities i.e., the existence of high column density clumps, star clusters, and H II regions at one or both the filament ends. Such filaments should ideally be observed as isolated clouds in 3D or PPP space. However, these filaments are generally identified as coherent velocity clouds in the PPV space. Theoretically, there is no restriction on the filament's parameter (i.e., length or radius) for it to collapse by the end-dominated process; instead, the global collapse of filament (specifically, the collapse timescale) is dependent on the aspect ratio (e.g., Toalá et al., 2012; Pon et al., 2012; Clarke & Whitworth, 2015). In Section 5.3.2, we found that the observed line mass of GMF G45.3+0.1 is larger than the virial line mass, suggesting that it is gravitationally unstable and prone to collapse. However, the central region of GMF G45.3+0.1, where the star formation activity is not dominated, shows the opposite nature. Previously, Dewangan et al. (2019b) also found that the central region of S242 filament shows higher virial mass compared to the observed line mass. This suggests that the cloud is self-gravitating and gravitational unstable at the edges compared to the central areas.

Based on our observational outcomes, we argue that the global collapse of GMF G45.3+0.1 is predominately end-dominated in nature. This argument is supported by the fact that the sites G45E and G45W are observed at the ends of GMF G45.3+0.1, where a large number of YSO clusterings and the presence of HII regions are also observed. The major column density peaks are also seen at the ends of GMF G45.3+0.1 (Figure 5.7c). We also note that the complex G45E is more extended than the G45W. It is probably possible because of the rapid structural evolution of G45E from the feedback of embedded stars. The fragmentation of GMF G45.3+0.1 appears to proceed in a hierarchy (i.e., into subfilaments) as seen in the dense gas site G45W. In the direction of complex G45W, the ATLASGAL map at 870 μm shows the presence of a filamentary structure (length $\sim$12 pc; see Figure 5.2c) connecting the two massive star-forming sites, IRAS 19110+1045 and IRAS 19111+1048. This subfilament is found to be denser than the parent filament, as it is traced in the relatively dense gas tracers of ^{13}CO/C^{18}O(3–2) emission (see Figures 5.4b, 5.11), thus indicating the hierarchical fragmentation of GMF G45.3+0.1. Some previous observational (e.g., Hacar et al., 2013; Tafalla & Hacar, 2015; Hacar et al., 2018) and theoretical (e.g., Smith et al., 2016; Clarke et al., 2017, 2020) works also favor the hierarchical fragmentation of filaments. These results significantly deviate from previous models of filament fragmentation which favour the formation of quasi-periodically spaced cores along filaments (e.g., Inutsuka & Miyama, 1992, 1997; Fischera & Martin, 2012). Clarke et al. (2020) argue that the hierarchical fragmentation of filaments diminishes the signature of characteristic fragmentation length-scale (related to the quasi-periodically spaced cores), and the cores are formed by the fragmentation of subfilaments rather than the main filament itself. We observed oscillations in the mean velocity profile along the long axis of GMF G45.3+0.1 (see Figures 5.6c and 5.7), which hints the signature of core formation (e.g., Beuther et al., 2015; Kainulainen et al., 2016) together with the possibility of large scale physical oscillations in the filament (Liu et al., 2019). However, based on the comparison of velocity and column density plots (Figure 5.7), we observed that the column density and velocity peaks toward G45E are shifted with respect to each other. This could be an indication of the presence of gravitationally bound cores (e.g., Hacar & Tafalla, 2011, see Figure 12 therein). Some of the other column density peaks along filament do not significantly correlate to the velocity oscillations, suggesting that the cores are not gravitationally bound.

We have observed linear gradients in the velocity profile along the long axis of GMF G45.3+0.1. At the eastern end of the filament (toward G45E), the linear gradient is negative and twice in magnitude to that of the positive gradient toward the western end. The origin of these adverse gradients at the filament's edges can probably be explained by the presence of sites G45E and G45W itself, where the feedback from massive stars in these sites appears to shape the cloud in terms of structure and kinematics.

5.4.2 Hub-filament systems and star formation scenario

The current understanding of star formation suggests that complex filaments initially form within molecular clouds, and subsequently undergo fragmentation processes leading to the formation of dense clumps/cores and eventually stellar clusters. This process is well-documented in the literature (e.g., Chen et al., 2020a; Abe et al., 2021; Hacar et al., 2013, and references therein). However, the formation of massive stars remains a challenging and enigmatic topic of research (e.g., Motte et al., 2018, and references therein). The mechanisms and conditions necessary for the formation of these massive stars are still not fully understood. In this context, the presence of a sufficient mass reservoir becomes crucial for the formation of massive stars. Filaments provide an ideal physical environment that can serve as such mass reservoirs, facilitating the accumulation of material necessary for the formation of massive stars. In this context, the necessity of the mass reservoir becomes vital for the formation of massive stars, which can be fulfilled in the physical environment of filaments.

In Section 5.4.2, we observed that the star-forming complexes G45E and G45W exhibit the characteristic morphology of parsec-scale HFSs. These HFSs are primarily observed in the vicinity of massive star-forming regions, such as the IRAS sources (i.e., IRAS sources; see Figures 5.2 and 5.12). The filaments associated with these complexes have lengths on the order of 5–10 pc. Notably, these filaments display a converging network pattern towards the hubs, where they either directly connect to the hubs or merge with other longer spines that approach the hubs. This configuration suggests the presence of a hierarchical structure in the filamentary network. The occurrence of edge-collapse processes and the presence of HFSs in the GMF G45.3+0.1 raise intriguing questions and offer new possibilities for understanding MSF and the formation of HFSs. These findings contribute to the ongoing MSF research (e.g., Motte et al., 2018; Wang et al., 2019a, and references therein). Further investigations into these phenomena will shed light on the underlying physical processes driving MSF and the formation of HFSs.

The EDC process can well explain the formation of star-forming sites G45E and G45W. However, the presence of HFSs in these sites itself hints the onset of global nonisotropic collapse (GNIC; Tigé et al., 2017; Motte et al., 2018; Treviño-Morales et al., 2019b). GNIC scenario supports the mass accretion onto the dense core from the large scale structures. In this paradigm, a density-enhanced hub hosts MDCs (size$\sim$0.1 pc), which in their starless phase harbor low-mass prestellar cores. Later, MDCs become protostellar, hosting only low-mass stellar embryos, which grow into high-mass protostars from gravitationally-driven inflows (see more details in Motte et al., 2018). Observational studies of HFSs report that the longitudinal flow rate along filaments is around 10^{-4}–10^{-3} $M_\odot$ yr^{-1} (e.g., Kirk et al., 2013; Chen et al., 2019; Treviño-Morales et al., 2019b) which is a close value to the sufficient inflow rate for MSF (e.g., Haemmerlé et al., 2016, and references therein). Hence, it is now believed that all massive stars favour forming in the density-enhanced hubs of HFSs (e.g., Motte et al., 2018; Anderson et al., 2021, and references therein). It has also been thought that the onset of collision process (see the review article by Fukui et al., 2021a, and references therein) can produce hubs with large networks of filaments. The filamentary structures, reminiscent of the HFSs are quite evident in the smoothed particle hydrodynamics simulations of two colliding clouds (Balfour et al., 2015). In this case, the shock-compressed layer is found to fragment into filaments. Furthermore, the pattern of filaments appears to have the morphology of HFSs, spider's web, and spokes system (Balfour et al., 2015).

Recent research by Clarke et al. (2020) has indicated that filaments have a tendency to fragment into subfilaments, which in turn contribute to the formation of hubs through their merging process. Additionally, cores formed at the edges of filaments tend to be more massive compared to those in the interior (Clarke et al., 2020). Based on these theoretical findings and the observational results from our study of GMF G45.3+0.1, we propose that the star formation activity in G45E and G45W is predominantly driven by the combined effects of EDC and HFSs. It is possible that the HFSs observed in the giant molecular filament are formed through the collision and merging of subfilaments, as well as the fragmentation of shock-compressed layers at the collision sites. It is noteworthy that the HFSs are preferentially located at the edges of GMF G45.3+0.1, where the EDC process is expected to generate massive end clumps. However, it is important to note that our observations are limited by the resolution of the available data, which becomes more challenging due to the large distance to our target site (8 kpc for GMF G45.3+0.1). The interpretation and understanding of these processes would benefit from higher-resolution observations in the future.

Thus, our observational outcomes reveal GMF G45.3+0.1 as an observational sample of filament, identified so far in the interstellar medium, where the edge collapse and the hub-filament configurations are simultaneously seen. Our observational results are more or less consistent with the outcomes from the numerical fragmentation study on filaments by Clarke et al. (2020). Such a study also helps us to understand the formation of HFSs and MSF.

5.5 Summary and Conclusions

This work is aimed to get new insights into the physical processes operating in the sites G45E and G45W, which are part of a large cloud complex in the Aquila constellation (l=45^o, b=0^o). We have performed the analysis of multiwavelength and multiscale data-sets toward an area (0°.67×0°.50) enclosing our target sites. The major outcomes from our observational study can be summarized as follows:

1. The analysis of ^{13}CO(1–0) line data reveals the presence of a filamentary cloud (length ∼75 pc) in the velocity range of ∼53–63 km s^{-1} having the mean velocity and standard deviation of 58.30±0.03 km s^{-1} and 2.34±0.03 km s^{-1}, respectively.

2. Using ^{13}CO(1–0) emission maps, the cloud mass is derived to be ∼1.1×10^6 M$_\odot$, which further results in the line mass of ∼1.5×10^4 M$_\odot$/pc. Our study thus uncovers a new giant molecular filament, which we named GMF G45.3+0.1.

3. The sites G45E and G45W are observed at the opposite ends of GMF G45.3+0.1. The clustering of YSOs is primarily focused at both ends of the filament, where the presence of HII regions and previously known massive star-forming sites are also observed.

4. The PV diagram along the major axis of GMF G45.3+0.1 shows the velocity oscillations, which could be originated by the combined effect of fragment/core formation and the physical oscillation in the filament. The velocity gradient at both ends of the filament is found to be opposite in sign, i.e., −0.064 km s^{-1} pc^{-1} toward G45E and +0.032 km s^{-1} pc^{-1} in the direction of G45W.

5. The sites IRAS 19110+1045 and IRAS 19111+1048, located in G45W, are primarily observed to be a part of ∼12 pc long dense subfilament. This presents strong evidence of hierarchical fragmentation of GMF G45.3+0.1.

6. The analysis of the dust continuum and molecular line data suggests that both the complexes (G45E and G45W) are associated with the HFSs, where several parsec scale filaments (∼5–10 pc) appear to converge toward dense regions (i.e., hubs). These hubs are identified in the direction of mas-

sive star-forming sites (i.e., IRAS 19120+1103, IRAS 19117+1107, IRAS 19110+1045, and IRAS 19111+1048).

Overall, our observational results suggest that the star-forming complexes in the GMF G45.3+0.1 are formed through the edge collapse scenario and the mass accumulation is evident in each hub through the gas flows along filaments.

Chapter 6

IC 5146 dark Streamer: is a first reliable candidate of edge collapse, hub-filament systems, and intertwined sub-filaments?[†]

6.1 Introduction

Studies of star-forming regions (SFRs) have consistently shown that dust and molecular filaments play a crucial role in various star formation processes. In the previous chapter (Chapter 5), we highlighted the simultaneous occurrence of the EDC process and mass accretion through subfilaments in the hub of a HFS hosting massive star-forming regions. It is exclusively found that the HFSs are favourable at the edges of a filament. While such sites are rare, a few potential locations where these signatures may be observed include NGC 6334 and IC 5146 dark Streamer. NGC 6334 has been extensively studied (e.g., Zernickel et al., 2013; Tigé et al., 2017; Shimajiri et al., 2019a; Li et al., 2020; Arzoumanian et al., 2021; Li et al., 2022a) and appears to be in an evolved state of EDC. On the other hand,

[†]Dewangan, L. K., **Bhadari, N. K.**, Men'shchikov, A., Chung, E. J., Devaraj, R., Lee, C. W., Maity, A. K., Baug, T., 2023, ApJ, 946, 22D, "IC 5146 Dark Streamer: The First Reliable Candidate of Edge Collapse, Hub-filament Systems, and Intertwined Sub-filaments"

IC 5146 dark Streamer, which is a nearby site (d ~600 pc), offers potential insights into other physical processes due to its proximity. It is important to consider that filaments hosting massive star-forming regions are often on the scale of $\gtrsim$10 pc. In addition to the longitudinal gas motion assumed in the EDC process, there may also be radial gas motion. However, theoretical insights on the cloud-scale dynamics involving both radial and longitudinal collapse are currently lacking in the literature and require further investigation. Therefore, it is strongly suggested that a range of star formation processes occurs within a single filamentary cloud, and understanding their connection is crucial. Further research is needed to explore and unravel the complexities of these processes within filaments hosting massive star-forming regions.

In addition to these two highlighted configurations (i.e., EDC and HFSs), observational evidences for the twisting/coupling of filaments (or intertwined filaments) have also been reported in only a couple of star-forming regions (e.g., NGC 6334 filament (Shimajiri et al., 2019a), Lynds Bright Nebulae (Dewangan et al., 2021)). However, the simultaneous signature of the HFSs, EDC, and twisted/intertwined filaments in a single SFR is not yet observed. At present, we do not know if there exists any connection/association between these three observational configurations of filaments (i.e., HFSs, EDC, and twisted nature), which is essential to understand the formation of YSOs and massive stars. In this context, the target of this work is the IC 5146 dark Streamer, which is a nearby promising site (d ~600 pc) to search for different observational configurations of filaments.

This work focuses on the IC 5146 dark Streamer/Northern Streamer/filamentary structure, which is one of the densest molecular clouds in IC 5146 (Herbig & Reipurth, 2008; Roy et al., 2011; Arzoumanian et al., 2013; Chung et al., 2021). The Cocoon Nebula and the Northern Streamer have been reported as the two main components of IC 5146 in the constellation Cygnus. Using the near-infrared (NIR) data, an extinction map of IC 5146 was produced by Lada et al. (1994). Embedded dust clumps, filaments, and signposts of star formation activities (i.e., YSOs and outflows) have been reported toward the

Cocoon Nebula and the Northern Streamer (Herbig & Reipurth, 2008; Harvey et al., 2008; Arzoumanian et al., 2011, 2019; Johnstone et al., 2017; Zhang et al., 2020). Chung et al. (2021) explored several molecular lines (i.e., ^{13}CO, $C^{18}O$, N_2H^+, HCO^+, CS, SO, NH_2D, and $H^{13}CO^+$) toward IC 5146 using the Taeduk Radio Astronomy Observatory (TRAO) 14-m telescope, and examined filaments and dense cores in IC 5146 (see also Dobashi et al., 1993; Lada et al., 1994). The clouds associated with the Cocoon Nebula and the Streamer were traced in velocity ranges of [6, 9] and [1, 7] km s^{-1}, respectively (Chung et al., 2021). Using the *Gaia* measurements, Wang et al. (2019a) reported distance estimations of 800±100 pc and 600±100 pc for the Cocoon and the Streamer, respectively. Based on the earlier reported works, the Cocoon Nebula and the Northern Streamer can be treated as two distinct sources (e.g., Chung et al., 2021).

Dust continuum maps revealed a long filamentary morphology of the IC 5146 dark Streamer (Kramer et al., 2003), and two prominent HFSs were investigated toward the eastern and the western parts (i.e., E-HFS and W-HFS) of the Streamer (e.g., Arzoumanian et al., 2011, 2019; Roy et al., 2011; Johnstone et al., 2017; Wang et al., 2017, 2019b,a; Chung et al., 2021, 2022). Several polarimetry studies were conducted toward the IC 5146 dark Streamer (Wang et al., 2017, 2019b,a; Chung et al., 2022), which allowed them to explore magnetic field structures. These earlier works showed the presence of uniform magnetic field vectors perpendicular to the dark Streamer. In general, recent *Planck* observations (Ade et al., 2016a) showed that the low column density filaments (striations; $N_{\rm H} < 10^{21.7}$ cm^{-2}) are parallel to the Galactic magnetic field whereas the magnetic field is perpendicular to the filaments with higher column density ($N_{\rm H} > 10^{21.7}$ cm^{-2}). These observations are consistent with the theoretical outcomes saying that the magnetic field supports the filaments against collapsing into its longer axis and guides the gravity-driven gas contraction (e.g., Nakamura & Li, 2008; Inutsuka et al., 2015). A curved magnetic field morphology was investigated toward both ends of IC 5146 (Wang et al., 2019b; Chung et al., 2022), and was proposed as an indication of the EDC process in long filaments. However, such signature is not yet assessed in potential and nearby EDC filaments.

Chung et al. (2021) found the supersonic nature of the E-HFS and W-HFS in IC 5146, and suggested a collision process of turbulent converging flows to explain the observed HFSs. Based on the positions of the observed HFSs at the long filament, the scenarios – EDC and accretion flows – were proposed in the Streamer (see Figure 9 in Chung et al., 2022). However, a careful and thorough investigation of the collision process is yet to be done. Furthermore, despite its proximity, the structures in the target site IC 5146 streamer have not been fully investigated. Several other nearby sites unveil the presence of multiple sub-filaments, cores as well (e.g., Hacar et al., 2013, 2018). In order to probe various physical processes operational in the Streamer, we have carefully examined the dust continuum maps from the HGBS project (e.g., André et al., 2010; Arzoumanian et al., 2011, 2019), and the velocity structures using the published TRAO ^{13}CO and C^{18}O line data. We have also employed the *hires* algorithm (Men'Shchikov, 2021) to produce high-resolution column density and temperature maps (resolution $\sim$13$''$.5).

Various observational data sets used in this work are presented in §6.2. The derived observational findings are reported in §6.3. §6.4 deals with a discussion of our observed outcomes. Finally, §6.5 presents a summary of the major findings of this study.

6.2 Data Sets and Analysis

In this work, we selected an area of $\sim$0°.746 × 0°.464 (central coordinates: l = 93°.659; b = −4°.419) around the IC 5146 dark Streamer. The positions of YSOs (i.e., Class I, Flat-spectrum, and Class II) were collected from Harvey et al. (2008). The published TRAO ^{13}CO (1–0) and C^{18}O (1–0) line data (resolution $\sim$49$''$; Chung et al., 2021) were utilized in this work. This work also uses an integrated C^{18}O (3–2) map obtained from James Clerk Maxwell Telescope (JCMT; proposal id: M06BGT02; rest frequency = 329.3305453 GHz). The C^{18}O (3–2) map is downloaded from the JCMT Science Archive/Canadian Astronomy Data

Centre (CADC), which is a pipeline product (with pixel scale ∼7.″3 and resolution ∼14″) and was observed in the scan (raster) mode using the Heterodyne Array Receiver Programme/Auto-Correlation Spectral Imaging System (HARP/ACSIS; Buckle et al., 2009) spectral imaging system to cover a larger area of the Streamer.

The HGBS images at 70–500 μm and the filament skeletons (e.g., Arzoumanian et al., 2011, 2019) were downloaded from the HGBS archive. The NRAO VLA Sky Survey (NVSS; resolution ∼45″; 1σ ∼0.45 mJy/beam; Condon et al., 1998) 1.4 GHz radio continuum map and the *Planck* sub-millimeter map at 353 GHz or 850 μm (resolution ∼294″; Ade et al., 2014) were also utilized.

We produced the *Herschel* H_2 column density and dust temperature maps at different resolutions (i.e., 13.″5, 18.″2, 24.″9, and 36.″3) using the *hires* method described in (Men'Shchikov, 2021, see also Section 2.3.3.2). Although, even excluding the 70 μm continuum image in the spectral fitting, the *hires* can still produce the images with a resolution of 8.″4 (i.e., the resolution of image at 70 μm; see Men'Shchikov, 2021, for more details). Our derived high-resolution column density and temperature maps at the resolution of 70 μm continuum image are noisy, possibly because of insignificant features present in the image at 70 μm. Therefore, in this work, we have utilized the column density and temperature maps at resolutions of ∼13.″5, 18.″2, 24.″9, and 36.″3.

6.3 Results

In this section, we present the results derived using a careful analysis of the *Herschel* data and the molecular line data, which have enabled us to uncover new insights into physical processes operating in the IC 5146 dark Streamer.

6.3.1 Signatures of two intertwined sub-filaments in the IC 5146 dark Streamer

Figures 6.1a and 6.1b display the *Herschel* column density ($N(H_2)$) and temperature (T_d) maps (resolution ∼13.″5) of our selected target area around the IC 5146 dark Streamer. For the first time, we present these high resolution maps of our target site, which have been produced using the *hires* method as discussed in Chapter 2. Visual inspection of the column density map shows several extended structures. Previously reported two HFSs (i.e., E-HFS and W-HFS) and filament skeletons are also shown in the *Herschel* column density map (see Figure 6.1c), which were identified using the HGBS column density map at the resolution of ∼18.″2 (e.g., Arzoumanian et al., 2019). In earlier works, a single long filament, designated as *fl*, hosting E-HFS and W-HFS at its opposite ends was mainly discussed. We have also marked several small circular regions (radii = 25″) along this long filament (see magenta circles in Figure 6.1c), where some physical parameters (such as column density, temperature etc.) are determined (see Section 6.3.3). In this work, the *Herschel* column density map at the resolution of ∼13.″5 reveals the presence of two intertwined sub-filaments (i.e., *fl-A* and *fl-B*; T_d ∼11–15 K), which are indicated by arrows in Figure 6.1a. We have considered the long filament *fl* as the main filament, which seems to be composed of two intertwined sub-structures. This is a new result in the IC 5146 dark Streamer. The implication of this outcome is discussed in Section 6.4.2.

Figure 6.2a shows the boundaries of different structures traced in the column density map. In order to identify these structures, we used the $N(H_2)$ contour at 5.22×10^{21} cm^{-2} and the *IDL* based *clumpfind* algorithm (Williams et al., 1994). The *clumpfind* algorithm divides two- and three-dimensional data into distinct emission clumps by contouring of data with a multiple of the rms noise (see more information in Williams et al., 1994). The identified structures primarily trace the eastern filament and the western HFS. We have also identified several clumps toward the structures as presented in Figure 6.2a. We used the $N(H_2)$ contours at [5.22, 9.3, and 12] $\times$ 10^{21} cm^{-2} to trace these clumps. In $N(H_2)$ map, we define the clumps as non-filamentary arbitrarily shaped structures (size ∼0.5 pc), while the cores are rather circularly shaped structures (size ≤0.1 pc; see Section 6.3.2). In standard terminology, clumps have a lower density (∼10^4 cm^{-3}) than the embedded cores (>10^5 cm^{-3}; Onishi et al., 2002; Saito et al., 2006). The locations and boundaries of the clumps are displayed in Figure 6.2b. Filled upside-down triangles show the clumps distributed toward the long filament *fl*,

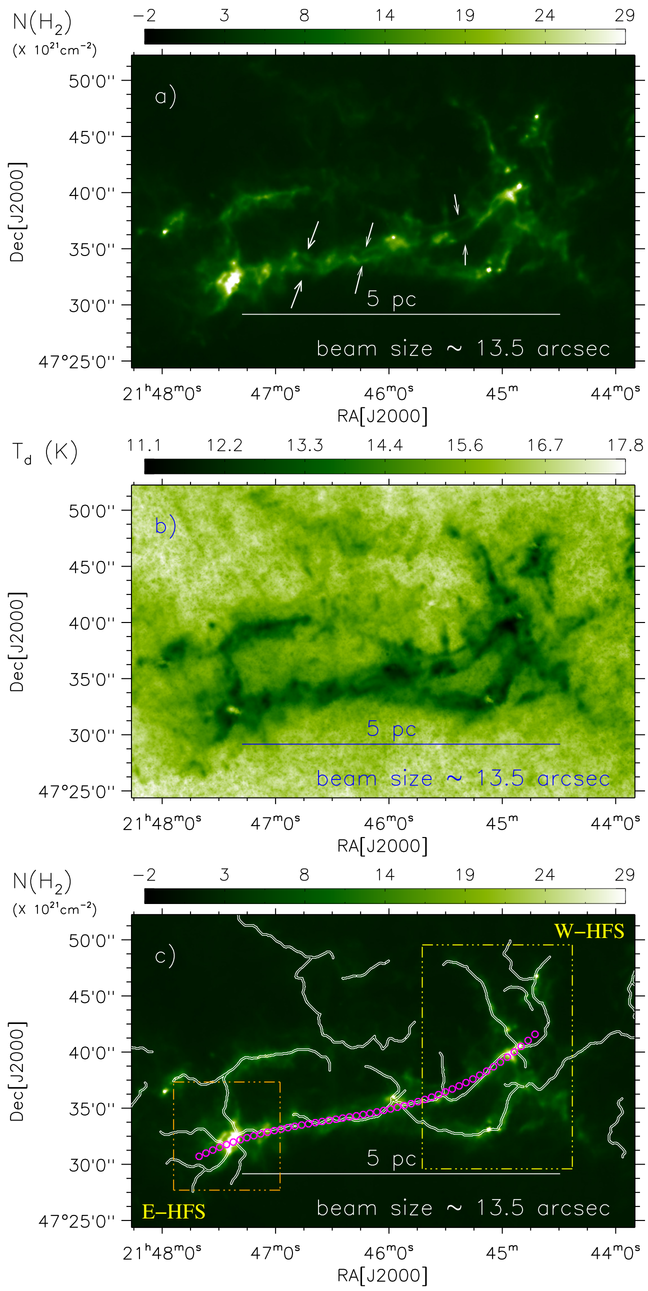

Figure 6.1: a) The panel shows the *Herschel* column density map (resolution ∼13.″5) of an area containing the IC 5146 dark Streamer (size ∼0°.746 × 0°.464). Different sub-filaments are indicated by arrows. b) The panel presents the *Herschel* temperature map (resolution ∼13.″5). c) Same as Figure 6.1a, but it shows the *Herschel* filament skeletons (see white curves from Arzoumanian et al., 2019) and several small circular regions (in magenta; radii = 25″) along the filamentary structure. Two dotted-dashed boxes indicate the locations of the HFSs, which are labeled as E-HFS and W-HFS. A scale bar corresponding to 5 pc (at a distance of 600 pc) is shown in each panel.

while the clumps located away from this structure are highlighted by open upside-down triangles. Figure 6.2c displays the distribution of the *Herschel* clumps, the ionized emission traced by the NVSS 1.4 GHz continuum contour, and the *Planck*

353 GHz or 850 μm continuum emission against the structures as presented in Figure 6.2a. We do not find any noticeable radio continuum emission toward the long filament *fl*, including both the HFSs. The elongated appearance is also evident in the *Planck* 353 GHz or 850 μm continuum map, which does not show any inner structures due to its coarse beam size.

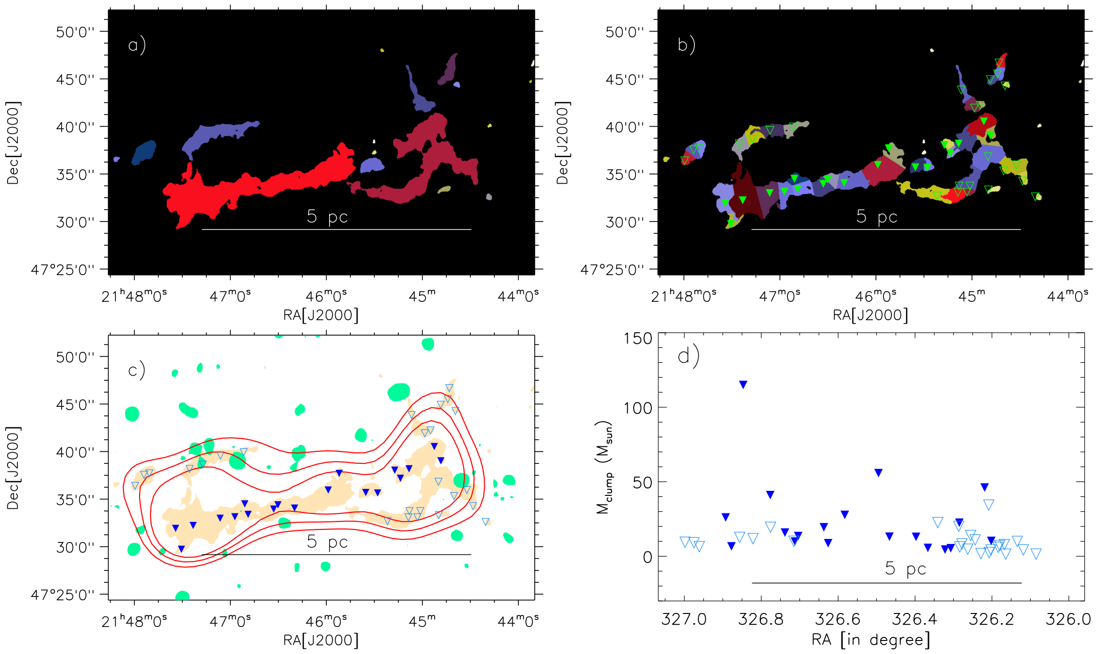

Figure 6.2: a) Several structures are presented, and are depicted in the column density map at a contour level of 5.22 × 10^{21} cm^{-2}. b) Spatial distribution of clumps identified toward the structures shown in Figure 6.2a. The positions of these clumps are indicated by filled and open upside down triangles. The boundary of each *Herschel* clump is also shown. Clumps highlighted by filled symbols are selected toward the elongated structure (see Figure 6.1c), while open symbols present clumps located away from the elongated structure. c) The panel shows a filled $N(H_2)$ contour (in moccasin) at 5.22 ×10^{21} cm^{-2}, a filled NVSS 1.4 GHz continuum contour (in spring green), and the emission contours at [4.92, 5.70, 6.42] MJy/sr from the *Planck* 353 GHz or 850 μm intensity map. Upside down triangles are the same as shown in Figure 6.2b. d) The panel shows a variation of clump masses against their corresponding longitudes (see filled and open upside down triangles in Figure 6.2b). A scale bar corresponding to 5 pc (at a distance of 600 pc) is shown in each panel.

We have also computed the mass of each *Herschel* clump using the Equation 2.14. Figure 6.2d presents the mass distribution against the position of all the clumps, allowing us to examine the mass distribution of clumps. Filled symbols show the clumps distributed toward the long filament *fl*, and massive ones appear to be present at its opposite ends.

In order to highlight two sub-filaments, a false color map is produced using the *Herschel* image at 250 μm (see Figure 6.3a). Previously reported positions of the Class I YSOs, flat-spectrum sources, and Class II YSOs (from Harvey et al., 2008) are shown on the *Herschel* image. We also employed the "Edge-DoG" algorithm on the *Herschel* image at 250 μm, and its outcome is presented in Figure 6.3b. The *IDL* based "Edge-DoG" filter enhances the extended brightness inhomogeneities (e.g., sharp edges) based on the Difference of Gaussians filters technique (Assirati et al., 2014). The positions of HFSs (i.e., E-HFS and W-HFS) and two possible sub-filaments are marked in Figure 6.3b. Figure 6.3c exhibits a zoom-in view of the *Herschel* column density map toward the IC 5146 dark Streamer, where the two sub-filaments *fl-A* and *fl-B* are indicated by arrows. Based on the visual inspection of *Herschel* images, we have presented a cartoon diagram displaying the possible configuration of *fl-A* and *fl-B* in Figure 6.3d. The overlapping areas of the sub-filaments are shown by filled hexagons, where either the YSOs or dense sources are identified. The implication of this configuration is discussed in Section 6.4.2.

6.3.2 Identification of filament skeletons and the dust continuum sources/cores on N(H_2) map at 13$''$.5

To identify the dust continuum sources (or cores) and filament skeletons present in our target site IC 5146 Streamer, we used the *getsf* tool presented in Men'Shchikov (2021). The *getsf* method is capable of extracting the sources and filaments from an astronomical image and requires only a single user input of the maximum size of the structure to extract. We employed *getsf* utility on the N(H_2) map at 13$''$.5. The maximum source and filament size were set to be 20$''$ and 200$''$, respectively. Figure 6.4a presents the overlay of *getsf* extracted sources on the N(H_2) map. The size of sources indicates their footprint size, which is plotted by their estimated major and minor axes. We have only selected the sources which lie within the N(H_2) contour value of 5.22$\times$10^{21} cm^{-2}. A total of 67 sources were found and displayed in Figure 6.4. The overlay of filament skeletons on the N(H_2) map at the spatial scale of $\sim$14$''$ is shown in Figure 6.4b. The presence of at least two close filaments along the major axis of *fl* is marked by arrows. We

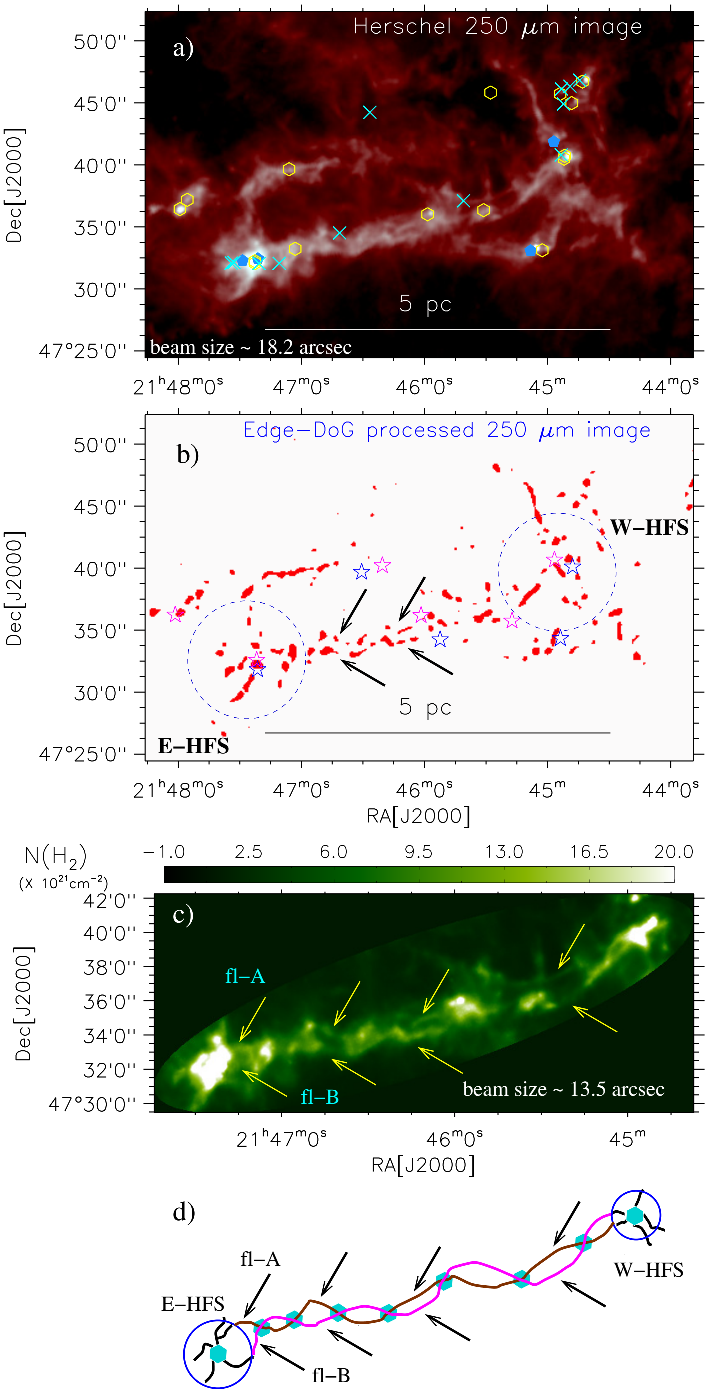

Figure 6.3: a) Overlay of the positions of YSOs (Harvey et al., 2008) on the *Herschel* image at 250 μm. Hexagons, filled pentagons, and multiplication signs represent Class I YSOs, flat-spectrum sources, and Class II YSOs, respectively. (b) The panel shows the *Herschel* image at 250 μm, which has been exposed to the "Edge-DoG" algorithm. Two sub-filaments and two HFSs (i.e., E-HFS and W-HFS) are indicated by arrows and dashed circles, respectively. Blue stars and magenta stars represent the blueshifted and redshifted outflow lobes (from Zhang et al., 2020), respectively. c) The panel presents a zoom-in view of the *Herschel* column density map (resolution $\sim$13$''$.5) toward the IC 5146 dark Streamer. A scale bar corresponding to 5 pc (at a distance of 600 pc) is shown in panels "a" and "b". d) A cartoon displaying the positions of E-HFS, W-HFS, and the possible distribution of intertwined filaments *fl-A* and *fl-B*. Filled hexagons signify the overlapping areas of *fl-A* and *fl-B*.

have overlaid the *getsf* sources on the image. The size of dots is proportional to the footprint area of *getsf* sources. The color scheme of sources infers their mass distribution. The mass of the sources is estimated by the same method presented in Section 6.3.1. This analysis suggests that the more massive cores are located at the hub locations (i.e., E-HFS and W-HFS) compared to the other areas. We cleaned the *getsf* identified filament skeletons by removing the spurious structures and the structures outside of our target region.

6.3.3 Kinematics of molecular gas

6.3.3.1 Variation of radial velocity and Mach number along the filament *fl*

We have re-examined the published TRAO ^{13}CO and C^{18}O line data (effective beam size $\sim$ 49″; Chung et al., 2021) toward the IC 5146 dark Streamer. Figures 6.5a and 6.5b display the integrated intensity (i.e., moment-0) maps of ^{13}CO(J =1−0) and C^{18}O(J =1−0) emission over velocity ranges of [0.8, 6] and [1.0, 5.5] km s^{-1}, respectively. The distribution of both the molecular emissions seems to closely follow the long filament *fl*, but the two sub-filaments (i.e., *fl-A* and *fl-B*) are not spatially resolved in the molecular maps due to their coarse beam sizes. Both molecular emissions are more intense towards the HFSs (i.e., E-HFS and W-HFS).

In Figure 6.6a, we show the distribution of *Herschel* clumps, YSOs (from Harvey et al., 2008), and outflow lobes (from Zhang et al., 2020) toward the IC 5146 dark Streamer. We also mark open circles to highlight the positions of several circular regions along the long filament *fl* (see also Figure 6.1). Average column density and average dust temperature are computed for each circular region using the *Herschel* column density and temperature maps at different resolutions (i.e., 13.″5, 18.″2, 24.″9, and 36.″3), respectively. With the help of these values, Figures 6.6b and 6.6c display the column density profile and the dust temperature profile along the filamentary structure, respectively. We find the column density peaks at the ends of the long filament *fl*, and the presence of cold dust emission

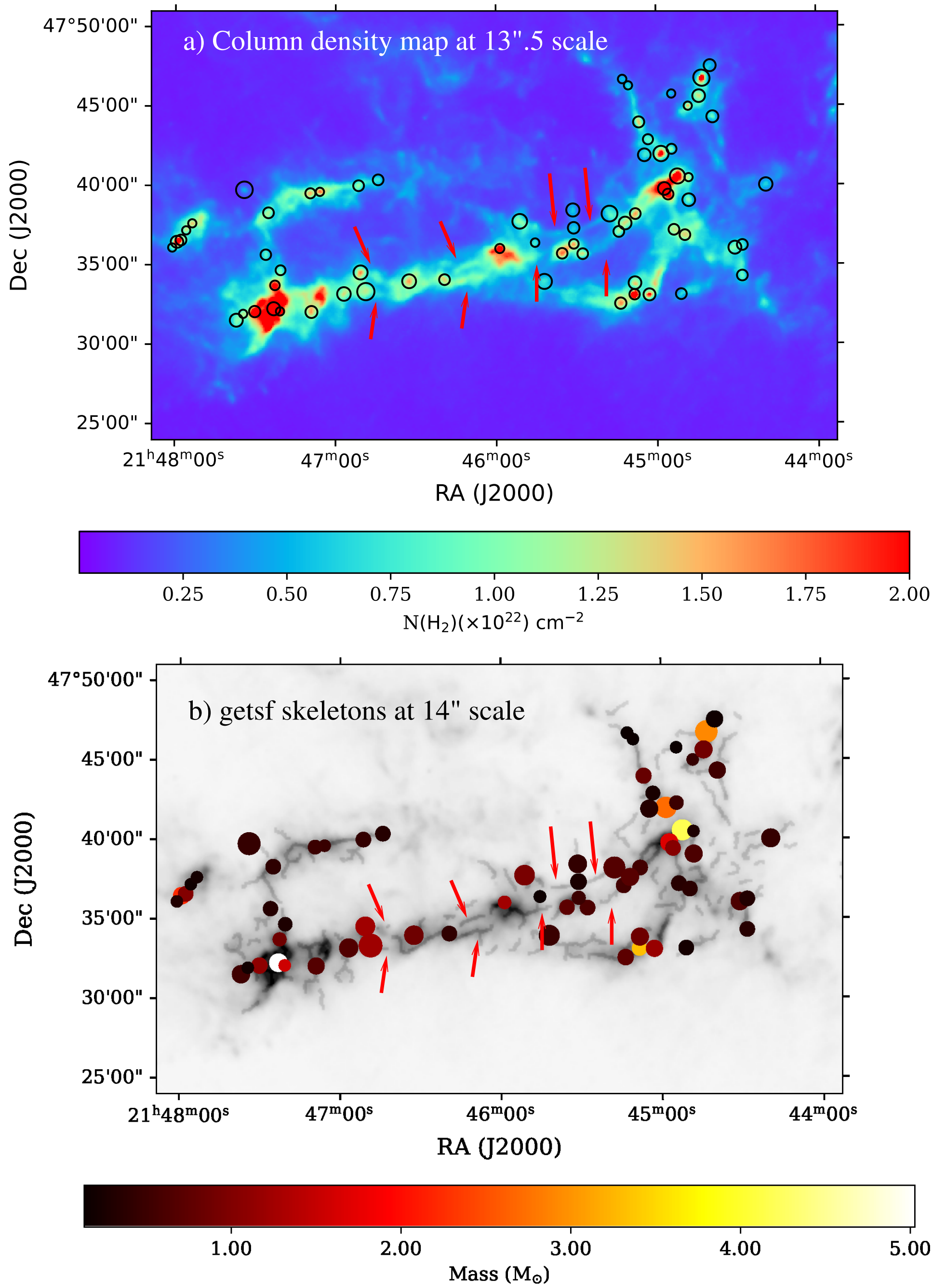

Figure 6.4: a) H_2 column density (N(H_2)) map at 13.″5 resolution. The *getsf* extracted sources are overlaid and shown by their footprint size (see text for more details). b) Overlay of the *getsf* identified skeletons at 14″ scale on the 13.″5 N(H_2) map. The size of dots is proportional to the footprint area of *getsf* sources. The arrows mark the sub-filaments *fl-A* and *fl-B* (see Figure 6.3).

($T_{\rm d}$ ∼11–15 K) toward the filament *fl*. These outcomes are consistent in all the *Herschel* column density and temperature maps at different resolutions.

We also produced average spectra of ^{13}CO and C^{18}O toward each circular region, enabling us to determine the mean velocity ($V_{\rm lsr}$) and the Full-Width Half

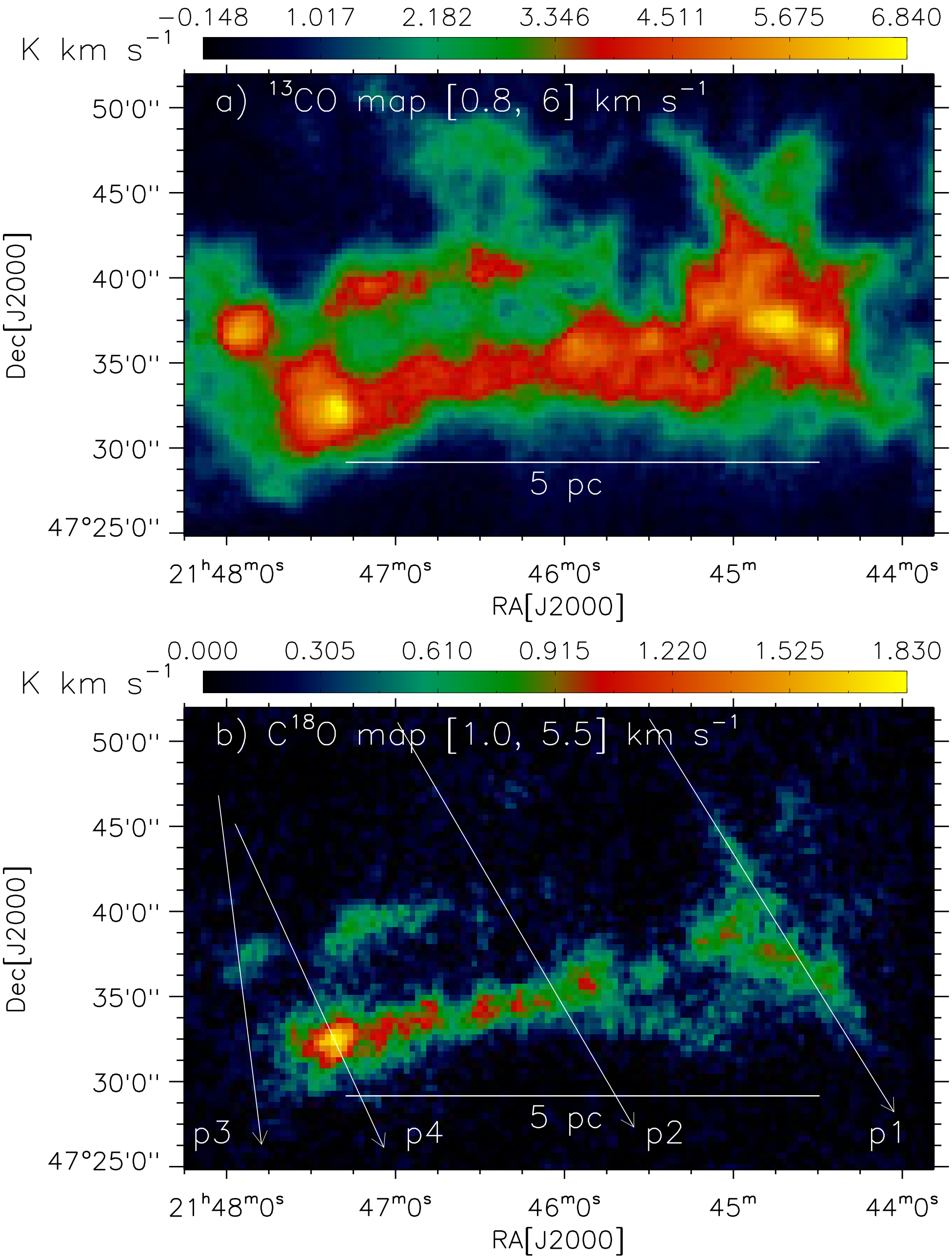

Figure 6.5: TRAO integrated intensity (or moment-0) maps of a) ^{13}CO and b) C^{18}O toward the IC 5146 dark Streamer. The molecular emission is integrated over a velocity interval, which is given in each panel (in km s^{-1}). In panel 'b', four arrows (p1–p4) are indicated, and p-v diagrams along these paths are presented in Figure 6.7. A scale bar corresponding to 5 pc (at a distance of 600 pc) is shown in each panel.

Maximum (FWHM) line width (ΔV) of each spectrum. The $V_{\rm lsr}$ and ΔV are estimated by the Gaussian fitting of each averaged spectrum. In Figures 6.6d and 6.6e, we present the ^{13}CO and C^{18}O velocity profiles and the ^{13}CO and C^{18}O line width profiles along the filamentary structure, respectively. The variation of $V_{\rm lsr}$ and ΔV along the filament is seen. In other words, there is a hint of velocity

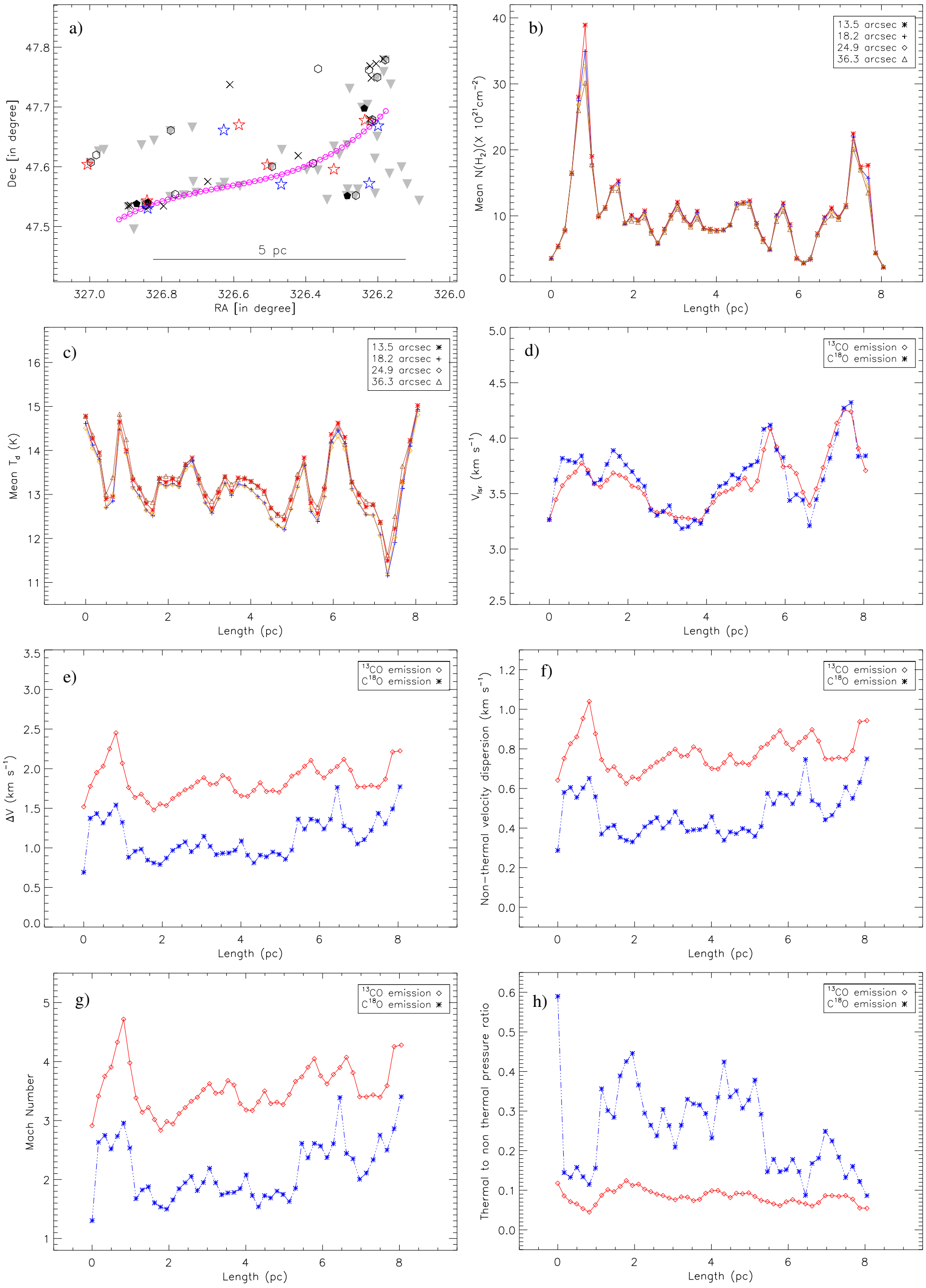

Figure 6.6: a) The panel presents the distribution of *Herschel* clumps (filled upside down triangles), infrared excess sources (i.e., Class I YSOs (hexagons), flat-spectrum sources (filled pentagons), Class II YSOs (multiplication signs)) from Harvey et al. (2008), and outflow lobes (stars; from Zhang et al., 2020, see also Figures 6.2 and 6.3). Open circles (in magenta) represent the positions of several selected regions along the filamentary structure (see also Figure 6.1c), where average molecular spectra, average column densities, and average dust temperatures are computed. b–f) The panel displays a variation of the column density, dust temperature, radial velocity, FWHM line width, $\sigma_{\rm NT}$, Mach number, ratio of thermal to non-thermal gas pressure along the filamentary structure highlighted in Figure 6.6a. In the direction of each circle marked in Figure 6.6a, the values of dust temperature and column density are computed from the *Herschel* temperature and column density maps having different resolutions, while other physical parameters are extracted using the ^{13}CO and C^{18}O line data.

oscillation along the filament. The knowledge of the line width value is also used to compute the $\sigma_{\rm NT}$, Mach number, and ratio of thermal to non-thermal pressure toward each circular region. Mach number is defined as the ratio of $\sigma_{\rm NT}$ to sound speed (c_s). The sound speed c_s ($= (kT_{kin}/\mu m_H)^{1/2}$) can be estimated using the value of gas kinetic temperature ($T_{\rm kin}$) and mean molecular weight (μ=2.37; approximately 70% H and 28% He by mass). Here, we used the average dust temperature instead of $T_{\rm kin}$, which has been estimated to be ∼14.2 K from the *Herschel* temperature map. Based on the recommendations of Lada et al. (2003), we have computed the ratio of thermal to non-thermal (or turbulent) pressure (i.e., $R_p = c_s^2/\sigma_{NT}^2$). Following Equation 2.6, we estimated the $\sigma_{\rm NT}$. Here, $\sigma_{\rm T}$ ($= (kT_{kin}/30m_H)^{1/2}$ for $C^{18}O$ and $= (kT_{kin}/29m_H)^{1/2}$ for ^{13}CO) is the thermal broadening at $T_{\rm kin}$ (or $T_{\rm d}$ ∼14.2 K).

Figures 6.6f, 6.6g, and 6.6h display the variation of the $\sigma_{\rm NT}$, Mach number, and ratio of thermal to non-thermal gas pressure for ^{13}CO and $C^{18}O$ along the filamentary structure, respectively. Using the ^{13}CO and $C^{18}O$ emissions, the Mach number is found to be larger than 1, and the low ratios of thermal to non-thermal pressure (< 1) is evident for all the selected circular regions. It implies the presence of supersonic and non-thermal motion in the filamentary structure. Furthermore, higher values of $N(H_2)$, Mach number, and lower values of R_p are found toward the central hub of the E-HFS compared to the other HFS (i.e., W-HFS).

6.3.3.2 Signatures of two velocity components toward the filament *fl*

We have examined the position-velocity (p-v) diagrams of the ^{13}CO and $C^{18}O$ emissions along several lines passing through the shorter axis of *fl*. In this work, we have only presented the p-v diagrams along four arrows p1–p4 (see Figure 6.5b). One can notice that the paths/arrows p1 and p4 pass through the HFS-W and HFS-E, respectively. The p-v diagrams of ^{13}CO along p1, p2, p3, and p4 are presented in Figures 6.7a, 6.7c, 6.7e, and 6.7g, respectively. Figures 6.7b, 6.7d, 6.7f, and 6.7h present p-v diagrams of $C^{18}O$ along p1, p2, p3, and p4, respectively. In the direction of both the HFSs, p-v diagrams hint at the presence of two velocity components around 2 and 4 km s^{-1}, which are connected in the velocity space. We have also studied the velocity channel maps of the ^{13}CO emission (not shown in this work), supporting the existence of two velocity components (i.e., [1, 2] and [3, 4] km s^{-1}). In this context, we show the intensity weighted mean velocity (i.e., moment-1) maps of ^{13}CO and C^{18}O emission in Figures 6.8a and 6.8b, respectively.

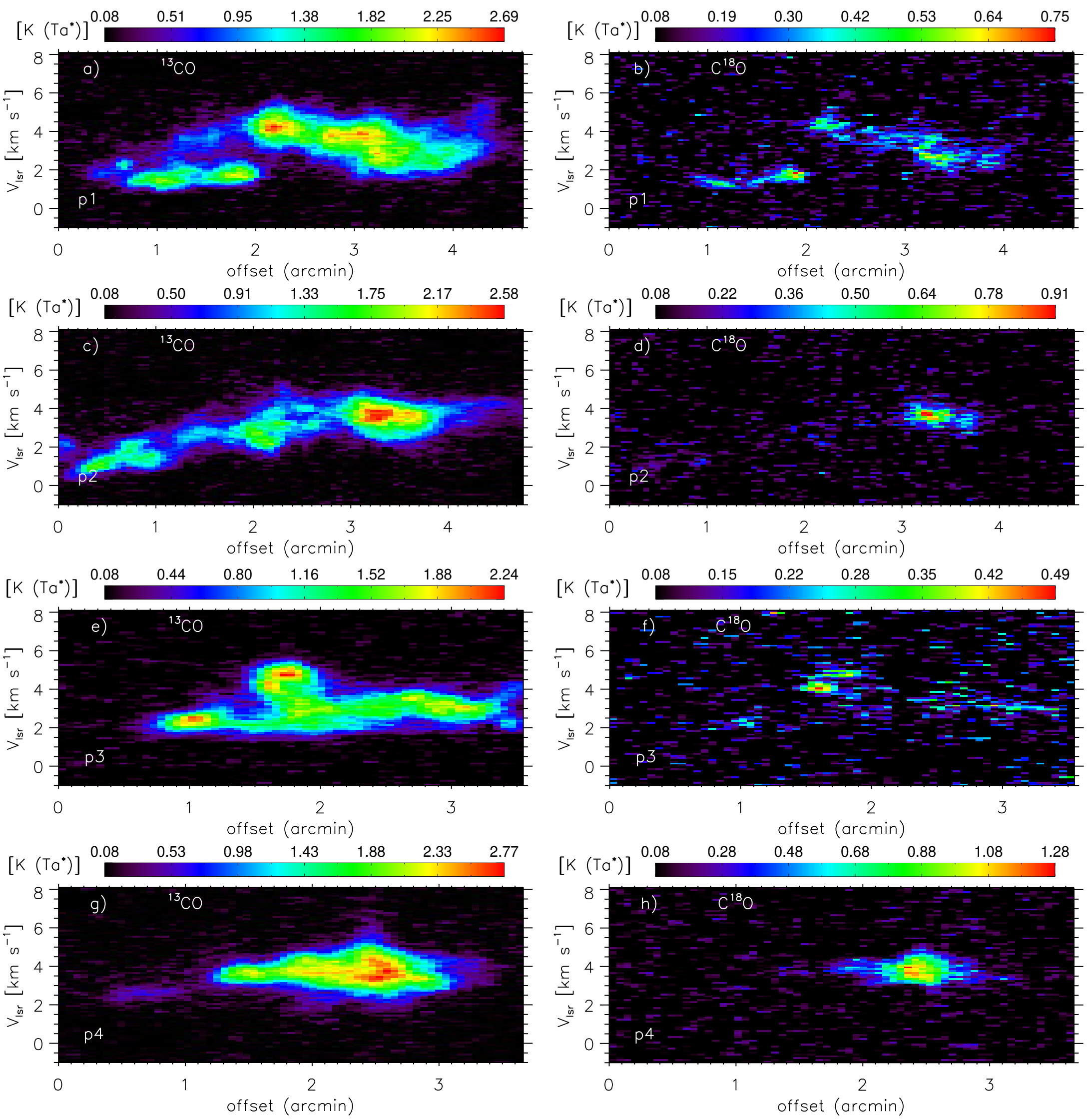

Figure 6.7: Left column (a, c, e, g): p-v diagrams of ^{13}CO along four arrows "p1–p4". Right column (b, d, f, h): p-v diagrams of C^{18}O along four arrows "p1–p4". These arrows "p1–p4" are indicated in Figure 6.5b.

Based on a careful examination of the molecular line data, we have produced integrated intensity maps for two different velocity ranges (see Figures 6.8c and 6.8d). The ^{13}CO emission maps at [0.8, 2.5] and [3, 6] km s^{-1}, and the C^{18}O emission maps at [1, 2.5] and [3, 6] km s^{-1} have been generated (see Figures 6.8c and 6.8d). Figures 6.8e and 6.8f display the intensity weighted velocity dispersion (i.e., moment-2) maps of ^{13}CO and C^{18}O emission, respectively. In Figure 6.8c, we find the overlapping zones of the two cloud components, where both the HFSs and the central part of the long filament *fl* are spatially depicted (see also the C^{18}O emission in Figure 6.8d). In these locations, higher velocity dispersions are also found, inferring the presence of either multiple velocity components (see Figures 6.8c and 6.8e) or the presence of non-thermal gas motions (see Figures 6.8d and 6.8f). Together, the molecular line data support the physical connection of the two cloud components (around 2 and 4 km s^{-1}) in both physical and velocity space.

6.3.3.3 Existence of two intertwined molecular filaments toward the filament *fl*?

The cloud component at [3, 6] km s^{-1} (or around 4 km s^{-1}) traced using both the molecular lines has an elongated appearance similar to the long filament *fl*, while the second component around 2 km s^{-1} does not show any elongated morphology like *fl* (see Figure 6.8d). The previously reported N-filament (see Figure 6.8d in this work and Figure 2 in Chung et al., 2022) toward the western end of *fl* is associated with the cloud around 2 km s^{-1}. Concerning the cloud component around 4 km s^{-1}, Figure 6.9a shows the moment-1 map of the C^{18}O emission, revealing the presence of velocity variations along the filamentary feature. To further infer velocity variations, using the moment-1 maps of ^{13}CO and C^{18}O, we extracted the velocity profiles along an arrow highlighted in Figure 6.9a (see Figure 6.9b). A velocity variation/oscillation is traced in both molecular emissions. In the direction of the eastern and central parts of the IC 5146 dark Streamer, the *Herschel* image at 250 μm and the integrated JCMT C^{18}O (3–2) map are presented in Figures 6.9c and 6.9d, respectively. Due to the limited sensitivity, the existing JCMT C^{18}O (3–2) map could only hint at the existence of two intertwined molecular filaments (see arrows in Figure 6.9d) as investigated in the *Herschel* maps (i.e., *fl-A* and *fl-B*). For comparison purposes, we also mark arrows over the *Herschel* image at 250 μm. To further study these molecular filaments,

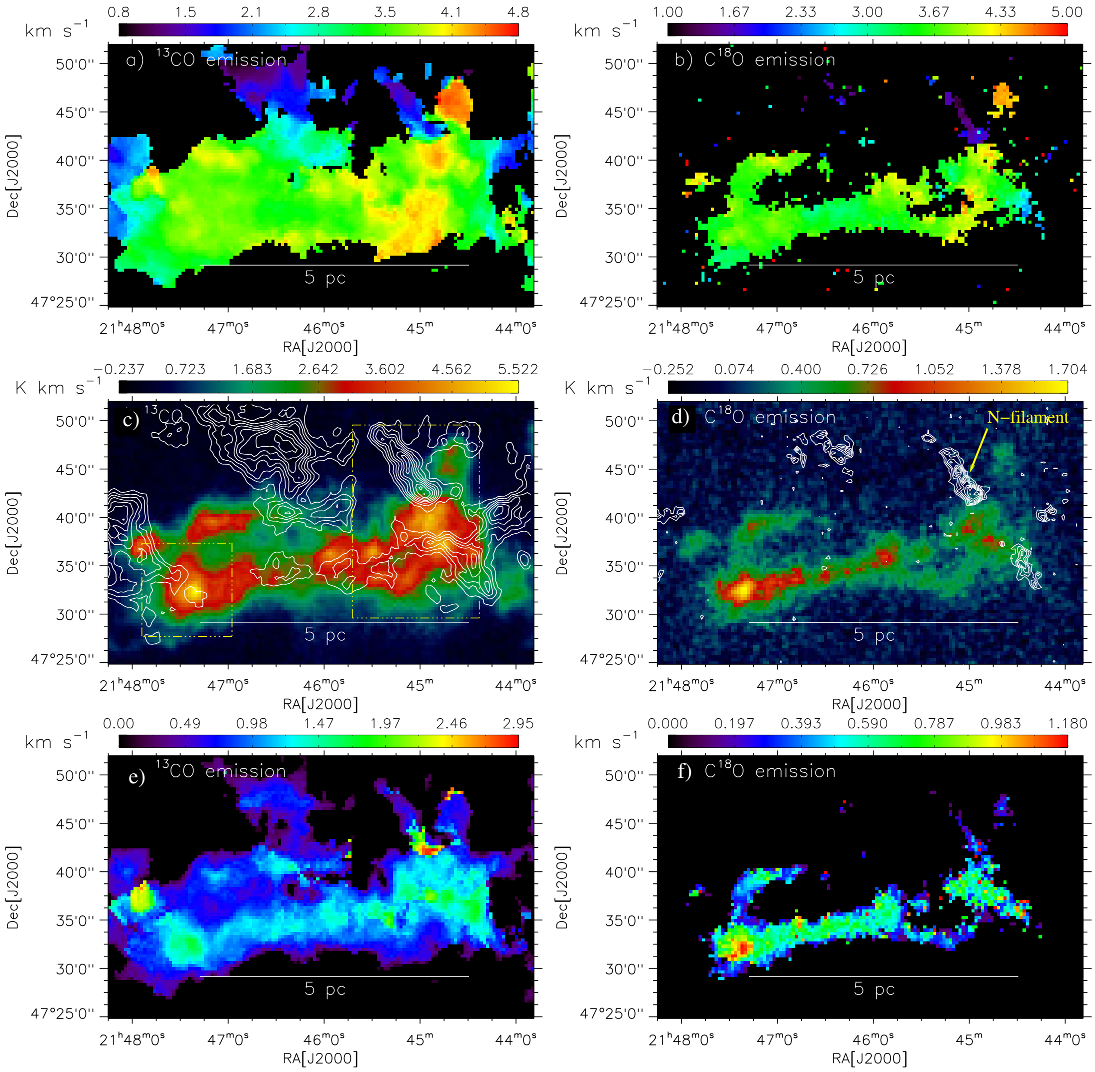

Figure 6.8: a) ^{13}CO moment-1 map of our selected target area (Figure 6.1a). b) C^{18}O moment-1 map. c) Overlay of the ^{13}CO integrated intensity emission contours at [0.8, 2.5] km s^{-1} on the ^{13}CO integrated intensity map at [3, 6] km s^{-1}. The contour levels are 2.56 K (in T$_a$*) km s^{-1} $\times$ (0.2, 0.3, 0.4, 0.5, 0.6, 0.7, 0.8, 0.9). d) Overlay of the C^{18}O integrated intensity emission contours at [1, 2.5] km s^{-1} on the C^{18}O integrated intensity map at [3, 6] km s^{-1}. The contour levels are 0.45 K (in T$_a$*) km s^{-1} $\times$ (0.3, 0.4, 0.5, 0.6, 0.7, 0.8, 0.9). e) ^{13}CO moment-2 map. f) C^{18}O moment-2 map. A scale bar corresponding to 5 pc (at a distance of 600 pc) is shown in each panel.

one will need new high-resolution and high-sensitivity molecular line data for a larger area around the IC 5146 dark Streamer. We found that the high-resolution C^{18}O maps (resolution ∼15–20″) at different transitions (i.e., J =1–0, J =2–1, and J =3–2) of IC 5146 dark Streamer presented in Bell (2008) reveal the similar morphology as seen in the *Herschel* maps. Thus, the continuum and the molecular maps hint at the existence of two intertwined sub-filaments.

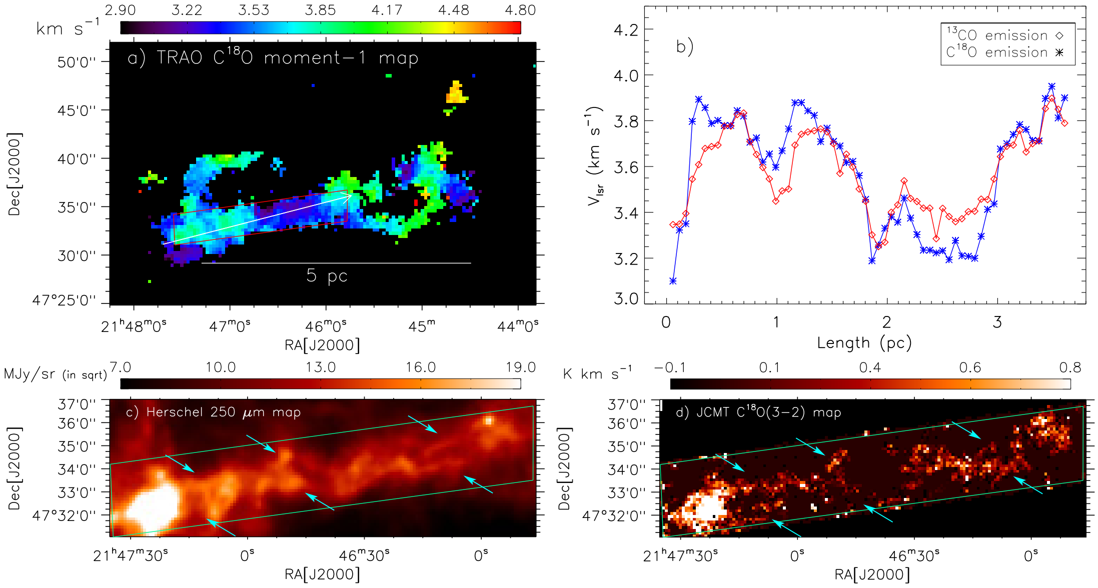

Figure 6.9: a) The panel shows the TRAO $C^{18}O$ moment-1 map of our selected target area (Figure 6.1a), which is generated for the molecular cloud at [2.9, 6] km s^{-1} (see Figure 6.8f). A scale bar corresponding to 5 pc (at a distance of 600 pc) is presented. b) The panel displays a variation of radial velocities along an arrow marked in Figure 6.9a, which are extracted using the ^{13}CO and $C^{18}O$ moment-1 maps. c) The panel shows areas toward the eastern and central parts of the IC 5146 dark Streamer using the *Herschel* 250 μm image. d) The panel presents an integrated JCMT $C^{18}O$ (3–2) map. In panels "a", "c", and "d", a solid box highlights the area covered in the JCMT $C^{18}O$ (3–2) map.

6.4 Discussion

Based on several previously published works, the dark Streamer of IC 5146 has been considered as a single and long filament *fl* having an aspect ratio larger than 5 (Arzoumanian et al., 2011, 2019; Johnstone et al., 2017; Wang et al., 2017, 2019b,a; Zhang et al., 2020; Chung et al., 2021, 2022), which is also indicated in Figure 6.1c. One prominent HFS has been traced toward the east-end (E-HFS) and the west-end (W-HFS) of the dark Streamer (see Figure 6.1c). Chung et al. (2022) presented a cartoon showing the observed configuration of the Streamer (see Figure 9 in their work). In our high resolution *Herschel* column density map, both the HFSs are associated with the regions of high column densities (see Figure 6.6b). Noticeable YSOs and outflow lobes (e.g., Harvey et al., 2008; Zhang et al., 2020) have been reported toward both the ends of the dark Streamer (i.e., E-HFS and W-HFS; see Figure 6.6a), supporting the ongoing star formation activities (e.g., Chung et al., 2021, 2022). The absence of radio continuum emission and high column density areas toward the E-HFS and W-HFS hints at the potential sites of future massive star formation (see Figure 6.2). Earlier published results together were interpreted in favour of the EDC and fragmentation scenario in the dark Streamer (see Wang et al., 2019b; Chung et al., 2022, and references therein). Additionally, in support of the proposed edge collapse scenario, the curved B-field morphology in core-scale HFSs toward both ends was detected (see Wang et al., 2019b; Chung et al., 2022, and references therein). Apart from the IC 5146 Streamer, we have verified this signature in the other nearby EDC filaments as well.

6.4.1 Magnetic Field orientations in nearby candidate EDC filaments

In the introduction section, we have highlighted the candidate filaments experiencing edge collapse. Apart from the IC 5146 dark Streamer (d ∼600 pc), we find three other EDC filaments (i.e., Mon R1 (d ∼760 pc), S242 (d ∼2.1 kpc), and NGC 6334 (d ∼1.3 kpc)), which are nearby EDC filamentary systems (d $\lesssim$ 2 kpc). The existing observations of dust polarised emission from the *Planck* telescope have been employed to study the large-scale magnetic field of the four EDC filaments. We used the *Planck* 353 GHz Stokes I, Q, and U maps to estimate the linear polarization angles (PAs) of polarized dust emission caused by the anisotropic dust grains in our target sites. The stokes I, Q, and U maps were converted from the cosmic microwave background (CMB) temperature (K_{cmb}) scale to MJy sr^{-1} using the unit conversion factor of 246.54 (e.g., Adam et al., 2016b). We also smoothed the stokes maps by *astropy* based Gaussian 2D-kernel (input parameter x_stddev=2) to increase the signal-to-noise ratio. We estimated the PAs in Galactic coordinates using the conventional relation of $\theta_{\rm GAL} = 0.5\times$ arctan2$(-{\rm U}, {\rm Q})$, where $-$U is used to follow the IAU convention (see more details in Ade et al., 2015) and a two-argument function arctan2 is used to avoid the π-ambiguity in the estimation of PAs. The magnetic field orientations were then computed by adding 90° in the electric field polarization PAs (e.g., Ade et al., 2016b,c). We term this angle as B_{Gal} throughout the work, which is measured from galactic north to east along the counter-clockwise direction.

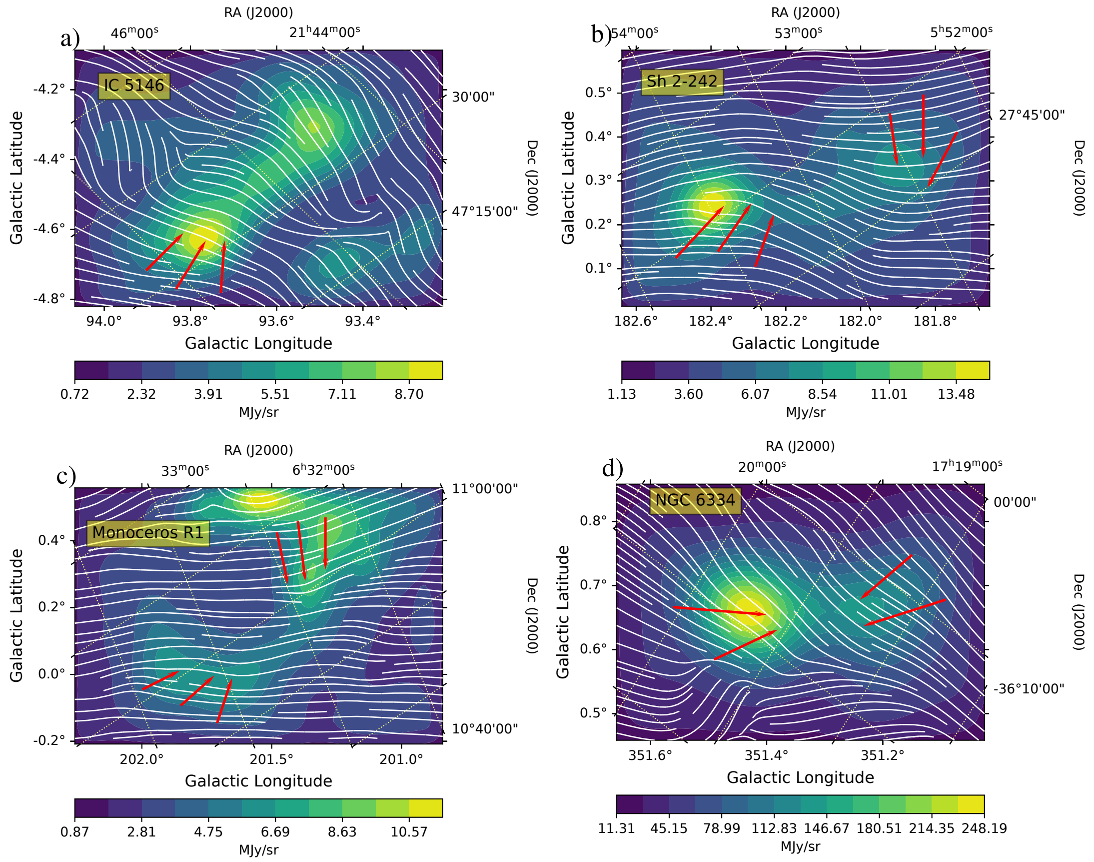

Figure 6.10: *Planck* 353 GHz I-stoke images of EDC filaments IC 5146, Sh 2-242, Monoceros R1, and NGC 6334 overlaid by streamlines displaying POS magnetic field. The streamlines are displayed using *streamplot* in *matplotlib* for a density parameter of 1.0. The red arrows indicate the B-field curvature at the filament edges. The Stokes Q and U maps were used to calculate the POS magnetic field position angles (see text for more details).

The distribution of the plane of sky (POS) magnetic field in the direction of our selected EDC filaments IC 5146 dark Streamer, S242, Mon R1, and NGC 6334 is displayed by streamlines in Figure 6.10. We used *streamplot* in *matplotlib* to display the magnetic field orientations toward our selected targets. The magnetic field direction is nearly perpendicular to all the filaments, consistent with the observations of other targets (e.g., Palmeirim et al., 2013; Ade et al., 2016a; Cox et al., 2016). The ^{13}CO emission at the velocity range of [0.8, 2.5] km s^{-1} (see Figure 6.8c) appears to be parallel to the B-field orientation shown in Figure 6.10a. It is reported that faint filaments (striations) are well aligned to the magnetic fields, and the main filament can gain its mass from these striations (e.g., Palmeirim et al., 2013; Zhang et al., 2020). Therefore, the ^{13}CO emissions parallel to the B-field show that IC 5146 dark Streamer is not isolated but interacts with the natal clouds. However, interestingly the B-field direction is curved at the edges of our target filaments. As discussed by Wang et al. (2019b) and Chung et al. (2022), the B-field directions in the EDC filaments make a shape of ")" and "(" at the filament edges (hereafter, the bending effect). This is because of the material pile up at the edges, which itself moves toward the center of the filament (e.g., Clarke & Whitworth, 2015). This longitudinal motion of gaseous material from the ends to the center of the filament can have sufficient ram pressure that pinches the magnetic field lines and forms the U-shaped magnetic field morphology (or bending effect; see more details in Gómez et al., 2018; Wang et al., 2019b,a). This effect is most prominently seen in the S242 and Mon R1 filament than in the other sources (e.g., IC 5146 dark Streamer and NGC 6334; see arrows in Figure 6.10). We suspect that the bending effect at one of the edges of the IC 5146 dark Streamer is not prominent because of the contamination caused by the presence of the HFS. However, still, this effect is significant toward the south-eastern clump of the IC 5146 dark Streamer (see also Figure 7 of Chung et al., 2022). Similarly, the NGC 6334 also shows the signature of HFSs at its edges (see Figure 2 of Tigé et al., 2017) and does not show the strong bending effect in Figure 6.10. However, the high-resolution polarization map (beam $\sim 14''$) of NGC 6334 by Arzoumanian et al. (2021) indeed shows the bending effect at the dense eastern region (Figure 6.10) revealing the longitudinal gas motion along the filament. The direction of the magnetic field at the other end of the NGC 6334 is randomly oriented in the high-resolution map of Arzoumanian et al. (2021). However, our *Planck* magnetic field map shows the signature of curvature at this end, too (see Figure 6.10). It is discussed in the literature that the magnetic field distortions can be caused by the outflow-driven shocks, feedback from expanding ionized fronts, and gravity-driven gas flows (e.g., Arzoumanian et al., 2021; Eswaraiah et al., 2021). Also, recent observations signify that the curved magnetic field can be originated by the effect of gravity and the collision of clouds (e.g., Wang et al., 2019a, 2022). Therefore, it is quite possible that the intense star formation activity and the presence of HFSs at the filament edges can distort the initial bending effect in EDC filaments. Although our target filaments are promising EDC candidates, their non-linearity can diminish the bending effect at low-resolution *Planck* magnetic field maps. Thus, we confirm that the other linear EDC filaments (if HFSs are not present) should show the bending effect.

Figure 6.11 displays the spatial distribution of magnetic field position angle (B_{Gal}) toward selected EDC filaments. The derived B_{Gal} maps are masked out for regions of low intensity and used to obtain the histograms of B_{Gal} (see column 2 of Figure 6.11). The mean B_{Gal} is found to be 48.37, 87.96, 96.44, and 56.70 degrees for the IC 5146 dark Streamer, S242, Mon R1, and NGC 6334, respectively. To derive the B_{Gal} distribution in the IC 5146 dark Streamer, we have considered only the region containing elongated filament. Hence we have masked out the southern-west region seen in Figure 6.10. Interestingly, these two filaments are nearly perpendicular to the Galactic plane. Mon R1, however, is a highly curved filament having its ends nearly perpendicular and parallel to the Galactic plane. A positive gradient in B_{Gal} can be seen from where the Mon R1 filament gets perpendicular to the Galactic plane. The distribution of B_{Gal} along the long axis of selected filaments is presented by blue curves in Figure 6.11. To quantify the distribution of the magnetic field toward the target filaments, we estimated the magnetic field position angle with respect to the filament's major axis from the direction of its head ($B_{Filament}$). The distribution of $B_{Filament}$ vs filament's length ($B_{Filament}$–L) is shown by red curves in Figure 6.11. Interestingly, for all the filaments, the global trend follows a negative slope in a range of [-0.04, -0.02] degree arcsec^{-1}. We estimated the slope by fitting a straight line (see black dotted line) on the $B_{Filament}$–L plot. The negative slope in $B_{Filament}$–L distribution agrees well with the idea of magnetic field bending effect by Wang et al. (2019b). Ideally, a straight filament having magnetic field lines perpendicular toward its central regions and curved magnetic fields (i.e., shapes of ")" and "(") toward the respective edges (see Figure 13 of Wang et al., 2019b), should show the global increasing or decreasing trend in $B_{Filament}$–L plot. The negative or positive trend will depend upon the choice of reference direction (i.e., filament's head or tail) from which the magnetic field angle is measured. In our target filaments, a global linear trend in B_{Filament}–L plot hints at the EDC signature. However, despite the linear trend, we witness local oscillations as well. This is possible because of the non-linearity of the filament (or sky-projection effect) and the contamination caused by other ongoing processes.

6.4.2 Physical processes operating in the IC 5146 dark Streamer

Based on the examination of the TRAO molecular line data, a collision of turbulent converging flows was suggested to explain the existence of HFSs, which also includes the role of mass flow along the filaments to the dense cores in IC 5146 (Chung et al., 2021). In order to further explore the collision process in the Streamer, we revisited the TRAO ^{13}CO and C^{18}O line data (see Section 6.3.3). Our analysis of the molecular line data shows the existence of two cloud components around 2, and 4 km s^{-1} in the direction of the IC 5146 dark Streamer, and a velocity connection of these components is also found. The areas of the E-HFS and W-HFS, where the higher level of clumpiness is observed, are seen toward the common zones of the cloud components (see Section 6.3.3.2). Earlier works on the cloud-cloud collision (CCC) recommend a spatial and velocity connection of two cloud components as a reliable tracer of CCC (see Fukui et al., 2021a; Maity et al., 2022, and references therein for more details). In general, colliding gas flows are thought to be operated in the low-density medium, while the high-density phase of colliding gas flows could refer to CCC (e.g., Beuther et al., 2020; Dewangan, 2022).

Central hubs of HFSs, hosting massive stars and clusters of YSOs, are thought to gain the inflow material from very large scales of 1-10 pc, which can be funneled along molecular filaments (see Tigé et al., 2017; Motte et al., 2018, for more details). Theoretical works favor the existence of HFSs by the colliding clouds or large-scale colliding flows (Balfour et al., 2015; Inoue et al., 2018), and this scenario is also supported in the recent review article on CCC (Fukui et al.,

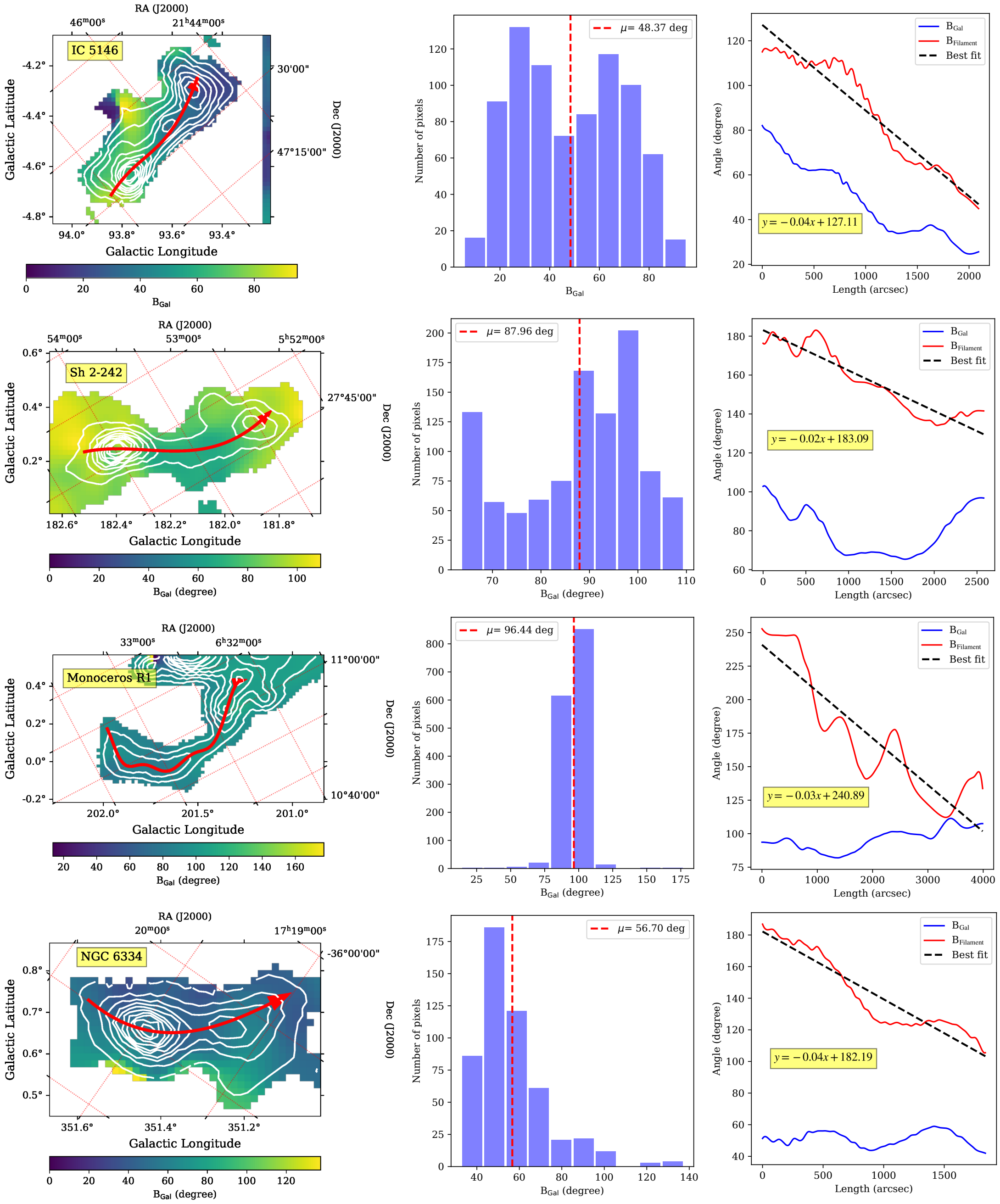

Figure 6.11: Distribution of the POS magnetic field angle with respect to the Galactic north to the anticlockwise direction (B_{Gal}) toward selected EDC filaments. The first column displays the spatial distribution of B_{Gal} of EDC filaments IC 5146, Sh 2-242, Monoceros R1, and NGC 6334. The overlaid contours refer to the *Planck* 353 GHz intensity (see Figure 6.10). The second column presents the histograms of B_{Gal} corresponding to the targets shown in the first column. A vertical red dashed line indicates the mean B_{Gal} of histogram distribution. The third column displays the variation of B_{Gal} and $B_{Filament}$ along the long axis of filaments (see red curves in the first column). $B_{Filament}$ is the magnetic field position angle measured from the filament's major axis to the anticlockwise direction (see text for more details). A best fitted line for $B_{Filament}$ distribution is shown and labelled.

2021a). Based on our findings, it is likely that the IC 5146 dark Streamer may be influenced by the collision process, and both the HFSs appear to be originated in the shock-compressed interface layer by the colliding clouds/flows (see also Chung et al., 2021). The massive sources are exclusively found to reside at the hub locations (see Figure 6.4).

Now, we have examined why HFSs are formed at the edges of the filament *fl*. It was already explained by the onset of the EDC in the filament *fl*, which has a higher aspect ratio (see Wang et al., 2019b; Chung et al., 2022, and references therein). In the EDC process, density enhancement is expected at each end of the filament due to high gas acceleration (Bastien, 1983; Pon et al., 2012; Clarke & Whitworth, 2015; Hoemann et al., 2022).

The present work reveals the existence of two coupled (or intertwined) sub-filaments (i.e., *fl-A* and *fl-B*) toward the main filament *fl*, showing almost a double helix-like pattern (see Figures 6.3d, 6.4, and Section 6.3.1). The TRAO ^{13}CO and C^{18}O line data do not reveal this configuration due to a coarse beam size. However, the JCMT C^{18}O (3–2) map seems to support the detected structures in the *Herschel* maps. Hence, such intertwined configuration is seen in both the dust and molecular emissions. A cartoon diagram displaying the physical configuration of sub-filaments *fl-A* and *fl-B* (Figure 6.3d) is motivated by their simultaneous detection in the dust continuum and the molecular emission maps. However, the existing molecular line data do not allow us to trace the velocity information along each sub-filament. Previously, Dewangan et al. (2021) found the velocity oscillation along two intertwined filaments in site LBN 140.07+01.64. The physical configuration of sub-filaments in IC 5146 Streamer appears very similar to the sub-filaments identified in LBN 140.07+01.64 (see Figures 3 and 7 therein). Therefore, due to such limited sites in literature, the presence of intertwined filaments or their double helix-like pattern and their role in star formation demand more observational as well as theoretical insights. The sub-filaments *fl-A* and *fl-B* appear to spatially overlap with each other along the major axis, forming multiple common areas where the *Herschel* clumps and YSOs are seen. This is another new outcome of this work. In this relation, we examined the existing “fray and fragment” scenario of the formation of intertwined sub-structures (Tafalla & Hacar, 2015; Clarke et al., 2017), which firstly predicts the formation of the main filament by a collision of two supersonic turbulent gas flows, and then the scenario favors the origin of the intertwined system of velocity-coherent sub-structures in the main filament due to residual turbulent motions and self-gravity (see also Smith et al., 2014; Shimajiri et al., 2019a). This scenario was proposed in the NGC 6334 filament (Shimajiri et al., 2019a) and the Taurus filament (Tafalla & Hacar, 2015).

Additionally, we have also investigated a noticeable velocity oscillation along the filament *fl* (see Section 6.3.3.2). Previously, in the case of a filament G350.5-N associated with the cloud G350.54+0.69, Liu et al. (2019) reported a large-scale periodic velocity oscillation. To explain this aspect, on the basis of gravitational-instability-induced core formation models, they proposed a proposal with the combination of longitudinal gravitational instability and a large-scale physical oscillation along the filament. Considering two sub-filaments and the distribution of the *Herschel* clumps toward the long filament *fl*, the observed velocity oscillations/variations seem to support the presence of two coupled or intertwined sub-filaments and fragment/clump formation along the filament, where the non-thermal (or turbulent) pressure seems to be dominated (see Section 6.3.3.2).

Taken together, our findings reveal the onset of multiple physical processes in the IC 5146 dark Streamer, which includes the edge collapse, CCC, accretion flows, and “fray and fragment” scenario.

6.5 Summary and Conclusions

In order to probe ongoing physical processes in a nearby star-forming site IC 5146 dark Streamer (d ∼600 pc), we have conducted a study using the multi-wavelength data. The dark Streamer resembles a single and long filament, *fl*, having an aspect ratio > 5. The eastern and the western ends of *fl* harbor one HFS. Simultaneous detections of the HFSs and the edge-collapse have been reported in the filament *fl*. High resolution *Herschel* column density map (resolution $\sim$13.″5) is produced in this work and shows higher column densities toward both the HFSs. The *Herschel* column density map also displays two intertwined sub-filaments (i.e., *fl-A* and *fl-B*) toward the main filament *fl*. Such configuration displays almost a double helix-like pattern, which is also seen in the integrated intensity map of the JCMT $C^{18}O$(3–2) emission.

Using the TRAO ^{13}CO(1–0) and $C^{18}O$(1–0) line data cubes, we have found the existence of two cloud components (around 2 and 4 km s^{-1}) toward the main filament. The cloud component around 4 km s^{-1} has an elongated appearance like the main filament *fl*. Both the HFSs are spatially seen at the common regions of the cloud components. The origin of HFSs in *fl* may be explained by the CCC process. A careful analysis of the ^{13}CO and $C^{18}O$ emission shows the presence of non-thermal motion in *fl* with a larger Mach number. The central hub of the E-HFS shows higher values of $N(H_2)$, Mach number, and lower values of R_p compared to the W-HFS. The study of velocity profiles along the filament *fl* shows an oscillatory-like velocity pattern, favoring the presence of the intertwined structures and the fragments along *fl*. The origin of the intertwined sub-structures in *fl* seems to be explained by the scenario "fray and fragment". The study of the *Planck* polarimetric maps of potential and nearby EDC filaments (d $\lesssim$ 2 kpc) supports the detection of a curved magnetic field morphology as a signature for the edge collapse as discussed in Wang et al. (2019b). In IC 5146 dark Streamer, we suspect that the bending effect of the magnetic field toward the western hub may be diminished by the presence of evolved HFS (i.e., W-HFS). The magnetic field position angle measured from the filament's major axis shows a linear trend along the filament. This signature is confirmed in the other nearby EDC filaments. Thus, this analysis may present a more quantitative observational proxy of the EDC scenario. Taking into account all our derived results, the IC 5146 dark Streamer can be considered the first reliable candidate of edge collapse, HFSs, and intertwined sub-filaments.

Chapter 7

Unveiling the innermost environments of a hub-filament system hosting massive stars[†]

7.1 Introduction

While the preceding chapters concentrate on the ongoing physical processes occurring within filaments at larger scales, the focus of this chapter is to explore the innermost physical environment of a known HFS region in the W42 region that harbors a MYSO (Dewangan et al., 2022c). The following sections provide an overview of the interplay between turbulence and gravity in star formation, followed by the background information concerning our target site, the W42 region.

Unlike the low-mass stars, where clear evolutionary steps have been established through theory and observations (e.g., Shu et al., 1987; McKee & Ostriker, 2007), the evolution of young massive stars has no well-defined stages (Motte et al., 2018). Recent theoretical and numerical simulations have shown that the mass of newly formed stars is determined not only by small-scale mass ac-

[†]**Bhadari, N. K.**, Dewangan, L. K., Lev, E. Pirogov, Pazukhin, A. G., Zinchenko, I. I., Maity, A. K., Sharma, Saurabh, 2023, MNRAS, 526, 4402, "Fragmentation and dynamics of dense gas structures in the proximity of W42-MME"

cretion but also by large-scale, filamentary mass inflow/accretion (e.g., Padoan et al., 2020), which agrees with recent multi-scale and multi-wavelength observations (e.g., Yuan et al., 2017b; Dewangan et al., 2022c; Liu et al., 2022b; Li et al., 2022a; Xu et al., 2023; Liu et al., 2023). The low efficiency in star formation (around 1–2% in a single free-fall time scale of a cloud; e.g., Myers et al., 1986; Krumholz & McKee, 2005; Vutisalchavakul et al., 2016; Kim et al., 2021) hints that the turbulence and magnetic fields prevent the gravitational collapse of molecular clouds (Myers & Goodman, 1988; Vazquez-Semadeni et al., 2000; Bergin & Tafalla, 2007; Hennebelle & Inutsuka, 2019; Krumholz & Federrath, 2019). Also, the profound work by Larson (1981) and follow up studies (e.g., Goodman et al., 1998; Solomon et al., 1987; Bolatto et al., 2008; Heyer et al., 2009; Cen, 2021; Zhou et al., 2022, and references therein) suggest that turbulence dissipates into the smaller regions of clumps and cores which are more prone to gravitational collapse and subsequent star formation. Consequently, the non-thermal motions on the scale of dense star-forming cores ($\sim$0.1 pc) can be sonic (e.g., Myers & Goodman, 1988; Caselli et al., 2002), which agrees with the observations of filamentary, low-mass star-forming clouds (Hacar & Tafalla, 2011; Hacar et al., 2017; Pineda et al., 2015). However, the nature of turbulence in the massive star-forming clumps/cores remains ambiguous, as previous studies have shown a range of supersonic ($\mathcal{M}$ $\geq$2; e.g., Carolan et al., 2009) to subsonic ($\mathcal{M}$ $\leq$1; e.g., Li et al., 2020) non-thermal velocity dispersion.

Recent observations hint that the MSF involves simultaneous onset of multiple physical processes from the scales of molecular clouds (>10 pc) to cores ($\leq$0.1 pc; Fukui et al., 2021a; Hacar et al., 2022; Bhadari et al., 2022, and references therein). This may be possible because of the hierarchical fragmentation process (i.e., fragmentation of cloud to high density structures of filaments, clumps and cores) that is primarily driven by the effect of turbulence and gravity (Goodman et al., 2009; Inoue & Fukui, 2013; Padoan et al., 2020; Fukui et al., 2021b,a; Federrath et al., 2021). The gas motions of molecular clouds are coherent across scales of >10 pc to $\sim$0.1 pc, and exhibit a universal velocity-size scaling relation observed in different environments (e.g., Solomon et al., 1987; Zhou et al., 2022;

Liu et al., 2022a). This indicates that the dense fragments at different spatial scales are kinematically connected (Rosolowsky & Leroy, 2006; Rosolowsky et al., 2008; Goodman et al., 2009). In context to recent studies, the velocity dispersion-size relation appear to follow the Larson (1981) first relation of $\Delta V \propto R^{0.38}$ with power law index in the range of 0.3–1.2 for larger scales (100–0.1 pc) (e.g., Fuller & Myers, 1992; Goodman et al., 1998; Heyer et al., 2009; Falgarone et al., 2009; Cen, 2021; Izquierdo et al., 2021), where ΔV and R are the velocity dispersion and radius of cloud. The observed relation resembles the energy cascade in turbulent systems, indicating that turbulence dissipates from larger spatial scales to smaller ones. The other two Larson's relations imply the virial equilibrium with the constant surface densities over all the spatial scales. However, at the smaller scales of clouds where the density becomes high and multiple centers of collapse form, the role of both gravity and turbulence become important and hence at these scales the Larson's relations are debatable (i.e.,$<$0.1 pc; Ballesteros-Paredes et al., 2006, 2011; Traficante et al., 2018a,b). As a result, the effect of gravity and turbulence during the early stages of star formation including the massive ones, is one of the current hot topics in star formation research (e.g., Ballesteros-Paredes et al., 2018; Federrath et al., 2021, and references therein).

The recent advancement of observational facilities such as the ALMA has provided a great insights to the core scales in star-forming regions. It extends our limit of studying the gas kinematics of dense structures form cloud to the core scales. This work primarily makes use of the ALMA $H^{13}CO^+$ (4–3) data and presents a comprehensive study of the dense gas kinematics of a small area in W42 region (distance $\sim$3.8 kpc; see Dewangan et al., 2022c, and references therein), known to host a bipolar HII region and Class II 6.7 GHz MME (Dewangan et al., 2015). The HII region is powered by an O5-O6 star (O5.5, hereafter; Blum et al., 2000), and the ionized and molecular gas have similar velocities of about 60 km s^{-1}, suggesting they are part of the same physical system (Quireza et al., 2006; Anderson et al., 2009; Dewangan et al., 2015). The infra-red counterpart of 6.7 GHz MME in W42 (W42-MME, hereafter) is a rare young massive protostar (or massive young stellar object; MYSO hereafter), believed to be in an early evolutionary stage (Dewangan et al., 2015, 2022c; De Buizer et al., 2022). It has a luminosity of approximately 4.5 $\times$ 10^4 $L_\odot$ and is located at the center of a parsec-scale bipolar outflow in H_2 image (see Dewangan et al., 2015, for more details). Figure 7.1a shows the ALMA 1.35 mm image of an extended area ($\sim$45$''$.4 $\times$ 45$''$.4) in the direction of W42-MME, which is further zoomed in to the 865 μm continuum image in Figure 7.1b. The positions of W42-MME and the O5.5 star are also marked. Recent high-resolution ($\sim$0$''$.3) molecular line study based on the ALMA data shows that the dusty envelope ($\sim$9000 AU) surrounding W42-MME hosts at least five continuum peaks (Dewangan et al., 2022c). One of the major peaks associated with W42-MME shows the signature of bipolar outflow and a disk-like feature with velocity gradients. This study by Dewangan et al. (2022c) suggests that MYSO W42-MME gains mass from its disk and the dusty envelope simultaneously. In the larger physical extent of $\sim$3–5 pc, these authors found the presence of HFS which hosts our target region of study at its central hub region ($\sim$1–2 pc; see Figure 14 in Dewangan et al., 2022c). It is to be noted that both the main sequence O5.5 star and the MYSO belong to the hub region. The radio continuum emission is also observed at 6 cm wavelength in the target area (see Figure 1c in Dewangan et al., 2022c). Targeting such region for high-resolution multi-wavelength and multi-scale study provides us a comprehensive understanding of different factors involved in MSF from the molecular cloud ($> 5 - 10$ pc) to core scale (< 0.1 pc).

In this work we primarily utilized the high-resolution ALMA $H^{13}CO^+$ data to study the physical and kinematic properties of immediate surroundings of MYSO W42-MME, including the dusty envelope. The work is structured as follows: Section 8.1 serves as an introduction to the study, Section 7.2 provides the description of data used in this study, and Section 7.3 outlines the results obtained from dendrogram analysis. Finally we discuss the consequences of the derived results in Section 7.4 and summarize the outcomes in Section 7.5.

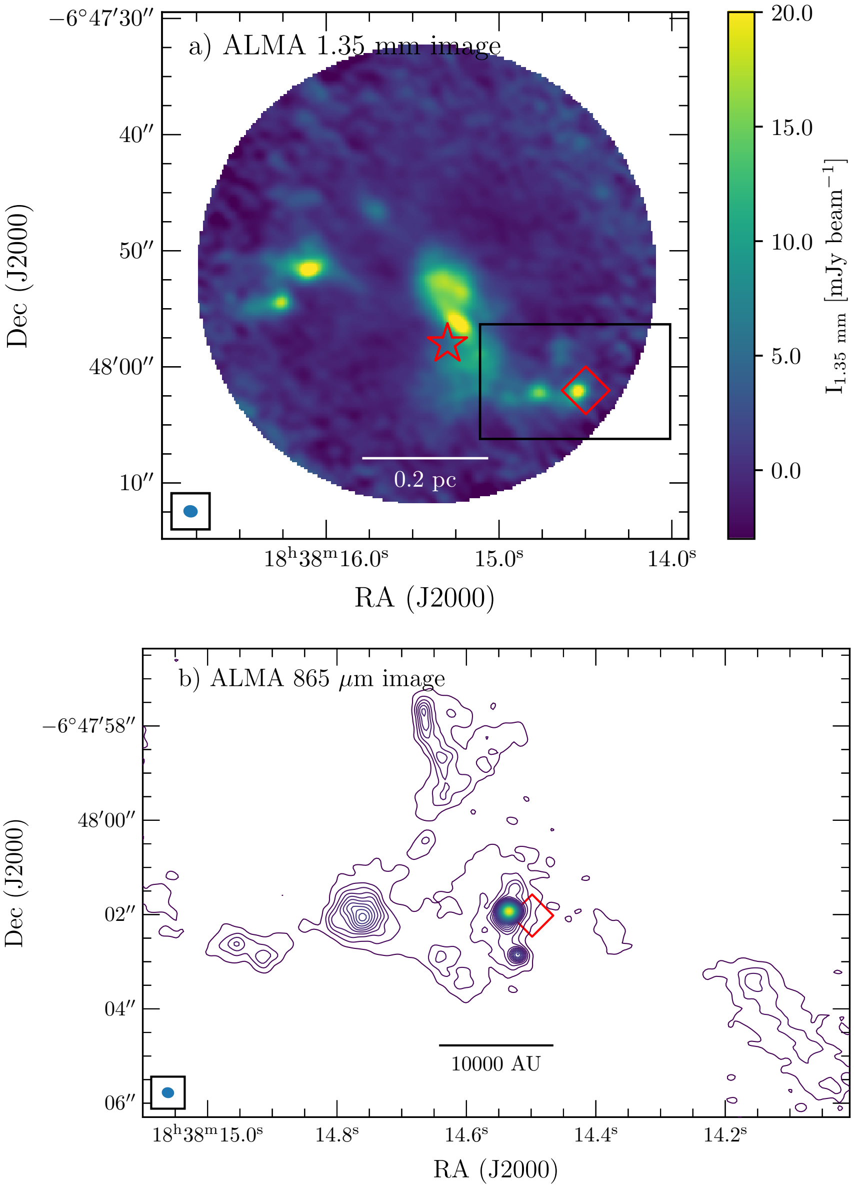

Figure 7.1: a) ALMA 1.35 mm continuum emission map of an extended area around W42-MME. b) ALMA 865 μm dust continuum contour map of an area marked by rectangular box in panel "(a)". The emission contour ranges from 0.4 to 43.55 mJy beam^{-1} (i.e., maximum intensity of the image) in steps of 0.43 mJy beam^{-1}. The positions of the 6.7 GHz MME and ionizing O-type star are marked by diamond and star symbols, respectively. The scale bars are shown at d = 3.8 kpc. The beam size of ALMA images are shown in bottom-left corner.

7.2 ALMA Data Sets

This work utilizes HCO$^+$(4–3) (ν ~356.734 GHz), H^{13}CO$^+$(4–3) (ν ~346.998 GHz), and CH$_3$CCH (21_K–20_K) (ν ~358.709–818 GHz) data obtained from the ALMA in Band 7, acquired under project ID: #2018.1.01318.S (PI: Lokesh Kumar Dewangan). The observed data has a beam size of 0″.31× 0″.25. The details of data acquisition and reduction are given in Dewangan et al. (2022c). Additionally, we have utilized the ALMA continuum data at 865 μm ($\nu \sim$346.5 GHz) from Dewangan et al. (2022c), which has a similar resolution to that of the line data. Furthermore, the publicly available ALMA continuum map at 1.35 mm (resolution $\sim$1$''$.2 $\times$ 1$''$.1) is obtained from the ALMA science archive (project ID #2019.1.00195.L; PI: Molinari, Sergio). It is used to display the large area around W42-MME in Figure 7.1a. The high-resolution Very Large Telescope (VLT) NAOS-CONICA (NACO) NIR adaptive-optics image at K_s band (λ=2.18 μm; resolution $\sim$0$''$.2) is also utilized from Dewangan et al. (2015, see more details in their paper).

We used the ALMA $H^{12}CO^+$/$H^{13}CO^+$ data to analyze the dense gas kinematics and the CH_3CCH (21_K–20_K) data to estimate the temperature of the dense gas. In addition, we employed dust continuum maps to determine the mass of dense gas.

7.3 Results

7.3.1 Dendrogram analysis of ALMA $H^{13}CO^+$(4–3)

Dendrogram analysis is a powerful tool for studying the physical properties of hierarchical structure of star-forming molecular clouds. The dendrogram methodology, as described by Rosolowsky et al. (2008), involves creating a tree diagram that characterizes emission structures based on their three-dimensional intensity isocontours. This method allows us to extract the emission structures at different spatial scales in a position-position-velocity (*p-p-v*) space, which is critical for understanding the complex interplay between dense gas kinematics, temperature, and star formation (e.g., Shetty et al., 2012). The dendrogram is a hierarchical tree structure composed of two components: branches and leaves. Branches can split into multiple sub-structures (i.e., new branches and leaves), while leaves have no sub-structures. In this context, leaves (i.e., potential star-forming cores) represent the small-scale, bright structures at the tips of the tree that do not break down into further substructures. Branches (i.e., clumps), on the other hand, represent the large-scale, fainter structures lower in the tree that do break down into substructures.

To perform the dendrogram analysis, we utilized the python-based *astrodendro*[*] package. This tool offers a method for determining the dendrogram structures within astronomical data in either 2D position-position (p-p) maps or 3D p-p-v data cubes. The algorithm *astrodendro* works by dividing the p-p-v data cube into a set of regions based on the distribution of intensity. The regions are then grouped together based on the specified similarity criterion, such as a threshold emission. This grouping process is repeated recursively until all of the regions are grouped together into a single structure. The result of this process is a tree-like diagram, or dendrogram, which represents the hierarchical structure of the cloud.

7.3.1.1 Structure Identification and $H^{13}CO^+$ (4–3) moment maps

We applied the dendrogram analysis to the ALMA $H^{13}CO^+$ (4–3) data (in p-p-v space) on 0.304 × 0.181 pc^2 area of our target region (see area footprint in Figure 7.1b) in order to extract the hierarchical structure of the dense gas in the W42-MME region. The ALMA $H^{13}CO^+$ (4–3) line emission reveals mostly single peaked profiles toward the entire area of our target site, which is noticeable from Figure 7.2 presenting the overlay of averaged $H^{13}CO^+$ spectra over the regular grids of $0''.864 \times 0''.432$ toward our target site. The background image is $H^{13}CO^+$ integrated intensity map (see following text in this Section). The hierarchical tree diagram of dendrogram structures is extracted and is shown in Figure 7.3. This exercise allowed us to identify and classify the different scales of the dense gas emission in the cloud, from the small-scale structures (i.e., $\lesssim$ 0.01 pc) to relatively larger structures($\geq$ 0.05 pc). Below are the steps we followed to identify the dendrogram structures.

To enhance the performance of the dendrogram algorithm, pixels with noise levels lower than three times the local noise level were masked out. By analyzing

[*]https://dendrograms.readthedocs.io/en/stable/index.html

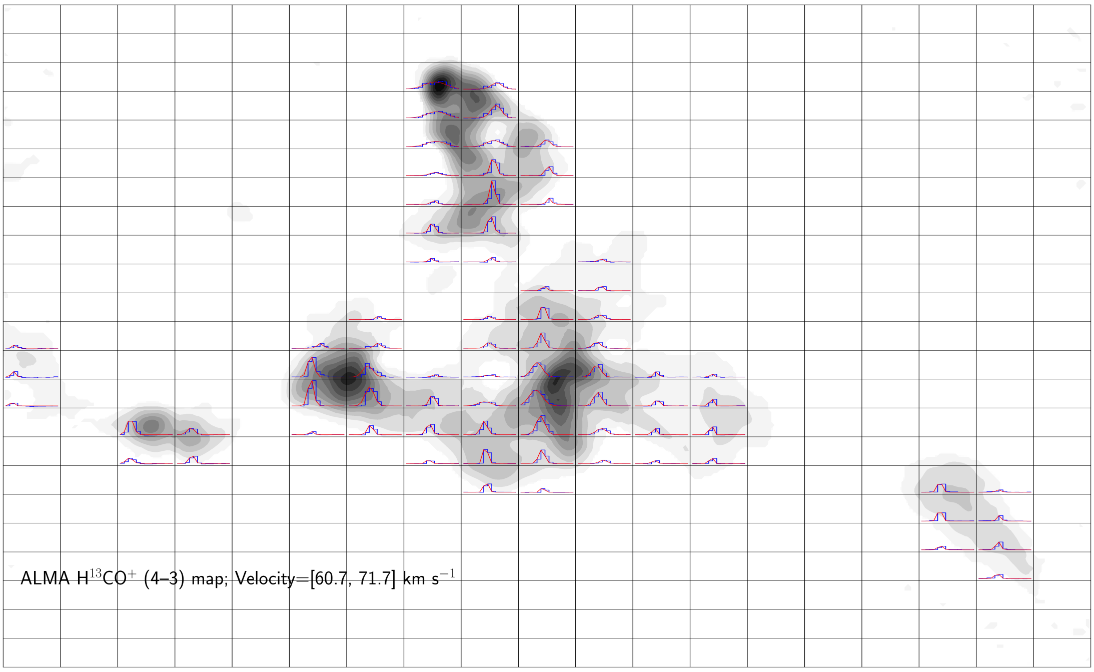

Figure 7.2: ALMA $H^{13}CO^{+}$(4–3) moment-0 map overlaid with the averaged velocity profiles extracted along the regular grids of size $0''.864 \times 0''.432$. The extent of figure is identical to that of the Figure 7.1b. Profiles in red are the 1-D Gaussian fit to the observed spectra (in blue). The y-scale ranges from −2.94 to 89.14 mJy beam^{-1}, while x-scale is V_{LSR} from 60.73 to 71.70 km s^{-1}.

the source/emission free individual velocity channels, we found that the local noise (or rms) varies from 1.6 to 3 mJy beam^{-1} with mean value of $\sigma_{\rm rms}$=2.3 mJy beam^{-1}. The estimated $\sigma_{\rm rms}$ value is close to that of obtained by Dewangan (2022) for a spectral resolution of 0.242 MHz. We therefore masked out the noisy pixels which are below 3$\sigma_{\rm rms}$ (=7 mJy beam^{-1}) from the $H^{13}CO^{+}$ (4–3) data cube. This step is equivalent to set the "min_value" parameter of *astrodendro* algorithm, which signifies the minimum emission in the Dendrogram tree structure. We further specified the values of other two crucial parameters used as inputs for the *astrodendro* algorithm. These are "min_delta", and "min_npix". The parameter "min_delta", that indicates the minimum difference between two intensity peaks such that they can be considered as separate structures, was set to be 1$\sigma_{\rm rms}$ (=2.3 mJy beam^{-1}). The another parameter "min_npix" indicates the minimum number of spatial-velocity pixels required for a leaf structure to be considered as independent entity. We have chosen this value such that a dendrogram structure contains at least two synthesized beam of ALMA $H^{13}CO^{+}$ (4–3) data. This is essential in order to measure the structure size and line width (Rosolowsky &

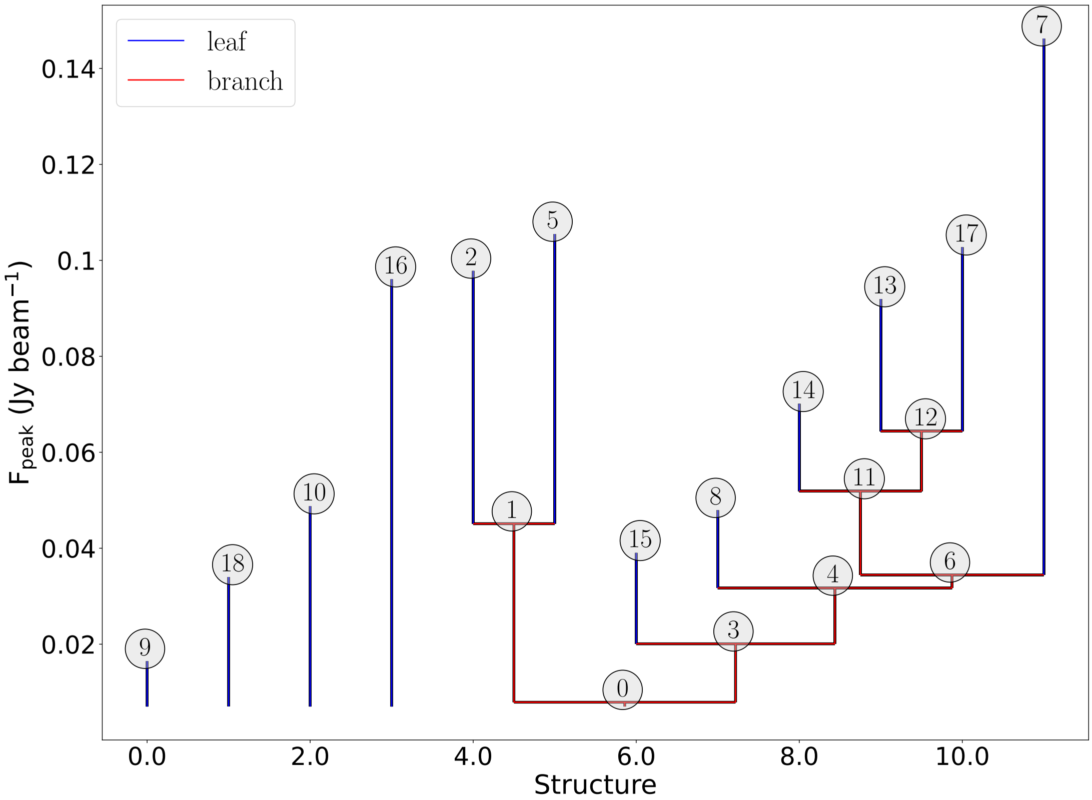

Figure 7.3: Dendrogram tree of hierarchical structures identified from ALMA $H^{13}CO^+$(4–3) data. The leaves and branches are marked in the tree structure (see also Figure 7.4).

Leroy, 2006). Thus, "min_npix" was set to be 74 pixels (1 pixel= 0″.048). The algorithm ultimately identified 19 structures including 7 branches and 12 leaves. Figure 7.3 displays the branches and leaves structures in the dendrogram tree.

We have superimposed the spatial distribution of the identified leaf structures on the peak intensity (F_{peak}) map of the ALMA $H^{13}CO^+$ (4–3) data, as shown in Figure 7.4a. Each leaf structure is marked with its corresponding structure ID. The map provides a snapshot of the overall peak intensity distribution of the dense molecular gas. The dendrogram methodology can be understood by comparing the dendrogram tree structure (see Figure 7.3) and the peak intensity map (see Figure 7.4a). Figure 7.4b presents the peak velocity (V_{peak}) map of the ALMA $H^{13}CO^+$ (4–3) data which infers the gas velocity at peak intensity. A coherent velocity structure is noticeable along the *Dec* $\sim -06°47''02'$ at velocity of [62, 66] km s^{-1}. The northern structure, however, is seen at the redshifted velocities (see more discussion in Section 7.4). Figure 7.4b also shows the overlay of leaf structures on the V_{peak} map of $H^{13}CO^+$ emission, by their corrected sky-projected size. To infer the presence of point-like sources in our target area, we have displayed the VLT/NACO adaptive-optics K_s band image of our target region in Figure 7.4c and overlaid the footprints of leaves and branches. As can be seen in Figures 7.4a–c (for comparison see Figure 7.3), the central region is identified as dendrogram structure B0, which is separated from the other structures. This branch is further divided into 6 sub-branches and 8 leaves. Notably, leaf L17 belongs to the W42-MME, which has been previously described in (Dewangan, 2022). Based on the VLT/NACO adaptive-optics K_s band image, here we note that most of the point sources do not lie in the direction of identified structures. In other words, the turbulence in most of the dendrogram structures do not seem to be influenced by the presence of point-like sources.

We have also computed the moment statistics of ALMA $H^{13}CO^+$ (4–3) data. In millimeter–radio astronomy, moment maps provide a way to characterize the distribution of emission over a region of the sky. The first three moments i.e., moment-0; $M_0 = \int I_v dv$, moment-1; $M_1 = \frac{\int v I_v dv}{M_0}$, and moment-2; $M_2 = \sqrt{8ln2} \times \sqrt{\frac{\int I_v (v - M_1)^2 dv}{M_0}}$, refer the integrated intensity over spectral/velocity axis, intensity weighted centroid velocity, and intensity weighted velocity dispersion (full width at half maximum (FWHM)), respectively. Figure 7.5a presents the M_0 map of ALMA $H^{13}CO^+$ emission in the direction of our target region, inferring the overall intensity/density distribution of dense gas. The velocity range of [60.73, 71.70] km s^{-1} has been used for generating the M_0 map and identifying the dendrogram structures in p-p-v space. Figure 7.5b shows the M_1 map providing the information of gas velocity distribution. The M_2 map of extended area around W42-MME is shown in Figure 7.5c, revealing the ALMA $H^{13}CO^+$ FWHM linewidth distribution. The high value of velocity dispersion in the northern knot (leaf ID L2) is possible because of the presence of multiple velocity components (see blue spectra in Figure 7.2). However in the direction of W42-MME (leaf ID L17) and other leaves (ID L8 and L13), the high-dispersion value is observed regardless of the absence of multiple velocity components in $H^{13}CO^+$ spectra (see Figure 7.2).

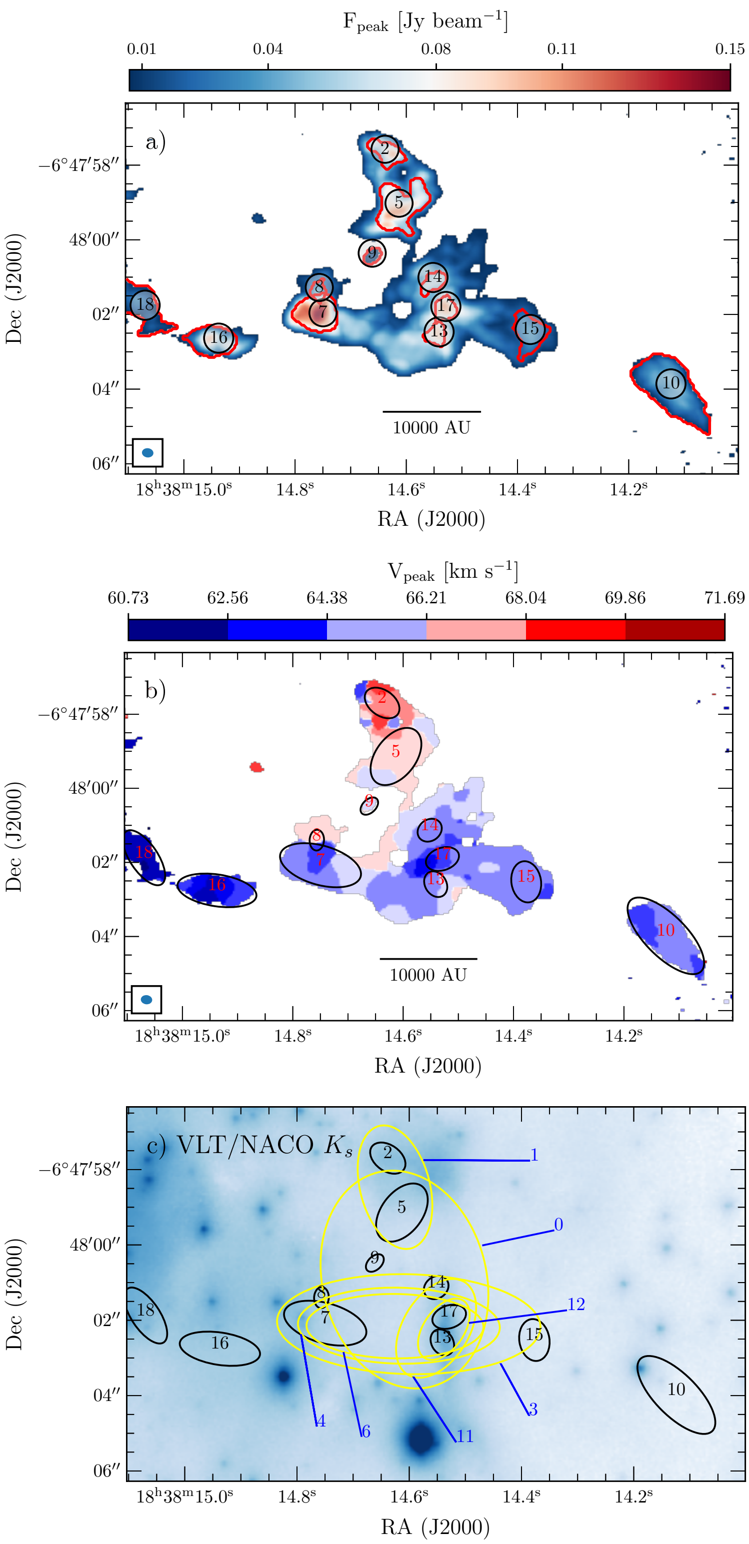

Figure 7.4: a) ALMA H^{13}CO$^+$(4–3) peak intensity map of region hosting W42-MME. The *astrodendro* identified leaf structures are overlaid and shown with contours and associated IDs, respectively. (b) Peak velocity map derived using ALMA H^{13}CO$^+$(4–3) emission. c) VLT/NACO adaptive-optics K_s band image. In panels "b" and "c", the ellipses approximating the leaves (in black) and branches (in yellow) are shown. The structure ID for leaves and branches are displayed.

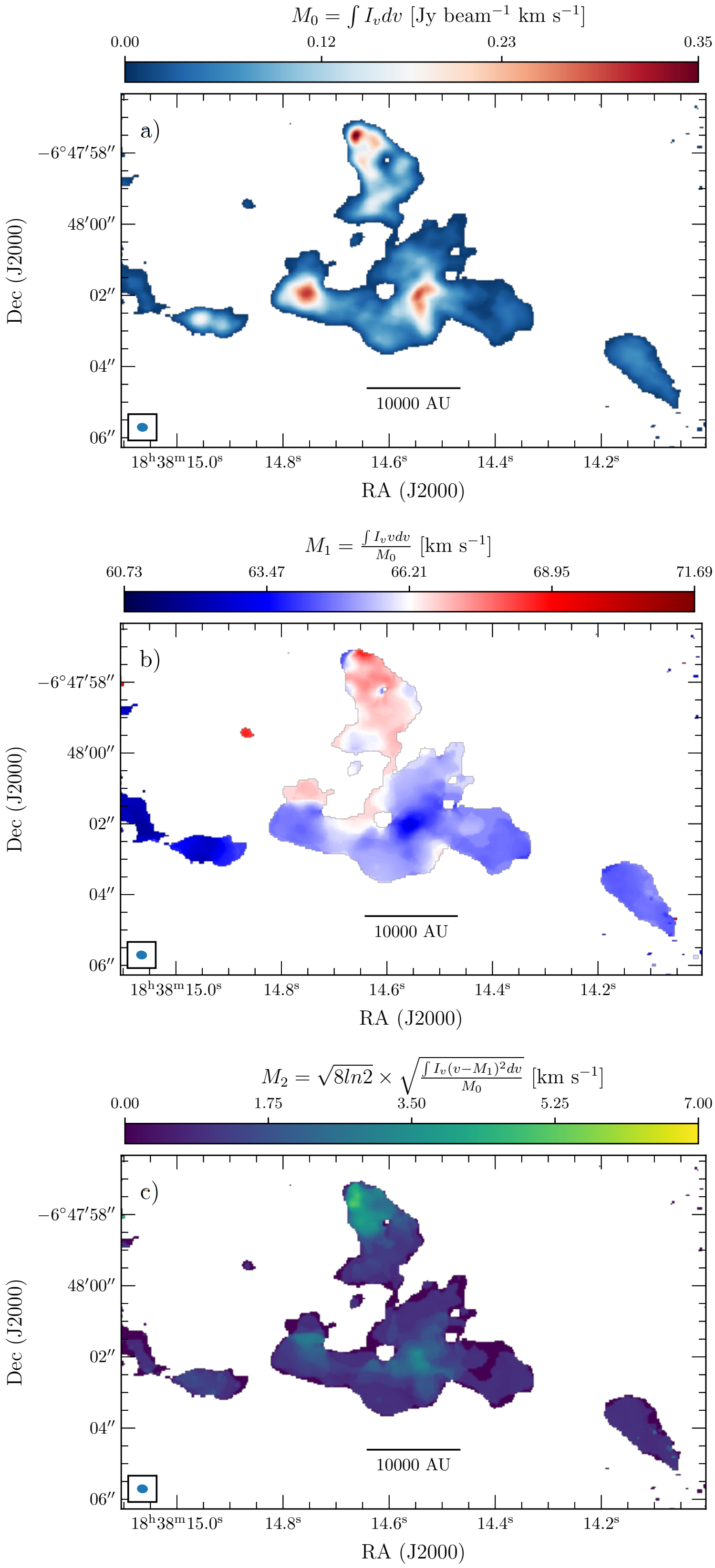

Figure 7.5: ALMA $H^{13}CO^+$ emission map of a) integrated intensity in the velocity range of [60.73, 71.70] km s^{-1} (moment-0 map), b) intensity weighted velocity (moment-1 map) and b) intensity weighted FWHM velocity dispersion (moment-2 map) toward region hosting W42-MME.

7.3.2 Physical parameters of dendrogram structures

The major and minor axis of dendrogram structures are related to *astrodendro* output parameters of "major_sigma" and "minor_sigma", which represent the 2nd spatial moments along longer and shorter direction, respectively. To obtain the physical extension of dendrogram structures (or major axis $\times$ minor axis), we need to multiply the outputs (i.e.,"major_sigma" and "minor_sigma") by $\sqrt{8\ \ln 2}$. We have also taken account of the filling factor (f) as discussed in Liu et al. (2022a). In other words, the *astrodendro* derived major and minor axis are less by a factor of $f = \sqrt{A_{\rm exact}/A_{\rm ellipse}}$, where $A_{\rm exact}$ and $A_{\rm ellipse}$ are the exact and calculated areas of Dendrogram structures in the sky plane (see also Rosolowsky et al., 2008; Liu et al., 2022a).

Table 7.1 lists the physical parameters of all identified structures, including structure ID, sky coordinates, integrated flux ($F^{\rm int}$), structure size (major axis($''$) $\times$ minor axis($''$)), structure length (L), position angle (PA; measured counter-clockwise from the RA axis), gas kinetic temperature ($T_{\rm kin}$), weighted mean velocity ($\langle V_{\rm lsr}\rangle$), velocity variation ($\delta V_{\rm lsr}$), observed weighted mean velocity dispersion ($\langle\sigma_{\rm obs}\rangle$), non-thermal velocity dispersion ($\langle\sigma_{\rm nt}\rangle$), three-dimensional (3D) Mach number ($\mathcal{M}_{\rm 3D}$), and the number of ALMA beams (N) that can fit within each structure. The estimation of $T_{\rm kin}$ is presented in Section 7.3.2.1. We have also computed the gas mass ($M_{\rm s}$), virial mass ($M_{\rm vir}$), virial parameter ($\alpha_{\rm vir}$), and gas density (n) of each dendrogram structure in Section 7.3.2.2.

We estimated the size of dendrogram structures by taking the geometric mean of corrected major and minor axes using the formula

$$L({\rm AU}) = {\rm D(pc)}\ \sqrt{\text{major axis}('') \times \text{minor axis}('')}, \tag{7.1}$$

where $D(= 3.8 \times 10^3)$ pc is the distance of W42. The $\langle V_{\rm lsr}\rangle$ represents the error-weighted mean velocity and is estimated using the M_1 map (see Figure 7.5b) and the corresponding uncertainty map. Similarly, the weighted line-of-sight velocity dispersion/linewidth, $\langle\sigma_{\rm obs}\rangle$, is inferred from the M_2 map (see Figure 7.5c) and the respective error map. The uncertainties in the M_1 and M_2 maps are derived using Equations 5 and 6 from Teague (2019, not shown here). The final error in

Table 7.1: Physical parameters of Dendrogram structures identified using ALMA $H^{13}CO^+$ data in W42 region.

ID	$RA(J2000)$	$Dec.(J2000)$	$F^{int}_{H^{13}CO^+}$	$F^{int}_{865\ \mu m}$	major × minor axis	L	PA	T_{kin}	$\langle V_{lsr} \rangle$	δV	$\langle \sigma \rangle$	$\langle \sigma_{nt} \rangle$	$\mathcal{M}_{3D}$	M_s	M_{vir}	α_{vir}	n	N
	hh:mm:sss	dd:mm:sss	Jy	mJy	arcsec × arcsec	($\times10^3$) AU	deg	K	km s^{-1}	km s^{-1}	km s^{-1}	km s^{-1}		$M_\odot$	$M_\odot$		($\times10^5$) cm^{-3}	
					Leaves													
L2	18:38:14.64	-6:47:57.66	0.76	10.72	1.05 × 0.7	3.24	144.67	64.28 ± 5.25	67.18 ± 0.01	0.37 ± 0.02	1.38 ± 0.02	1.37 ± 0.02	5.0	0.2	12.44	64.54	13.77	7.0
L5	18:38:14.61	-6:47:59.14	1.5	22.18	1.77 × 1.1	5.27	52.26	61.84 ± 6.78	66.59 ± 0.02	0.3 ± 0.01	0.53 ± 0.02	0.52 ± 0.02	1.91	0.42	4.54	10.9	6.91	18.0
L7	18:38:14.75	-6:48:02.05	2.61	76.41	2.27 × 1.07	5.91	164.47	45.02 ± 1.99	65.18 ± 0.02	0.45 ± 0.02	0.52 ± 0.02	0.51 ± 0.02	2.22	2.08	4.11	1.98	24.56	22.0
L8	18:38:14.76	-6:48:01.37	0.08	4.46	0.57 × 0.4	1.79	87.28	64.02 ± 8.27	66.24 ± 0.04	0.65 ± 0.06	0.83 ± 0.05	0.82 ± 0.05	2.99	0.09	2.97	36.79	34.48	2.0
L9	18:38:14.66	-6:48:00.47	0.03	1.78	0.57 × 0.36	1.72	223.34	–	66.04 ± 0.13	0.23 ± 0.02	0.24 ± 0.1	–	–	–	–	–	–	2.0
L10	18:38:14.13	-6:48:03.96	1.1	38.44	2.72 × 1.13	6.64	135.23	52.09 ± 11.81	64.62 ± 0.03	0.22 ± 0.01	0.34 ± 0.02	0.32 ± 0.03	1.28	0.88	3.05	3.47	7.31	28.0
L13	18:38:14.54	-6:48:02.56	0.39	12.32	0.74 × 0.58	2.48	122.97	63.56 ± 2.79	64.96 ± 0.02	0.36 ± 0.03	0.85 ± 0.03	0.84 ± 0.03	3.08	0.23	4.46	19.88	35.64	4.0
L14	18:38:14.55	-6:48:01.12	0.22	4.03	0.7 × 0.58	2.41	215.05	34.79 ± 8.92	65.16 ± 0.03	0.15 ± 0.01	0.49 ± 0.05	0.48 ± 0.05	2.39	0.15	1.69	11.22	26.3	4.0
L15	18:38:14.38	-6:48:02.52	0.23	4.14	1.12 × 0.81	3.61	99.23	33.1 ± 2.84	64.67 ± 0.04	0.05 ± 0.01	0.4 ± 0.05	0.39 ± 0.05	1.96	0.17	1.79	10.88	8.5	8.0
L16	18:38:14.94	-6:48:02.74	1.12	20.19	2.17 × 0.86	5.19	171.56	–	63.37 ± 0.03	0.56 ± 0.02	0.44 ± 0.03	–	–	–	–	–	–	17.0
L17	18:38:14.53	-6:48:01.87	0.65	67.05	0.93 × 0.61	2.85	198.2	69.71 ± 2.7	64.06 ± 0.01	0.41 ± 0.03	0.98 ± 0.02	0.97 ± 0.02	3.42	1.11	6.18	5.62	115.81	5.0
L18	18:38:15.07	-6:48:01.84	0.24	5.19	1.73 × 0.76	4.34	124.16	–	62.37 ± 0.04	0.34 ± 0.02	0.2 ± 0.03	–	–	–	–	–	–	12.0
					Branches													
B0	18:38:14.61	-6:48:00.90	18.36	237.21	5.87 × 4.38	19.27	104.41	58.94 ± 3.87	65.8 ± 0.02	0.82 ± 0.01	0.43 ± 0.01	0.41 ± 0.01	1.56	4.71	13.75	2.92	1.6	234.0
B1	18:38:14.63	-6:47:58.45	5.88	57.56	3.36 × 1.86	9.51	104.98	62.03 ± 3.27	66.66 ± 0.02	0.57 ± 0.01	0.66 ± 0.02	0.65 ± 0.02	2.41	1.08	10.53	9.78	3.05	57.0
B3	18:38:14.60	-6:48:02.09	12.23	263.92	7.05 × 2.66	16.43	178.62	56.08 ± 2.04	65.33 ± 0.02	0.67 ± 0.01	0.43 ± 0.01	0.41 ± 0.01	1.58	5.55	9.49	1.71	3.04	170.0
B4	18:38:14.62	-6:48:02.12	9.32	222.2	5.4 × 2.02	12.55	178.8	57.0 ± 2.44	65.44 ± 0.02	0.7 ± 0.01	0.52 ± 0.01	0.51 ± 0.02	1.96	4.59	9.11	1.99	5.64	99.0
B6	18:38:14.63	-6:48:02.12	7.24	183.69	4.73 × 1.71	10.81	179.47	57.09 ± 3.71	65.48 ± 0.02	0.74 ± 0.01	0.56 ± 0.02	0.53 ± 0.02	2.05	3.79	8.26	2.19	7.27	74.0
B11	18:38:14.55	-6:48:02.20	4.22	135.47	2.89 × 1.77	8.59	57.99	64.33 ± 3.52	64.92 ± 0.02	0.57 ± 0.01	0.62 ± 0.02	0.6 ± 0.02	2.19	2.44	8.98	3.69	9.34	46.0
B12	18:38:14.54	-6:48:02.23	1.98	96.85	1.85 × 1.08	5.35	54.69	68.23 ± 2.62	64.53 ± 0.01	0.59 ± 0.02	0.81 ± 0.02	0.8 ± 0.02	2.81	1.63	8.18	5.03	25.86	18.0

the mean of a parameter, denoted as P (i.e., $V_{\rm lsr}$ or $\sigma_{\rm obs}$), is computed as :

$$\Delta\langle P\rangle = \frac{1}{k}\sqrt{\sum_{i}^{k}\Delta p_i^2}, \tag{7.2}$$

where Δp_i and k are the uncertainty in measurements of P at i^{th} pixel and the total number of pixels within the footprint of dendrogram structures, respectively. The velocity variation, $\delta V_{\rm lsr}$, representing the plane-of-sky velocity dispersion, is estimated as the standard deviation of $V_{\rm lsr}$ within the structure. Its uncertainty is given by $\delta V_{\rm lsr}/\sqrt{2(k-1)}$.

Additionally, we derived the non-thermal velocity dispersion as:

$$\langle\sigma_{\rm nt}\rangle = \sqrt{\langle\sigma_{\rm obs}^2\rangle - \sigma_{\rm th}^2}, \tag{7.3}$$

where $\sigma_{\rm th}$ is the thermal velocity dispersion for dendrogram structure, and is given by

$$\sigma_{\rm th} = \sqrt{\frac{k_{\rm B}\ T_{{\rm kin},i}}{\mu m_{\rm H}}}. \tag{7.4}$$

In Equation 7.4, μ=30 is the the molecular weight of the $H^{13}CO$ molecule, $m_{\rm H}$ is the mass of atomic hydrogen (approximating to proton mass), $k_{\rm B}$ is the Boltzmann constant, and $T_{{\rm kin},i}$ is the gas kinetic temperature of the i^{th} structure derived using CH_3CCH (21_K–20_K) emission (see Section 7.3.2.1). The value of sound speed $c_{\rm s}$ in a medium is influenced by all the gas particles present in it. This can be determined using Equation 7.4 with a mean molecular weight per free particle of μ=2.37 (Kauffmann et al., 2008). The 3D Mach number, $\mathcal{M}_{\rm 3D}$, is estimated by $\sqrt{3}\sigma_{\rm nt}/c_{\rm s}$.

7.3.2.1 Dense gas temperature ($T_{\rm kin}$) estimation

Previous studies show that the low excitation level (e.g., J =5–4) transitions from CH_3CCH molecule give a good estimate of the kinetic temperature at gas density of $\sim10^{3-4}$ cm^{-3} (Kuiper et al., 1984; Bergin et al., 1994) . However, the higher level transitions can trace gas density $\geq10^{5-6}$ cm^{-3} (e.g., Aladro et al., 2010; Santos et al., 2022), which can be used to estimate the gas temperature of dense environment as traced by HCO^+ (4–3) transition with a critical density of (i.e., $\sim 3.5 \times 10^6$ to 2×10^6 cm^{-3} for the temperature range of 10–100 K, respectively; Shirley, 2015). Therefore, we utilized the ALMA Band 7 CH_3CCH data to estimate the gas kinetic temperature ($T_{\rm kin}$) of dendrogram structures identified in $H^{13}CO^+$ (4–3) transition. The observed data contains five components of the CH_3CCH (21–20) K-ladder with K = 0-4, and we generated the corresponding averaged spectrum for each dendrogram leaf and branch structure. The rotational temperatures for the dendrogram leaf and branch structures are determined using these transitions. The spectrum and corresponding rotation diagrams of leaf L17 are presented in Figure 7.6. The diagram plots the values proportional to natural logarithm of the measured integrated line intensity, S_ν, against the upper energy level E_u of specified molecule. The $y-$axis corresponds to a parameter defined by the quantum numbers J and K, the transition frequency ν, the dipole moment μ, the degeneracy g_K associated with the internal quantum number K, and the statistical weight g_I associated with the nuclear spin. The slope a of the fitted straight line, $y = ax + b$, is related to the kinetic temperature, $T_{\rm kin} = -\frac{1}{a}$, while the uncertainty in the estimation of $T_{\rm kin}$ is $\Delta T_{\rm kin} = \frac{\Delta a}{a^2}$.

The temperature estimates for leaf structures ranged from 33 to 70 K, with the mean (median) values of 54.27 (61.84) K, while for branches the range is [56.08, 68.23] K with mean (median) value of 60.53 (58.94) K. It is important to note that in the case of leaves L9, L16, and L18, weak emission is observed in CH_3CCH (21–20) line, which made it difficult to define $T_{\rm kin}$ of these structures.

7.3.2.2 Dense gas mass (M_s) and virial parameter ($\alpha_{\rm vir}$) estimation

The dust/gas mass can be estimated from the knowledge of the dust emission in the interstellar medium (ISM). With the assumption of spherical dust grains and the optically thin dust emission as a modified black body emission in the Rayleigh-Jeans limit, the gas mass can be estimated as:

$$M_{\rm s} = \frac{F_\nu \; D^2 \; R_t}{B_{(\nu,T_d)} \; k_\nu}, \tag{7.5}$$

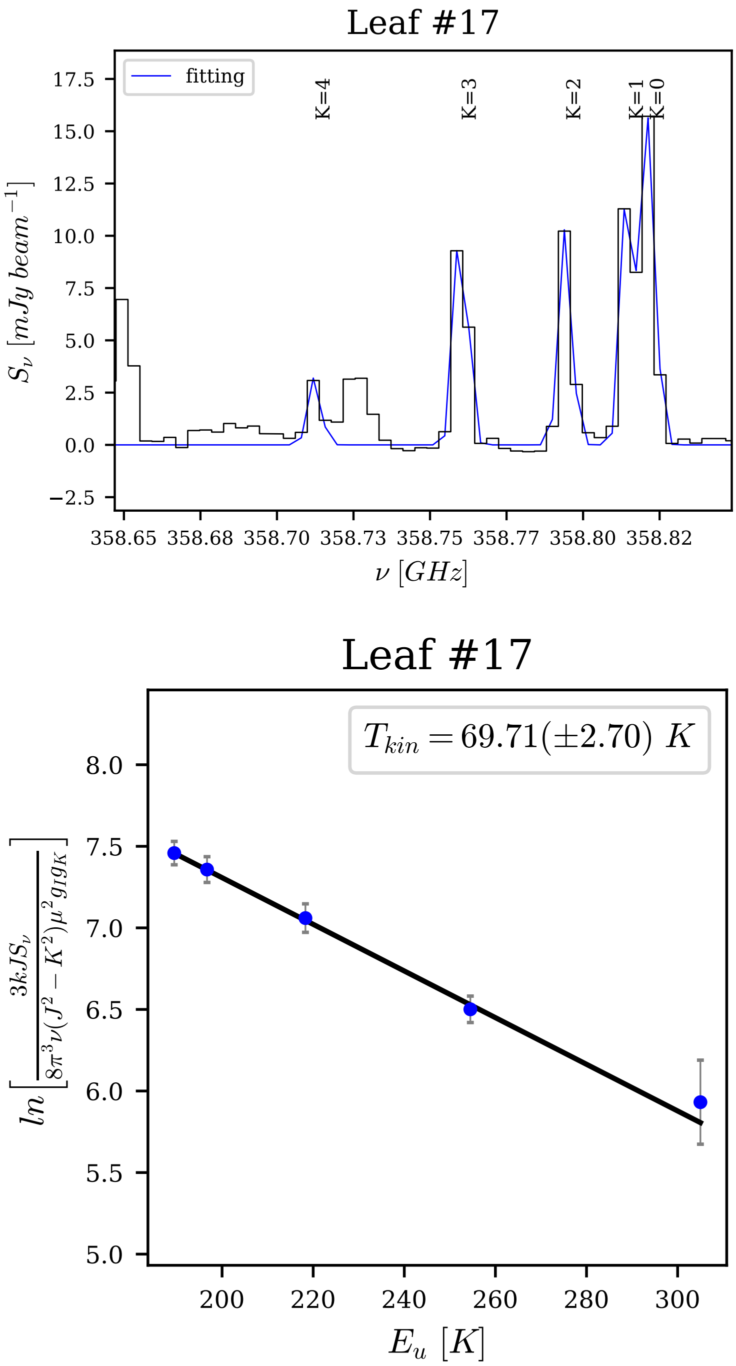

Figure 7.6: *Upper panel*: Averaged CH_3CCH (21_K–20_K) spectra (in black) and best fit model of CH_3CCH lines (in blue) for Dendrogram leaf L17. *Lower panel*: CH_3CCH rotation diagrams of leaf L17 (see text for details). A best fit line to the 5 CH_3CCH transitions is shown and corresponding $T_{\rm kin}$ is labeled.

where F_ν, D, $B_{(\nu,T_d)}$, R_t, and k_ν are total integrated flux at observing frequency ν, distance of object, Planck function at dust/gas temperature T$_d$, gas-to-dust mass ratio, and dust absorption coefficient, respectively.

By adding up the emission inside the boundary of each dendrogram structure, we calculated F_ν at ν = 346.58 GHz (or 865 μm) for each one. We derived the k_ν by adopting a relation $k_\nu = 10\left(\frac{\nu}{1.2\ (\mathrm{THz})}\right)^p$, where $p = 1.5$ is adopted for all the dense cores (e.g., Bracco et al., 2017, and references therein). We therefore used $k^{865\mu m}_{346.58\ \mathrm{GHz}}$= 1.55 cm^2 g^{-1} for the mass estimation. Using the derived gas temperatures in Section 7.3.2.1, D = 3.8 kpc, and R_t = 100 (Weingartner & Draine, 2001), we estimated the gas mass for each dendrogram structure, which is tabulated in Table 7.1. The primary source of uncertainty in mass estimation is the dust emissivity, which is uncertain by a factor of a few. We used the assumption of spherical symmetry for the dense cores that were identified and calculated their volume densities using the M_s and effective radius (i.e., $R_\mathrm{eff} = L/2$). The formula used for this purpose was $n_{\mathrm{H}_2} = \frac{M_\mathrm{s}}{(\frac{4}{3}\pi R^3_\mathrm{eff})(2.8\ m_\mathrm{H})}$. The volume densities for leaf (branch) structures varied from 3.49 (0.16)$\times 10^6$cm^{-3} to 12.75 (2.59)$\times 10^6$cm^{-3}, with mean and medium values of 3.08 (0.8)$\times 10^6$cm^{-3} and 2.36 (0.56)$\times 10^6$cm^{-3}.

We have also estimated the virial mass of identified structures using equation (Bertoldi & McKee, 1992; Singh et al., 2021)

$$M_\mathrm{vir} = \frac{5}{\beta_1 \beta_2}\frac{\sigma^2_\mathrm{total} R_\mathrm{eff}}{G}, \tag{7.6}$$

where $\sigma^2_\mathrm{total} = \sqrt{\sigma^2_\mathrm{nt} + c^2_s}$ is the total velocity dispersion with the sound speed of c_s, and G is the gravitational constant. The parameters, $\beta_1 = \frac{(1-b/3)}{(1-2b/5)}$ belongs to a power-law density profile of $\rho \propto r^{-b}$ with $b = 1.6$ (e.g., Pirogov, 2009) and $\beta_2 = \frac{sin^{-1}(e)}{e}$ is a geometry factor with eccentricity $e = \sqrt{1 - f^2_\mathrm{int}}$ of elliptical structures. The intrinsic axis ratio (f_int) is related to the observed axis ratio (f_obs; see also Figure 7.8) as (Fall & Frenk, 1983; Li et al., 2013a)

$$f_\mathrm{int} = \frac{2}{\pi}\ f_\mathrm{obs}\ \mathcal{F}_1(0.5, 0.5, -0.5, 1.5, 1, 1 - f^2_\mathrm{obs}), \tag{7.7}$$

where $\mathcal{F}_1$ is the Appell hypergeometric function of the first kind. The power-law density profile of $\rho \propto r^{-b}$ with $b = 1.6$ is observed for the inner regions of the sample of 16 cores associated with MSF (e.g., Pirogov, 2009). For low-mass star-forming regions b is usually higher. The derived β_2 value of dendrogram structures varies from 1.1 to 1.4.

Based on the derived gas mass (M_s) and virial mass (M_vir) of structures, we estimated the virial parameter, $\alpha_\mathrm{vir} = \left(\frac{M_\mathrm{vir}}{M_\mathrm{s}}\right)$, that infers the dynamical state of gas structure. Table 7.1 lists the estimated mass and virial parameter of dendrogram structures.

7.3.2.3 Spectral profiles of dendrogram leaves

To investigate the core scale gas kinematics, we have extracted the ALMA $H^{12}CO^+$ and $H^{13}CO^+$ spectral line data. Figure 7.7 presents the spectral profiles of dendrogram leaves averaged over their footprint size (see Table 7.1). The profiles are displayed for $H^{12}CO^+$ (optically thick) and $H^{13}CO^+$ (optically thin) emission. The dendrogram leaves L2 and L8 exhibit double-peaked profiles in both the $H^{12}CO^+$ and $H^{13}CO^+$ line tracers. Leaf L17 displays a double-peaked profile in $H^{12}CO^+$ only, while all other structures (i.e., L5, L7, L9, L10, L13, L14, L15, L16, and L18) exhibit single peaks. The asymmetry in $H^{12}CO^+$ line profiles are indicative of significant dynamical activity (e.g., Traficante et al., 2018a). To quantitatively estimate the asymmetry in the $H^{12}CO^+$ line profiles, we derived the nondimensional asymmetry parameter (A) for dendrogram leaves as (see more details in Mardones et al., 1997):

$$A = \frac{V_\mathrm{thick} - V_\mathrm{thin}}{\Delta V_\mathrm{thin}}, \tag{7.8}$$

where V_thick and V_thin are the mean velocities of $H^{12}CO^+$ and $H^{13}CO^+$ line profiles, respectively. The ΔV_thin denotes the FWHM linewidth of $H^{13}CO^+$ line profile. We estimated the V_thick, V_thin, and ΔV_thin from the Gaussian fitting of spectral profiles. The parameter A for each leaf is labeled in the respective panels of their spectral profiles in Figure 7.7. Most of the leaves except L2, L5, L8, L13, and L14 have positive A values, indicating a blue asymmetry, which is suggestive of infall (e.g., Gregersen et al., 1997; Mardones et al., 1997).

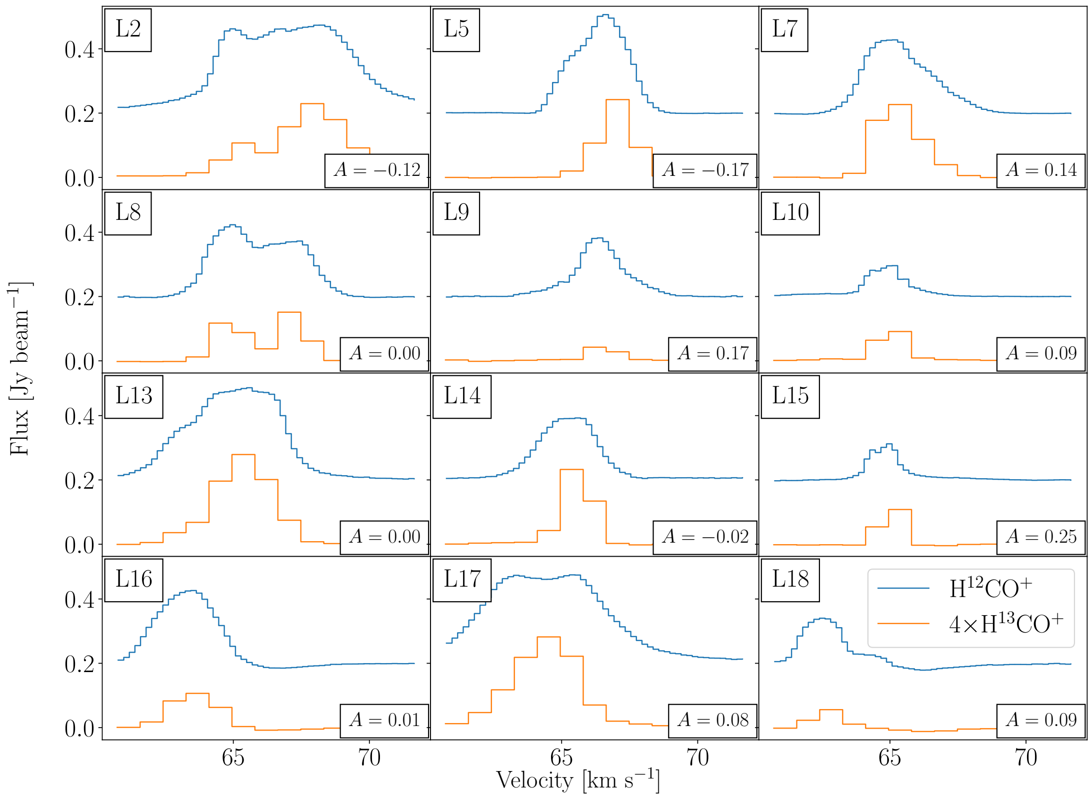

Figure 7.7: Averaged spectral profiles of dendrogram leaves. In each panel, the dendrogram leaf ID and asymmetry parameter (A) are labeled (see text for details). In all the panels, $H^{12}CO^+$ profiles are vertically offset by 0.2 Jy beam^{-1}, while the $H^{13}CO^+$ profiles are scaled up by a factor of 4.

7.3.3 Distribution of Physical Parameters and spatio-kinematic analysis

Figure 7.8 shows the histogram distribution of various physical parameters identified in Section 7.3.1.1. The high-resolution ALMA $H^{13}CO^+$ (4–3) data allow us to trace the structures within the physical extent of ∼2000 AU (∼0.01 pc), revealing the core scale properties. The histogram distribution of dendrogram structure size (L) is presented in Figure 7.8a. The branches are larger in size compared to the leaves, and consistent with the definitions of these structures (Section 7.3.1). The distribution of axis ratio $\left(\frac{\text{minor axis}}{\text{major axis}}\right)$ for identified structures is shown in Figure 7.8b. The axis ratio for branches lies lower side than that of leaves indicating that leaves tend to be more circular (or spherical) than branches. The gas kinematic temperature ($T_{\rm kin}$) distribution is presented in Figure 7.8c. The statistical parameters related to $T_{\rm kin}$ are mentioned in Section 7.3.2.1.

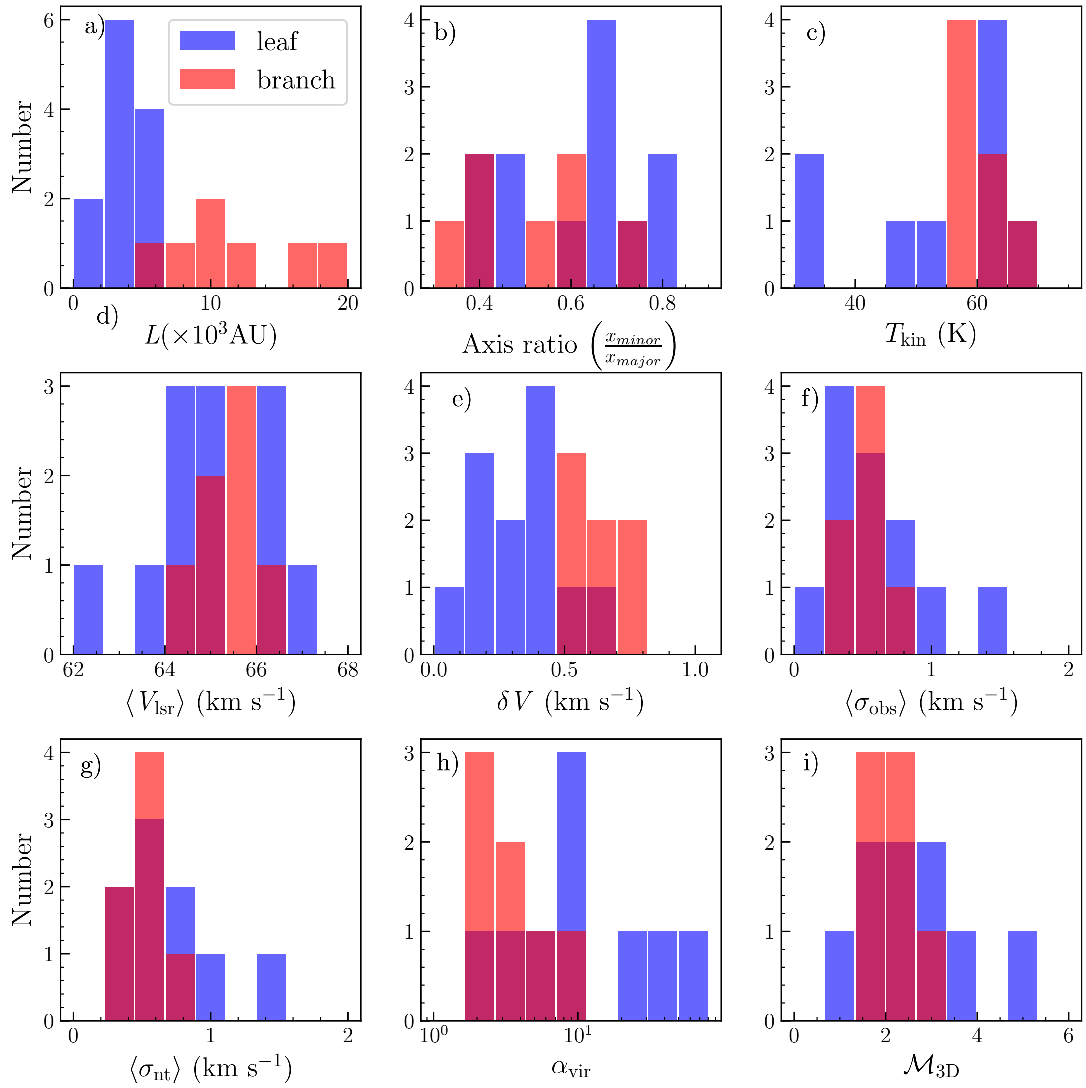

Figure 7.8: Histograms of different properties of *astrodendro* identified structures. These include structure size (L in AU), axis ratio $\left(\frac{\text{minor axis}}{\text{major axis}}\right)$, mean velocity ($\langle V_{\mathrm{lsr}} \rangle$), velocity variation ($\delta V_{\mathrm{lsr}}$), observed mean velocity dispersion ($\langle \sigma_{\mathrm{obs}} \rangle$), non-thermal velocity dispersion ($\langle \sigma_{\mathrm{nt}} \rangle$), gas kinetic temperature (T_{kin}), virial parameter (α_{vir}), and Mach number ($\mathcal{M}_{3\mathrm{D}}$). Histograms in blue and red correspond to leaf and branch structures, respectively.

Figures 7.8d-7.8i display the kinematic properties of dendrogram structures. The weighted mean velocity of leaves and branches (see Figure 7.8d) are found to be similar with a value of ∼65 km s^{-1}. However, the branches show narrower distribution (range = [64.53, 66.65] km s^{-1}) compared to leaves (range = [62.37, 67.17] km s^{-1}). This is possible because the fewer leaves that are separated from the central zone (i.e., leaves L10, L16, and L18; see Figure 7.4), are identified at lower velocities and do not have their parent branches. A clear separation in the δV_{lsr} distribution for leaves and branches is noticeable in Figure 7.8e. The leaves, overall have less $\delta V_{\rm lsr}$ (range = [0.05, 0.65] km s^{-1}, mean= 0.34 km s^{-1}, median= 0.35 km s^{-1}) compared to branches (range = [0.56, 0.82] km s^{-1}, mean= 0.66 km s^{-1}, median= 0.67 km s^{-1}).

The histogram distribution of $\langle\sigma_{\rm obs}\rangle$ and its non-thermal contribution, $\langle\sigma_{\rm nt}\rangle$, for the identified structures are presented in Figures 7.8f and 7.8g, respectively. The branches, overall, tend to have narrower velocity dispersion range (i.e., $\langle\sigma_{\rm obs}\rangle$; range = [0.42, 0.80] km s^{-1}, mean= 0.57 km s^{-1}, median= 0.54 km s^{-1}) compared to that of leaves (i.e., $\langle\sigma_{\rm obs}\rangle$; range = [0.19, 1.37] km s^{-1}, mean= 0.60 km s^{-1}, median= 0.50 km s^{-1}). The similar trend is reflected in the non-thermal velocity dispersion. For branches, the $\langle\sigma_{\rm nt}\rangle$ ranges from 0.40 to 0.79 km s^{-1} with mean and median values of 0.56 km s^{-1} and 0.53 km s^{-1}, respectively, while for leaves, $\langle\sigma_{\rm nt}\rangle$ is observed in the range = [0.31, 1.37] km s^{-1} with mean and median values of 0.69 km s^{-1} and 0.51 km s^{-1}, respectively. The $\alpha_{\rm vir}$ distribution is shown in Figure 7.8h. Branches have less $\alpha_{\rm vir}$ (mean=3.89 and median=2.92) compared to leaves (mean=18.36 and median=10.89). The distribution of $\mathcal{M}_{\rm 3D}$ (see Figure 7.8i) reveals the transonic–supersonic (1$\leq \mathcal{M}_{\rm 3D} \leq$5) nature of dendrogram structures. The mean (median) values of $\mathcal{M}_{\rm 3D}$ for leaves and branches are 2.69 (2.39) and 2.08 (2.04), respectively.

7.3.4 Line-width size ($\sigma - L$) relation

The linewidth-size ($\sigma - L$) relationship of the molecular clouds has been investigated extensively in the literature (see Section 8.1). Typically, this relationship is well described by a power law with an index ranging from 0.2 to 0.6 (Larson, 1981; Solomon et al., 1987; Goodman et al., 1998; Heyer & Brunt, 2004; Heyer et al., 2009; Falgarone et al., 2009; Hacar et al., 2016; Dewangan et al., 2019a, 2022b), and is commonly known as first of the three "Larson's Relations". Since the nature of turbulence and star formation is closely linked to these relationships, it is crucial to evaluate the $\sigma - L$ correlations in various environments and scales to gain a comprehensive understanding of the star-forming regions. To understand the nature of turbulence in a star-forming environment, we investigated the $\sigma_{\rm nt} - L$ relationship of regions in the immediate vicinity of W42-MME (see

Figure 7.1b). This is of the type–4 $\sigma - L$ relation as discussed by Goodman et al. (1998). Earlier, Goodman et al. (1998) devised four types of $\sigma - L$ relations, which are the combinations of line tracers (i.e., single or multiple) and the target of interest (i.e., single or multiple molecular clouds). In this way type–1 relation is for multitracer, multicloud intercomparison, type–2 is for single-tracer, multicloud intercomparison, type–3 is for multitracer study of a single cloud, and type–4 indicates the single-tracer study of a single cloud. Here we study this relation by two approaches, one using dispersion–size plot for dendrogram structures, and other by estimating the velocity structure function (VSF) for the entire region of study.

7.3.4.1 Scaling relations from Dendrogram Structures

In the analysis below, we explore two scaling relationships concerning the dendrogram density structures (i.e., leaves and branches) identified in W42 region. Two parameters, σ and $\delta V_{\rm lsr}$ are used to measure internal gas motions (e.g., Storm et al., 2014; Liu et al., 2022a). The parameter σ indicates the internal gas motion in the direction of an individual structure (line-of-sight velocity dispersion or linewidth), while $\delta V_{\rm lsr}$ traces the gas motion across different directions within the structure (plane-of-sky velocity dispersion). At the cloud scale (¿10 pc), the choice of these parameters is insignificant as these two parameters are similar and commonly trace the internal gas motion of the cloud. However, at smaller scales (¡0.1 pc), local effects become more important and gas properties become distinguishable. Therefore, in particular, we are interested in the scaling relationships of $\delta V_{\rm lsr} - L$ and $\sigma_{\rm nt} - L$. Figure 7.9a presents the $\delta V_{\rm lsr} - L$ plot for the identified dendrogram structures. The best fit power-law has the form $\delta V_{\rm lsr} = (0.20 \pm 0.06) \times L^{0.46\pm0.14}$, which closely follows the generalized Larson's law with power-law scaling exponent of $\sim$0.5 at a constant column density of $\sim 10^{23}$ cm^{-2} (e.g., Heyer & Brunt, 2004). We have also marked the lines of constant column density in Figure 7.9 following the equation, $\sigma = \sqrt{2G\Sigma L}$, where Σ is the column density, G is the universal gravitational constant, and L is the structure size (see Ballesteros-Paredes et al., 2011, for details). This equation is valid if the collapsing scenario is applicable to all scales within the molecular cloud and the non-thermal motions are of gravitational origin. However, such equation is also applicable for the case of virial equilibrium, with a difference by a factor of $\sqrt{2}$ less (see more details in Ballesteros-Paredes et al., 2011). The power-law exponent in the $\delta V_{\rm lsr} - L$ relation for branch structures is found to be shallower with the value of 0.27$\pm$0.10 compared to the global trend. We have marked the footprint of Larson's law with the scaling coefficient ranging from 0.08 to 0.8 by shaded area in Figure 7.9.

We further estimated the Pearson Correlation Coefficient (PCC) which is a measure of linear correlation between two sets of data. The PCC correlation coefficient r indicates the strength of the linear relationship, while the significance is measured by the probability value p. It is to be noted that the r ranges from -1 to $+1$ signifying the strong anti-correlation ($r = -1$), no correlation ($r = 0$), and strong positive correlation ($r = +1$), respectively. The smaller p value indicates more significant relationship. In general p <0.05 signifies statistically significant correlation. For $\delta V_{\rm lsr} - L$ plot, we obtained the r–value and p–value of 0.69, and 2.92×10^{-3}, respectively. This indicates the positive correlation between $\delta V_{\rm lsr}$ and (L) of dendrogram structures.

Figure 7.9b shows the $\sigma_{\rm nt} - L$ plot for the identified structures. This plot overall shows negative trend with scaling exponents of -0.31 ± 0.14, which is obtained from the best fit power-law over all the identified structures. With $p = 0.056$, the correlation coefficient $r = -0.4$ between $\sigma_{\rm nt}$ and L is marginally statistically significant. In $\sigma_{\rm nt} - L$ plot, a steeper negative trend with a power-law exponent of -0.55 ± 0.06 is found for the branch structures only. The PCC $p-$value of 2.04×10^{-3} with $r = -0.93$ suggests its statistical significance. The possible origin of these outcomes are discussed in Section 7.4.

7.3.4.2 Velocity Structure Function

An important statistical description of interstellar turbulence or the gas dynamics can be inferred by the generalized VSF (e.g., Miesch & Bally, 1994; Heyer &

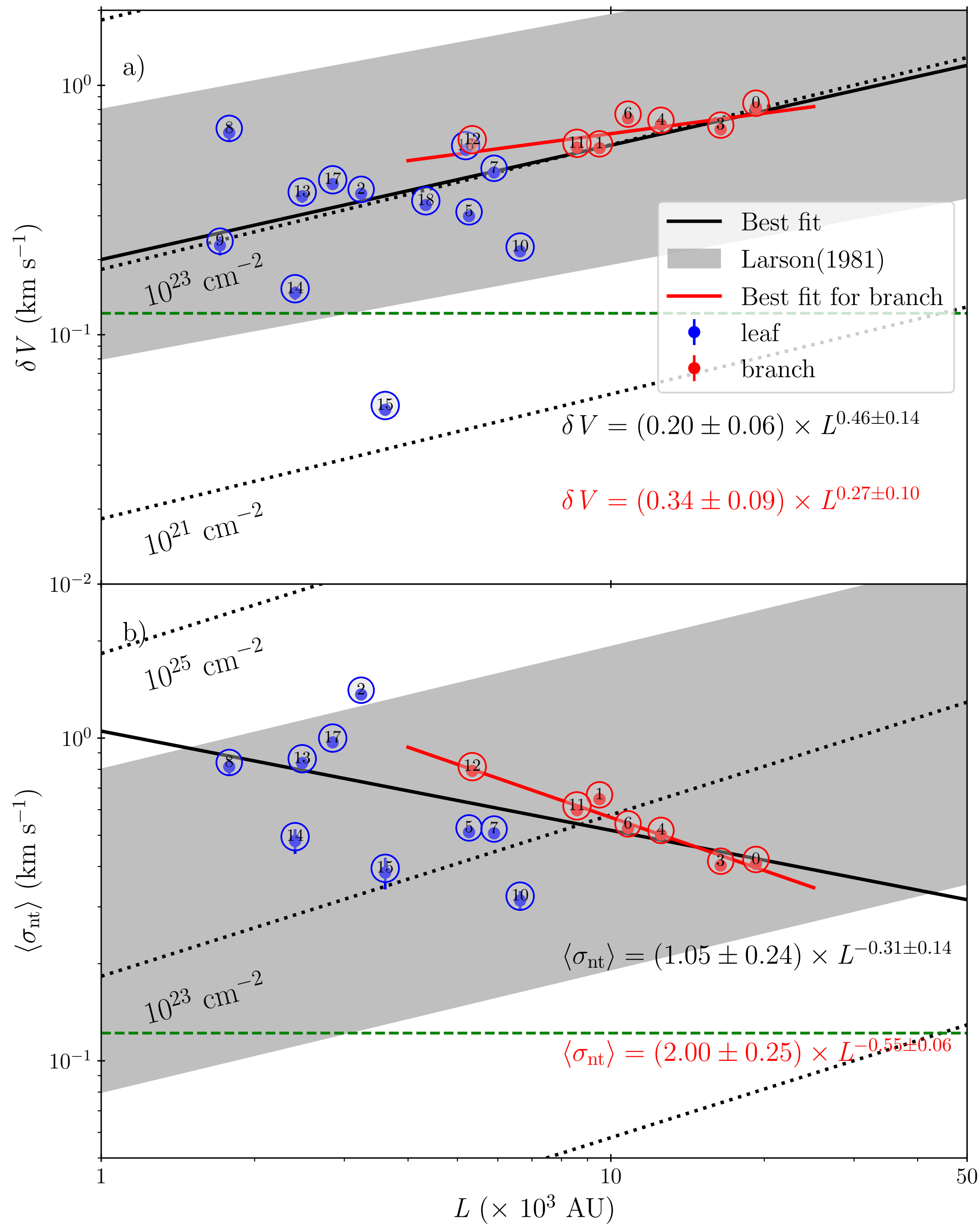

Figure 7.9: a) $\delta V_{\rm lsr}$–L plot. b) $\langle\sigma_{\rm nt}\rangle$–$L$ plot. In both the panels, blue and red dots correspond to leaf and branch structures, respectively. We have also labeled the corresponding structure IDs. The best fit power-law for all the dendrogram structures (solid black line) and for only branch (red solid line) are displayed and labeled. The Larson (1981) relation ($L \propto \sigma^{0.38}$) is shown by shaded region with the coefficient range of 0.08 to 0.8 km s^{-1}. A green dashed line indicates thermal velocity dispersion of 0.129 km s^{-1} at mean gas temperature of dendrogram structures (i.e., 54 K). The dotted lines denote the lines of constant column density (see labels) if non-thermal motions are driven by the self gravity.

Brunt, 2004; Chira et al., 2019)

$$S_p(l) = \langle |(v(r) - v(r+l))\,|^p\rangle, \tag{7.9}$$

where, l is known as lag (i.e., the spatial displacement between two points within a three dimensional volume), p is the order of VSF, and the average is taken out for the entire volume of the gas. The VSF is described as a power-law over a finite spatial range and often reframed as a power-law expression by taking p^{th} root; i.e., $S_p(l)^{1/p} = v_o\ l^{\gamma}$, where v_o is a scaling coefficient and γ is a scaling exponent (Heyer & Brunt, 2004). In our analysis, we calculated the reframed 2^{nd} order structure function in velocity $\delta v = S_2(l)^{1/2}$ (e.g., Hacar et al., 2016; Dewangan et al., 2019a) using $H^{13}CO^{+}$(4–3) data of entire region of our study (see Figure 7.1b). In our calculations, we adopted only those data points which have peak intensities greater than 0.01 Jy beam^{-1} and have velocity dispersion (FWHM) $<$ 2.5 km s^{-1}. Applying these conditions, the total number of data points were 7566 (i.e., ∼11% of available points). We then estimated $S_2(l)^{1/2}$ using moment-1 map of $H^{13}CO^{+}$ and the total range of angular separations (i.e., $0''.05$–$19''.2$) were divided into sub-ranges (or lags) of $0''.13$ (or ∼500 AU in spatial scale).

Figure 7.10 shows the $S_2(l)^{1/2} - l$ plot for $H^{13}CO^{+}$ (blue points) data. We have estimated the best fit power-law form of $H^{13}CO^{+}$ $S_2(l)^{1/2}$, which is obtained as $S_2(l)^{1/2} = (0.34 \pm 0.01) \times l^{0.40\pm0.01}$. Here we also note that there is no significant deviation in the $S_2(l)^{1/2}$ for $H^{13}CO^{+}$ and $H^{12}CO^{+}$ data (not shown here). In general, the $S_2(l)^{1/2}$ shows a linear trend in the spatial range within ∼6000 AU. The form of this linear trend is obtained as $S_2(l)^{1/2} = 0.23 \times l^{0.73\pm0.01}$, and is more steeper than the global trend with the form of $S_2(l)^{1/2} \propto l^{0.40\pm0.01}$. However, for larger separations ($\gtrsim$6000 AU), the VSF rises slightly, and shows oscillatory behavior. This form of VSF is seen previously by other authors as well (e.g., Hacar et al., 2016; Dewangan et al., 2019a, 2022b).

We have further investigated the variation of scaling coefficient (v_o) and scaling exponent (γ) for each dendrogram structure by computing the $H^{13}CO^{+}$ $S_2(l)^{1/2}$ in Figure 7.11. The histograms of γ for leaves and branches are shown in Figures 7.11a and 7.11b, respectively. Here we note that the γ is related to a linear regime in log-log plots of $S_2(l)^{1/2}$ of each structure (for comparison, see Figure 7.10). To perform such an analysis, we first masked out the area that does

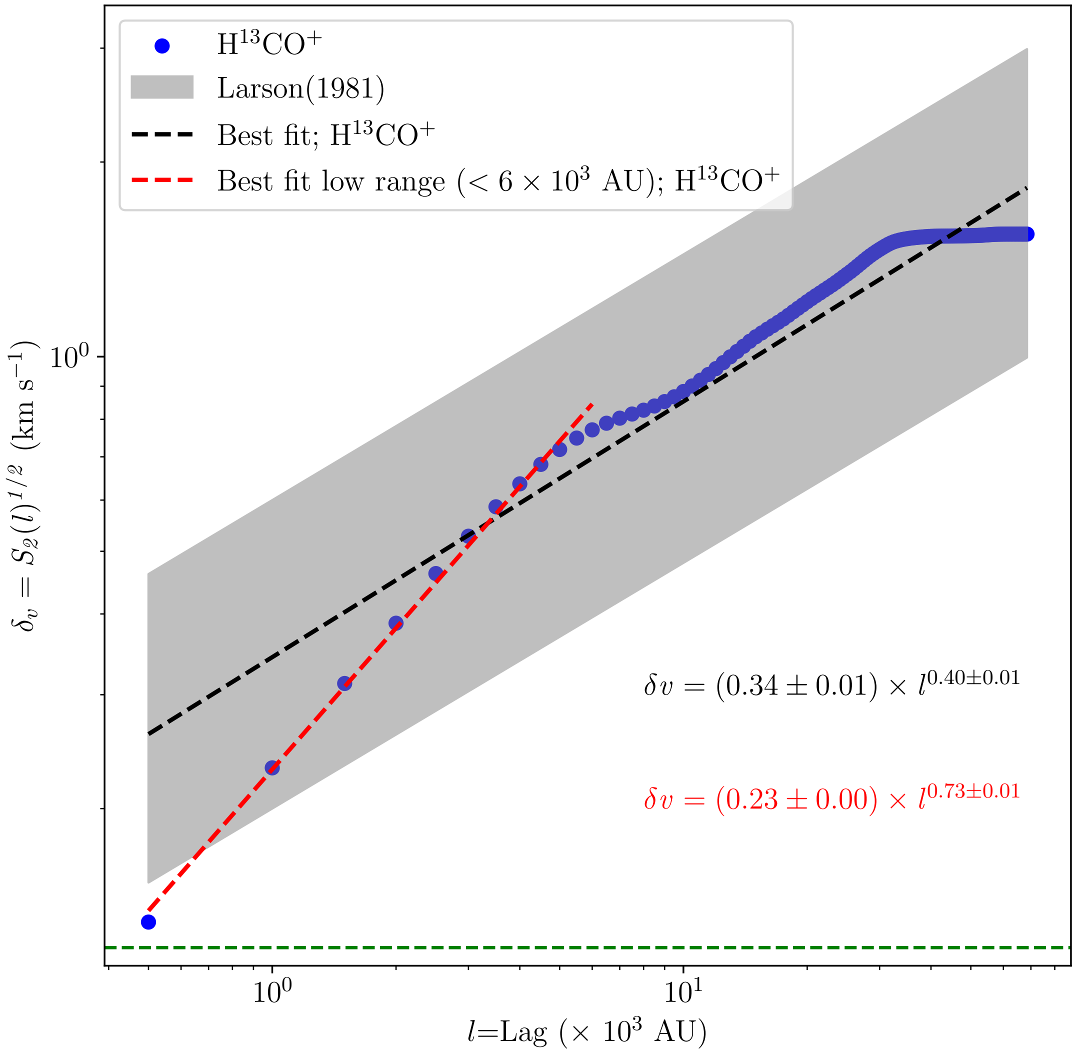

Figure 7.10: Structure function in velocity ($S_2(l)^{1/2}$) as a function of lag (l). The lag is sampled at the steps of 500 AU. A green dashed line indicates $\sigma_{\rm th}$ of 0.129 km s^{-1} at mean gas temperature of 54 K.

not include our region of interest (i.e., each dendrogram structure) and then computed the VSF. Due to the small structure sizes, here the VSF analysis is exempted from the conditions defined earlier (i.e., imposing cut-off in peak intensity and velocity dispersion). The total number of data points range from 62 to 943 for leaves, while for branches the data points were in the range of 675–5947. Figure 7.11c displays the distribution of γ and v_o as a function of structure size. The distribution of γ is scattered for leaves, while it shows a negative trend for the branches. The distribution of v_o is nearly constant for the branches.

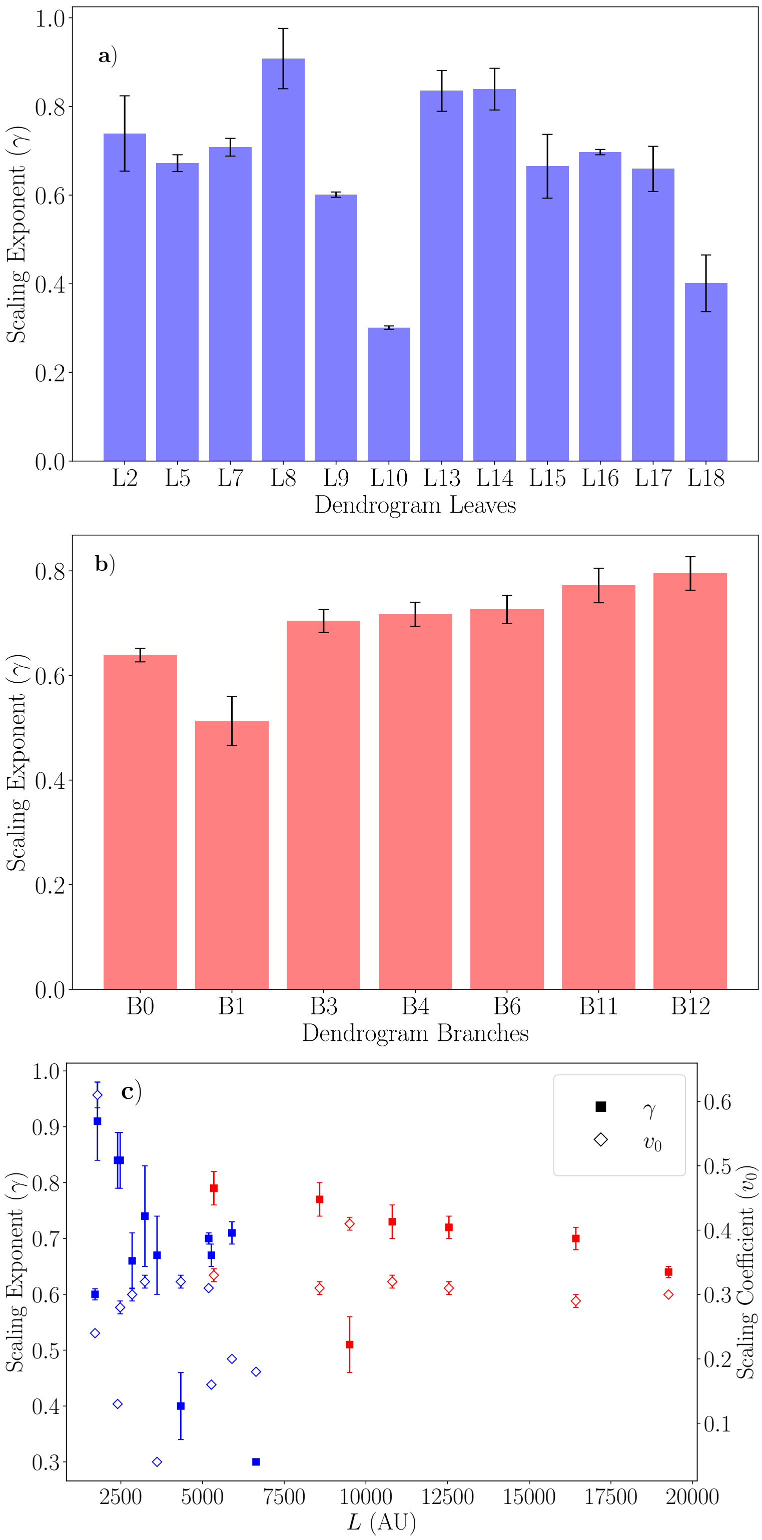

Figure 7.11: Distribution of scaling exponent (γ) defined in the VSF of second order $S_2(l)^{1/2} = \delta v = v_0 l^{\gamma}$ for a) dendrogram leaves and b) branches. c) Variation of γ and v_0 with respect to the structure size. Blue and red colors indicate the leaves and branches, respectively. The parameters γ and v_0 are obtained from the power-law best fit for the $S_2(l)^{1/2}$ of each dendrogram structure. The errors denote 1 sigma standard errors on the fitted parameters.

7.3.4.3 Mass–size and density–size relations

To understand the nature of detected dendrogram structures, we computed the mass–size ($M - R$) and density–size ($n - R$) relations for the dendrogram structures in Figure 7.12. These relations can be derived from one another, implying that the column density of structures with various masses, sizes, and evolutionary states is constant. Collectively, these relations are known as Larson's third relation. The $M - R$ relation has a best fit power-law with a form of $M \propto R_{\rm eff}^{1.73\pm0.23}$, where $R_{\rm eff}$ is the effective radius of dendrogram structures and defined earlier. The obtained PCC r–value and p–value of $M - R$ plot are 0.92, and 5.4×10^{-7}, respectively. This indicates the strong positive correlation between mass and radius of dendrogram structures, which is consistent with previous studies (e.g., Kauffmann et al., 2010a,b; Kauffmann & Pillai, 2010; Ballesteros-Paredes et al., 2019). In the case of nearby molecular clouds, the $M - R$ power-law index is close to 2 (e.g., Lombardi et al., 2010; Lada & Dame, 2020; Cahlon et al., 2023, and references therein). For distant clouds spread over the entire Galaxy this index is found to be >2 (e.g., Miville-Deschênes et al., 2017; Traficante et al., 2018b). However, Ballesteros-Paredes et al. (2019) suggest that the larger power-law index could result from the superposition of line-of-sight dust emission. Additionally, they also pointed out that the $M - R$ relation is dependent on how the cloud structure is defined, e.g., the column density cutoff leads to the power-law index of 2, while the volume density definitions results in the index value of 3 (see also Cahlon et al., 2023).

Earlier, Kauffmann & Pillai (2010) proposed an empirical mass–size threshold for MSF which is based on the clouds with and without MSF. These authors showed that density structures with $m(r) > 870\ M_{\odot}(r/pc)^{1.33}$ are prone to form massive stars. In our analysis, we noticed that only leaf L17 lies within this relation. Infact, leaf L17 was earlier proposed and confirmed as young massive protostar by Dewangan et al. (2015); Dewangan (2022) (see also De Buizer et al., 2022). In a similar way, a plot of mass vs. surface density ($\Sigma = \frac{M}{\pi R_{\rm eff}^2}$; not shown here) displays a scatter with only leaf L17 statisfying the condition of MSF with

$\Sigma > 1$ g cm^{-2} (e.g., Urquhart et al., 2014; Saha et al., 2022).

Figure 7.12b shows the $n - R$ relation for dendrogram structures. The PCC r–value and p–values are -0.5, and 0.05, respectively implying the marginally statistically significant anti-correlation between density and size. The power-law form of density–size relation is observed as $n \propto R_{\rm eff}^{-1.26\pm0.23}$. Here we note a caveat that some of the anti-correlation in the $n - R$ relation is there by construction, given that both the axes depend on the value of $R_{\rm eff}$ (i.e., $L = 2 \times R_{\rm eff}$ and $n_{\rm H_2} = \frac{M_{\rm s}}{(\frac{4}{3}\pi R_{\rm eff}^3)(2.8\ m_{\rm H})}$;see Section 7.3.2.2).

7.3.5 ALMA 865 μm dust continuum cores

In Section 7.3.1.1, we extracted dendrogram leaf structures from the ALMA $H^{13}CO^+$ emission and estimated their physical properties, including mass, virial mass, and virial parameter. We noticed that larger values of virial parameters can arise due to the lack of significant dust emission within structures where $H^{13}CO^+$ emission is observed, as shown in Table 7.1. To address this issue, we identified dust cores (or leaf structures in dust continuum map) using the dendrogram methodology on the ALMA 865 μm continuum map and estimated the aforementioned physical parameters. In order to identify the cores, the parameters "min_value" and "min_delta" were set to be 0.5 mJy beam^{-1} and 0.2 mJy beam^{-1}, respectively. The parameter "min_npix" was chosen such that the cores contains at least 2 beams of the ALMA 865 μm map (see Section 7.3.1.1). The analysis resulted in the identification of 14 cores. These dust cores are found to be spatially coexisted with the leaf structures identified in $H^{13}CO^+$ emission (for comparison see Figures 7.4 and 7.13). The size of these dust cores ranges from 1700–6850 AU with mean and median values of 3000 and 2340 AU. The observed mass of dust cores varies from 0.04 to 1.64 $M_\odot$, and is relatively lower than the mass of $H^{13}CO^+$ dendrogram leaves (i.e., 0.08–2.1 $M_\odot$; see Table 7.1). However, the observed mass of these small scale structures is possible because of the missed continuum flux at high resolution ALMA observations, as the interferometric observations are sensitive to strong and compact sources but miss more diffuse and extended emission. Based on this statement the statistics could be

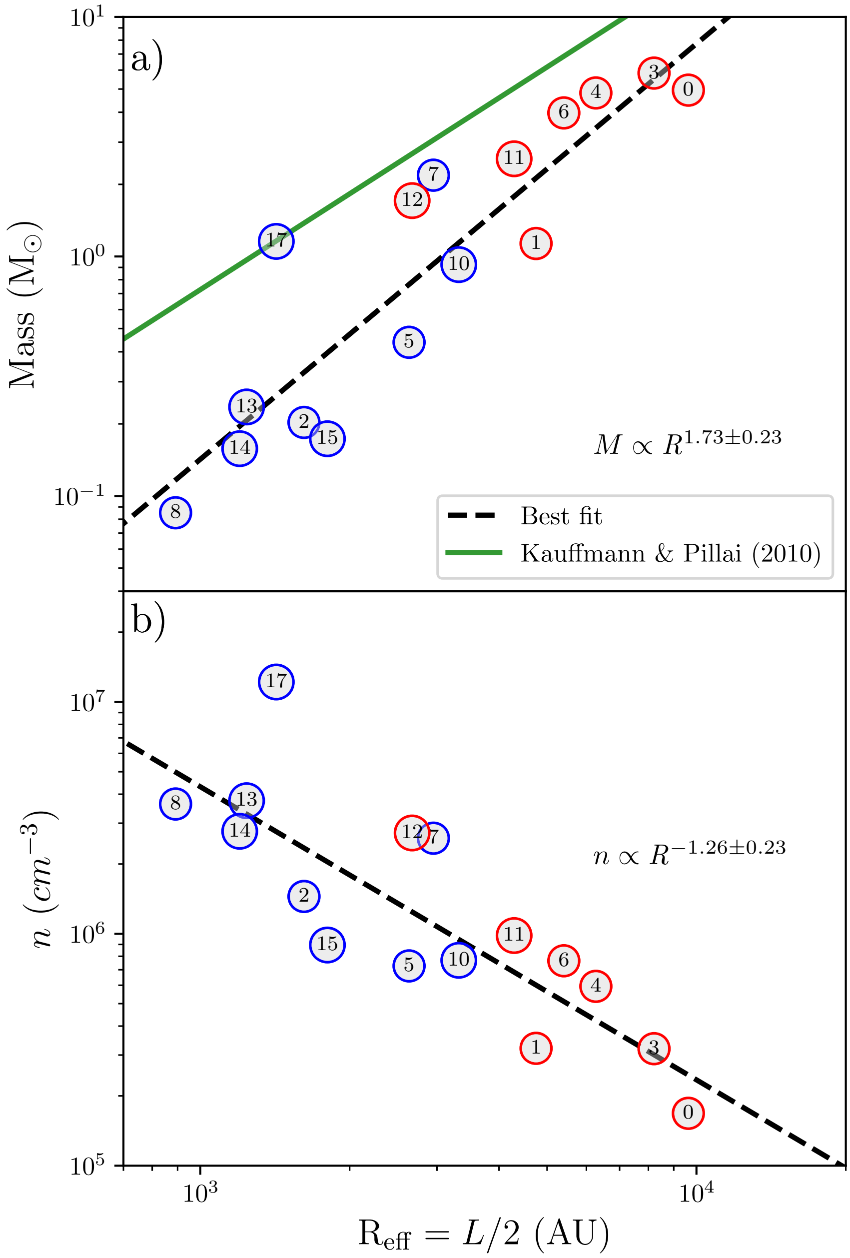

Figure 7.12: a) Mass–size relation and b) density–size relation of dendrogram structures. Blue (red) circles with labels denote the leaf (branch) structures. A green line indicates the mass–size law of $m(r) > 870\ M_\odot (r/pc)^{1.33}$ for massive star forming clumps proposed by Kauffmann & Pillai (2010), while dashed line in each panel represents the best fit. The best fit equation is also labeled in each panel.

slightly biased. Moreover, on scales of ∼1000 AU, gas-to-dust mass ratios could differ significantly from the canonical value of 100 used for mass calculations on larger scales (Weingartner & Draine, 2001). Thus, the low values of mass for these structures (including L17, hosting MYSO) is alone insufficient to discuss their star-forming nature. Also, earlier study by Dewangan (2022) suggest that the MYSO W42-MME continues to gain mass from its surroundings, which may be true for other dense structures. Figure 7.13 presents an overlay of the identified core positions by dots on the ALMA 865 μm map displayed with continuum contours. The dot size is proportional to the structure's footprint area, and the color scale represents the virial parameter information. To estimate the virial mass, we used a mean gas temperature of 54 K, and the mean velocity dispersion for each core was derived using the M_2 map of the ALMA $H^{13}CO^+$ emission (see Section 7.3.2). The resulting virial parameter values for the dust cores ranged from ∼4 to 30, with mean and median values of 15.14 and 14.95, respectively. These values indicate that the dense cores in the W42 region are in overvirial state.

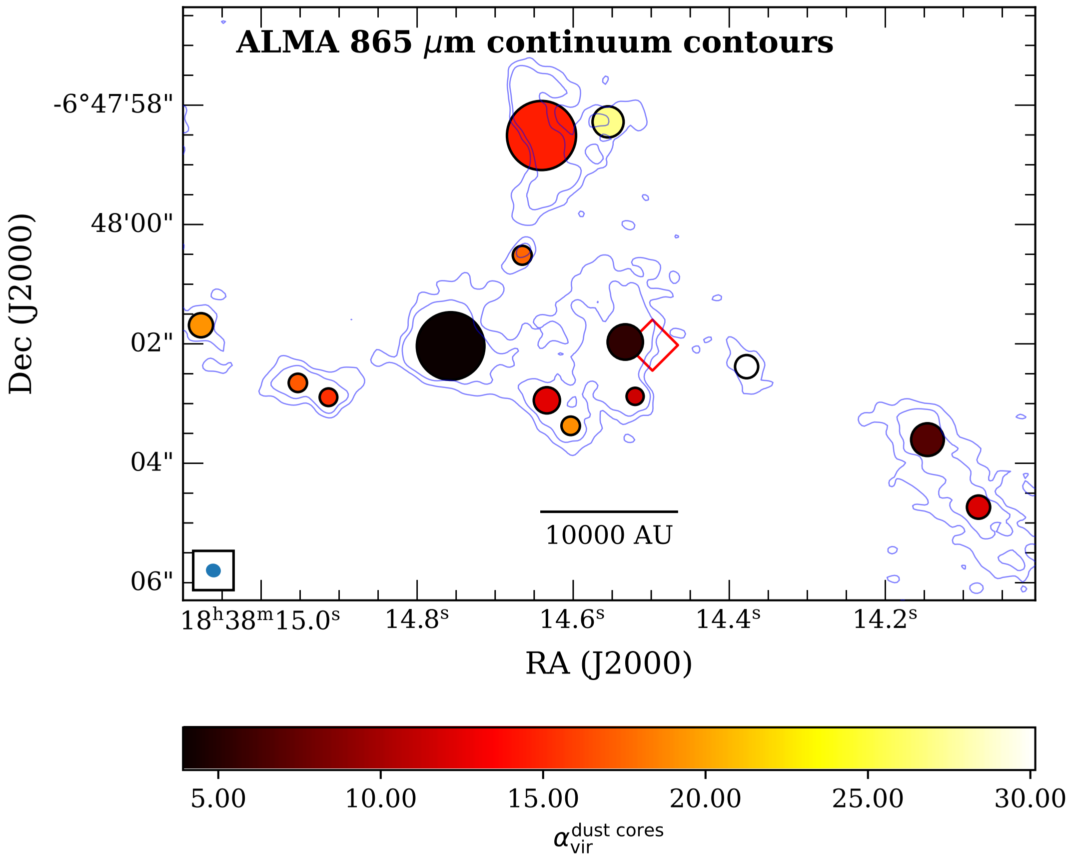

Figure 7.13: ALMA 865 μm continuum emission contours (levels=[0.4, 1] mJy beam^{-1}) overlaid with the positions of dust cores. The size of dots is proportional to the footprint area of dust cores identified in ALMA 865 μm continuum emission map. Color scale signifies the virial parameter of dust cores. The beam size and a scale bar is shown in the image.

7.4 Discussion

To examine the physical surroundings of the young massive protostar W42-MME, which is enclosed in a dusty cocoon/envelope (∼9000 AU) and influenced by the radiative feedback from a nearby massive O5.5-type star (Dewangan, 2022), the investigation of the dense gas kinematics is crucial. Our target site is important since it experiences different environmental conditions compared to young massive protostars that do not belong to the feedback-affected regions by existing nearby massive star (Liu et al., 2022b; Saha et al., 2022). It is worth mentioning that our target site is a part of large filament-hub (extent ∼1–2 pc; see Figure 14 in Dewangan, 2022). These HFSs are widely recognized among the research community as the initial stages of MSF (e.g., Motte et al., 2018; Kumar et al., 2020; Bhadari et al., 2022; Maity et al., 2022; Dewangan et al., 2023,?, and references therein). Therefore, the study of hierarchical structures of clouds, including clumps and cores, is crucial in understanding how dense cores form within the cloud and the underlying factors involved in this process.

7.4.1 Dynamical state of dense structures

The accurate study of the dynamics of clouds and dense structures in space relies on understanding the nature of gas motion. The leaf structures identified in the dendrogram analysis of ALMA $H^{13}CO^+$ data are found to have relatively higher line-of-sight velocity dispersion compared to the branches (see Figure 7.8). Additionally, all of the identified structures exhibit transonic–supersonic gas motions (i.e., 1¡$\mathcal{M}$¡5). These observations are also reflected in the negative trend in $\sigma_{\rm nt} - L$ plot (see Figure 7.9). Such a negative trend in the $\sigma_{\rm nt} - L$ relation is not commonly observed in star-forming clouds. However, some studies show either shallower power-law slope or no correlation as well (Caselli et al., 2002; Traficante et al., 2018b). Widely studied Larson's first law, on the other hand, suggests a different trend, where large fragments are expected to have higher dispersion compared to smaller ones. The Larson's relation is found to be consistent at larger scales ($>$ 0.1 pc, e.g., Falgarone et al., 2009; Ballesteros-Paredes et al., 2011), but at a smaller scales the studies are limited (e.g., Li et al., 2020; Liu et al., 2022b; Saha et al., 2022; Li et al., 2022b). In this context, our observed $\sigma_{\rm nt} - L$ relation appear to support the theoretical framework proposed by Ballesteros-Paredes et al. (2018), which emphasizes that the generalized Larson's relation can have a gravitational origin. Furthermore, for varying column densities, the $\sigma_{\rm nt} - L$ relation need not necessarily follow Larson's law. The authors suggest that as the cores collapse, their sizes become smaller, while the column densities and velocity dispersion become larger. This results in an reverse/oblique trend compared to Larson's relation (see Figure 2 in Ballesteros-Paredes et al., 2018), which can be explained by the consequences of the hierarchical and chaotic collapse scenario. This suggests the emergence of local collapse centers within the entire cloud as it itself undergoes collapse. In such case, the gravitational energy converts to the kinetic enery and developes the virial-like relation (see Figure 2 in Ballesteros-Paredes et al., 2018). We observed the infall gas signature in most of the leaf structures (see Figure 7.7). Additionally, the identified structures exhibit overvirial ($\alpha_{\rm vir} > 2$) states, which, as found, are similar to the time evolution of collapsing cores (Ballesteros-Paredes et al., 2018). These results, present an ambiguous picture if we compare our results with the literature provoking that branches (or clumps) tend to be more turbulent than the leaves (or cores). However, some studies support our observations and advocate the overviriality of cores (Ballesteros-Paredes et al., 2018; Traficante et al., 2018b; Singh et al., 2021; Ramírez-Galeano et al., 2022, and references therein). According to Ballesteros-Paredes et al. (2018), the excess overvirial states is because of the assumption that the gravitational energy is estimated by the energy of isolated homogeneous sphere. They also stress out that such excess disappears when the gravitational energy is correctly estimated from the actual spatial mass distribution. Therefore, the Larson's $\sigma_{\rm nt} - L$ relation does not hold when the column densities spanning a large dynamic range are considered. In general, the deviation from the Larson's scaling can be the signature of gravity-driven chaotic gas motions as predicted by global hierarchical collapse (GHC) model (Ballesteros-Paredes et al., 2011; Vázquez-Semadeni et al., 2019). Our observed scaling relations suggest that the gas motion in the vicinity of W42-MME is transonic-supersonic. The supersonic nature of molecular clouds can arise because of random turbulent motions, gravity-driven chaotic motions, or even ordered motions like localized rotation and outflows, or large-scale directional gas flows (e.g., Li & Burkert, 2016; Traficante et al., 2018a,b). In general, the point sources are not promisingly evident in our target region (see Figure 7.4c), however the dense gas profiles convey the signatures of infall/outflow activities (see Figure 7.7). These processes can also give rise to high-dispersion values at the smaller scales.

In another approach, the $\delta V_{\rm lsr} - L$ relation for all the dendrogram structures and $S_2(l)^{1/2}$ for entire region of study, reveal a positive trend and closely follow the generalized Larson's relation (e.g., Heyer & Brunt, 2004) with a nearly constant column density of $\sim 10^{23}$ cm^{-2} and positive scaling exponents of 0.46$\pm$0.14 and 0.30$\pm$0.01, respectively. $S_2(l)^{1/2}$, however, tend to be more linear in the regime of <6000 AU with steeper scaling exponent of 0.68$\pm$0.02. This power-law dependence may indicate general behaviour of velocity field of the gas in the viscinity of W42-MME. It may be possible that the supersonic vortices created by gas motion primarily dominate at the physical scales of leaves (e.g., Dewangan et al., 2019a). The power-break in $S_2(l)^{1/2}$ at some length scales has no clear boundary, but our results suggest that the spectral break can occur at around $\sim$6000-8000 AU scale. This finding requires verification through more studies conducted at the physical scales of cores (i.e., $\lesssim$0.05 pc). The spatial distance of $\sim$6000 AU, interestingly, is closely matched with the maximum structure size of dendrogram leaves (i.e., $\sim$6600 AU). The variation in γ defined in the VSF of second order $S_2(l)^{1/2} = \delta v = v_0 l^{\gamma}$ for dendrogram leaves is found to be larger compared to that of branches (see Figure 7.11). This suggests that the local gas motions driven by embedded sources and associated activities (i.e., inflow/outflow) primarily contributes in shaping the VSF power-law over time evolution (e.g., Chira et al., 2019, see Figure 1 therein). For larger fragments of clouds (e.g., clumps), the effect seems to be averaged out and hence the structures tend to show a less scatter in the γ.

Here we note that both $S_2(l)^{1/2}$ and δV (indicating the standard deviation of mean velocities within the spatial structures) closely follow the similar statistics and infer the information of gas motion across the sky plane. Hence they appear to show similar positive trends with L. However, σ, which represents the weighted mean of standard deviations of line profiles at each pixel within the structure, provides information about the gas motions along the line-of-sight. At larger spatial scales, all these parameters can be equivalent as the gas kinematic properties will be averaged out, but at smaller scales where we expect localized gas motion, they may indicate different physical phenomena.

Overall, our observations support theoretical insights from studies that stress the non-universality of Larson's relations (Ballesteros-Paredes et al., 2018). In contrast to this, several previous studies support that turbulence plays important role at large scales while gravity primarily works at smaller scales. We, however, suggest that the roles of turbulence and gravity cannot be differentiated by non-thermal gas motion alone at the spatial scales of sub-parsec regime, primarily in the environment where the feedback processes are dominant (e.g., Traficante et al., 2018a). Earlier, Goodman et al. (2009) suggested that, apart from the well-cited role of turbulence at large scales, self-gravity plays a significant role in all possible scales of cloud fragments. Similarly, Ballesteros-Paredes et al. (2011) and their subsequent studies (Ballesteros-Paredes et al., 2018, 2019) emphasize the role of turbulence at smaller core scales. These studies suggest that velocity dispersion in molecular clouds do not entirely depend on spatial scales, but also include surface gas densities. Hence, more observational studies of star-forming regions at sub-parsec scales are required to clearly understand the roles of gravity and turbulence (i.e., driving factors of cloud dynamics).

7.4.2 Star formation Scenario

The multi-wavelength study at larger scale of W42 region by Dewangan et al. (2015) shows that the massive O5.5 star and W42-MME form at a $\sim$3$\times$3 pc^2 junction of several converging filaments ($\sim$1–3 pc). This junction itself is situated at the waist of a bipolar H II region. This picture emphasize the role of filaments in MSF as discussed by Motte et al. (2018) in their evolutionary scheme of MSF.

The HFSs are widely popular and thought to provide a suitable environment for the formation of massive stars (e.g., Kumar et al., 2020). However, within a hub one can expect the interplay of different physical processes driven by gravity, turbulence, and magnetic fields. In our site, the young massive protostar W42-MME resides in close proximity to the O5.5 star (Dewangan, 2022). The massive O5.5 star drives enough mechanical energy in the form of its pressure components (i.e., from H II region, radiation, wind, and by self-gravity; see Dewangan et al., 2015, for detailed calculations) at the vicinity of W42-MME, thus can overall increase the turbulent properties of gas.

A filamentary morphology of coherent velocity structure (61–66 km s^{-1}) of size ∼0.3 pc spanning east-west direction is observed in H^{13}CO^{+} data, containing the dendrogram leaves L18, L16, L7, L17 (including L13, L14), L15, and L10 (see Figures 7.4b and 7.5b). It is interesting to note that the spatial separation between the leaf pairs of L17–L7 (∼3$''$.4) and L17–L15 (∼2$''$.4) is more or less similar. Similarly, it is true for leaf pairs of L17–L16 (∼6$''$.1) and L17–L10 (∼6$''$.6). This may hint at the filament fragmentation by the combined effect of gravity and turbulence (Inutsuka & Miyama, 1992; Nakamura et al., 1995; Inutsuka & Miyama, 1997). Earlier Dewangan (2022) pointed out the presence of at least 5 continuum peaks within a dusty envelope (or branch B11 in our analysis) that hosts W42-MME. We note that only one continuum peak (see peak B in Figure 4 in Dewangan, 2022, also see Figure 7.13) falls within the ALMA beam. The H^{13}CO^{+} data however trace a peak (L14) which is not prominent in the continuum image at 865 μm. It is possible that the W42-MME (L17) compete for material with the nearby sources L13 and L14, which is supported by the potency of MSF in leaf L17 from $M-R$ plot (Figure 7.12) and infall signature in the H^{12}CO^{+} spectral profile. However, the further high-resolution line data with the dense gas modeling can infer the onset of the competitive accretion process (Bonnell et al., 2001; Bonnell & Bate, 2006). The remaining leaves are observed in the feedback-affected zone, which can be seen in the redshifted velocity range of 66–72 km s^{-1} (Figure 7.4b). Leaves L5 and L2 appear to have potentially accumulated by the outflow emanating from W42-MME (L17).

7.5 Summary and Conclusion

We carried out an analysis of the dense gas structures in the immediate surroundings of a young massive protostar W42-MME using high-resolution ($0''.31\times 0''.25$) ALMA dust continuum and line data. A dendrogram analysis is performed in the *p-p-v* space, allowing us to trace multi-scale structures and their spatio-kinematic properties. We analyzed the fragmentation and dynamic states of dense structures, considering scales as small as ∼2000 AU. The major results of our study are as follows:

- The dendrogram analysis of the ALMA $H^{13}CO^+$ (4–3) data resulted in the identification of 19 dense gas structures, out of which 12 are leaves (mean size ∼3780 AU) and 7 are branches (mean size ∼11780 AU). The gas motions in these structures are transonic to supersonic ($1< \mathcal{M} < 5$) and they show overvirial ($\alpha_{\rm vir} \geq 2$) states. The infall signature is observed in the $H^{12}CO^+$ (4–3) line profiles of most of the leaves.

- The non-thermal line-width size relation ($\sigma_{\rm nt} - L$) of dendrogram structures overall shows a weak negative correlation. However, velocity-variation ($\delta V_{\rm lsr}$) displays strong positive correlation with the structure size and the relation follows the generalized Larson's law with steeper exponent of 0.46±0.14 at a constant column density of $\sim10^{23}$ cm^{-2}. These results agree with the study of Ballesteros-Paredes et al. (2018) and support the hierarchical and chaotic collapse scenario.

- Velocity structure function analysis of $H^{13}CO^+$ data reveals the strong power-law dependencies ($\propto\ L^{0.73\pm0.01}$) with $L \lesssim$6000 AU. The overall mean scaling exponents of structure funtion for branch structures is found to be relatively larger compared to that for leaves.

- The mass-size relation of dendrogram structures shows positive trend with a power-law exponent of 1.73±0.23. The density, however, displays a marginally statistically significant anti-correlation with size. The leaf L17 that hosts W42-MME, meets the mass-size conditions for MSF as discussed by Kauffmann & Pillai (2010); Urquhart et al. (2014).

Overall, the star formation history in the vicinity of W42-MME appears to have been influenced by the effect of scale dependent physical processes, that include the combined role of turbulence and gravity.

Chapter 8

Formation and interaction of O-type stars in filaments: insights from the S305 HII Region[†]

8.1 Introduction

This chapter focuses on the formation of massive stars in a filamentary cloud and primarily explores their feedback effects on the surrounding environment. This section serves as a brief background in this aspect followed with the information of target sites.

Massive OB-type stars drive powerful energetics, which allow them to control the physical state of the ISM. The EUV photons ($h\nu \geq$13.6 eV) from such massive stars ionize the hydrogen atoms and create HII regions. Due to the thermal pressure difference between the ionized region and the surrounding neutral/molecular environment, an HII region continues to grow in size, and may trigger star formation in numerous ways (see the review article by Elmegreen, 1998). However, the study of the interaction of massive stars with their surrounding environment is still an open research topic in astrophysics.

[†] **Bhadari, N. K.**, Dewangan, L. K., Zemlyanukha, P. M., Ojha, D. K., Zinchenko, I. I., Sharma, Saurabh, 2021, ApJ, 922, 207, "Probing gas kinematics and PDR structure around O-type stars in Sh 2-305 HII region"

The surroundings of the HII regions, where the FUV radiation (6 eV$\leq$ $h\nu$ $\leq$13.6 eV) plays a significant role in the heating and/or chemistry of the gas, are referred to as PDRs (e.g., Tielens & Hollenbach, 1985a,b; Hollenbach & Tielens, 1999). The FUV photons can dissociate the molecules and photoionize those elements having ionization potential less than the Lyman limit. The gas is primarily neutral in PDRs, but still includes the tracers of singly ionized species (e.g., C^+, S^+, Si^+, and Fe^+), molecular gas (e.g., H_2 and CO), and PAH emission (e.g., Hollenbach & Tielens, 1999; Kaufman et al., 2006). Hence, the PDRs specify the transition zone between ionized and molecular gas (see Figure 1 in Tielens & Hollenbach, 1985a). Being a major coolant in PDRs, the $^2P_{3/2}$–$^2P_{1/2}$ fine structure line of ionized carbon, [CII] 158 μm offers a unique probe of kinematic and radiative interaction of massive stars with their surroundings (e.g., Abel et al., 2007; Schneider et al., 2020, and references therein).

In this work, we employed the observations of 158 μm [CII] line to study the gas dynamics of PDRs in a promising Galactic HII region, Sh 2-305 (hereafter, S305) powered by two O-type stars. In addition to the study of the spatio-kinematic structure of PDRs in S305, this work presents evidence of expanding [CII] shells (also abbreviated as neutral shells in this work), hinting the applicability of the triggered star formation scenario. In this work, we also highlight the extended physical environment of S305 HII region, which encompasses Sh 2-309 (hereafter, S309) and Sh 2-306 (hereafter, S306) HII regions. We present the initial results of our own uGMRT data (ID: 39_048, PI: Naval Kishor Bhadari) and a comparison with the ^{13}CO(1–0) line data. However, the detailed multi-wavelength analysis is performed in *Bhadari et al., under preparation*. Therefore, this chapter is only dedicated to the investigation of the formation of known massive stars in the S305 HII region, and their feedback processes.

We organize this work into six sections. Following the introduction in this section, we present an overview of the Galactic HII regions S305, S306, and S309 and extended dusty and gaseous environment in §8.2. §8.3 presents the description of data sets used in this work. The observational results are presented in §8.4. The implications of our derived findings are discussed in §8.5. Finally, we summarize our major outcomes in §8.6.

8.2 Overview of the extended environment around S305 HII region

Figure 8.1a and 8.1b present the *Herschel* 250μm view of an extended dusty region around S305 HII region, the specific focus of current study. The distribution of radio continuum emission in Figure 8.1b shows the locations of S309, S306, and S305 HII regions. Below, we provide an overview of these targets.

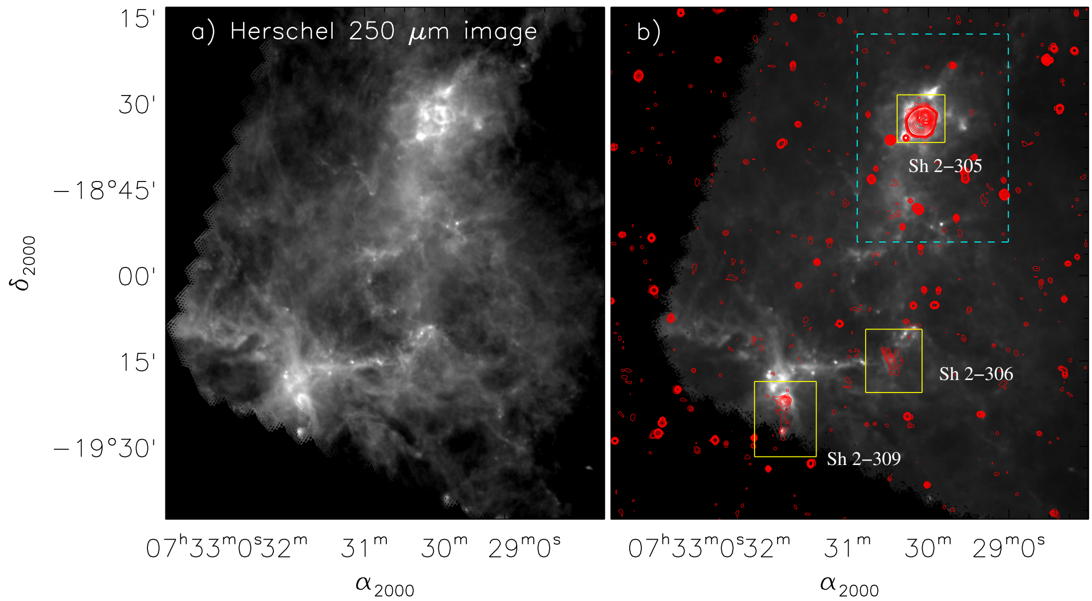

Figure 8.1: a) The *Herschel* 250 μm gray scale image of a cloud complex consisting S309, S306, and S305 HII regions. b) Overlay of the NVSS 1.4 GHz radio continuum emission on the *Herschel* 250 μm image. The three HII regions are marked by solid rectangular boxes, while a dashed rectangular box represent an area where ^{13}COgas emission is explored (see Figure 8.4).

8.2.1 S305 HII region

The S305 HII region is a part of a large molecular cloud complex located at a distance of ∼3.7 kpc (Pandey et al., 2020, hereafter Paper I). The molecular cloud associated with S305 has been depicted in a velocity range of [40, 48] km s^{-1} (Dewangan et al., 2020b, hereafter Paper II). In Figure 8.2a, we show a two-color composite map (*Spitzer* 4.5 μm (red); *Spitzer* 3.6 μm (green) images) of S305, displaying an extended shell-like structure. At the centre of the shell-like structure, two massive O-type stars (O8.5V: VM4 and O9.5V: VM2; Vogt & Moffat, 1975; Chini, 1985) are located and their positions are shown by star symbols in Figure 8.2a. The positions of Young Stellar Objects (YSOs; from Paper I) and the Giant Metrewave Radio Telescope (GMRT) 1.28 GHz continuum contours (from Paper II) are also overlaid on the color composite image.

In Figure 8.2b, we present the *Herschel* column density map overlaid with the NVSS (resolution $\sim$45″; Condon et al., 1998) 1.4 GHz continuum emission contours, allowing us to infer the spatial distribution of dense condensations against the ionized gas. Figure 8.2c displays the overlay of the FUGIN*(resolution $\sim$20″; Umemoto et al., 2017) ^{12}CO(1–0) molecular emission contours on the *Herschel* column density map. The previously known dust clumps (from Sreenilayam et al., 2014) are also labeled in Figure 8.2c. Noticeable YSOs are also found toward the dust clumps and molecular condensations, which are distributed in a regularly spaced manner around the S305 HII region. The extended structure traced in the *Herschel* temperature map of S305 is shown in Figure 8.2d. Collectively, Figure 8.2 shows the multi-wavelength view of S305, which was already presented and described in Papers I and II.

Previously in Papers I and II, the S305 HII region was proposed as a candidate site of triggered star formation. It was primarily investigated based on the observed morphology, dynamical age of HII region, and the fragmentation time scale of the associated molecular shell. However, a direct observational proof of the triggered star formation in S305 remains ambiguous.

8.2.2 S306 and S309 HII region

The HII regions S306 and S309 are part of the large molecular cloud at a distance of 4.2 kpc and $V_{LSR} \simeq 43$ km sec^{-1} (Russeil et al., 1995). Figure 8.3 shows the three-colour composite map (Red: *Planck* 857 GHz; Green: WISE 22 μm; Blue: Hα) of the target region which includes both the proposed star-formation sites. The positions of previously known massive O-type stars (in filled star symbols)

*FOREST Unbiased Galactic plane Imaging survey with the Nobeyama 45-m telescope

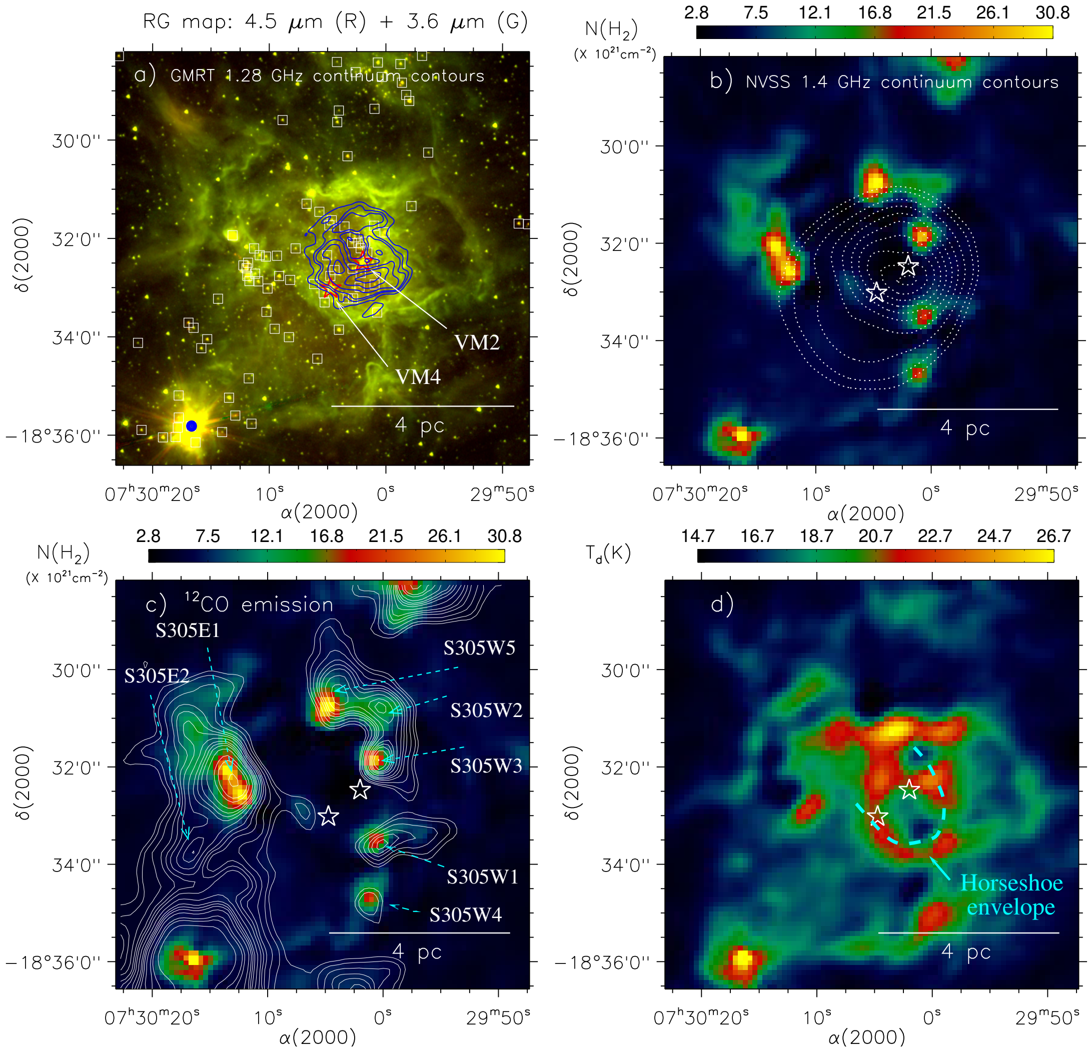

Figure 8.2: (a) Two-color composite image (Red: *Spitzer* 4.5 μm and Green: *Spitzer* 3.6 μm) of the S305 HII region. The GMRT 1.28 GHz continuum emission contours (in blue) are overlaid with the levels of (0.4, 0.46, 0.5, 0.6, 0.7, 0.8, 0.9, 0.98) $\times$ 22 mJy beam^{-1}, where 1σ $\sim$0.74 mJy beam^{-1}. The positions of YSOs (from Pandey et al., 2020) are marked by □. (b) *Herschel* column density map overlaid with the NVSS 1.4 GHz contours. The contour levels are (0.15, 0.2, 0.3, 0.4, 0.5, 0.6, 0.7, 0.8, 0.9, 0.98) $\times$ 144 mJy beam^{-1}. (c) Overlay of FUGIN ^{12}CO(1–0) emission (velocity $\sim$[39, 49] km s^{-1}) contours on the *Herschel* column density map. The contour levels are (0.2, 0.22, 0.25, 0.28, 0.3, 0.32, 0.35, 0.38, 0.4, 0.42, 0.45, 0.5, 0.53, 0.6) $\times$ 112.56 K km s^{-1}. The positions of the 850 μm continuum clumps (from Sreenilayam et al., 2014) are marked by arrows and labeled (see Figure 5 in their paper). (d) *Herschel* temperature map. A dashed curve (in cyan) indicates the footprint of the horseshoe envelope (see Dewangan et al., 2020b, for more details). In each panel, the positions of previously known massive O-type stars are marked by star symbols and labeled in panel "(a)". A scale bar referring to 4 pc (at a distance of 3.7 kpc) is also displayed.

and known HII regions (in open hexagons) are marked on the image. The strong Hα emission (in blue) traces the ionized emission near both the target HII regions. This indicates that the massive O-type stars toward these sites have a significant impact on the surroundings. We have overlaid the NVSS 1.4 GHz continuum emission contours (RMS, $1\sigma = 0.45$ mJy/beam; beam size $\sim 45''$) on the image. The NVSS observation reveals the extended morphology toward both the selected HII regions. One of the NVSS radio continuum peaks coincides with the position of an infrared source, RAFGL 5233 (see an open circle in Figure 8.3), while another peak is seen toward the previously known massive O-type star. However, with the available sensitivity and resolution of the NVSS 1.4 GHz continuum map, one cannot study the detailed morphology of the selected HII regions.

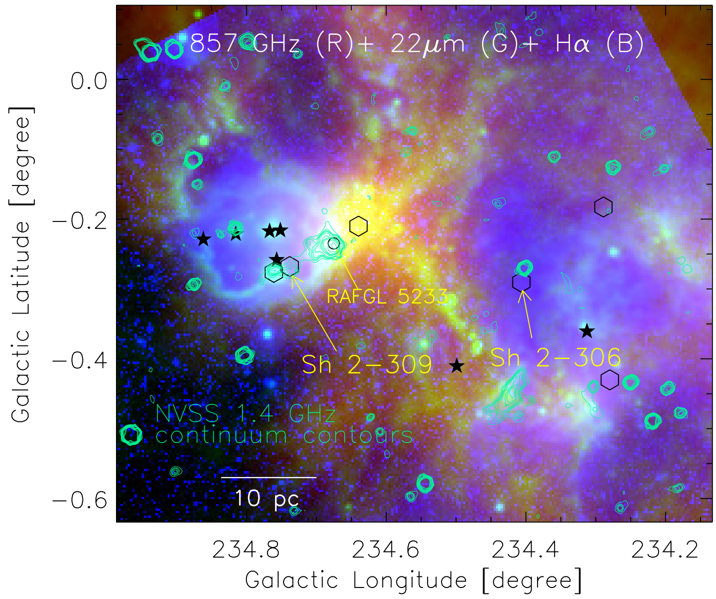

Figure 8.3: Three-colour composite image of the S306 and S309 HII region. Red: *Planck* 857 GHz; Green: WISE 22μm; Blue: Hα. NVSS 1.4 GHz radio emission contours (in spring green) are overlaid on the image. The contours are shown with the levels (3, 4, 4.5, 5, 6, 8, 9, 10, 12, 15, 17) $\times$ 1σ, where $1\sigma = 0.45$ mJy beam $^{-1}$. The positions of known HII regions and O-type stars are indicated by open hexagon and filled star symbols, respectively. The locations of major HII regions, S306 and S309 and an infrared source (RAFGL 5233; see an open circle) are marked and labeled by arrows. A scale bar representing the physical length of 10 pc (at d= 4.2 kpc) is shown in the bottom-left corner.

Based on our preliminary multi-wavelength analysis, the selected site S309 appears to be a part of HFS. In general, the HFS represents the complex of filamentary molecular clouds merging at the central hub. Such systems are considered as the promising sites for MSF (e.g., Motte et al., 2018). The filamentary features are evident in the IR/submillimeter images and show the existence of the HFS morphology (see Figure 8.3). Although the site S306 does not display the direct association with the HFS, an ionized region is evident with the extended morphology. Hence, to further explore the detailed morphology and nature of the selected HII regions, the high-sensitive and high-resolution radio continuum observations are required. Therefore, to investigate these sources further, we conducted observations using the uGMRT at Bands-3, 4, and 5. The standard procedure of uGMRT data reduction was followed in `CASA` and we primarily used the `CASA-CAPTURE` pipeline to produce the radio continuum maps (see more detials in Kale & Ishwara-Chandra, 2021). However further improvement in image cleaning is still required. A comparison between our preliminary results from the uGMRT observations and the NVSS is shown in Figure 8.4. This demonstrate the improved sensitivity of GMRT images than the NVSS. We are currently working on a detailed analysis, and the comprehensive results will be presented in a forthcoming publication by Bhadari *et al.* (under preparation), as part of our immediate future plans (see Chapter 9).

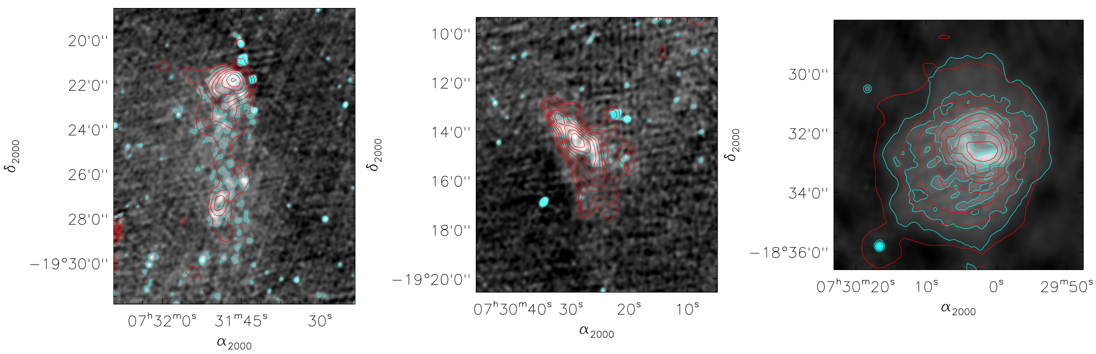

Figure 8.4: Comparison of uGMRT Band-3 (∼375 MHz) and NVSS images of the HII regions, S309 (*left panel*) and S306 (*middle panel*) regions. The GMRT data at Band-5 (∼1280 MHz) for S305 HII region (*right panel*) is obtained from Paper II and is utilized in this chapter. In each panel, the radio continuum emission from GMRT is shown by cyan contours and gray scale image, while the emission from NVSS is indicated by red contours.

8.3 Data sets

8.3.1 SOFIA [CII] observations

In this work, we used the science ready 158 μm [CII] line data cube of S305 (Project ID: 06_0226; PI: Loren Dean Anderson), which was obtained from the InfraRed Science Archive[†]. The line observations were taken with the Strato-

[†]https://irsa.ipac.caltech.edu/applications/sofia

spheric Observatory for Infrared Astronomy (SOFIA)/upGREAT[‡] instrument. The [CII] line data have a half-power beamwidth of 14.″1 and a velocity resolution of 0.385 km s^{-1} (see Anderson et al., 2019; Schneider et al., 2020, for data reduction procedure). We smoothed the original line data cube with a Gaussian function having 3 pixels half-power beamwidth (i.e., 21.″15, where 1 pixel corresponds to 7.″05), which improved the image sensitivity. The resulting resolution of the line data cube is 25.″4.

8.3.2 Ancillary Data

We used multi-scale and multi-wavelength data sets, which were obtained from different existing surveys e.g., the Warm-*Spitzer* GLIMPSE360 Survey (λ = 3.6 and 4.5 μm; resolution ∼2″; Benjamin et al., 2003; Whitney et al., 2011), Wide-field Infrared Survey Explorer (*WISE*; λ = 12 μm; resolution ∼6.″5; Wright et al., 2010), the NVSS, and the FUGIN survey (^{12}CO/^{13}CO (J=1–0); resolution ∼20″–21″). Apart from these data sets, we also utilized the *Herschel* temperature and column density maps (resolution ∼12″) from Molinari et al. (2010a) which were generated for the *EU-funded ViaLactea project*. The Bayesian *PPMAP* method (Marsh et al., 2015, 2017) was applied to build these *Herschel* maps. The GMRT radio continuum map at 1280 MHz (resolution ∼10″) was taken from Paper II.

8.4 Results

8.4.1 Association of S305 HII region with a filament

The analysis of ^{13}CO(1–0) data reveals the presence of a filamentary cloud associated with the S305 HII region. Figure 8.5a illustrates the moment-0 map of ^{13}CO emission within the velocity range of [39.4, 49.4] km s^{-1}. Notably, the known massive O-type stars are denoted by red stars and are observed to be spatially located at the center of the filamentary cloud. The velocity map of the

[‡]upGREAT(Risacher et al., 2016) is an enhanced version of the German Receiver for Astronomy at Terahertz Frequencies (GREAT).

cloud, presented in Figure 8.5b, shows a distribution of peak velocities. This distribution suggests that a single filamentary cloud consists of at least two distinct velocity clouds. This observation is consistent with the findings of Nakamura et al. (2014) in the Serpens South region, where the collision of filamentary ridges is associated with the formation of massive stars. Likewise, in the S305 region, the presence of two cloud components at V_{LSR} of approximately 42 and 45 km s^{-1} indicates a potential collision between them. This collision may have triggered the formation of a cluster, which includes the already known O-type stars. The PV diagram in Figure 8.6b provides additional support for the existence of these two clouds.

Furthermore, it is worth mentioning that the interaction between massive stars and filamentary cloud environments can have two possible outcomes. On one hand, it can lead to the destruction of lower density filaments, allowing ionized radiation to escape. On the other hand, it can result in the trapping of ionized radiation within high column density filaments. This understanding is supported by a recent model proposed by Whitworth & Priestley (2021), which explores the escape and trapping of ionizing radiation emitted by O-type stars forming within filaments. In the case of the S305 HII region, it appears to align with the scenario where the filament is destroyed by the intense radiative and mechanical feedback from two massive O-type stars. In the subsequent sections, we delve deeper into the study of the feedback from these massive stars on the surrounding environment.

In Paper II, molecular condensations, PAH emission, dust clumps, and H_2 emission have been traced toward the horseshoe envelope surrounding the ionized shell, where noticeable YSOs are also found (see Figure 8.2). The ionized shell is traced by the GMRT 1.28 GHz continuum emission (see Figure 8.2a), while the footprint of the horseshoe envelope is shown by a dashed curve in Figure 8.2d. In the following sections, we study new observations of the 158 μm [CII] line toward S305, enabling us to examine the spatial and velocity structure of PDRs in our target site.

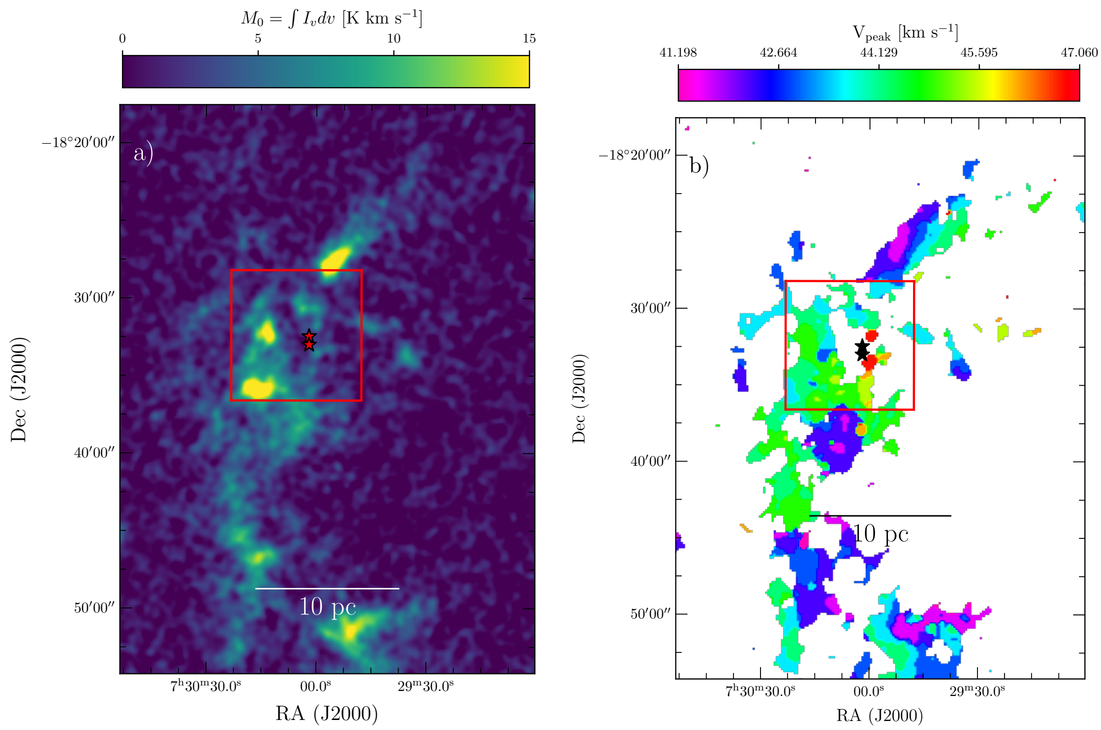

Figure 8.5: a) Integrated intensity map of ^{13}CO(1–0) emission (velocity = [39.4, 49.4] km s^{-1}) in the direction of S305 HII region. b) Peak velocity map of ^{13}CO(1–0) emission. In both the panel, stars indicate the locations of known massive stars, and a solid box is the area where further analysis is performed in the next figures. A scale bar is drawn considering the source distance of 3.7 kpc.

8.4.2 The spatial-kinematic structure of PDRs in S305

In Figure 8.7a, we show an moment-0 map of the [CII] emission around S305, where the [CII] emission is integrated over a velocity range of [39.4, 49.5] km s^{-1}. The NVSS 1.4 GHz continuum emission contours are also overlaid on the [CII] emission map. The integrated [CII] emission map hints the presence of two shell-like structures (i.e., inner and outer neutral shells) in S305. These shells can be regarded as the PDRs in S305 region (see Section 8.1). The inner neutral shell, having a compact ring-like appearance, is evident with a high intensity value of [56, 110] K km s^{-1}, and extends toward the eastern direction. A depreciation of the [CII] emission (i.e., a cavity), the radio continuum peak emission, and the position of the massive O9.5V star (i.e., VM2) spatially coincide, and are found at the centre of the inner neutral shell. The outer neutral shell is traced with the diffuse and more extended [CII] emission having a lower intensity value of [20, 55] K km s^{-1}, and surrounds the inner neutral shell. The massive O8.5V star

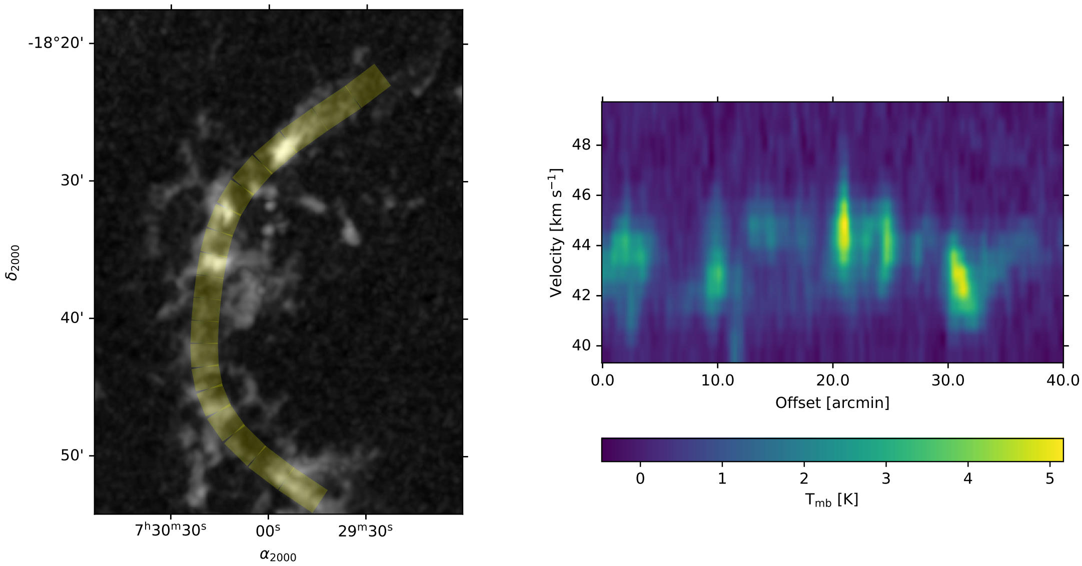

Figure 8.6: *Left:*^{13}CO(1–0) integrated intensity map of S305 HII region (see Figure 8.5a). A yellow strip is a path for studying the PV diagram. *Right:* PV diagram along a yellow strip (see left panel) as we move from south to north direction.

(i.e., VM4) appears to be located at the centre of the outer neutral shell. This particular morphology is also seen in the Hα image from Paper II (see Figure 9 therein), which suggests that VM4 may be the major source of feedback in the dusty HII region S305. The other [CII] emission peaks are also seen toward the north and south-east directions and lie toward the locations of the previously identified clusters of YSOs (e.g., Paper I).

We show a two-color composite map (Red: [CII] moment-0 map; Turquoise: *WISE* 12 μm image) of S305 in Figure 8.7b. The spatially extended structures seem to match well in both images. In Figure 8.7b, we have also marked twenty circular regions, where the gas spectra are extracted and examined. Figure 8.7c presents the [CII] moment-1 map that allows us to study the spatial distribution of the mean velocity of emitting gas. A nearly linear velocity gradient can be seen in the north-south direction. However, one can notice that the inner neutral shell is redshifted compared to the blueshifted outer/extended diffuse shell. The [CII] moment-1 map is also overlaid with the positions of previously identified ^{12}CO(2–1) molecular clumps and their velocities (Azimlu & Fich, 2011, see also Paper II). The velocities of these clumps are in agreement with the velocities of the [CII] gas at corresponding positions. Nearly eight molecular clumps are found to be spatially coincident with the inner neutral shell. Six out of eight molecular clumps (i.e., c5–c10) are seen in the direction of the horseshoe envelope (see Figure 8.2d).

In order to compare the spatial structure traced by the [CII] emission and the infrared continuum images, we present the *Spitzer* ratio map of 4.5 μm emission to 3.6 μm emission in Figure 8.7d. A detailed discussion on the ratio map is given in Paper II. The bright and dark emission zones in the ratio map detect the ionized emission and the PDR walls, respectively. One can notice from Figures 8.7a and 8.7d, that the boundaries of the [CII] shells are well traced by the dark structures in the ratio map. Thus, the analysis of multiwavelength data confirms the presence of two shells.

Figure 8.8 presents the velocity channel contours of the [CII] emission overlaid on the *WISE* 12 μm image, enabling us to explore the gas motion. We find the spatial match of the [CII] emission with the infrared structure traced in the *WISE* 12 μm image. In general, the *WISE* 12 μm image is known to cover the prominent PAH features at 11.3 μm. In the channel maps, based on the visual inspection, we marked the boundaries of two [CII] shells by dotted circles. The larger dotted circle (centre coordinates; RA = 07^{h} 30^{m} $04^{\mathrm{s}}.51$, Dec = -18° 32″ 32′.72, and radius = 205′) encloses the [CII] emission of the outer diffuse shell. The outer [CII] shell is clearly seen in the velocity range from 42.1 to 44.1 km s^{-1}, and has an incomplete circular (or broken ring) appearance. On the other hand, the smaller circle (centre coordinates; RA = 07^{h} 30^{m} $02^{\mathrm{s}}.39$, Dec = -18° 32″ 19′.95, and radius = 105′) surrounds the inner [CII] shell, which is evident in the velocity channel maps from 45.2 to 47.5 km s^{-1}. In the direction of inner shell structure, the [CII] channel maps show that the [CII] emission is blueshifted in the northern direction, while it is strongly redshifted in the southern direction. This implies that the gas is moving toward (away from) the observer in the northern (southern) directions (e.g., Mookerjea et al., 2021). Overall, these results suggest the expansion of the gas in PDRs (see Section 8.5 for detailed discussion).

In order to compare the kinematics of different gas components, we have analysed the spectral profiles of ^{12}CO/^{13}CO(1–0) and [CII] gas in Figure 8.9. Fig-

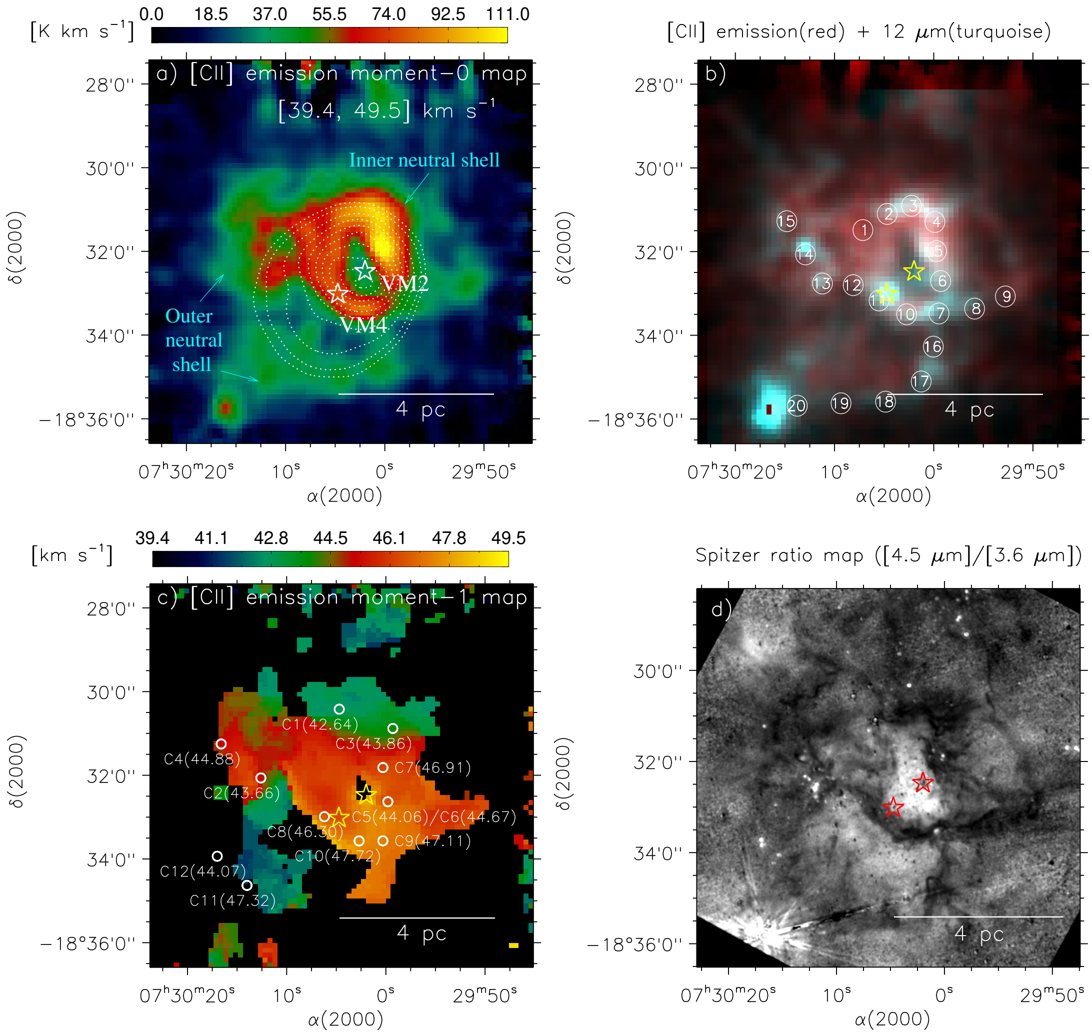

Figure 8.7: (a) The panel displays the [CII] integrated intensity (moment-0) map of S305. The map is overlaid with the NVSS 1.4 GHz continuum emission contours, which are the same as in Figure 8.2b. (b) Two-color composite image (Red: [CII] moment-0 map and Turquoise: *WISE* 12 μm image) of the S305 HII region. The twenty circles (radius =15$'$ each) represent the areas for which the gas spectra are extracted (see Figure 8.9). (c) [CII] moment-1 map overlaid with the positions of ^{12}CO(2–1) molecular clumps (from Azimlu & Fich, 2011). The clumps are highlighted by open circles and corresponding velocities are also labeled. (d) The *Spitzer* ratio map of 4.5 μm/3.6 μm emission (reproduced from Dewangan et al., 2020b). In all the panels, the stars are the same as in Figure 8.2.

ure 8.9 displays the line profiles of the [CII], ^{12}CO(1–0), and ^{13}CO(1–0) emission toward twenty circular regions (radius =15$'$ each) in the direction of S305. These regions are primarily selected toward the direction of prominent infrared features and the [CII] emission (see circles in Figure 8.7b). Each spectrum is produced by averaging the emission over the circular regions. In the direction of the compact ring feature (i.e., positions 1–15), [CII] line profiles are brighter and are either blue-skewed or have double-peaked structures compared to the ^{12}CO(1–0), and

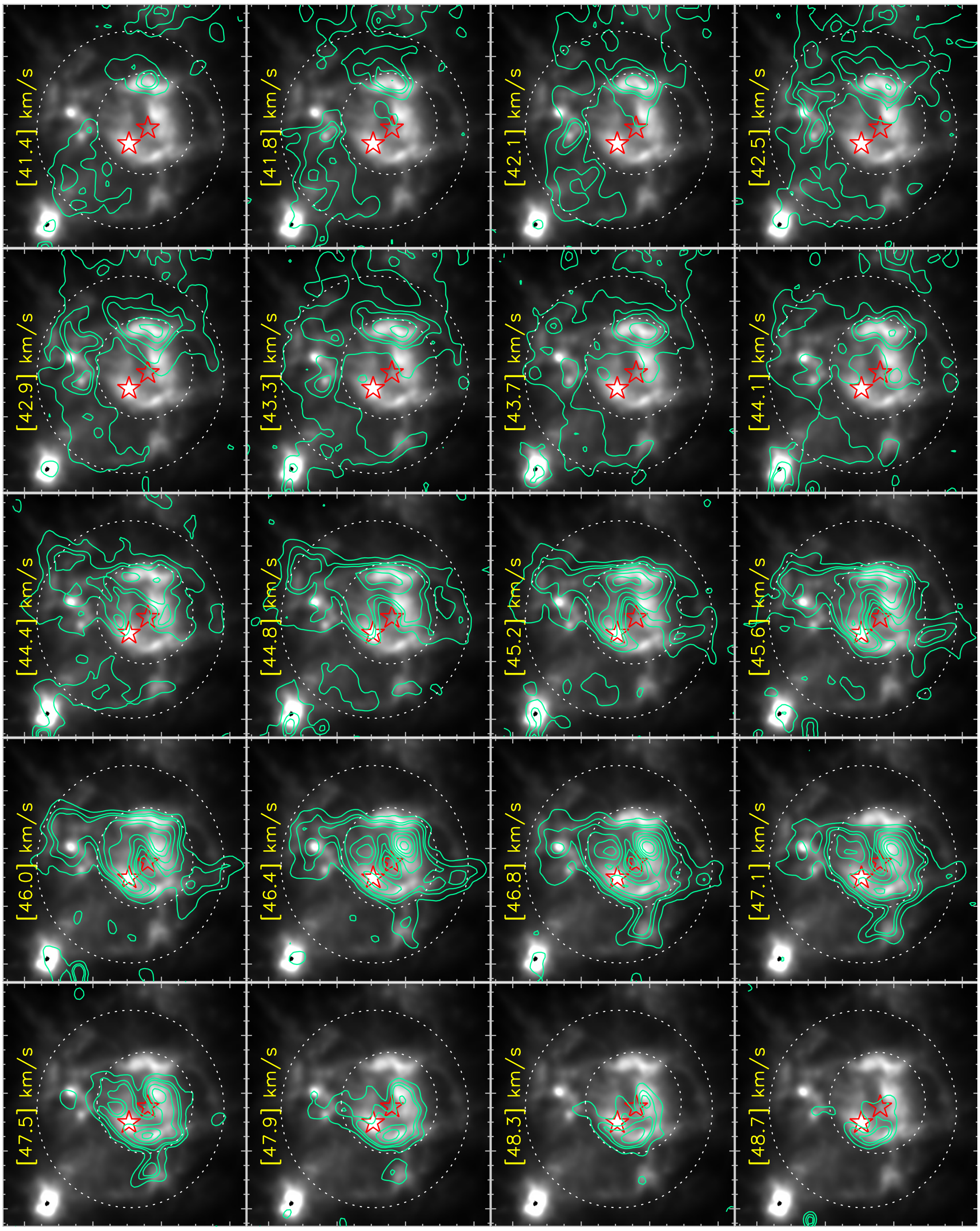

Figure 8.8: Velocity channel contours of the [CII] emission overlaid on the *WISE* 12 μm image. The velocity value is indicated in each panel (in km s^{-1}). The contours (in spring green) are shown with the levels of 5, 8, 10, 15, 20, 25, 30, and 35 K. The dotted circles represent the footprint of inner and outer [CII] shells. In each panel, the positions of known massive stars are marked by star symbols.

^{13}CO(1–0) profiles. The [CII] line profiles show double peaks at $\sim$43 and $\sim$47 km s^{-1}, and a dip around $\sim$44 km s^{-1}. On the other hand, the ^{12}CO(1–0) and ^{13}CO(1–0) profiles are single-peaked and lie between the double peaks of the [CII] spectra. Interestingly, all the double-peaked profiles have a brighter redshifted component than the blueshifted one (see Section 8.5 for more discussion).

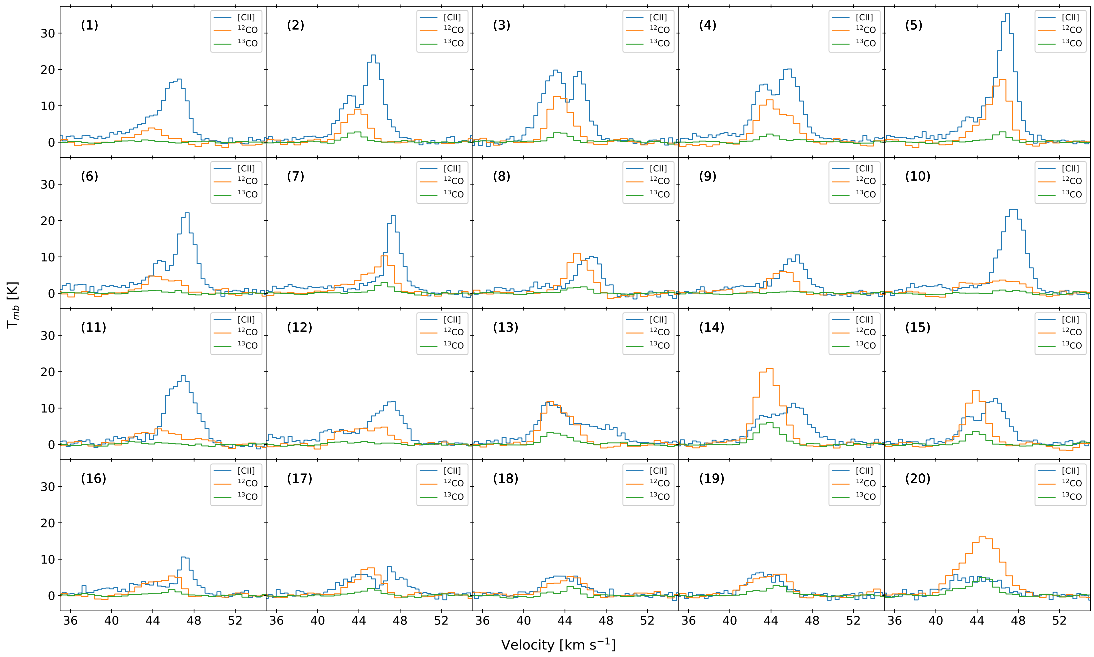

Figure 8.9: Profiles of the [CII], ^{12}CO(1–0), and ^{13}CO(1–0) emission toward twenty circular regions (radius =15′ each) in S305 (see circles in Figure 8.7b). The corresponding circle number is marked in each panel.

In Figure 8.10, we have shown the [CII] line profiles (similar to those presented in Figure 8.9) with color coded redshifted and blueshifted components. From the velocity channel maps (Figure 8.8), we have identified the velocity ranges of these components. The blueshifted component ([39.4, 44.4] km s^{-1}) is found to be associated with the outer shell structure, while the redshifted component ([44.4, 49.5] km s^{-1}) traces the inner shell structure. One can notice from Figure 8.10 that the peak of the redshifted component (i.e., 45.6 km s^{-1}; see panels 2, 3, and 4) shifts toward higher velocities as we move southwards from the northern direction (see Figure 8.7b). However, the blueshifted component peaks at 43.3 km s^{-1} in all the positions, and does not show much variation along the velocity axis. These results suggest the noticable gas expansion in the inner shell compared to the outer shell. However, considering the simplistic case, we assume a similar expansion velocity for both the shells to estimate their expansion timescales (see Section 8.4.3).

Based on the selected velocity ranges of redshifted and blueshifted components from Figure 8.10, we have examined the moment maps. Figures 8.11a and

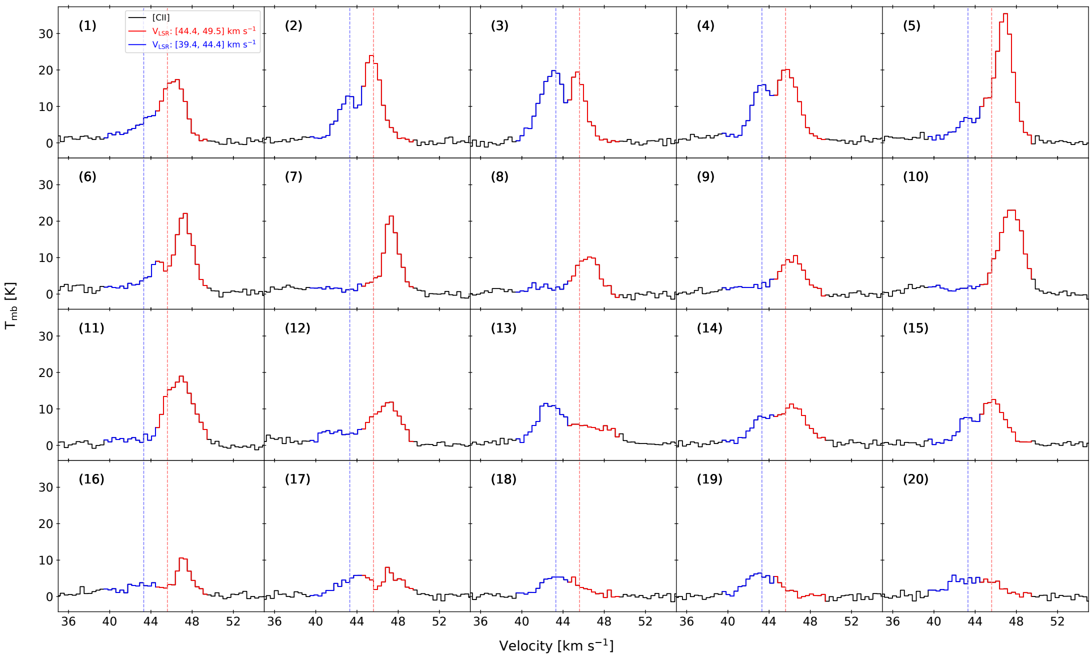

Figure 8.10: Profiles of the [CII] emission, similar to those shown in Figure 8.9. The blue and red components in the [CII] profiles correspond to the velocity range of [39.4, 44.4] km s^{-1} and [44.4, 49.5] km s^{-1}, respectively. These velocity ranges are used to disentangle the inner and outer [CII] shells (see Section 8.4.2 for more details). The vertical dashed lines in blue and red represent the velocities of 43.3 and 45.6 km s^{-1}, respectively.

8.11b show the moment-0 and moment-1 maps for the redshifted component, respectively. The moment-0 map shows the inner shell structure having the compact ring like appearance, while the moment-1 map in Figure 8.11b reveals the velocity gradient along the north-south direction of the inner shell. The velocity at the shell's rim is bluer than the centre, which favors the shell expansion. Generally, the outward displacement of the shell with increasing or decreasing velocity is referred to as the kinematic signature of an expanding shell (e.g., Pabst et al., 2019, see Figure 6 therein). Similarly, Figures 8.11c and 8.11d display the moment-0 and moment-1 maps for the blueshifted component, respectively. The outer shell is evident in the moment-0 map (Figure 8.11c) and has a broken ring morphology. The moment-1 map in Figure 8.11d traces the velocity field in the outer shell. A nearly linear velocity gradient is seen in the east-west direction, which may infer the direction of gas expansion in the outer shell. However, the velocity structure is more complex in the outer shell than the inner shell, which makes it more difficult to interpret.

In order to compare the spatial distribution of different components of gas (i.e.,

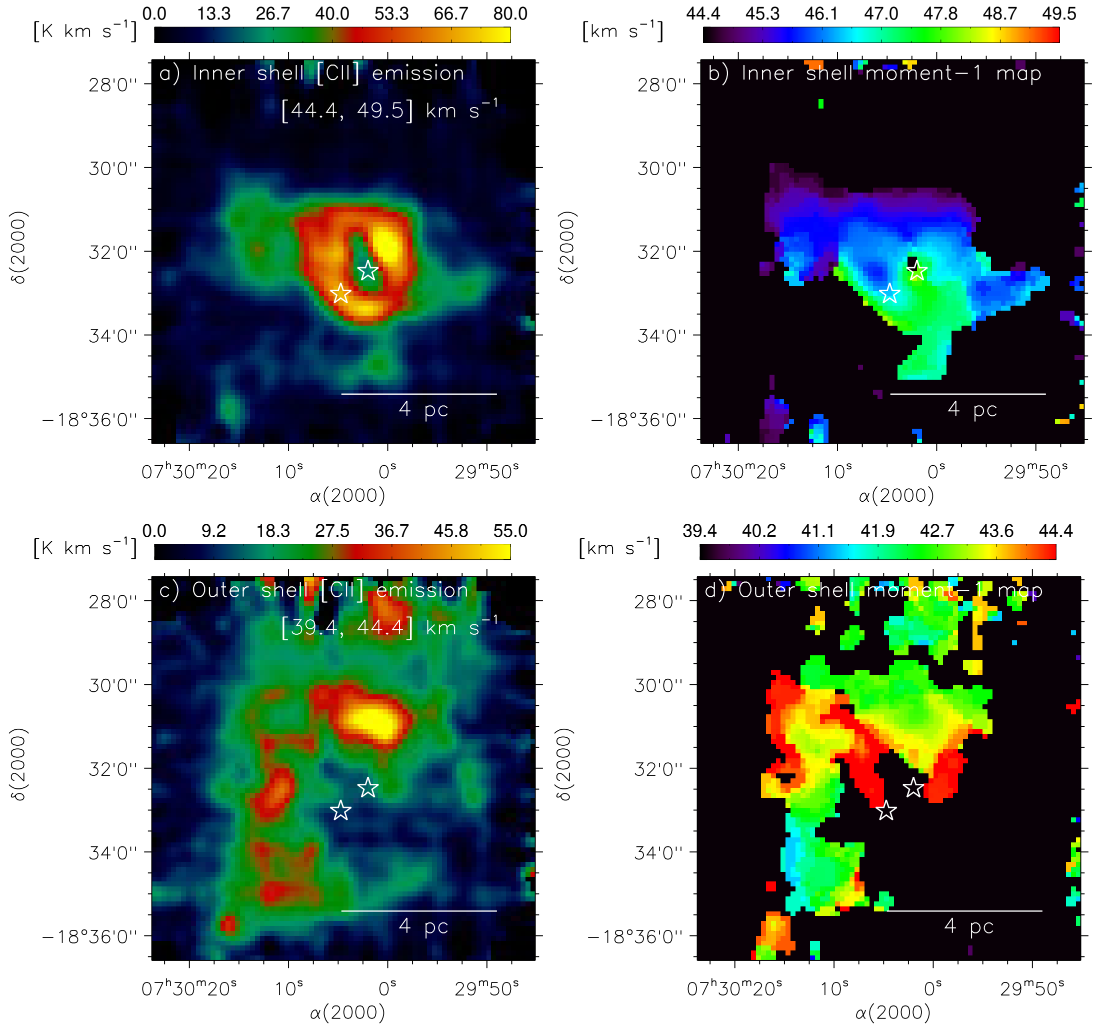

Figure 8.11: Top panels display (a) moment-0 map and (b) moment-1 map of the [CII] emission in the velocity range of [44.4, 49.5] km s^{-1} (see red component of the [CII] profiles in Figure 8.10). Bottom panels show the similar maps as of top panels, but for the outer [CII] shell (see blue component of the [CII] profiles in Figure 8.10). In all the panels, the stars are the same as in Figure 8.2.

ionized, neutral, and molecular) in S305, we show a three-color (Red: GMRT 1.28 GHz, Green: FUGIN ^{12}CO(1–0), Blue: SOFIA [CII] 158 μm) composite image in Figure 8.12a. All the three components of gas are clearly distinguishable. In the direction of the observed [CII] emission, the molecular CO is less abundant or mostly absent (see also Figure 8.9). The distribution of the molecular gas is clumpy rather than a diffuse appearance. Figure 8.12b displays the [CII] emission contours for the inner and outer shell structures (see Figures 8.11a and 8.11c). The detailed interpretation of the shell structures is discussed in Section 8.5.1.

To study the spatial-kinematic structures of the PDRs in S305, we have studied the PV diagrams of different gas components. Figures 8.13a and 8.13b show the PV diagrams of [CII], ^{12}CO(1–0), and ^{13}CO(1–0) emission in two different directions; i.e., perpendicular and along to the line joining the stars VM2 and VM4, respectively. The positive offsets in the positions are measured along the south-west and north-west directions for the two PV diagrams. We have overlaid the emission contours of ^{13}CO(1–0) (in red) and [CII] (in violet) on the ^{12}CO(1–0) PV emission map, allowing us to study the spatial-kinematic structures of different components of gas. The 1.28 GHz radio brightness profile is also shown in each panel, specifying the position of the HII region. The detailed outcomes from this analysis are discussed in Section 8.5.

8.4.3 Physical parameters of the [CII] shells

We have estimated the neutral hydrogen column density (N(H)) and the mass of the [CII] emitting gas toward the compact as well as the extended feature (i.e., inner and outer neutral shells). The column density depends on the luminosity ratio of the [CII] line in the PDR to that of the HII region as follows (see equation A4 in Kaufman et al., 2006)

$$N(\mathrm{H}) = \left(\frac{L_{\mathrm{CII}}(\mathrm{PDR})}{L_{\mathrm{CII}}(\mathrm{HII})}\right) \frac{Z n_e^{1/3} \Phi_{49}^{1/3} f_{\mathrm{C}^+}}{15} \times 10^{21}\ (\mathrm{cm}^{-2}), \tag{8.1}$$

where $\Phi_i = 10^{49}\Phi_{49}$ s^{-1} is the absolute luminosity of ionizing EUV photons, f_{C^+} is the fraction of singly ionized carbon, $Z = 1$ relates to the standard abundance or metalicity, and n_e is the number density of electrons. From the [CII] integrated intensity map, we have estimated the value of $\frac{L_{\mathrm{CII}}(\mathrm{PDR})}{L_{\mathrm{CII}}(\mathrm{HII})}$ around 9. In this exercise, we consider that the [CII] emission, which spatially overlaps with the 1.28 GHz continuum emission (i.e., HII region), belongs to the HII region and the rest of emission corresponds to the part of PDRs.

For the typical values of $Z = 1$, $n_e = 500$ cm^{-3}, $\Phi_i = 10^{49}$ s^{-1}, and $f_{\mathrm{C}^+} = 0.1$ (adopted from Kaufman et al., 2006; Kirsanova et al., 2020), the derived N(H) and the total mass of the [CII] emitting gas in the PDRs are $\sim 5 \times 10^{20}$ cm^{-2} and $\sim$565 M$_\odot$, respectively. The mass calculation is based on the assumption that PDRs

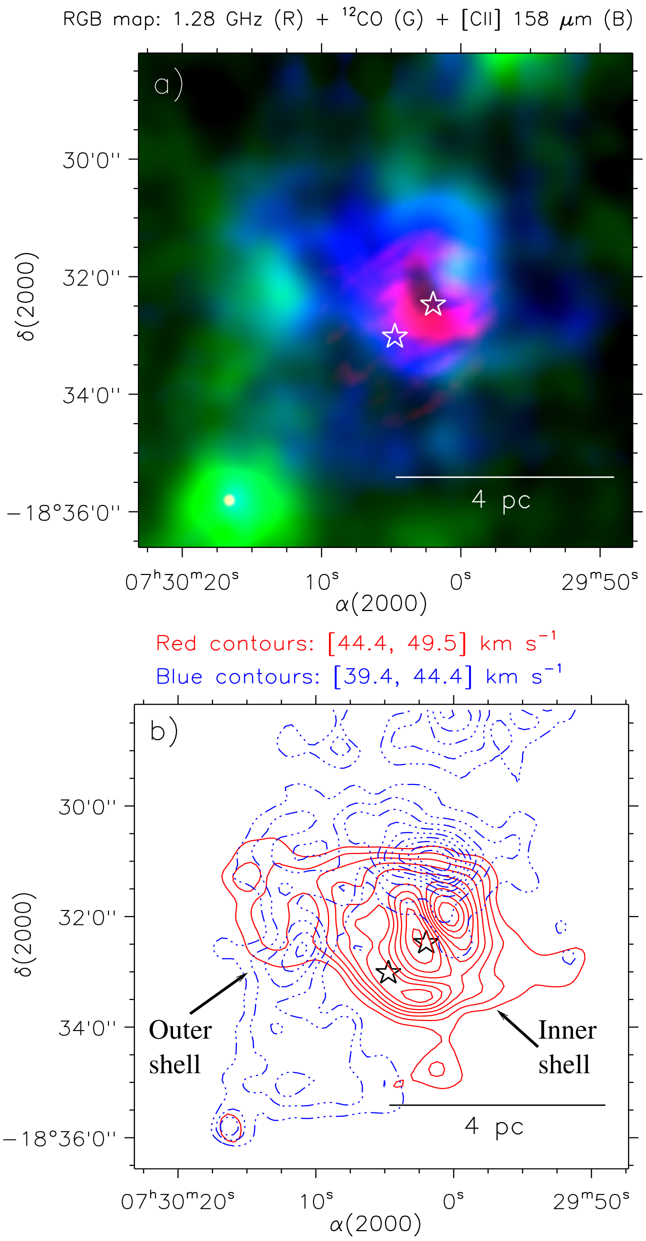

Figure 8.12: (a) Three-color (Red: GMRT 1.28 GHz, Green: FUGIN ^{12}CO(1–0), Blue: SOFIA [CII] 158 μm) composite map of S305. (b) The [CII] emission contours for the inner (in red) and outer (in blue) shell structures. The red contour levels range from 23.34 to 93.36 K km s^{-1} in steps of 7.78 K km s^{-1}, while the blue contour levels range from 19.57 to 65.24 K km s^{-1} in steps of 5.07 K km s^{-1}. The stars are the same as in Figure 8.2.

have the shape of layers on the sphere, and all the material is in the form of neutral hydrogen. We calculated the layer widths from the PV diagrams (Figure 8.13). To compute the total mass of the shells, we used the mass-column density relation of $M_{\rm shell} = m_{\rm H}\, a_{\rm shell}\, \Sigma N({\rm H})$, where $a_{\rm shell}$ is the shell area, $m_{\rm H}$ is the mass of hydrogen atom, and $\Sigma N({\rm H})$ is the integrated column density over the shell area. In this exercise, the uncertainty caused by the noise is around 10%, but the assumptions

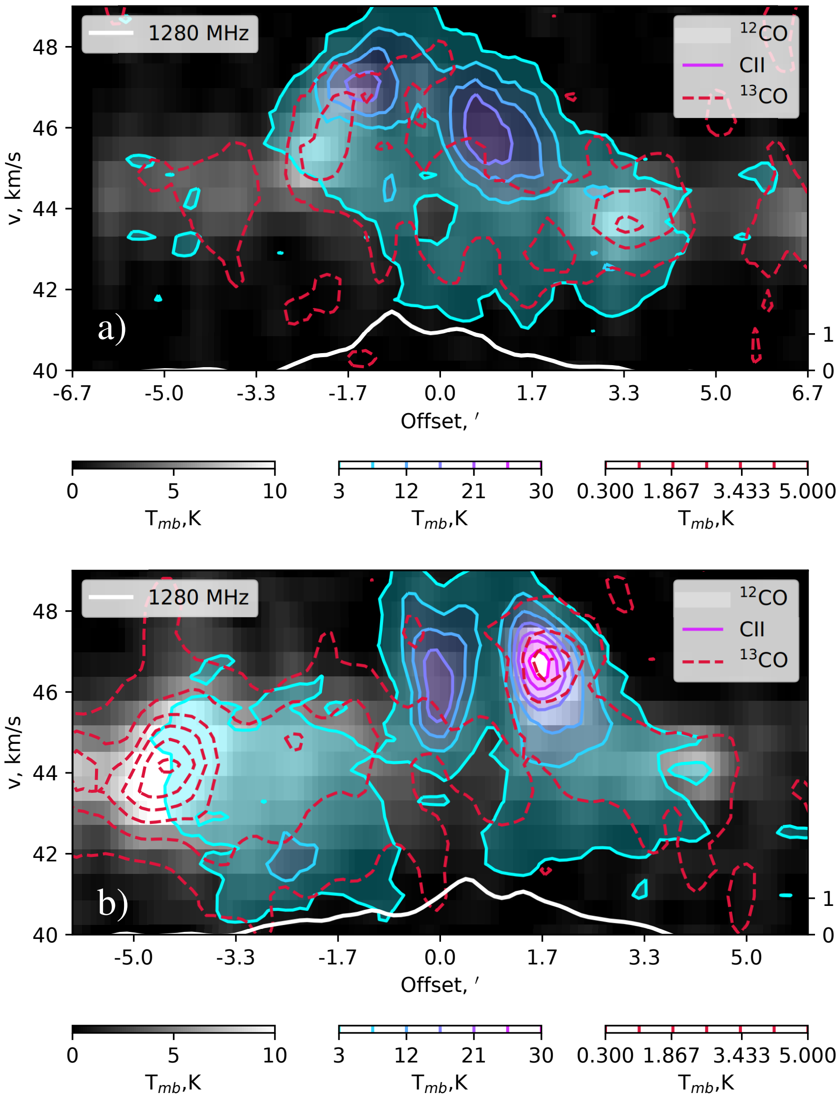

Figure 8.13: Position-velocity diagrams of the ^{12}CO(1–0) (grey emission), ^{13}CO(1–0) (dashed contours), and [CII] (thick contours) emission; (a) perpendicular to the line joining VM2 and VM4, (b) along the line joining VM2 and VM4. The corresponding color bars are shown below the panels. In each panel, the 1280 MHz radio continuum emission profile (a thick white curve) is also shown, which is multiplied by a factor of 100. The radio continuum brightness scale bar is shown in right to each panel and has a unit of mJy beam^{-1}.

of different parameters (e.g., n_e, f_{C^+}, and Φ_i from Kaufman et al., 2006; Kirsanova et al., 2020) can change the outcomes accordingly. The hydrogen column density (or shell mass) can also be derived from the [CII] emission, which first requires the estimation of [CII] column density (N([CII])). Since the optically thin [^{13}CII] line is not detected in present observations, we can assume [CII] emission as optically thin and then compute N([CII]) using equation 4 in Kirsanova et al. (2020). Assuming a typical excitation temperature of T_{ex}=120 K, the observed average $N([\text{C}\,\textsc{ii}])$ is $\sim 4\times10^{17}$ cm^{-2}. Now, using the gas-phase carbon abundance of [C/H]$= 1.6\times10^{-4}$ (Sofia et al., 2004), we evaluated the $N(\text{H})$ as $\sim 2\times10^{21}$ cm^{-2}, which is almost close to the previously calculated $N(\text{H})$ value of $\sim 5\times10^{20}$ cm^{-2}.

We have also estimated the expansion timescale of each [C II] shell, considering that the expansion is caused by a continuous flow of stellar winds (e.g., Castor et al., 1975; Weaver et al., 1977). The radii (R_s) of the inner and outer shells are computed from the PV diagrams and the velocity channel maps (see dotted circles in Figure 8.8), and are ∼1.9 pc and ∼3.7 pc, respectively. We have evaluated the expansion velocity of v_exp ∼1.3 km s^{-1}, assuming that the shells expand in both directions (e.g., Pabst et al., 2020, see Section 3.2.2 and Appendix B therein). Here, we also note that the expansion velocity can range from 1–4 km s^{-1} (see PV diagrams in Figure 8.13), and for the calculation purpose, we have used our calculated value of ∼1.3 km s^{-1}. Considering a similar expansion velocity of v_exp ∼1.3 km s^{-1} for both the shells, the expansion timescales of the inner and outer shells are determined to be ∼0.9 Myr and ∼1.7 Myr, respectively. To compute the expansion timescale, we used the following equation (e.g., Weaver et al., 1977; Pabst et al., 2020)

$$t_\text{exp} \simeq 0.6 \left(\frac{R_\text{s}}{1\ \text{pc}}\right)\left(\frac{1\ \text{km s}^{-1}}{v_\text{exp}}\right) \text{Myr}. \tag{8.2}$$

Here, one can note that the systematic uncertainties in the estimation of shell extent, the expansion velocity, and the expansion timescale are about 30–50%.

8.5 Discussion

In this work, for the first time, we examined the structure and gas dynamics of PDRs in S305 using the neutral gas tracer, 158 μm [C II] line. The neutral gas is traced in the velocity range of [39.4, 49.5] km s^{-1}, which is consistent in velocity with the molecular gas (see Figure 8.9 and Paper II). The ionized, neutral, and molecular gas are spatially distributed in the hierarchy manner (i.e., adjacent to one another; see Figure 8.12a) in S305, which agrees well with the one-dimensional models of PDR (e.g., Tielens & Hollenbach, 1985a, see Figure 1 therein). In Figure 8.12a, the boundary, traced by the [CII] gas, is well distinct to that of ionized gas and molecular CO. This is probably possible because the CO molecules, in the direction of massive stars and our line of sight are mostly dissociated and the carbon is ionized, which contribute to the [CII] emission in PDRs around S305. It seems that the [CII] emission traces the unshielded H_2 gas in PDRs, where molecular gas tracer CO is photodissociated.

8.5.1 Double [CII] shells in PDRs around S305

The two [CII] shells in S305 are evident from the channel maps shown in Figure 8.8. The outer shell has a more extended diffuse structure and unveils its broken morphology, while the inner shell reveals a compact ring like feature (see Section 8.4.2 and Figure 8.11). Recently, Kirsanova et al. (2020) performed the spherically symmetric chemo-dynamical model of expanding HII regions in the site S235. The PV diagrams shown in Figure 8.13 are close to the numerical model by Kirsanova et al. (2020). In the direction of the line joining stars VM2 and VM4, the shape of the PV diagram is somewhat symmetrical for the individual shells and has a typical double-peaked structure (i.e., similar to the dumbbell shape; see Figure 8.13b). The footprint of the diffuse shell can be seen in the positive and negative offsets ([CII] contour of 3 K), while the compact shell is seen toward the positive offset ([CII] contours of 6–30 K) only. The velocity of the extended diffuse shell is around $\sim$44 km s^{-1} compared to the compact shell having a velocity of $\sim$46.5 km s^{-1}. The molecular gas walls are formed around the diffuse shell as seen in ^{12}CO(1–0) and ^{13}CO(1–0) peaks at $\sim$44 km s^{-1}.

The PV diagram (Figure 8.13b) also infers the geometric distribution of the two [CII] shells. In the direction of the compact shell, the molecular gas wall, which is kinematically related to the diffuse shell wall, shows a peak emission at $\sim$46 km s^{-1}. This molecular peak emission exactly matches with one of the two [CII] peaks (located at $1'.7$ offset and $\sim$46 km s^{-1}). The other [CII] peak related to the compact shell (located at $0'$ offset and $\sim$46 km s^{-1}) in the PV diagram is situated in the center of the diffuse shell. The absence of the molecular wall in this peak suggests that the compact zone is embedded into the extended diffuse shell. This particular observation provides the only evidence of geometrically inner (compact shell) and outer (diffuse shell) morphology of the [CII] emitting gas. The PV structures in the different directions are far from symmetry, as shown in the PV diagram in the perpendicular direction of the line joining stars VM2 and VM4 (see Figure 8.13a). Such asymmetry can arise from the inhomogeneity of the surrounding gas. These kinematical structures may be explained by the triggered formation scenario of the compact zone, where the parental gas is compressed by the expansion of the diffuse shell. The HII zone lies at the centre of the diffuse shell as shown by the 1.28 GHz continuum emission profile and is the outcome of EUV flux from both the stars VM2 and VM4 (Paper II). The gas is being pushed to the observer leading to the doppler-shift of the [CII] emission. The compact HII zone expands to the inner regions of the diffuse shell, which can explain the asymmetry in the PV diagrams. The gas expansion in the inner [CII] shell is clearly evident from the velocity channel maps (Figure 8.8) and moment-1 map (Figure 8.11b). However, it is not very significant in case of the outer shell, which although show the south-east to south-west velocity gradient (see Figure 8.11d).

The shells are not kinematically homogeneous but are close to the expanding bubbles. In Section 8.4.3, the expansion timescales of the inner and outer shells are determined to be $\sim$0.9 Myr and $\sim$1.7 Myr, respectively. The expansion timescales of the shells agree with the dynamical age of the S305 HII region (i.e., $\sim$0.5–1.7 Myr; Paper II), and with the average age of the stellar population in S305 (i.e., $\sim$1.8 Myr; Paper I). These results infer that the inner shell is younger than the outer shell, suggesting that the shells have formed sequentially. This may be possible that the star VM4 played a major role in the formation of the outer shell, while the inner shell formation seems to be linked with the star VM2 (see also Figures 8.7 and 8.8). Furthermore, based on the morphology and kinematics of the [CII] shells, we cannot rule out the possibility of the influence of the star VM4 in the formation of the star VM2. However, it requires the proper age estimation of these stars, which is beyond the scope of this work.

In the direction of S305, we find the double-peaked line profiles of the [CII] emission compared to the single-peaked line profiles of ^{12}CO(1–0) and ^{13}CO(1–

0) (see Figure 8.9). From the analysis of the [CII] spectra taken at different positions in S305 (Figure 8.10), we found that the blueshifted and redshifted components spatially trace the outer and inner shell morphology, respectively (see Figure 8.11). It is quite interesting to note that the outer shell which is more diffuse compared to the inner shell, lies in front of the inner shell. We note that the double-peaked [CII] profiles are dominant in the northern high intensity zone of the inner neutral shell (see Figures 8.7b and 8.10), which spatially lies to the overlapping zones of the inner and outer [CII] shells (see also Figure 8.12b). It has been shown in the previous studies that the presence of an enhanced redshifted peak in the significant optically thick lines is the signature of expansion scenario (e.g., Pavlyuchenkov et al., 2008). In S305, the majority of the [CII] profiles (Figure 8.9) are either double-peaked (with brighter redshifted component) or blue-skewed, suggesting the gas expansion in PDRs, which is further confirmed by the [CII] channel maps and the PV diagrams.

8.5.2 Star formation scenario in S305

In the literature, it has been a common practice to use the mid-infrared images as a tool for qualitative identification of bubble structures or triggered star formation sites (e.g., Deharveng et al., 2005, 2010; Zavagno et al., 2006, 2007). Different scenarios of triggered/sequential star formation are available in the literature (e.g., Elmegreen, 1998). The expansion of an HII region may initiate the instability in pre-existing dense regions of gas (i.e., "radiation driven implosion" scenario; Bertoldi, 1989; Lefloch & Lazareff, 1994) or may accumulate the layers of dust and gas between the ionization and shock fronts which later become gravitationally unstable and form next-generation stars (i.e., "collect and collapse" scenario; Elmegreen & Lada, 1977; Whitworth et al., 1994). Despite of the enumerable wealth of literature in theoretical works, the direct observational evidence of "triggered/sequential star formation" is still lacking (e.g., Deharveng et al., 2010; Dale et al., 2015, and references therein).

In the mid-infrared images, the 24 μm emission correlates to the ionized zone, while the 8 μm emission traces the boundary of dust condensation and the ionization front. The shock front can be traced by H_2 emission. In S305, the H_2 emission is prominently found in the direction of the horseshoe envelope (see Figure 3 in Paper II). The presence of regularly spaced massive fragments in the periphery or along the direction of PDRs is evident in the dust emission at 850 μm (see Figure 8.2c), and in the form of molecular clumps (see Figure 8.7c). These clumps are spatially seen in the direction and/or the boundary of the [CII] shells, which are also kinematically related to the [CII] emitting gas. The masses of dust and molecular clumps are in the range of $M_{\rm clumps}^{850\ \mu m}$ ~10–10^3 $M_\odot$ (see Table 6 in Sreenilayam et al., 2014) and $M_{\rm clumps}^{\rm CO(2-1)}$ ~10^2–10^3 $M_\odot$ (see Table 3 in Azimlu & Fich, 2011), respectively. Apart from this, Paper I identified the massive dense clumps/fragments using the *Herschel* column density map. These clumps have size extensions in parsec (i.e., radii ~0.28–1.32 pc) and their masses range from 35 to 1565 $M_\odot$. Hence, it is possible that during the expansion of an HII region, the dense materials have been collected between the ionization and shock fronts, which now appear in the form of dense fragments.

Therefore, all the outcomes together confirm the gas expansion in PDRs followed by the collection of materials (e.g., dust and gas) around it. The presence of massive neutral shells, dust and gas clumps around HII region S305 strengthens the applicability of "collect and collapse" scenario as suggested in Paper II.

8.6 Summary and Conclusion

The present work is benefited with analysis of the unpublished 158 μm [CII] line data, which enable us to study the kinematics of gas in PDRs around the HII region S305 hosting two massive O-type stars (i.e., VM2 and VM4). Using the [CII] line data, the neutral gas in PDRs is examined in a velocity range of [39.4, 49.5] km s^{-1}. Two shell-like structures (i.e., inner: an intense ring-like shell and outer: the extended and diffuse neutral shell) are found in the [CII] moment-0 map, and velocity channel maps. In the direction of S305, the [CII] line profiles are double-peaked (with enhanced redshifted component), which peaks at ~43 and ~47 km s^{-1} and shows a dip at ~44 km s^{-1}. The dip in double-peaked

[CII] profiles lie to the peaks of ^{12}CO/^{13}CO(1–0) line profiles. The double-peaked [CII] spectra spatially trace two shells in PDRs around S305. The PV diagrams confirm that the compact shell is geometrically embedded in the outer diffuse shell, and both the shells are enclosed by the molecular gas walls. Based on the [CII] emission, the estimated average neutral hydrogen column density and the mass of the [CII] shells are $\sim 5 \times 10^{20}$ cm^{-2} and $\sim$565 M$_{\odot}$, respectively. The PV diagrams, including the spectral profiles and velocity channel maps, unveil the signatures of gas expansion in PDRs. The expansion velocity of $v_{\rm exp}$ $\sim$1.3 km s^{-1} implies the expansion timescales of $\sim$0.9 Myr and $\sim$1.7 Myr for the inner and outer shells, respectively. This suggests that the two [CII] shells are formed sequentially in S305. The consistent velocity and spatial structures of regularly spaced massive dust and molecular fragments to that of the neutral gas/PDRs confirm that these fragments are the outcome of the gravitational collapse of a shell of collected materials.

Chapter 9

Summary and future prospective

9.1 Summary

This thesis highlights the significance of interstellar filaments in the processes of MSF. The filaments play a crucial role in enhancing mass accumulation through various ongoing physical processes, ultimately leading to MSF. Based on recent results, it is important to note that MSF is a multi-scale physical process driven by the interplay between self-gravity, turbulence, and magnetic fields within molecular clouds. Filaments are formed at one of the stages of these processes, which eventually collapse to form stars. It is interesting to note that cloud-scale filaments generally retain more material and their collapse can result in larger yet denser regions, serving as mass reservoirs for MSF. The universality of HFSs is widely recognized as the birth places of most massive stars in the literature (Kumar et al., 2020). Typically, once a massive star forms, it tends to disrupt the parent clump or cloud structure (Motte et al., 2018). Therefore, identifying a promising HFS that is still in its early phases, prior to the formation of an UC HII region, is observationally rare. This thesis introduces a site named RAFGL 5085, which can be considered a perfect HFS as the ionized region formed within a hub has not yet destroyed the surrounding environment. In addition to the well-known HFSs, the role of isolated filaments in star formation has been relatively less explored. This thesis presents at least three filamentary clouds that undergo collapse through the EDC process. In this way, the observed number of filaments experiencing EDC are now nearly 6 in the literature. These include NGC 6334 (Zernickel et al., 2013), Sh 2-242 (or S242; Dewangan et al., 2019b; Yuan et al., 2020), IC 5146 (Wang et al., 2019b), Monoceros R1 (or Mon R1; Bhadari et al., 2020), G341.244-00.265 (Yu et al., 2019), and G45.3+0.1 (Bhadari et al., 2022). However, only few of them clearly trace the signatures of EDC. Apart from the S242 filament, this thesis presents Mon R1 and IC 5146 dark Streamer as most promising sites of EDC. Mon R1 filament is the first reported filament that hosts evolved star-forming sites at both of its edges. In another case, IC 5146 dark Streamer shows early stages of filament collapse as it does not host massive stars yet. However the simultaneous signatures of HFSs and EDC suggest the muli-step processes of mass accumulation. The GMF G45.3+0.1 shows the onset of EDC and a hierarchical HFSs.

Interestingly, the HFSs are predominantly found at the edges of filaments, which can be explained by the gravitational focusing of subfilaments towards dense clumps or hubs formed by the EDC process. Additionally, magnetic fields can play an important role in the formation of hubs at the edges of EDC filaments (Wang et al., 2019b). In this scenario, the isolated filament first undergoes collapse through the EDC process, forming end clumps. Subsequently, subfilaments forms via the interplay between gravity and magnetic fields which ultimately feed these end clumps, resembling HFSs. Finally, mass accumulation in the hubs occurs through material accretion from the cloud scale via subfilaments. Therefore, the EDC process is equally important because HFSs are found at the edges of the EDC filaments. Additionally, this thesis explores the feedback of massive stars using neutral gas tracer [CII] line data from SOFIA. The core-scale environments are investigated using ALMA observations, and the roles of gravity and turbulence are studied.

The major results derived from this thesis are highlighted below:

- The visual inspection and the application of *getsf* on the *Herschel* sub-mm images reveal a prominent hub-filament configuration in RAFGL 5085, which consists of a central region (M_{clump} ~225 $M_{\odot}$) surrounded by at least five parsec-scale filaments. We derived the $N(H_2)$ and T_d maps and found that the filaments are identified with higher aspect ratios (length/diameter) and lower N(H_2) values (∼0.1–2.4 $\times 10^{21}$ cm^{-2}), while the central hub (i.e., T_d ∼[19, 22.5] K) is found with a lower aspect ratio and higher N(H_2) values (∼3.5–7.0 $\times 10^{21}$ cm^{-2}). With comparison to the schematic model given by Motte et al. (2018), we propose that RAFGL 5085 is a perfect HFS candidate hosting early phase of MSF and not yet influenced by UV radiation from the HII region.

- The analysis of ^{12}CO/^{13}CO line data traces two clouds at V_LSR [−5, 1] and [2, 10] km s^{-1} in Monoceros R1 complex. The cloud having V_LSR ∼ −2 km s^{-1} has filamentary morphology (i.e., Mon R1 filament) and is found to be supercritical. At both ends of Mon R1 filament where massive star-forming sites were previously reported, the higher surface density of YSOs (i.e., 4–125 YSOs pc^{-2}) is also observed. In addition to this, the relatively higher velocity gradients (∼0.6 km s^{-1} pc^{-1}) compared to the central regions (∼0.4 km s^{-1} pc^{-1}), at the filament's edges together support the longitudinal gas motion, and hence the onset of EDC process in the Mon R1 filament (∼1465 $M_\odot$, length ∼14 pc) as predicted by Pon et al. (2012); Clarke & Whitworth (2015).

- Based on the analysis of ^{13}CO(1–0) line data, a GMF (length ∼75 pc, mass ∼1.1×10^6 $M_\odot$) in the velocity range of ∼53–63 km s^{-1} is discovered, which we named GMF G45.3+0.1. The massive star-forming complexes are located at the edges of GMF G45.3+0.1 and exhibit HFSs, where several parsec scale (∼5-10 pc) filaments appear to converge toward dense hubs hosting known massive star-forming sites. This target site represents the first observed filamentary cloud that exhibits both EDC and hub-filament configurations simultaneously.

- We derived the high resolution *Herschel* column density map (resolution ∼13.″5) using *hires* tool for the potential and nearby massive star-forming site IC 5146 dark Streamer. The derived map unravel the possible presence of two intertwined subfilaments (i.e., *fl-A* and *fl-B*) toward the main filament *fl*. Such configuration displays almost a double helix-like pattern, which is also confirmed in the integrated intensity map of the JCMT $C^{18}O$(3–2) emission. We interpret these features with the "fray and fragment" scenario of intertwined filaments. The Planck dust polarization maps reveal the presence of curved magnetic fields at the edges of the filament, which is believed to be a novel indicator of the EDC process. Altogether, IC 5146 dark Streamer can be considered the first reliable candidate for EDC, HFSs, and intertwined subfilaments.

- Using the ALMA $H^{13}CO^{+}$ (4–3) data, the inner environment of a known HFS in W42 region harbouring an O5.5 star and a massive YSO (IR counterpart of 6.7 GHz methanol maser emission) named W42-MME is explored. We applied dendrogram methodology to trace multi-scale dense structures and studied velocity dispersion–size relations. We explored the universality of Larson's relations and found that the non-thermal velocity dispersion–size relation ($\sigma_{\rm nt} - L$) of dendrogram structures shows a weak negative correlation, while the velocity dispersion across the sky ($\delta\, V_{\rm lsr}$) correlates positively with structure size (L). Blue asymmetry is observed in the $H^{12}CO^{+}$ (4–3) line profiles of most of the leaves, indicating infall. Overall, our results observationally support the role of gravity driven turbulence at the smaller scales (e.g., Ballesteros-Paredes et al., 2018) and favoring hierarchical and chaotic collapse scenario in the proximity of the W42-MME.

- The analysis of FUGIN ^{13}CO(1–0) data unveils the presence of two filamentary ridges at $V_{\rm LSR}$ of ∼42 and ∼45 km s^{-1} in the site S305. The collisions between these two ridges, similar to that observed in Serpens South by Nakamura et al. (2014), may have triggered the formation of a cluster including the known O-type stars. The present structure seem to follow the idea of Whitworth & Priestley (2021), where the filament is eroded by the strong ionization feedback from massive stars. Using the [CII] line data at 158 μm, we further investigated the feedback of these massive O-type stars and found the presence of two expanding photo-dissociation region (PDR) shells. In addition, the presence of dust and molecular condensation around the HII region and PDR shells hints at the “collect and collapse” scenario in the S305 region.

Overall, this thesis provides new insights into the mass accumulation processes and the potency of interstellar filaments in MSF.

9.2 Future Prospective

As high-resolution data can resolve a seemingly single source into multiple sources, it is expected that the apparently single filament can be resolved into thinner subfilaments. This is demonstrated in Chapter 6, where subfilaments are identified in a nearby filamentary cloud IC 5146 dark Streamer. However, it is still unclear whether this holds true for all filaments, and addressing this question requires the use of high-resolution continuum and line data. The work presented in the thesis is limited by low resolution of data which does not allow us to trace the innermost structures of each individual sites. Hence, to understand the complete picture of ongoing star formation and various physical processes within a molecular cloud, the multi-scale data is necessary. Also, to study these aspects in detail, further high-resolution data for nearby site (e.g., IC 5146 dark Streamer and Mon R1) are essential. The interconnection between various physical processes within filaments, such as the EDC, intertwined subfilaments, and HFSs, along with multi-scale mass accumulation processes in MSF, poses demanding future challenges. The findings presented in this thesis, derived from diverse target observations, can be extended to enhance our existing understanding of the mass accumulation process in MSF. Furthermore, these results can serve as a guide for the development of new theoretical approaches aimed at solving the MSF problem.

Following are some future works that we plan to pursue in the near future:

1. In the near future, we plan to conduct a detailed analysis of the S306 and S309 HII regions to collectively understand the role of filaments, feedback processes of massive stars, and the importance of substructures, gravity,

and turbulence in MSF processes. Our obtained new data from uGMRT will primarily provide the energy budget of HII regions.

2. To revisit the Mon R1 filament, we will utilize high-resolution dust polarization data and dense gas tracers to further explore the possible presence of HFSs and intertwined subfilaments.

3. To conduct a systematic search of EDC candidates from the scale of cloud to core spanning the entire Galactic environment using available survey data from the ground and space-based facilities and investigating the link between various physical processes in filaments.

Bibliography

Abe, D., Inoue, T., Inutsuka, S.-i., & Matsumoto, T. 2021, The Astrophysical Journal, 916, 83, doi: 10.3847/1538-4357/ac07a1 [Cited on page 117.]

Abel, N. P., Sarma, A. P., Troland, T. H., & Ferland, G. J. 2007, The Astrophysical Journal, 662, 1024, doi: 10.1086/517987 [Cited on page 192.]

Abergel, A., Boulanger, F., Mizuno, A., & Fukui, Y. 1994, The Astrophysical Journal, 423, L59, doi: 10.1086/187235 [Cited on page 15.]

Abreu-Vicente, J., Ragan, S., Kainulainen, J., et al. 2016a, Astronomy & Astrophysics, 590, A131, doi: 10.1051/0004-6361/201527674 [Cited on page 16.]

—. 2016b, Astronomy and Astrophysics, 590, A131, doi: 10.1051/0004-6361/201527674 [Cited on page 115.]

Adam, R., Ade, P. A., Aghanim, N., et al. 2016a, Astronomy and Astrophysics, 586, 1, doi: 10.1051/0004-6361/201425044 [Cited on page 15.]

—. 2016b, Astronomy and Astrophysics, 594, A8, doi: 10.1051/0004-6361/201525820 [Cited on page 142.]

Ade, P. A., Aghanim, N., Armitage-Caplan, C., et al. 2014, Astronomy and Astrophysics, 571, A9, doi: 10.1051/0004-6361/201321531 [Cited 3 times on pages 36, 72, and 127.]

Ade, P. A., Aghanim, N., Alina, D., et al. 2015, Astronomy and Astrophysics, 576, A104, doi: 10.1051/0004-6361/201424082 [Cited 2 times on pages 15 and 142.]

Ade, P. A., Aghanim, N., Alves, M. I., et al. 2016a, Astronomy and Astrophysics, 586, A138, doi: 10.1051/0004-6361/201525896 [Cited 2 times on pages 125 and 143.]

—. 2016b, Astronomy and Astrophysics, 586, A136, doi: 10.1051/0004-6361/201425305 [Cited on page 143.]

Ade, P. A., Aghanim, N., Arnaud, M., et al. 2016c, Astronomy and Astrophysics, 594, A19, doi: 10.1051/0004-6361/201525821 [Cited on page 143.]

Aguirre, J. E., Ginsburg, A. G., Dunham, M. K., et al. 2011, Astrophysical Journal, Supplement Series, 192, 4, doi: 10.1088/0067-0049/192/1/4 [Cited 2 times on pages 36 and 52.]

Aladro, R., Martín-Pintado, J., Martín, S., Mauersberger, R., & Bayet, E. 2010, Astronomy and Astrophysics, 525, A89, doi: 10.1051/0004-6361/201014090 [Cited on page 165.]

Anderson, L. D., Bania, T. M., Jackson, J. M., et al. 2009, Astrophysical Journal, Supplement Series, 181, 255, doi: 10.1088/0067-0049/181/1/255 [Cited on page 153.]

Anderson, L. D., Makai, Z., Luisi, M., et al. 2019, The Astrophysical Journal, 882, 11, doi: 10.3847/1538-4357/ab1c59 [Cited 2 times on pages 36 and 198.]

Anderson, M., Peretto, N., Ragan, S. E., et al. 2021, Monthly Notices of the Royal Astronomical Society, 508, 2964, doi: 10.1093/mnras/stab2674 [Cited 2 times on pages 93 and 118.]

André, P., Di Francesco, J., Ward-Thompson, D., et al. 2014, in Protostars and Planets VI, ed. H. Beuther, R. S. Klessen, C. P. Dullemond, & T. Henning, 27 [Cited 4 times on pages 13, 20, 21, and 86.]

Andre, P., Ward-Thompson, D., & Barsony, M. 1999, doi: 10.48550/arXiv.astro-ph/9903284 [Cited 2 times on pages 5 and 6.]

André, P., Men'Shchikov, A., Bontemps, S., et al. 2010, Astronomy and Astrophysics, 518, L102, doi: 10.1051/0004-6361/201014666 [Cited 11 times on pages 10, 13, 15, 16, 17, 18, 20, 64, 86, 93, and 126.]

Aniano, G., Draine, B. T., Gordon, K. D., & Sandstrom, K. 2011, Publications of the Astronomical Society of the Pacific, 123, 1218, doi: 10.1086/662219 [Cited on page 40.]

Arzoumanian, D., André, P., Peretto, N., & Könyves, V. 2013, Astronomy and Astrophysics, 553, A119, doi: 10.1051/0004-6361/201220822 [Cited 3 times on pages 18, 19, and 124.]

Arzoumanian, D., André, P., Didelon, P., et al. 2011, Astronomy and Astrophysics, 529, L6, doi: 10.1051/0004-6361/201116596 [Cited 6 times on pages 13, 20, 125, 126, 127, and 141.]

Arzoumanian, D., André, P., Könyves, V., et al. 2019, Astronomy and Astrophysics, 621, A42, doi: 10.1051/0004-6361/201832725 [Cited 6 times on pages 125, 126, 127, 128, 129, and 141.]

Arzoumanian, D., Furuya, R. S., Hasegawa, T., et al. 2021, Astronomy and Astrophysics, 647, A78, doi: 10.1051/0004-6361/202038624 [Cited 2 times on pages 123 and 144.]

Assirati, L., Silva, N., Berton, L., Lopes, A., & Bruno, O. 2014, in Journal of Physics Conference Series, Vol. 490, Journal of Physics Conference Series, 12020 [Cited on page 131.]

Azimlu, M., & Fich, M. 2011, Astronomical Journal, 141, 123, doi: 10.1088/0004-6256/141/4/123 [Cited 3 times on pages 201, 203, and 215.]

Balfour, S. K., Whitworth, A. P., Hubber, D. A., & Jaffa, S. E. 2015, Monthly Notices of the Royal Astronomical Society, 453, 2471, doi: 10.1093/mnras/stv1772 [Cited 2 times on pages 119 and 146.]

Ballesteros-Paredes, J. 2004, Astrophysics and Space Science, 292, 193, doi: 10.1023/B:ASTR.0000045018.50154.b0 [Cited on page 2.]

Ballesteros-Paredes, J., Hartmann, L. W., Vázquez-Semadeni, E., Heitsch, F., & Zamora-Avilés, M. A. 2011, Monthly Notices of the Royal Astronomical Society, 411, 65, doi: 10.1111/j.1365-2966.2010.17657.x [Cited 2 times on pages 13 and 153.]

Ballesteros-Paredes, J., Hartmann, L. W., Vázquez-Semadeni, E., Heitsch, F., & Zamora-Avilés, M. A. 2011, MNRAS, 411, 65, doi: 10.1111/j.1365-2966.2010.17657.x [Cited 5 times on pages 173, 174, 183, 184, and 186.]

Ballesteros-Paredes, J., Klessen, R. S., Mac Low, M. M., & Vazquez-Semadeni, E. 2006, Protostars and Planets V, 63, doi: 10.48550/arXiv.astro-ph/0603357 [Cited 2 times on pages 2 and 153.]

Ballesteros-Paredes, J., Román-Zúñiga, C., Salomé, Q., Zamora-Avilés, M., & Jiménez-Donaire, M. J. 2019, Monthly Notices of the Royal Astronomical Society, 490, 2648, doi: 10.1093/mnras/stz2575 [Cited 2 times on pages 179 and 186.]

Ballesteros-Paredes, J., Vázquez-Semadeni, E., Palau, A., & Klessen, R. S. 2018, Monthly Notices of the Royal Astronomical Society, 479, 2112, doi: 10.1093/mnras/sty1515 [Cited 5 times on pages 153, 184, 186, 188, and 220.]

Bally, J., Aguirre, J., Battersby, C., et al. 2010, Astrophysical Journal, 721, 137, doi: 10.1088/0004-637X/721/1/137 [Cited on page 54.]

Barnard, E. E. 1907, The Astrophysical Journal, 25, 218, doi: 10.1086/141434 [Cited on page 14.]

Bastien, P. 1983, Astrophysical Journal, 119, 109 [Cited 7 times on pages 14, 22, 28, 67, 89, 115, and 148.]

Bastien, P., Arcoragi, J.-P., Benz, W., Bonnell, I., & Martel, H. 1991, The Astrophysical Journal, 378, 255, doi: 10.1086/170424 [Cited on page 22.]

Battersby, C., Bally, J., Ginsburg, A., et al. 2011, Astronomy and Astrophysics, 535, A128, doi: 10.1051/0004-6361/201116559 [Cited 2 times on pages 39 and 40.]

Baug, T., Ojha, D. K., Dewangan, L. K., et al. 2015, Monthly Notices of the Royal Astronomical Society, 454, 4335, doi: 10.1093/mnras/stv2269 [Cited on page 65.]

Baug, T., Dewangan, L. K., Ojha, D. K., et al. 2018, The Astrophysical Journal, 852, 119, doi: 10.3847/1538-4357/aaa429 [Cited 2 times on pages 64 and 65.]

Bell, G. S. 2008, HARP-B and Wide-Field Imaging of Molecular Clouds [Cited on page 140.]

Benjamin, R. A., Churchwell, E., Babler, B. L., et al. 2003, Publications of the Astronomical Society of the Pacific, 115, 953, doi: 10.1086/376696 [Cited 4 times on pages 36, 72, 97, and 198.]

Bergin, E. A., Goldsmith, P. F., Snell, R. L., & Ungerechts, H. 1994, The Astrophysical Journal, 431, 674, doi: 10.1086/174518 [Cited on page 165.]

Bergin, E. A., & Tafalla, M. 2007, Annual Review of Astronomy and Astrophysics, 45, 339, doi: 10.1146/annurev.astro.45.071206.100404 [Cited on page 152.]

Bertoldi, F. 1989, The Astrophysical Journal, 346, 735, doi: 10.1086/168055 [Cited on page 214.]

Bertoldi, F., & McKee, C. F. 1992, The Astrophysical Journal, 395, 140, doi: 10.1086/171638 [Cited on page 168.]

Bestenlehner, J. M., Crowther, P. A., Caballero-Nieves, S. M., et al. 2020, Monthly Notices of the Royal Astronomical Society, 499, 1918, doi: 10.1093/mnras/staa2801 [Cited on page 8.]

Beuther, H. 2002, PhD thesis, Max-Planck-Institute for Radioastronomy, Bonn [Cited on page 10.]

—. 2006, Proceedings of the International Astronomical Union, 2, 148, doi: 10.1017/S1743921307001378 [Cited on page 11.]

Beuther, H., Churchwell, E. B., McKee, C. F., & Tan, J. C. 2006. https://arxiv.org/abs/0602012 [Cited on page 10.]

Beuther, H., Ragan, S. E., Johnston, K., et al. 2015, Astronomy and Astrophysics, 584, A67, doi: 10.1051/0004-6361/201527108 [Cited 6 times on pages 15, 20, 68, 89, 115, and 116.]

Beuther, H., Mottram, J. C., Ahmadi, A., et al. 2018, Astronomy & Astrophysics, 617, A100, doi: 10.1051/0004-6361/201833021 [Cited on page 13.]

Beuther, H., Wang, Y., Soler, J., et al. 2020, Astronomy and Astrophysics, 638, A44, doi: 10.1051/0004-6361/202037950 [Cited on page 146.]

Bhadari, N. K., Dewangan, L. K., Ojha, D. K., Pirogov, L. E., & Maity, A. K. 2022, The Astrophysical Journal, 930, 169, doi: 10.3847/1538-4357/ac65e9 [Cited 6 times on pages 24, 29, 31, 152, 183, and 218.]

Bhadari, N. K., Dewangan, L. K., Pirogov, L. E., & Ojha, D. K. 2020, The Astrophysical Journal, 899, 167, doi: 10.3847/1538-4357/aba2c6 [Cited 7 times on pages 24, 29, 30, 93, 108, 115, and 218.]

Bhadari, N. K., Dewangan, L. K., Pirogov, L. E., et al. 2023, MNRAS, 526, 4402, doi: 10.1093/mnras/stad2981 [Cited 2 times on pages 29 and 32.]

Bhadari, N. K., Dewangan, L. K., Zemlyanukha, P. M., et al. 2021, The Astrophysical Journal, 922, 207, doi: 10.3847/1538-4357/ac2a44 [Cited 2 times on pages 29 and 32.]

Bica, E., Dutra, C. M., & Barbuy, B. 2003, Astronomy and Astrophysics, 397, 177, doi: 10.1051/0004-6361:20021479 [Cited on page 50.]

Blum, R. D., Conti, P. S., & Damineli, A. 2000, The Astronomical Journal, 119, 1860, doi: 10.1086/301317 [Cited on page 153.]

Blum, R. D., & McGregor, P. J. 2008, Astronomical Journal, 135, 1708, doi: 10.1088/0004-6256/135/5/1708 [Cited on page 95.]

Bolatto, A. D., Leroy, A. K., Rosolowsky, E., Walter, F., & Blitz, L. 2008, The Astrophysical Journal, 686, 948, doi: 10.1086/591513 [Cited on page 152.]

Bonnell, I. A., & Bate, M. R. 2006, Monthly Notices of the Royal Astronomical Society, 370, 488, doi: 10.1111/j.1365-2966.2006.10495.x [Cited 4 times on pages 9, 12, 49, and 187.]

Bonnell, I. A., Bate, M. R., Clarke, C. J., & Pringle, J. E. 2001, Monthly Notices of the Royal Astronomical Society, 323, 785, doi: 10.1046/j.1365-8711.2001.04270.x [Cited 2 times on pages 49 and 187.]

Bonnell, I. A., Bate, M. R., & Zinnecker, H. 1998, Monthly Notices of the Royal Astronomical Society, 298, 93, doi: 10.1046/j.1365-8711.1998.01590.x [Cited on page 9.]

Bonnell, I. A., Vine, S. G., & Bate, M. R. 2004, Monthly Notices of the Royal Astronomical Society, 349, 735, doi: 10.1111/j.1365-2966.2004.07543.x [Cited 2 times on pages 9 and 49.]

Bontemps, S., André, P., Könyves, V., et al. 2010, Astronomy and Astrophysics, 518, L85, doi: 10.1051/0004-6361/201014661 [Cited on page 18.]

Bourke, T. L., Garay, G., Lehtinen, K. K., et al. 1997, The Astrophysical Journal, 476, 781, doi: 10.1086/303642 [Cited on page 43.]

Bracco, A., Palmeirim, P., André, P., et al. 2017, A&A, 604, A52, doi: 10.1051/0004-6361/201731117 [Cited on page 168.]

Bressert, E., Bastian, N., Gutermuth, R., et al. 2010, Monthly Notices of the Royal Astronomical Society: Letters, 409, L54, doi: 10.1111/j.1745-3933.2010.00946.x [Cited 2 times on pages 47 and 85.]

Brown, A. G. A., Vallenari, A., Prusti, T., et al. 2021, Astronomy & Astrophysics, 649, A1, doi: 10.1051/0004-6361/202039657 [Cited on page 51.]

Buckle, J. V., Hills, R. E., Smith, H., et al. 2009, Monthly Notices of the Royal Astronomical Society, 399, 1026, doi: 10.1111/j.1365-2966.2009.15347.x [Cited 4 times on pages 36, 51, 52, and 127.]

Burkert, A., & Hartmann, L. 2004, The Astrophysical Journal, 616, 288, doi: 10.1086/424895 [Cited 2 times on pages 22 and 67.]

Cahlon, S., Zucker, C., Goodman, A., Lada, C., & Alves, J. 2023, arXiv e-prints, arXiv:2308.14794, doi: 10.48550/arXiv.2308.14794 [Cited on page 179.]

Cannon, A., & Pickering, E. 1993, VizieR Online Data Catalog, III/135A [Cited on page 69.]

Carey, S. J., Noriega-Crespo, A., Mizuno, D. R., et al. 2009in , 76–97 [Cited 2 times on pages 36 and 97.]

Carolan, P. B., Khanzadyan, T., Redman, M. P., et al. 2009, Monthly Notices of the Royal Astronomical Society, 400, 78, doi: 10.1111/j.1365-2966.2009.15441.x [Cited on page 152.]

Carpenter, J. M., Heyer, M. H., & Snell, R. L. 2000, The Astrophysical Journal Supplement Series, 130, 381, doi: 10.1086/317352 [Cited 2 times on pages 50 and 63.]

Caselli, P., Benson, P. J., Myers, P. C., & Tafalla, M. 2002, The Astrophysical Journal, 572, 238, doi: 10.1086/340195 [Cited 2 times on pages 152 and 183.]

Casertano, S., & Hut, P. 1985, The Astrophysical Journal, 298, 80, doi: 10.1086/163589 [Cited 3 times on pages 47, 85, and 111.]

Casey, S. C., & Harper, D. A. 1990, The Astrophysical Journal, 362, 663, doi: 10.1086/169304 [Cited on page 69.]

Castor, J., Weaver, R., & McCray, R. 1975, The Astrophysical Journal, 200, L107, doi: 10.1086/181908 [Cited on page 211.]

Cen, R. 2021, The Astrophysical Journal Letters, 906, L4, doi: 10.3847/2041-8213/abcecb [Cited 2 times on pages 152 and 153.]

Cesaroni, R. 2005, Proceedings of the International Astronomical Union, 1, 59, doi: 10.1017/S1743921305004369 [Cited on page 11.]

Chabrier, G. 2007, in The Initial Mass Function 50 Years Later, ed. E. Corbelli, F. Palla, & H. Zinnecker (Dordrecht: Springer Netherlands), 41–50 [Cited on page 7.]

Chen, C. Y., Mundy, L. G., Ostriker, E. C., Storm, S., & Dhabal, A. 2020a, Monthly Notices of the Royal Astronomical Society, 494, 3675, doi: 10.1093/MNRAS/STAA960 [Cited 2 times on pages 19 and 117.]

Chen, C. Y., & Ostriker, E. C. 2014, Astrophysical Journal, 785, 69, doi: 10.1088/0004-637X/785/1/69 [Cited on page 19.]

Chen, H.-R. V., Zhang, Q., Wright, M. C. H., et al. 2019, The Astrophysical Journal, 875, 24, doi: 10.3847/1538-4357/ab0f3e [Cited on page 118.]

Chen, M. C.-Y., Francesco, J. D., Rosolowsky, E., et al. 2020b, The Astrophysical Journal, 891, 84, doi: 10.3847/1538-4357/ab7378 [Cited 2 times on pages 64 and 94.]

Chini, R. 1985, Symposium - International Astronomical Union, 106, 101, doi: 10.1017/s0074180900242149 [Cited on page 194.]

Chira, R. A., Ibáñez-Mejía, J. C., Mac Low, M. M., & Henning, T. 2019, Astronomy and Astrophysics, 630, A97, doi: 10.1051/0004-6361/201833970 [Cited 2 times on pages 175 and 185.]

Chung, E. J., Lee, C. W., Kwon, W., et al. 2022, The Astronomical Journal, 164, 175, doi: 10.3847/1538-3881/ac8a43 [Cited 7 times on pages 125, 126, 139, 141, 142, 144, and 148.]

Chung, E. J., Lee, C. W., Kim, S., et al. 2021, The Astrophysical Journal, 919, 3, doi: 10.3847/1538-4357/ac0881 [Cited 8 times on pages 36, 124, 125, 126, 133, 141, 146, and 148.]

Churchwell, E. 1999, in NATO Advanced Study Institute (ASI) Series C, Vol. 540, The Origin of Stars and Planetary Systems, ed. C. J. Lada & N. D. Kylafis, 515. https://www.cfa.harvard.edu/research/rg/massive-star-formation [Cited on page 10.]

Churchwell, E., Povich, M. S., Allen, D., et al. 2006, The Astrophysical Journal, 649, 759, doi: 10.1086/507015 [Cited on page 10.]

Clarke, S. D., & Whitworth, A. P. 2015, Monthly Notices of the Royal Astronomical Society, 449, 1819, doi: 10.1093/mnras/stv393 [Cited 11 times on pages 14, 22, 23, 28, 67, 89, 94, 115, 144, 148, and 219.]

Clarke, S. D., Whitworth, A. P., Duarte-Cabral, A., & Hubber, D. A. 2017, Monthly Notices of the Royal Astronomical Society, 468, 2489, doi: 10.1093/mnras/stx637 [Cited 3 times on pages 21, 116, and 149.]

Clarke, S. D., Whitworth, A. P., & Hubber, D. A. 2016, Monthly Notices of the Royal Astronomical Society, 458, 319, doi: 10.1093/mnras/stw407 [Cited 2 times on pages 21 and 88.]

Clarke, S. D., Whitworth, A. P., Spowage, R. L., et al. 2018, Monthly Notices of the Royal Astronomical Society, 479, 1722, doi: 10.1093/mnras/sty1675 [Cited on page 21.]

Clarke, S. D., Williams, G. M., & Walch, S. 2020, Monthly Notices of the Royal Astronomical Society, 497, 4390, doi: 10.1093/mnras/staa2298 [Cited 2 times on pages 116 and 119.]

Condon, J. J., Cotton, W. D., Greisen, E. W., et al. 1998, The Astronomical Journal, 115, 1693, doi: 10.1086/300337 [Cited 8 times on pages 36, 50, 52, 63, 72, 76, 127, and 194.]

Cortes, P. C., Hull, C. L. H., Girart, J. M., et al. 2019, The Astrophysical Journal, 884, 48, doi: 10.3847/1538-4357/ab378d [Cited on page 13.]

Cox, N. L., Arzoumanian, D., André, P., et al. 2016, Astronomy and Astrophysics, 590, A110, doi: 10.1051/0004-6361/201527068 [Cited 2 times on pages 20 and 143.]

Csengeri, T., Bontemps, S., Wyrowski, F., et al. 2017, Astronomy & Astrophysics, 600, L10, doi: 10.1051/0004-6361/201629754 [Cited on page 13.]

Dale, J. E., Haworth, T. J., & Bressert, E. 2015, Monthly Notices of the Royal Astronomical Society, 450, 1199, doi: 10.1093/mnras/stv396 [Cited on page 214.]

De Buizer, J. M., Lim, W., Karnath, N., Radomski, J. T., & Bonne, L. 2022, The Astrophysical Journal, 933, 60, doi: 10.3847/1538-4357/ac6fd8 [Cited 2 times on pages 154 and 179.]

Deharveng, L., Zavagno, A., & Caplan, J. 2005, Astronomy and Astrophysics, 433, 565, doi: 10.1051/0004-6361:20041946 [Cited 2 times on pages 8 and 214.]

Deharveng, L., Schuller, F., Anderson, L. D., et al. 2010, Astronomy and Astrophysics, 523, A6, doi: 10.1051/0004-6361/201014422 [Cited 2 times on pages 8 and 214.]

Dewangan, L. K. 2019, The Astrophysical Journal, 884, 84, doi: 10.3847/1538-4357/ab4189 [Cited on page 27.]

—. 2021, Monthly Notices of the Royal Astronomical Society, 504, 1152, doi: 10.1093/mnras/stab1008 [Cited 2 times on pages 65 and 94.]

—. 2022, Monthly Notices of the Royal Astronomical Society, 513, 2942, doi: 10.1093/mnras/stac967 [Cited 10 times on pages 15, 65, 94, 146, 158, 160, 179, 181, 183, and 187.]

Dewangan, L. K., Baug, T., Ojha, D. K., et al. 2017a, The Astrophysical Journal, 845, 34, doi: 10.3847/1538-4357/aa7da2 [Cited on page 14.]

Dewangan, L. K., Bhadari, N. K., Maity, A. K., et al. 2022a, Journal of Astrophysics and Astronomy, 44, 23, doi: 10.1007/s12036-022-09907-7 [Cited 2 times on pages 29 and 30.]

Dewangan, L. K., Bhadari, N. K., Maity, A. K., et al. 2023, Journal of Astrophysics and Astronomy, 44, 23, doi: 10.1007/s12036-022-09907-7 [Cited on page 183.]

Dewangan, L. K., Bhadari, N. K., Men'shchikov, A., et al. 2023, The Astrophysical Journal, 946, 22, doi: 10.3847/1538-4357/acbccc [Cited 3 times on pages 29, 31, and 94.]

Dewangan, L. K., Bhadari, N. K., Men'shchikov, A., et al. 2023, ApJ, 946, 22, doi: 10.3847/1538-4357/acbccc [Cited on page 183.]

Dewangan, L. K., Devaraj, R., Baug, T., & Ojha, D. K. 2017b, The Astrophysical Journal, 848, 51, doi: 10.3847/1538-4357/aa8a79 [Cited 7 times on pages 14, 65, 68, 86, 90, 93, and 115.]

Dewangan, L. K., Dhanya, J. S., Bhadari, N. K., Ojha, D. K., & Baug, T. 2021, Monthly Notices of the Royal Astronomical Society, 506, 6081, doi: 10.1093/mnras/stab2137 [Cited 3 times on pages 26, 124, and 148.]

Dewangan, L. K., Luna, A., Ojha, D. K., et al. 2015, Astrophysical Journal, 811, 79, doi: 10.1088/0004-637X/811/2/79 [Cited 2 times on pages 36 and 153.]

Dewangan, L. K., Luna, A., Ojha, D. K., et al. 2015, ApJ, 811, 79, doi: 10.1088/0004-637X/811/2/79 [Cited 2 times on pages 186 and 187.]

Dewangan, L. K., Mayya, Y. D., Luna, A., & Ojha, D. K. 2015, Astrophysical Journal, 803, 100, doi: 10.1088/0004-637X/803/2/100 [Cited 3 times on pages 154, 156, and 179.]

Dewangan, L. K., Ojha, D. K., & Baug, T. 2017c, The Astrophysical Journal, 844, 15, doi: 10.3847/1538-4357/aa79a5 [Cited on page 94.]

Dewangan, L. K., Ojha, D. K., Baug, T., & Devaraj, R. 2019a, The Astrophysical Journal, 875, 138, doi: 10.3847/1538-4357/ab10dc [Cited 7 times on pages 68, 87, 89, 90, 172, 176, and 185.]

Dewangan, L. K., Ojha, D. K., Luna, A., et al. 2016a, The Astrophysical Journal, 819, 66, doi: 10.3847/0004-637x/819/1/66 [Cited on page 44.]

Dewangan, L. K., Ojha, D. K., Sharma, S., et al. 2020a, The Astrophysical Journal, 903, 13, doi: 10.3847/1538-4357/abb827 [Cited 3 times on pages 64, 65, and 94.]

Dewangan, L. K., Ojha, D. K., Zinchenko, I., Janardhan, P., & Luna, A. 2016b, The Astrophysical Journal, 834, 22, doi: 10.3847/1538-4357/834/1/22 [Cited 3 times on pages 48, 83, and 85.]

Dewangan, L. K., Pirogov, L. E., Bhadari, N. K., & Maity, A. K. 2022b, Monthly Notices of the Royal Astronomical Society, 516, 2988, doi: 10.1093/mnras/stac2334 [Cited 2 times on pages 172 and 176.]

Dewangan, L. K., Pirogov, L. E., Ryabukhina, O. L., Ojha, D. K., & Zinchenko, I. 2019b, The Astrophysical Journal, 877, 1, doi: 10.3847/1538-4357/ab1aa6 [Cited 6 times on pages 15, 24, 93, 108, 115, and 218.]

Dewangan, L. K., Sharma, S., Pandey, R., et al. 2020b, The Astrophysical Journal, 898, 172, doi: 10.3847/1538-4357/ab9c27 [Cited 4 times on pages 36, 193, 195, and 203.]

Dewangan, L. K., Zinchenko, I. I., Zemlyanukha, P. M., et al. 2022c, The Astrophysical Journal, 925, 41, doi: 10.3847/1538-4357/ac36dd [Cited 6 times on pages 36, 151, 152, 153, 154, and 156.]

Dhabal, A., Mundy, L. G., Rizzo, M. J., Storm, S., & Teuben, P. 2018, The Astrophysical Journal, 853, 169, doi: 10.3847/1538-4357/aaa76b [Cited on page 21.]

Dobashi, K., Onishi, T., Iwata, T., et al. 1993, The Astronomical Journal, 105, 1487, doi: 10.1086/116527 [Cited on page 125.]

Draine, B. 2003, Annual Review of Astronomy and Astrophysics, 41, 241, doi: 10.1146/annurev.astro.41.011802.094840 [Cited on page 15.]

Elia, D., Schisano, E., Molinari, S., et al. 2010, Astronomy and Astrophysics, 518, L97, doi: 10.1051/0004-6361/201014651 [Cited on page 50.]

Elia, D., Molinari, S., Schisano, E., et al. 2017, Monthly Notices of the Royal Astronomical Society, 471, 100, doi: 10.1093/mnras/stx1357 [Cited on page 25.]

Elmegreen, B. 1998, in Astronomical Society of the Pacific Conference Series, Vol. 148, Origins, ed. C. E. Woodward, J. M. Shull, & J. Thronson Harley A., 150 [Cited 3 times on pages 3, 191, and 214.]

Elmegreen, B. G., & Lada, C. J. 1977, The Astrophysical Journal, 214, 725, doi: 10.1086/155302 [Cited on page 214.]

Elmegreen, B. G., & Scalo, J. 2004, Annual Review of Astronomy and Astrophysics, 42, 211, doi: 10.1146/annurev.astro.41.011802.094859 [Cited on page 2.]

Enoch, M. L., Evans II, N. J., Sargent, A. I., et al. 2008, The Astrophysical Journal, 684, 1240, doi: 10.1086/589963 [Cited 2 times on pages 5 and 54.]

Eswaraiah, C., Li, D., Furuya, R. S., et al. 2021, The Astrophysical Journal Letters, 912, L27, doi: 10.3847/2041-8213/abeb1c [Cited on page 144.]

Fabricius, C., Luri, X., Arenou, F., et al. 2021, Astronomy and Astrophysics, 649, A5, doi: 10.1051/0004-6361/202039834 [Cited on page 51.]

Falgarone, E., Pety, J., & Hily-Blant, P. 2009, Astronomy and Astrophysics, 507, 355, doi: 10.1051/0004-6361/200810963 [Cited 3 times on pages 153, 172, and 183.]

Fall, S. M., & Frenk, C. S. 1983, The Astronomical Journal, 88, 1626, doi: 10.1086/113452 [Cited on page 168.]

Federrath, C., Klessen, R. S., Iapichino, L., & Beattie, J. R. 2021, Nature Astronomy, 5, 365, doi: 10.1038/s41550-020-01282-z [Cited 2 times on pages 152 and 153.]

Fiege, J. D., & Pudritz, R. E. 2000, Monthly Notices of the Royal Astronomical Society, 311, 105, doi: 10.1046/j.1365-8711.2000.03067.x [Cited on page 22.]

Fischera, J., & Martin, P. G. 2012, Astronomy and Astrophysics, 542, A77, doi: 10.1051/0004-6361/201218961 [Cited 3 times on pages 17, 20, and 116.]

Flaherty, K. M., Pipher, J. L., Megeath, S. T., et al. 2007, The Astrophysical Journal, 663, 1069, doi: 10.1086/518411 [Cited on page 84.]

Frerking, M. A., Langer, W. D., & Wilson, R. W. 1982, The Astrophysical Journal, 262, 590, doi: 10.1086/160451 [Cited 2 times on pages 43 and 105.]

Fukui, Y., Habe, A., Inoue, T., Enokiya, R., & Tachihara, K. 2021a, Publications of the Astronomical Society of Japan, 73, S1, doi: 10.1093/pasj/psaa103 [Cited 5 times on pages 12, 26, 118, 146, and 152.]

Fukui, Y., Inoue, T., Hayakawa, T., & Torii, K. 2021b, Publications of the Astronomical Society of Japan, 73, S405, doi: 10.1093/pasj/psaa079 [Cited on page 152.]

Fuller, G. A., & Myers, P. C. 1992, The Astrophysical Journal, 384, 523, doi: 10.1086/170894 [Cited on page 153.]

Garden, R. P., Hayashi, M., Hasegawa, T., Gatley, I., & Kaifu, N. 1991, The Astrophysical Journal, 374, 540, doi: 10.1086/170143 [Cited on page 43.]

Getman, K. V., Feigelson, E. D., Garmire, G., Broos, P., & Wang, J. 2007, The Astrophysical Journal, 654, 316, doi: 10.1086/509112 [Cited 2 times on pages 47 and 109.]

Ginsburg, A., Bressert, E., Bally, J., & Battersby, C. 2012, Astrophysical Journal Letters, 758, L29, doi: 10.1088/2041-8205/758/2/L29 [Cited on page 12.]

Ginsburg, A., Glenn, J., Rosolowsky, E., et al. 2013, Astrophysical Journal, Supplement Series, 208, 14, doi: 10.1088/0067-0049/208/2/14 [Cited 3 times on pages 36, 51, and 54.]

Goldsmith, P. F., Heyer, M., Narayanan, G., et al. 2008, The Astrophysical Journal, 680, 428, doi: 10.1086/587166 [Cited on page 20.]

Gómez, G. C., Vázquez-Semadeni, E., & Zamora-Avilés, M. 2018, Monthly Notices of the Royal Astronomical Society, 480, 2939, doi: 10.1093/mnras/sty2018 [Cited on page 144.]

Gong, H., & Ostriker, E. C. 2011, Astrophysical Journal, 729, 120, doi: 10.1088/0004-637X/729/2/120 [Cited on page 19.]

Gonzalez-Aviles, M., Lizano, S., & Raga, A. C. 2005, The Astrophysical Journal, 621, 359, doi: 10.1086/427470 [Cited on page 11.]

Goodman, A. A., Barranco, J. A., Wilner, D. J., & Heyer, M. H. 1998, The Astrophysical Journal, 504, 223, doi: 10.1086/306045 [Cited 4 times on pages 152, 153, 172, and 173.]

Goodman, A. A., Rosolowsky, E. W., Borkin, M. A., et al. 2009, Nature, 457, 63, doi: 10.1038/nature07609 [Cited 3 times on pages 152, 153, and 186.]

Goodman, A. A., Alves, J., Beaumont, C. N., et al. 2014, Astrophysical Journal, 797, 53, doi: 10.1088/0004-637X/797/1/53 [Cited on page 16.]

Gregersen, E. M., Evans, Neal J., I., Zhou, S., & Choi, M. 1997, ApJ, 484, 256, doi: 10.1086/304297 [Cited on page 169.]

Griffin, M. J., Abergel, A., Abreu, A., et al. 2010, Astronomy and Astrophysics, 518, L3, doi: 10.1051/0004-6361/201014519 [Cited 2 times on pages 16 and 50.]

Guieu, S., Rebull, L. M., Stauffer, J. R., et al. 2010, Astrophysical Journal, 720, 46, doi: 10.1088/0004-637X/720/1/46 [Cited on page 109.]

Gupta, Y., Ajithkumar, B., Kale, H. S., et al. 2017, Current Science, 113, 707, doi: 10.18520/cs/v113/i04/707-714 [Cited on page 36.]

Gutermuth, R. A., Megeath, S. T., Myers, P. C., et al. 2009, Astrophysical Journal, Supplement Series, 184, 18, doi: 10.1088/0067-0049/184/1/18 [Cited 5 times on pages 47, 52, 83, 85, and 110.]

Hacar, A., Clark, S., Heitsch, F., et al. 2022, arXiv e-prints, arXiv:2203.09562, doi: 10.48550/arXiv.2203.09562 [Cited 4 times on pages 12, 15, 50, and 152.]

Hacar, A., Kainulainen, J., Tafalla, M., Beuther, H., & Alves, J. 2016, Astronomy and Astrophysics, 587, A97, doi: 10.1051/0004-6361/201526015 [Cited 6 times on pages 15, 68, 89, 90, 172, and 176.]

Hacar, A., & Tafalla, M. 2011, Astronomy and Astrophysics, 533, A34, doi: 10.1051/0004-6361/201117039 [Cited 5 times on pages 64, 87, 88, 117, and 152.]

Hacar, A., Tafalla, M., & Alves, J. 2017, Astronomy and Astrophysics, 606, A123, doi: 10.1051/0004-6361/201630348 [Cited 3 times on pages 26, 64, and 152.]

Hacar, A., Tafalla, M., Forbrich, J., et al. 2018, Astronomy and Astrophysics, 610, A77, doi: 10.1051/0004-6361/201731894 [Cited 3 times on pages 94, 116, and 126.]

Hacar, A., Tafalla, M., Kauffmann, J., & Kovács, A. 2013, Astronomy and Astrophysics, 554, A55, doi: 10.1051/0004-6361/201220090 [Cited 6 times on pages 16, 21, 64, 116, 117, and 126.]

Haemmerlé, L., Eggenberger, P., Meynet, G., Maeder, A., & Charbonnel, C. 2016, Astronomy and Astrophysics, 585, A65, doi: 10.1051/0004-6361/201527202 [Cited on page 118.]

Hartmann, L., & Burkert, A. 2007, The Astrophysical Journal, 654, 988, doi: 10.1086/509321 [Cited on page 26.]

Hartmann, L., Megeath, S. T., Allen, L., et al. 2005, The Astrophysical Journal, 629, 881, doi: 10.1086/431472 [Cited 2 times on pages 47 and 109.]

Harvey, P. M., Huard, T. L., Jørgensen, J. K., et al. 2008, The Astrophysical Journal, 680, 495, doi: 10.1086/587687 [Cited 7 times on pages 125, 126, 131, 132, 133, 136, and 141.]

Helfand, D. J., Becker, R. H., White, R. L., Fallon, A., & Tuttle, S. 2006, The Astronomical Journal, 131, 2525, doi: 10.1086/503253 [Cited 2 times on pages 36 and 97.]

Hennebelle, P., & Inutsuka, S. I. 2019, Frontiers in Astronomy and Space Sciences, 6, 5, doi: 10.3389/fspas.2019.00005 [Cited on page 152.]

Herbig, G., & Reipurth, B. 2008, in Handbook of Star Forming Regions, Volume I, ed. B. Reipurth, Vol. 4, 108 [Cited 2 times on pages 124 and 125.]

Herbst, E., & van Dishoeck, E. F. 2009, Annual Review of Astronomy and Astrophysics, 47, 427, doi: 10.1146/annurev-astro-082708-101654 [Cited on page 11.]

Herbst, W., Warner, J. W., Miller, D. P., & Herzog, A. 1982, The Astronomical Journal, 87, 98, doi: 10.1086/113085 [Cited on page 69.]

Heyer, M., Krawczyk, C., Duval, J., & Jackson, J. M. 2009, Astrophysical Journal, 699, 1092, doi: 10.1088/0004-637X/699/2/1092 [Cited 3 times on pages 152, 153, and 172.]

Heyer, M. H., Brunt, C., Snell, R. L., et al. 1998, The Astrophysical Journal Supplement Series, 115, 241, doi: 10.1086/313086 [Cited on page 50.]

Heyer, M. H., & Brunt, C. M. 2004, The Astrophysical Journal, 615, L45, doi: 10.1086/425978 [Cited 5 times on pages 172, 173, 174, 176, and 185.]

Hildebrand, R. H. 1983, Quarterly Journal of the Royal Astronomical Society, 24, 267. https://arxiv.org/abs/9809069v1 [Cited 2 times on pages 44 and 58.]

Hirschi, R. 2017, in Handbook of Supernovae (Cham: Springer International Publishing), 567–600. http://link.springer.com/10.1007/978-3-319-21846-5{_}120 [Cited on page 8.]

Hoemann, E., Heigl, S., & Burkert, A. 2021, Monthly Notices of the Royal Astronomical Society, 507, 3486, doi: 10.1093/mnras/stab1698 [Cited on page 94.]

—. 2022, Monthly Notices of the Royal Astronomical Society, 521, 5152, doi: 10.1093/mnras/stad852 [Cited 6 times on pages 14, 28, 67, 94, 115, and 148.]

Hollenbach, D., & Tielens, A. 1999, Reviews of Modern Physics, 71, 173, doi: 10.1103/RevModPhys.71.173 [Cited on page 192.]

Hsu, W. H., Hartmann, L., Heitsch, F., & Gómez, G. C. 2010, Astrophysical Journal, 721, 1531, doi: 10.1088/0004-637X/721/2/1531 [Cited on page 22.]

Huang, R., & Yu, K. 1995, Stellar Astrophysics, Vol. 166, 133–133, doi: 10.1017/s0074180900227976 [Cited on page 6.]

Hunter, T. R., Phillips, T. G., & Menten, K. M. 1997, The Astrophysical Journal, 478, 283, doi: 10.1086/303775 [Cited on page 95.]

Inoue, T., & Fukui, Y. 2013, Astrophysical Journal Letters, 774, L31, doi: 10.1088/2041-8205/774/2/L31 [Cited on page 152.]

Inoue, T., Hennebelle, P., Fukui, Y., et al. 2018, Publications of the Astronomical Society of Japan, 70, S53, doi: 10.1093/pasj/psx089 [Cited on page 146.]

Inutsuka, S., & Miyama, S. M. 1997, The Astrophysical Journal, 480, 681, doi: 10.1086/303982 [Cited 6 times on pages 17, 20, 22, 67, 116, and 187.]

Inutsuka, S. I., Inoue, T., Iwasaki, K., & Hosokawa, T. 2015, Astronomy and Astrophysics, 580, A49, doi: 10.1051/0004-6361/201425584 [Cited on page 125.]

Inutsuka, S.-I., & Miyama, S. M. 1992, The Astrophysical Journal, 388, 392, doi: 10.1086/171162 [Cited 7 times on pages 17, 20, 22, 67, 86, 116, and 187.]

Izquierdo, A. F., Smith, R. J., Glover, S. C., et al. 2021, Monthly Notices of the Royal Astronomical Society, 500, 5268, doi: 10.1093/mnras/staa3470 [Cited on page 153.]

Jackson, J. M., Finn, S. C., Chambers, E. T., Rathborne, J. M., & Simon, R. 2010, Astrophysical Journal Letters, 719, L185, doi: 10.1088/2041-8205/719/2/L185 [Cited 2 times on pages 15 and 89.]

Johnstone, D., Ciccone, S., Kirk, H., et al. 2017, The Astrophysical Journal, 836, 132, doi: 10.3847/1538-4357/aa5b95 [Cited 2 times on pages 125 and 141.]

Kainulainen, J., Hacar, A., Alves, J., et al. 2016, Astronomy and Astrophysics, 586, A27, doi: 10.1051/0004-6361/201526017 [Cited 9 times on pages 14, 15, 68, 74, 87, 89, 90, 115, and 116.]

Kale, R., & Ishwara-Chandra, C. H. 2021, Experimental Astronomy, 51, 95, doi: 10.1007/s10686-020-09677-6 [Cited on page 197.]

Kauffmann, J., Bertoldi, F., Bourke, T. L., Evans, N. J., & Lee, C. W. 2008, Astronomy and Astrophysics, 487, 993, doi: 10.1051/0004-6361:200809481 [Cited 2 times on pages 58 and 165.]

Kauffmann, J., & Pillai, T. 2010, Astrophysical Journal Letters, 723, L7, doi: 10.1088/2041-8205/723/1/L7 [Cited 3 times on pages 179, 181, and 189.]

Kauffmann, J., Pillai, T., Shetty, R., Myers, P. C., & Goodman, A. A. 2010a, Astrophysical Journal, 712, 1137, doi: 10.1088/0004-637X/712/2/1137 [Cited on page 179.]

—. 2010b, Astrophysical Journal, 716, 433, doi: 10.1088/0004-637X/716/1/433 [Cited on page 179.]

Kaufman, M. J., Wolfire, M. G., & Hollenbach, D. J. 2006, The Astrophysical Journal, 644, 283, doi: 10.1086/503596 [Cited 3 times on pages 192, 208, and 210.]

Kennicutt, R. C., & Evans, N. J. 2012, Annual Review of Astronomy and Astrophysics, 50, 531, doi: 10.1146/annurev-astro-081811-125610 [Cited on page 1.]

Keto, E., & Wood, K. 2006, The Astrophysical Journal, 637, 850, doi: 10.1086/498611 [Cited on page 8.]

Kim, J.-G., Ostriker, E. C., & Filippova, N. 2021, The Astrophysical Journal, 911, 128, doi: 10.3847/1538-4357/abe934 [Cited on page 152.]

Kirk, H., Myers, P. C., Bourke, T. L., et al. 2013, Astrophysical Journal, 766, 115, doi: 10.1088/0004-637X/766/2/115 [Cited 3 times on pages 64, 94, and 118.]

Kirsanova, M. S., Ossenkopf-Okada, V., Anderson, L. D., et al. 2020, Monthly Notices of the Royal Astronomical Society, 497, 2651, doi: 10.1093/mnras/staa2142 [Cited 3 times on pages 208, 210, and 212.]

Klessen, R. S., Ballesteros-Paredes, J., Vazquez-Semadeni, E., & Duran-Rojas, C. 2005, The Astrophysical Journal, 620, 786, doi: 10.1086/427255 [Cited on page 19.]

Koch, E. W., & Rosolowsky, E. W. 2015, Monthly Notices of the Royal Astronomical Society, 452, 3435, doi: 10.1093/mnras/stv1521 [Cited on page 44.]

Könyves, V., André, P., Men'Shchikov, A., et al. 2010, Astronomy and Astrophysics, 518, L106, doi: 10.1051/0004-6361/201014689 [Cited on page 18.]

—. 2015, Astronomy and Astrophysics, 584, A91, doi: 10.1051/0004-6361/201525861 [Cited 2 times on pages 12 and 41.]

Könyves, V., André, P., Arzoumanian, D., et al. 2020, Astronomy & Astrophysics, 635, A34, doi: 10.1051/0004-6361/201834753 [Cited on page 12.]

Kramer, C., Richer, J., Mookerjea, B., Alves, J., & Lada, C. 2003, Astronomy and Astrophysics, 399, 1073, doi: 10.1051/0004-6361:20021823 [Cited on page 125.]

Kroupa, P. 2001, Monthly Notices of the Royal Astronomical Society, 322, 231, doi: 10.1046/j.1365-8711.2001.04022.x [Cited on page 7.]

Krumholz, M. R. 2014, Physics Reports, 539, 49, doi: 10.1016/j.physrep.2014.02.001 [Cited on page 2.]

Krumholz, M. R., & Burkhart, B. 2016, Monthly Notices of the Royal Astronomical Society, 458, 1671, doi: 10.1093/mnras/stw434 [Cited on page 2.]

Krumholz, M. R., & Federrath, C. 2019, Frontiers in Astronomy and Space Sciences, 6, 7, doi: 10.3389/fspas.2019.00007 [Cited on page 152.]

Krumholz, M. R., & McKee, C. F. 2005, The Astrophysical Journal, 630, 250, doi: 10.1086/431734 [Cited 2 times on pages 2 and 152.]

Kuiper, T. B. H., Kuiper, E. N. R., Dickinson, D. F., Turner, B. E., & Zuckerman, B. 1984, The Astrophysical Journal, 276, 211, doi: 10.1086/161604 [Cited on page 165.]

Kumar, M. S. N., Palmeirim, P., Arzoumanian, D., & Inutsuka, S. I. 2020, Astronomy & Astrophysics, 642, A87, doi: 10.1051/0004-6361/202038232 [Cited 5 times on pages 25, 94, 183, 187, and 217.]

Kurtz, S. 2005, Proceedings of the International Astronomical Union, 1, 111, doi: 10.1017/S1743921305004424 [Cited on page 11.]

Kurtz, S., Cesaroni, R., Churchwell, E., Hofner, P., & Walmsley, C. 2000, in Protostars and Planets IV, ed. V. Mannings, A. Boss, & S. Russell, 299–326 [Cited on page 11.]

Kurtz, S., & Franco, J. 2001, doi: 10.48550/arXiv.astro-ph/0111351 [Cited on page 11.]

Kutner, M. L., Machnik, D. E., Dickman, R. L., & Tucker, K. D. 1979, The Astrophysical Journal, 232, 724, doi: 10.1086/157332 [Cited 3 times on pages 68, 69, and 79.]

Lada, C. J. 1999, in NATO Advanced Study Institute (ASI) Series C, Vol. 540, The Origin of Stars and Planetary Systems, ed. C. J. Lada & N. D. Kylafis, 143–192 [Cited on page 6.]

Lada, C. J., Bergin, E. A., Alves, J. F., & Huard, T. L. 2003, The Astrophysical Journal, 586, 286, doi: 10.1086/367610 [Cited 3 times on pages 1, 60, and 137.]

Lada, C. J., & Dame, T. M. 2020, ApJ, 898, 3, doi: 10.3847/1538-4357/ab9bfb [Cited on page 179.]

Lada, C. J., Lada, E. A., Clemens, D. P., & Bally, J. 1994, The Astrophysical Journal, 429, 694, doi: 10.1086/174354 [Cited 2 times on pages 124 and 125.]

Larson, R. B. 1969, Monthly Notices of the Royal Astronomical Society, 145, 271, doi: 10.1093/mnras/145.3.271 [Cited on page 22.]

—. 1981, Monthly Notices of the Royal Astronomical Society, 194, 809, doi: 10.1093/mnras/194.4.809 [Cited 4 times on pages 152, 153, 172, and 175.]

—. 1985, Monthly Notices of the Royal Astronomical Society, 214, 379, doi: 10.1093/mnras/214.3.379 [Cited on page 22.]

Launhardt, R., Stutz, A. M., Schmiedeke, A., et al. 2013, Astronomy and Astrophysics, 551, A98, doi: 10.1051/0004-6361/201220477 [Cited 2 times on pages 39 and 58.]

Lawrence, A., Warren, S. J., Almaini, O., et al. 2007, Monthly Notices of the Royal Astronomical Society, 379, 1599, doi: 10.1111/j.1365-2966.2007.12040.x [Cited 3 times on pages 36, 72, and 97.]

Lefloch, B., & Lazareff, B. 1994, Astronomy and Astrophysics (ISSN 0004-6361), 289, 559 [Cited on page 214.]

Lenzen, R., Hartung, M., Brandner, W., et al. 2003, in Instrument Design and Performance for Optical/Infrared Ground-based Telescopes, ed. M. Iye & A. F. M. Moorwood, Vol. 4841, International Society for Optics and Photonics (SPIE), 944. https://doi.org/10.1117/12.460044 [Cited on page 36.]

Li, C., Qiu, K., Hu, B., & Cao, Y. 2021, The Astrophysical Journal Letters, 918, L2, doi: 10.3847/2041-8213/ac19bc [Cited on page 16.]

Li, D., Kauffmann, J., Zhang, Q., & Chen, W. 2013a, Astrophysical Journal Letters, 768, L5, doi: 10.1088/2041-8205/768/1/L5 [Cited on page 168.]

Li, G. X., & Burkert, A. 2016, Monthly Notices of the Royal Astronomical Society, 461, 3027, doi: 10.1093/mnras/stw1544 [Cited on page 185.]

Li, G. X., Wyrowski, F., Menten, K., & Belloche, A. 2013b, Astronomy and Astrophysics, 559, A34, doi: 10.1051/0004-6361/201322411 [Cited on page 115.]

Li, S., Zhang, Q., Liu, H. B., et al. 2020, The Astrophysical Journal, 896, 110, doi: 10.3847/1538-4357/ab84f1 [Cited 3 times on pages 123, 152, and 184.]

Li, S., Sanhueza, P., Lee, C. W., et al. 2022a, The Astrophysical Journal, 926, 165, doi: 10.3847/1538-4357/ac3df8 [Cited 2 times on pages 123 and 152.]

Li, S., Sanhueza, P., Lu, X., et al. 2022b, The Astrophysical Journal, 939, 102, doi: 10.3847/1538-4357/ac94d4 [Cited on page 184.]

Li, Y., Xu, Y., Sun, Y., et al. 2019, The Astrophysical Journal Supplement Series, 242, 19, doi: 10.3847/1538-4365/ab1e55 [Cited 2 times on pages 50 and 63.]

Liu, H. B., Jiménez-Serra, I., Ho, P. T., et al. 2012, Astrophysical Journal, 756, 10, doi: 10.1088/0004-637X/756/1/10 [Cited on page 94.]

Liu, H. L., Stutz, A., & Yuan, J. H. 2019, Monthly Notices of the Royal Astronomical Society, 487, 1259, doi: 10.1093/mnras/stz1340 [Cited 3 times on pages 103, 116, and 149.]

Liu, H. L., Tej, A., Liu, T., et al. 2022a, Monthly Notices of the Royal Astronomical Society, 511, 4480, doi: 10.1093/mnras/stac378 [Cited 4 times on pages 65, 153, 163, and 173.]

—. 2022b, Monthly Notices of the Royal Astronomical Society, 510, 5009, doi: 10.1093/mnras/stab2757 [Cited 3 times on pages 152, 183, and 184.]

Liu, H.-L., Tej, A., Liu, T., et al. 2023, Monthly Notices of the Royal Astronomical Society, doi: 10.1093/mnras/stad047 [Cited on page 152.]

Lombardi, M., Alves, J., & Lada, C. J. 2010, A&A, 519, L7, doi: 10.1051/0004-6361/201015282 [Cited on page 179.]

Lu, X., Zhang, Q., Liu, H. B., et al. 2018, The Astrophysical Journal, 855, 9, doi: 10.3847/1538-4357/aaad11 [Cited on page 89.]

Lumsden, S. L., Hoare, M. G., Urquhart, J. S., et al. 2013, Astrophysical Journal, Supplement Series, 208, 11, doi: 10.1088/0067-0049/208/1/11 [Cited 3 times on pages 50, 63, and 64.]

Maity, A. K., Dewangan, L. K., Bhadari, N. K., et al. 2023, Monthly Notices of the Royal Astronomical Society, 523, 5388, doi: 10.1093/mnras/stad1644 [Cited on page 27.]

Maity, A. K., Dewangan, L. K., Sano, H., et al. 2022, The Astrophysical Journal, 934, 2, doi: 10.3847/1538-4357/ac7872 [Cited 3 times on pages 27, 146, and 183.]

Mallick, K. K., Ojha, D. K., Tamura, M., et al. 2015, Monthly Notices of the Royal Astronomical Society, 447, 2307, doi: 10.1093/mnras/stu2584 [Cited 2 times on pages 40 and 56.]

Mangum, J. G., & Shirley, Y. L. 2015, Publications of the Astronomical Society of the Pacific, 127, 266, doi: 10.1086/680323 [Cited on page 43.]

Mardones, D., Myers, P. C., Tafalla, M., et al. 1997, ApJ, 489, 719, doi: 10.1086/304812 [Cited on page 169.]

Marsh, K. A., Whitworth, A. P., & Lomax, O. 2015, Monthly Notices of the Royal Astronomical Society, 454, 4282, doi: 10.1093/mnras/stv2248 [Cited 3 times on pages 43, 72, and 198.]

Marsh, K. A., Whitworth, A. P., Lomax, O., et al. 2017, Monthly Notices of the Royal Astronomical Society, 471, 2730, doi: 10.1093/MNRAS/STX1723 [Cited 3 times on pages 42, 72, and 198.]

Mattern, M., Kainulainen, J., Zhang, M., & Beuther, H. 2018, Astronomy and Astrophysics, 616, A78, doi: 10.1051/0004-6361/201731778 [Cited 2 times on pages 15 and 16.]

McKee, C. F., & Ostriker, E. C. 2007, Annual Review of Astronomy and Astrophysics, 45, 565, doi: 10.1146/annurev.astro.45.051806.110602 [Cited 3 times on pages 2, 115, and 151.]

McKee, C. F., & Tan, J. C. 2003, The Astrophysical Journal, 585, 850, doi: 10.1086/346149 [Cited 2 times on pages 9 and 12.]

McLean, B., Greene, G., Lattanzi, M., & Pirenne, B. 2000, in Astronomical Society of the Pacific Conference Series, Vol. 216, Astronomical Data Analysis Software and Systems IX, ed. N. Manset, C. Veillet, & D. Crabtree, 145 [Cited 2 times on pages 36 and 72.]

Men'Shchikov, A. 2013, Astronomy and Astrophysics, 560, A63, doi: 10.1051/0004-6361/201321885 [Cited on page 45.]

—. 2021, Astronomy and Astrophysics, 649, A89, doi: 10.1051/0004-6361/202039913 [Cited 8 times on pages 41, 42, 45, 56, 113, 126, 127, and 131.]

Men'shchikov, A., André, P., Didelon, P., et al. 2010, Astronomy and Astrophysics, 518, L103, doi: 10.1051/0004-6361/201014668 [Cited on page 18.]

Miesch, M. S., & Bally, J. 1994, The Astrophysical Journal, 429, 645, doi: 10.1086/174352 [Cited on page 174.]

Miville-Deschênes, M.-A., Murray, N., & Lee, E. J. 2017, ApJ, 834, 57, doi: 10.3847/1538-4357/834/1/57 [Cited on page 179.]

Moeckel, N., & Burkert, A. 2015, Astrophysical Journal, 807, 67, doi: 10.1088/0004-637X/807/1/67 [Cited on page 21.]

Molinari, S., Swinyard, B., Bally, J., et al. 2010a, Astronomy and Astrophysics, 518, L100, doi: 10.1051/0004-6361/201014659 [Cited 7 times on pages 15, 16, 36, 52, 72, 97, and 198.]

—. 2010b, Publications of the Astronomical Society of the Pacific, 122, 314, doi: 10.1086/651314 [Cited 2 times on pages 42 and 72.]

Molinari, S., Schisano, E., Elia, D., et al. 2016, Astronomy and Astrophysics, 591, A149, doi: 10.1051/0004-6361/201526380 [Cited on page 36.]

Montillaud, J., Juvela, M., Vastel, C., et al. 2019, Astronomy and Astrophysics, 631, A3, doi: 10.1051/0004-6361/201834903 [Cited on page 68.]

Mookerjea, B., Sandell, G., Veena, V. S., et al. 2021, Astronomy and Astrophysics, 648, A40, doi: 10.1051/0004-6361/202040217 [Cited on page 202.]

Mora, A., Merín, B., Solano, E., et al. 2001, Astronomy and Astrophysics, 378, 116, doi: 10.1051/0004-6361:20011098 [Cited on page 69.]

Motte, F., Bontemps, S., & Louvet, F. 2018, Annual Review of Astronomy and Astrophysics, 56, 41, doi: 10.1146/annurev-astro-091916-055235 [Cited 20 times on pages 8, 12, 14, 24, 25, 28, 30, 49, 64, 65, 93, 117, 118, 146, 151, 183, 186, 196, 217, and 219.]

Movsessian, T. A., Magakian, T. Y., & Dodonov, S. N. 2020, Monthly Notices of the Royal Astronomical Society, 500, 2440, doi: 10.1093/mnras/staa3302 [Cited on page 85.]

Myers, P. C. 2009, Astrophysical Journal, 700, 1609, doi: 10.1088/0004-637X/700/2/1609 [Cited 3 times on pages 14, 22, and 24.]

Myers, P. C., Dame, T. M., Thaddeus, P., et al. 1986, The Astrophysical Journal, 301, 398, doi: 10.1086/163909 [Cited on page 152.]

Myers, P. C., & Goodman, A. A. 1988, The Astrophysical Journal, 329, 392, doi: 10.1086/166385 [Cited on page 152.]

Nagai, T., Inutsuka, S., & Miyama, S. M. 1998, The Astrophysical Journal, 506, 306, doi: 10.1086/306249 [Cited on page 26.]

Nagasawa, M. 1987, Progress of Theoretical Physics, 77, 635, doi: 10.1143/PTP.77.635 [Cited on page 17.]

Nakamura, F., Hanawa, T., & Nakano, T. 1995, The Astrophysical Journal, 444, 770, doi: 10.1086/175650 [Cited 2 times on pages 67 and 187.]

Nakamura, F., & Li, Z. 2008, The Astrophysical Journal, 687, 354, doi: 10.1086/591641 [Cited on page 125.]

Nakamura, F., Sugitani, K., Tanaka, T., et al. 2014, Astrophysical Journal Letters, 791, L23, doi: 10.1088/2041-8205/791/2/L23 [Cited 3 times on pages 64, 199, and 220.]

Nassau, J., Stephenson, C., & McConnell, D. 1965, Hamburger Sternw. Warner & Swasey Obs., C06, 0 [Cited on page 69.]

Oliver, R. J., Masheder, M. R., & Thaddeus, P. 1996, Astronomy and Astrophysics, 315, 578, doi: 10.1017/s0074180900128517 [Cited on page 68.]

Olmi, L., Cunningham, M., Elia, D., & Jones, P. 2016, Astronomy & Astrophysics, 594, A58, doi: 10.1051/0004-6361/201628519 [Cited on page 64.]

Onishi, T., Mizuno, A., Kawamura, A., Tachihara, K., & Fukui, Y. 2002, The Astrophysical Journal, 575, 950, doi: 10.1086/341347 [Cited on page 128.]

Ostriker, J. 1964, The Astrophysical Journal, 140, 1056, doi: 10.1086/148005 [Cited 4 times on pages 16, 17, 22, and 86.]

Ouyang, X.-J., Chen, X., Shen, Z.-Q., et al. 2019, The Astrophysical Journal Supplement Series, 245, 12, doi: 10.3847/1538-4365/ab4db2 [Cited 2 times on pages 50 and 63.]

Pabst, C., Higgins, R., Goicoechea, J. R., et al. 2019, Nature, 565, 618, doi: 10.1038/s41586-018-0844-1 [Cited on page 206.]

Pabst, C. H., Goicoechea, J. R., Teyssier, D., et al. 2020, Astronomy and Astrophysics, 639, A2, doi: 10.1051/0004-6361/202037560 [Cited on page 211.]

Padoan, P., Juvela, M., Goodman, A. A., & Nordlund, A. 2001, The Astrophysical Journal, 553, 227, doi: 10.1086/320636 [Cited on page 19.]

Padoan, P., Pan, L., Juvela, M., Haugbølle, T., & Nordlund, Å. 2020, The Astrophysical Journal, 900, 82, doi: 10.3847/1538-4357/abaa47 [Cited 3 times on pages 49, 65, and 152.]

Palla, F., & Stahler, S. W. 1993, The Astrophysical Journal, 418, 414, doi: 10.1086/173402 [Cited on page 8.]

Palmeirim, P., André, P., Kirk, J., et al. 2013, Astronomy and Astrophysics, 550, A38, doi: 10.1051/0004-6361/201220500 [Cited 4 times on pages 20, 41, 143, and 144.]

Pandey, R., Sharma, S., Panwar, N., et al. 2020, The Astrophysical Journal, 891, 81, doi: 10.3847/1538-4357/ab6dc7 [Cited 2 times on pages 193 and 195.]

Paron, S., Cichowolski, S., & Ortega, M. E. 2009, Astronomy and Astrophysics, 506, 789, doi: 10.1051/0004-6361/200912646 [Cited on page 95.]

Pavlyuchenkov, Y., Wiebe, D., Shustov, B., et al. 2008, The Astrophysical Journal, 689, 335, doi: 10.1086/592564 [Cited on page 214.]

Penston, M. V. 1969, Monthly Notices of the Royal Astronomical Society, 145, 457, doi: 10.1093/mnras/145.4.457 [Cited on page 22.]

Peretto, N., Fuller, G. A., Duarte-Cabral, A., et al. 2013, Astronomy and Astrophysics, 555, A112, doi: 10.1051/0004-6361/201321318 [Cited 2 times on pages 13 and 94.]

Pilbratt, G. L., Riedinger, J. R., Passvogel, T., et al. 2010, Astronomy and Astrophysics, 518, L1, doi: 10.1051/0004-6361/201014759 [Cited on page 15.]

Pineda, J. E., Offner, S. S., Parker, R. J., et al. 2015, Nature, 518, 213, doi: 10.1038/nature14166 [Cited on page 152.]

Pirogov, L. 2009, Astronomy Reports, 53, 1127, doi: 10.1134/S1063772909120051 [Cited on page 168.]

Poglitsch, A., Waelkens, C., Geis, N., et al. 2010, Astronomy and Astrophysics, 518, L2, doi: 10.1051/0004-6361/201014535 [Cited on page 16.]

Pon, A., Johnstone, D., & Heitsch, F. 2011, Astrophysical Journal, 740, 88, doi: 10.1088/0004-637X/740/2/88 [Cited 5 times on pages 22, 67, 89, 90, and 92.]

Pon, A., Toalá, J. A., Johnstone, D., et al. 2012, Astrophysical Journal, 756, 145, doi: 10.1088/0004-637X/756/2/145 [Cited 11 times on pages 14, 22, 23, 28, 67, 89, 90, 92, 115, 148, and 219.]

Quireza, C., Rood, R. T., Balser, D. S., & Bania, T. M. 2006, The Astrophysical Journal Supplement Series, 165, 338, doi: 10.1086/503901 [Cited on page 153.]

Racine, R. 1968, The Astronomical Journal, 73, 233, doi: 10.1086/110624 [Cited on page 69.]

Ragan, S., Henning, T., Krause, O., et al. 2012, Astronomy and Astrophysics, 547, A49, doi: 10.1051/0004-6361/201219232 [Cited on page 10.]

Ragan, S. E., Henning, T., Tackenberg, J., et al. 2014, Astronomy and Astrophysics, 568, A73, doi: 10.1051/0004-6361/201423401 [Cited on page 115.]

Ramírez-Galeano, L., Ballesteros-Paredes, J., Smith, R. J., Camacho, V., & Zamora-Avilés, M. 2022, MNRAS, 515, 2822, doi: 10.1093/mnras/stac1848 [Cited on page 184.]

Rathborne, J. M., Jackson, J. M., & Simon, R. 2006, The Astrophysical Journal, 641, 389, doi: 10.1086/500423 [Cited 2 times on pages 2 and 10.]

Rathborne, J. M., Johnson, A. M., Jackson, J. M., Shah, R. Y., & Simon, R. 2009, Astrophysical Journal, Supplement Series, 182, 131, doi: 10.1088/0067-0049/182/1/131 [Cited 2 times on pages 95 and 96.]

Rigby, A. J., Moore, T. J., Plume, R., et al. 2016, Monthly Notices of the Royal Astronomical Society, 456, 2885, doi: 10.1093/mnras/stv2808 [Cited 2 times on pages 36 and 97.]

Risacher, C., Güsten, R., Stutzki, J., et al. 2016, Astronomy and Astrophysics, 595, A34, doi: 10.1051/0004-6361/201629045 [Cited on page 198.]

Rivera-Ingraham, A., Ade, P. A., Bock, J. J., et al. 2010, Astrophysical Journal, 723, 915, doi: 10.1088/0004-637X/723/1/915 [Cited 2 times on pages 95 and 96.]

Rodríguez, L. F. 2006, in Revista Mexicana de Astronomia y Astrofisica: Serie de Conferencias, ed. H. Beuther, R. S. Klessen, C. P. Dullemond, & T. Henning, Vol. 26, 18–21 [Cited 4 times on pages 8, 9, 12, and 49.]

Rolffs, R., & Schilke, P. 2011, EAS Publications Series, 52, 303, doi: 10.1051/eas/1152058 [Cited on page 11.]

Rosen, A. L., Offner, S. S., Sadavoy, S. I., et al. 2020, Space Science Reviews, 216, 62, doi: 10.1007/s11214-020-00688-5 [Cited 2 times on pages 49 and 64.]

Rosolowsky, E., & Leroy, A. 2006, Publications of the Astronomical Society of the Pacific, 118, 590, doi: 10.1086/502982 [Cited 2 times on pages 153 and 158.]

Rosolowsky, E. W., Pineda, J. E., Kauffmann, J., & Goodman, A. A. 2008, The Astrophysical Journal, 679, 1338, doi: 10.1086/587685 [Cited 3 times on pages 153, 156, and 163.]

Roy, A., Ade, P. A., Bock, J. J., et al. 2011, Astrophysical Journal, 730, 142, doi: 10.1088/0004-637X/730/2/142 [Cited 2 times on pages 124 and 125.]

Russeil, D., Georgelin, Y., Georgelin, Y., Le Coarer, E., & Marcelin, M. 1995, \Aaps, 114, 557 [Cited on page 194.]

Sadavoy, S. I., Di Francesco, J., André, P., et al. 2012, Astronomy and Astrophysics, 540, A10, doi: 10.1051/0004-6361/201117934 [Cited on page 40.]

Saha, A., Tej, A., Liu, H.-L., et al. 2022, Monthly Notices of the Royal Astronomical Society, 516, 1983, doi: 10.1093/mnras/stac2353 [Cited 3 times on pages 180, 183, and 184.]

Saito, H., Saito, M., Moriguchi, Y., & Fukui, Y. 2006, Publications of the Astronomical Society of Japan, 58, 343, doi: 10.1093/pasj/58.2.343 [Cited 3 times on pages 50, 63, and 128.]

Saito, H., Saito, M., Sunada, K., & Yonekura, Y. 2007, The Astrophysical Journal, 659, 459, doi: 10.1086/512058 [Cited 2 times on pages 50 and 63.]

Salaris, M., & Cassisi, S. 2006, Evolution of Stars and Stellar Populations, 1–374, doi: 10.1002/0470033452 [Cited on page 7.]

Salpeter, E. E. 1955, The Astrophysical Journal, 121, 161, doi: 10.1086/145971 [Cited on page 7.]

Sanhueza, P., Contreras, Y., Wu, B., et al. 2019, The Astrophysical Journal, 886, 102, doi: 10.3847/1538-4357/ab45e9 [Cited 2 times on pages 12 and 13.]

Santos, J. C., Bronfman, L., Mendoza, E., et al. 2022, The Astrophysical Journal, 925, 3, doi: 10.3847/1538-4357/ac36cc [Cited on page 165.]

Schneider, N., Csengeri, T., Bontemps, S., et al. 2010, Astronomy and Astrophysics, 520, A49, doi: 10.1051/0004-6361/201014481 [Cited on page 20.]

Schneider, N., Csengeri, T., Hennemann, M., et al. 2012, Astronomy and Astrophysics, 540, L11, doi: 10.1051/0004-6361/201118566 [Cited 3 times on pages 24, 64, and 93.]

Schneider, N., Simon, R., Guevara, C., et al. 2020, Publications of the Astronomical Society of the Pacific, 132, 1, doi: 10.1088/1538-3873/aba840 [Cited 3 times on pages 36, 192, and 198.]

Schneider, S., & Elmegreen, B. G. 1979, The Astrophysical Journal Supplement Series, 41, 87, doi: 10.1086/190609 [Cited on page 15.]

Schuller, F., Menten, K. M., Contreras, Y., et al. 2009, Astronomy and Astrophysics, 504, 415, doi: 10.1051/0004-6361/200811568 [Cited 2 times on pages 36 and 97.]

Shetty, R., Beaumont, C. N., Burton, M. G., Kelly, B. C., & Klessen, R. S. 2012, Monthly Notices of the Royal Astronomical Society, 425, 720, doi: 10.1111/j.1365-2966.2012.21588.x [Cited on page 156.]

Shimajiri, Y., André, P., Ntormousi, E., et al. 2019a, Astronomy and Astrophysics, 632, A83, doi: 10.1051/0004-6361/201935689 [Cited 5 times on pages 20, 26, 123, 124, and 149.]

Shimajiri, Y., André, P., Palmeirim, P., et al. 2019b, Astronomy & Astrophysics, 623, A16, doi: 10.1051/0004-6361/201834399 [Cited on page 20.]

Shirley, Y. L. 2015, Publications of the Astronomical Society of the Pacific, 127, 299, doi: 10.1086/680342 [Cited on page 166.]

Shu, F. H. 1977, The Astrophysical Journal, 214, 488, doi: 10.1086/155274 [Cited on page 22.]

Shu, F. H., Adams, F. C., & Lizano, S. 1987, Annual Review of Astronomy and Astrophysics, 25, 23, doi: 10.1146/annurev.aa.25.090187.000323 [Cited 3 times on pages 4, 8, and 151.]

Singh, A., Matzner, C. D., Friesen, R. K., et al. 2021, The Astrophysical Journal, 922, 87, doi: 10.3847/1538-4357/ac20d2 [Cited 2 times on pages 168 and 184.]

Skrutskie, M. F., Cutri, R. M., Stiening, R., et al. 2006, The Astronomical Journal, 131, 1163, doi: 10.1086/498708 [Cited 4 times on pages 36, 52, 72, and 97.]

Smith, M. D. 2004, The Origin of Stars (PUBLISHED BY IMPERIAL COLLEGE PRESS AND DISTRIBUTED BY WORLD SCIENTIFIC PUBLISHING CO.), doi: 10.1142/p353. https://www.worldscientific.com/worldscibooks/10.1142/p353 [Cited 6 times on pages 1, 2, 3, 4, 5, and 6.]

Smith, R. J., Glover, S. C., & Klessen, R. S. 2014, Monthly Notices of the Royal Astronomical Society, 445, 2900, doi: 10.1093/mnras/stu1915 [Cited 2 times on pages 26 and 149.]

Smith, R. J., Glover, S. C., Klessen, R. S., & Fuller, G. A. 2016, Monthly Notices of the Royal Astronomical Society, 455, 3640, doi: 10.1093/mnras/stv2559 [Cited 2 times on pages 21 and 116.]

Smith, R. J., Longmore, S., & Bonnell, I. 2009, Monthly Notices of the Royal Astronomical Society, 400, 1775, doi: 10.1111/j.1365-2966.2009.15621.x [Cited on page 13.]

Sofia, U. J., Lauroesch, J. T., Meyer, D. M., & Cartledge, S. I. B. 2004, The Astrophysical Journal, 605, 272, doi: 10.1086/382592 [Cited on page 211.]

Solomon, P. M., Rivolo, A. R., Barrett, J., & Yahil, A. 1987, The Astrophysical Journal, 319, 730, doi: 10.1086/165493 [Cited 3 times on pages 114, 152, and 172.]

Sousbie, T. 2011, Monthly Notices of the Royal Astronomical Society, 414, 350, doi: 10.1111/j.1365-2966.2011.18394.x [Cited on page 44.]

Sreenilayam, G., Fich, M., Ade, P., et al. 2014, Astronomical Journal, 147, 53, doi: 10.1088/0004-6256/147/3/53 [Cited 3 times on pages 194, 195, and 215.]

Sridharan, T. K., Beuther, H., Saito, M., Wyrowski, F., & Schilke, P. 2005, The Astrophysical Journal, 634, L57, doi: 10.1086/498644 [Cited on page 10.]

Stahler, S. W., & Palla, F. 2005, The formation of stars (Oxford: Wiley) [Cited on page 68.]

Storm, S., Mundy, L. G., Fernández-López, M., et al. 2014, Astrophysical Journal, 794, 165, doi: 10.1088/0004-637X/794/2/165 [Cited on page 173.]

Su, Y., Zhang, S., Shao, X., & Yang, J. 2015, Astrophysical Journal, 811, 134, doi: 10.1088/0004-637X/811/2/134 [Cited on page 115.]

Su, Y., Yang, J., Zhang, S., et al. 2019, The Astrophysical Journal Supplement Series, 240, 9, doi: 10.3847/1538-4365/aaf1c8 [Cited 2 times on pages 36 and 52.]

Suri, S., Sánchez-Monge, Á., Schilke, P., et al. 2019, Astronomy and Astrophysics, 623, A142, doi: 10.1051/0004-6361/201834049 [Cited on page 21.]

Svoboda, B. E., Shirley, Y. L., Traficante, A., et al. 2019, The Astrophysical Journal, 886, 36, doi: 10.3847/1538-4357/ab40ca [Cited 2 times on pages 12 and 13.]

Syed, J., Soler, J. D., Beuther, H., et al. 2022, Astronomy & Astrophysics, 657, A1, doi: 10.1051/0004-6361/202141265 [Cited on page 16.]

Tafalla, M., & Hacar, A. 2015, Astronomy and Astrophysics, 574, A104, doi: 10.1051/0004-6361/201424576 [Cited 3 times on pages 21, 116, and 149.]

Takahira, K., Shima, K., Habe, A., & Tasker, E. J. 2018, Publications of the Astronomical Society of Japan, 70, doi: 10.1093/pasj/psy011 [Cited on page 27.]

Takahira, K., Tasker, E. J., & Habe, A. 2014, The Astrophysical Journal, 792, 63, doi: 10.1088/0004-637X/792/1/63 [Cited on page 27.]

Teague, R. 2019, Research Notes of the AAS, 3, 74, doi: 10.3847/2515-5172/ab2125 [Cited 2 times on pages 37 and 163.]

Tielens, A. G. 2008, Annual Review of Astronomy and Astrophysics, 46, 289, doi: 10.1146/annurev.astro.46.060407.145211 [Cited on page 76.]

Tielens, A. G. G. M., & Hollenbach, D. 1985a, The Astrophysical Journal, 291, 722, doi: 10.1086/163111 [Cited 2 times on pages 192 and 211.]

—. 1985b, The Astrophysical Journal, 291, 747, doi: 10.1086/163112 [Cited on page 192.]

Tigé, J., Motte, F., Russeil, D., et al. 2017, Astronomy & Astrophysics, 602, A77, doi: 10.1051/0004-6361/201628989 [Cited 6 times on pages 25, 65, 118, 123, 144, and 146.]

Toalá, J. A., Vázquez-Semadeni, E., & Gómez, G. C. 2012, Astrophysical Journal, 744, 190, doi: 10.1088/0004-637X/744/2/190 [Cited 2 times on pages 22 and 115.]

Traficante, A., Fuller, G. A., Smith, R. J., et al. 2018a, Monthly Notices of the Royal Astronomical Society, 473, 4975, doi: 10.1093/mnras/stx2672 [Cited 6 times on pages 12, 13, 153, 169, 185, and 186.]

Traficante, A., Duarte-Cabral, A., Elia, D., et al. 2018b, Monthly Notices of the Royal Astronomical Society, 477, 2220, doi: 10.1093/mnras/sty798 [Cited 5 times on pages 153, 179, 183, 184, and 185.]

Treviño-Morales, S. P., Fuente, A., Sánchez-Monge, Á., et al. 2019a, Astronomy & Astrophysics, 629, A81, doi: 10.1051/0004-6361/201935260 [Cited 3 times on pages 16, 64, and 65.]

Treviño-Morales, S. P., Fuente, A., Sánchez-Monge, et al. 2019b, Astronomy and Astrophysics, 629, A81, doi: 10.1051/0004-6361/201935260 [Cited 3 times on pages 24, 94, and 118.]

Umemoto, T., Minamidani, T., Kuno, N., et al. 2017, Publications of the Astronomical Society of Japan, 69, 78, doi: 10.1093/pasj/psx061 [Cited 5 times on pages 36, 71, 72, 97, and 194.]

Urquhart, J. S., Moore, T. J., Csengeri, T., et al. 2014, Monthly Notices of the Royal Astronomical Society, 443, 1555, doi: 10.1093/mnras/stu1207 [Cited 2 times on pages 180 and 189.]

Urquhart, J. S., König, C., Giannetti, A., et al. 2018, Monthly Notices of the Royal Astronomical Society, 473, 1059, doi: 10.1093/mnras/stx2258 [Cited 3 times on pages 95, 96, and 104.]

van den Bergh, S. 1966, The Astronomical Journal, 71, 990, doi: 10.1086/109995 [Cited on page 68.]

Van Loo, S., Keto, E., & Zhang, Q. 2014, Astrophysical Journal, 789, 37, doi: 10.1088/0004-637X/789/1/37 [Cited on page 26.]

Vázquez-Semadeni, E., González-Samaniego, A., & Colín, P. 2017, Monthly Notices of the Royal Astronomical Society, 467, 1313, doi: 10.1093/mnras/stw3229 [Cited on page 49.]

Vazquez-Semadeni, E., Ostriker, E., Passot, T., Gammie, C., & Stone, J. 2000, in Protostars and Planets IV, ed. V. Mannings, A. Boss, & S. Russell, 3 [Cited on page 152.]

Vázquez-Semadeni, E., Palau, A., Ballesteros-Paredes, J., Gómez, G. C., & Zamora-Avilés, M. 2019, Monthly Notices of the Royal Astronomical Society, 490, 3061, doi: 10.1093/mnras/stz2736 [Cited 2 times on pages 13 and 49.]

Vázquez-Semadeni, E., Palau, A., Ballesteros-Paredes, J., Gómez, G. C., & Zamora-Avilés, M. 2019, MNRAS, 490, 3061, doi: 10.1093/mnras/stz2736 [Cited on page 184.]

Vazquez-Semadeni, E., Gomez, G. C., Jappsen, A. K., et al. 2007, The Astrophysical Journal, 657, 870, doi: 10.1086/510771 [Cited 2 times on pages 19 and 22.]

Vig, S., Ghosh, S. K., Kulkarni, V. K., Ojha, D. K., & Verma, R. P. 2006, The Astrophysical Journal, 637, 400, doi: 10.1086/498389 [Cited on page 95.]

Vink, J. S. 2015, Astrophysics and Space Science Library, Vol. 412, Very Massive Stars in the Local Universe, ed. J. S. Vink (Cham: Springer International Publishing), 1–8, doi: 10.1007/978-3-319-09596-7_1. https://link.springer.com/10.1007/978-3-319-09596-7 [Cited on page 8.]

Virtanen, P., Gommers, R., Oliphant, T. E., et al. 2020, Nature Methods, 17, 261, doi: 10.1038/s41592-019-0686-2 [Cited on page 98.]

Vogt, N., & Moffat, A. 1975, Astronomy & Astrophysics, 45, 405 [Cited on page 194.]

Vutisalchavakul, N., Evans II, N. J., & Heyer, M. 2016, The Astrophysical Journal, 831, 73, doi: 10.3847/0004-637x/831/1/73 [Cited on page 152.]

Vzquez-Semadeni, E., Gómez, G. C., Jappsen, A. K., Ballesteros-Paredes, J., & Klessen, R. S. 2009, Astrophysical Journal, 707, 1023, doi: 10.1088/0004-637X/707/2/1023 [Cited on page 49.]

Wang, J.-W., Lai, S.-P., Clemens, D. P., et al. 2019a, The Astrophysical Journal, 888, 13, doi: 10.3847/1538-4357/ab5c1c [Cited 4 times on pages 118, 125, 141, and 144.]

Wang, J.-W., Lai, S.-P., Eswaraiah, C., et al. 2017, The Astrophysical Journal, 849, 157, doi: 10.3847/1538-4357/aa937f [Cited 2 times on pages 125 and 141.]

—. 2019b, The Astrophysical Journal, 876, 42, doi: 10.3847/1538-4357/ab13a2 [Cited 10 times on pages 24, 26, 125, 141, 142, 144, 145, 148, 150, and 218.]

Wang, J.-W., Koch, P. M., Tang, Y.-W., et al. 2022, The Astrophysical Journal, 931, 115, doi: 10.3847/1538-4357/ac6872 [Cited on page 144.]

Wang, K., Testi, L., Burkert, A., et al. 2016, The Astrophysical Journal Supplement Series, 226, 9, doi: 10.3847/0067-0049/226/1/9 [Cited on page 114.]

Ward-Thompson, D., Kirk, J. M., André, P., et al. 2010, Astronomy and Astrophysics, 518, L92, doi: 10.1051/0004-6361/201014618 [Cited on page 18.]

Weaver, R., McCray, R., Castor, J., Shapiro, P., & Moore, R. 1977, The Astrophysical Journal, 218, 377, doi: 10.1086/155692 [Cited on page 211.]

Weingartner, J., & Draine, B. 2001, The Astrophysical Journal, 548, 296, doi: 10.1086/318651 [Cited 3 times on pages 44, 168, and 181.]

Whitney, B., Benjamin, R., Meade, M., et al. 2011, in American Astronomical Society Meeting Abstracts, Vol. 217, American Astronomical Society Meeting Abstracts #217, 241.16 [Cited 4 times on pages 36, 52, 82, and 198.]

Whitworth, A. P., Bhattal, A. S., Chapman, S. J., Disney, M. J., & Turner, J. A. 1994, Monthly Notices of the Royal Astronomical Society, 268, 291, doi: 10.1093/mnras/268.1.291 [Cited on page 214.]

Whitworth, A. P., & Priestley, F. D. 2021, Monthly Notices of the Royal Astronomical Society, 504, 3156, doi: 10.1093/mnras/stab1125 [Cited 3 times on pages 28, 199, and 220.]

Williams, G. M., Peretto, N., Avison, A., Duarte-Cabral, A., & Fuller, G. A. 2018, Astronomy and Astrophysics, 613, A11, doi: 10.1051/0004-6361/201731587 [Cited on page 88.]

Williams, J. P., de Geus, E. J., & Blitz, L. 1994, The Astrophysical Journal, 428, 693, doi: 10.1086/174279 [Cited 2 times on pages 74 and 128.]

Wilson, R. W., Jefferts, K. B., & Penzias, A. A. 1970, The Astrophysical Journal, 161, L43, doi: 10.1086/180567 [Cited on page 14.]

Wood, D. O. S., & Churchwell, E. 1989, The Astrophysical Journal Supplement Series, 69, 831, doi: 10.1086/191329 [Cited on page 95.]

Wright, E. L., Eisenhardt, P. R., Mainzer, A. K., et al. 2010, Astronomical Journal, 140, 1868, doi: 10.1088/0004-6256/140/6/1868 [Cited 5 times on pages 36, 52, 72, 97, and 198.]

Wu, Y., Wei, Y., Zhao, M., et al. 2004, Astronomy and Astrophysics, 426, 503, doi: 10.1051/0004-6361:20035767 [Cited 2 times on pages 50 and 63.]

Wyrowski, F., Güsten, R., Menten, K. M., et al. 2016, Astronomy & Astrophysics, 585, A149, doi: 10.1051/0004-6361/201526361 [Cited on page 13.]

Xu, F.-W., Wang, K., Liu, T., et al. 2023, Monthly Notices of the Royal Astronomical Society, 520, 3259, doi: 10.1093/mnras/stad012 [Cited on page 152.]

Xu, J. L., Xu, Y., Zhang, C. P., et al. 2018, Astronomy and Astrophysics, 609, A43, doi: 10.1051/0004-6361/201629189 [Cited on page 43.]

Yang, A. Y., Urquhart, J. S., Thompson, M. A., et al. 2021, Astronomy & Astrophysics, 645, A110, doi: 10.1051/0004-6361/202038608 [Cited on page 11.]

Yorke, H. W., & Sonnhalter, C. 2002, The Astrophysical Journal, 569, 846, doi: 10.1086/339264 [Cited on page 9.]

Yu, N. P., Xu, J. L., & Wang, J. J. 2019, Astronomy and Astrophysics, 622, A155, doi: 10.1051/0004-6361/201832962 [Cited 5 times on pages 24, 68, 90, 115, and 218.]

Yuan, J., Li, J.-Z., Wu, Y., et al. 2017a, The Astrophysical Journal, 852, 12, doi: 10.3847/1538-4357/aa9d40 [Cited on page 13.]

Yuan, J., Wu, Y., Ellingsen, S. P., et al. 2017b, The Astrophysical Journal Supplement Series, 231, 11, doi: 10.3847/1538-4365/aa7204 [Cited on page 152.]

Yuan, L., Li, G. X., Zhu, M., et al. 2020, Astronomy and Astrophysics, 637, A67, doi: 10.1051/0004-6361/201936625 [Cited 2 times on pages 24 and 218.]

Zamora-Avilés, M., Ballesteros-Paredes, J., & Hartmann, L. W. 2017, Monthly Notices of the Royal Astronomical Society, 472, 647, doi: 10.1093/MNRAS/STX1995 [Cited on page 21.]

Zavagno, A., Deharveng, L., Comerón, F., et al. 2006, Astronomy and Astrophysics, 446, 171, doi: 10.1051/0004-6361:20053952 [Cited on page 214.]

Zavagno, A., Pomarès, M., Deharveng, L., et al. 2007, Astronomy and Astrophysics, 472, 835, doi: 10.1051/0004-6361:20077474 [Cited on page 214.]

Zernickel, A., Schilke, P., & Smith, R. J. 2013, Astronomy and Astrophysics, 554, L2, doi: 10.1051/0004-6361/201321425 [Cited 7 times on pages 24, 68, 89, 91, 115, 123, and 218.]

Zhang, M., Kainulainen, J., Mattern, M., Fang, M., & Henning, T. 2019, Astronomy and Astrophysics, 622, A52, doi: 10.1051/0004-6361/201732400 [Cited 2 times on pages 114 and 115.]

Zhang, S., Yang, J., Xu, Y., et al. 2020, The Astrophysical Journal Supplement Series, 248, 15, doi: 10.3847/1538-4365/ab879a [Cited 6 times on pages 125, 132, 133, 136, 141, and 144.]

Zhou, J. W., Wyrowski, F., Neupane, S., et al. 2023, A&A, 676, A69, doi: 10.1051/0004-6361/202346500 [Cited on page 24.]

Zhou, J. X., Li, G. X., & Chen, B. Q. 2022, Monthly Notices of the Royal Astronomical Society, 513, 638, doi: 10.1093/mnras/stac900 [Cited on page 152.]

Zinnecker, H., & Yorke, H. W. 2007, Annual Review of Astronomy and Astrophysics, 45, 481, doi: 10.1146/annurev.astro.44.051905.092549 [Cited 3 times on pages 8, 10, and 49.]

Zucker, C., Battersby, C., & Goodman, A. 2018, The Astrophysical Journal, 864, 153, doi: 10.3847/1538-4357/aacc66 [Cited on page 16.]